UNIVERSITY OF CANTERBURY

Development of photoelectrochemical anodes for solar redox flow batteries

---

Author:

Maxime SAVOIE

Supervisors:

A./Prof. Aaron T MARSHALL

A./Prof. Vladimir GOLOVKO

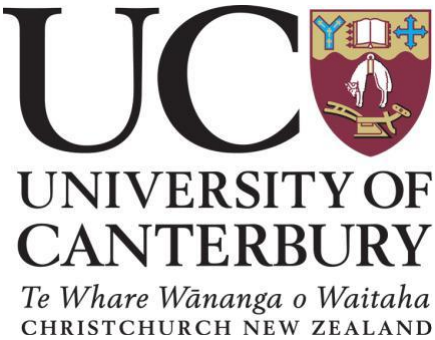

A thesis submitted in fulfilment of the requirements

for the degree of Doctor of Philosophy

in the

Department of Chemical and Process Engineering

College of Engineering

July 1, 2020

University of Canterbury

Abstract

College of Engineering

Development of photoelectrochemical anodes for solar redox flow batteries

by Maxime SAVOIE

Photoelectrochemical processes have been widely studied for water splitting and dye-sensitized solar cells. Lately, a new concept has emerged, the photoelectrochemical redox flow battery. A photoelectrochemical redox battery is charged by using a semiconducting electrode to convert solar energy into stored chemical energy. Currently, the majority of published photoelectrochemical tests are conducted using two-electrode measurements with V^{4+}/V^{5+} as redox couple in the anodic electrolyte. Here, the behavior of a TiO_2 photoanode is studied using a three-electrode measurement, to gain a greater understanding of the factors which limit photoelectrochemical redox batteries. The recorded linear sweep voltammetry measurements had two different regions. The first region between 0.4 V to 0.7 V vs Ag|AgCl typically shows photo-oxidation of V^{4+} to V^{5+}, confirmed by UV Vis spectroscopy and oxidation of V^{3+} to V^{4+} in the dark. The second region was between 0 V and 0.4 V vs Ag|AgCl, wherein electrochemical reduction of V^{4+} to V^{3+} occurred in parallel with the photoxidation of V^{3+} species to V^{4+}. By changing the deposition process, and the used solvent used, the photoactivity of the TiO_2 photoanode has been improved for $VOSO_4$ photo-oxidation. The addition of titanium isopropoxide formed an interconnection between the TiO_2 particles and the substrate. Finally, the addition of an underlayer grown directly on the FTO substrate improves the TiO_2 performance by creating a proper contact between the TiO_2 film and the FTO substrate (350 $\mu A\ cm^{-2}\ mg^{-1}$). The TiO_2 performance can be increased by doping the TiO_2 layer or through the deposition of gold nanoparticles and nanoclusters: The addition of 1.7 wt% Au nanoparticles to a standard photoelectrode leads to the photocurrent enhanced by 30 % and an addition of 8.5 wt% of Au_6 nanoclusters leads to a photocurrent increase of 50%, due to the extension of the absorption range.

The effect of different redox couples in hydrochloric acid and an organic solvent was studied. A promising redox couple was a standard dye-sensitised redox couple, I_3/I^- coupled with $Fe^{3+/}Fe^{2+}$. The $Fe^{3+/}Fe^{2+}$ was shown to give a photocurrent of 119 ± 8 µA cm^{-2} mg^{-1} at 0.5 V *vs.* Ag|AgCl. Therefore, by combining the the materials with the best photocurrent of each study, a photocurrent of 82 ± 0.5 µA cm^{-2} (410.2 ± 0.5µA cm^{-2} mg^{-1}) could be achieved for $VOSO_4$ electrolyte at 0.5 V *vs.* Ag|AgCl with the addition of 8.5 Wt% Au_6 nanoclusters to the hydrothermal growth film and an additional 85% P-25 15% TTIP film. The triiodide electrolyte gave a photocurrent of 99.3 ± 0.2 µA cm^{-2} (496.3± 0.2 µA cm^{-2} mg^{-1}) ^{at} 0.5 V *vs.* Ag|AgCl. The Fe^{2+} electrolyte allowed a photocurrent of 107 ± 0.4 µA cm^{-2} (535 ± 0.4 µA cm^{-2} mg^{-1}) at 0.5 V *vs.* Ag|AgCl

Acknowledgements

The journey of a PhD student is long, complicated and challenging. Fortunately, it is not a solo adventure but a team effort to extract the best out of the thesis subject. That is why I wish to thanks the following people who make this journey by my side.

First, I wish to thanks my both supervisors equally: A./Prof. Aaron T Marshall and A./Prof. Vladimir Golovko. A./Prof. Aaron T Marshall for his day to day support, his interest and even excitement for the research we conduct and for all his ideas which first look challenging to realise but finally show me the way to go through these challenges. Thanks a lot. A./Prof. Vladimir Golovko for his huge help during the session of brainstorming and for his capability to bring me to the ground and avoiding to go too far in the fantasy. For his constant support, thanks a lot.

A special thanks also to Paula C. Angelomé for the preparation of mesoporous underlayer and Sam Nesbitt for his help on the preparation of hydrothermal underlayer and his help with some part of the background literature.

Then, I wish to thanks the technician of chemical and process engineering department (CAPE): Stephen Beuzenberg, Graham Mitchell, Leigh Richardson, David Rathgen, Graham Furniss, Frank Weerts for their massive help on the design and conception of the photoelectrochemical cell and the ultrasonic and airbrush spray robot. Glenn Wilson for the support on the chemicals ordering and Michael Sandridge and Rayleen Fredericks for making the labs running perfectly

I wish thanks the rest of the CAPE staff for their support during this PhD. Especially Joanne Pollard and Rachel Rogers for all the administrative parts of my PhD. I wish to thanks all my friends and former PhD students for their personal and scientific support. I want to thank, in particular, Sam Nesbitt and Maryam Shojaei for their help on the solar redox flow battery, being three people on the same project create a unique team dynamic. Samuel Martin Treceno and Wasim Khan for their moral support. Leatham Landon Lane for his help on the electrochemical science. Finally, I wish to thanks the nature and landscape of New Zealand, which allowed me to be less stressed and give me peace and quiet environment to be able to focus on myself.

Contents

List of Abbreviations

FTO	**F**luorine doped **T**in **O**xide
PV	**P**hotovoltaic
RFB	**R**edox **F**low **B**attery
LED	**L**ight-**E**mitting **D**iode
UV	**U**ltra-**V**iolet
NHE	**N**ormal **h**ydrogen **E**lectrode
SHE	**S**tandard **h**ydrogen **E**lectrode
DI	**De**i**o**nized
ITO	**I**ndium doped **T**in **O**xide
N	**N**umber of FTO glass
PVDF	**P**oly **V**iny**D**ylene **F**luorine
CMC	**C**arboxyl **M**ethyl **C**ellulose
SBR	**S**tyrene **B**utadiene **R**ubber
SEM	**S**canning **E**lectronic **M**icroscopy
bpy	**b**i**py**ridine
acac	**ac**etyl**ac**etone

Physical Constants

Speed of light	c_0	$= 2.99 \times 10^{-8}$	$m\ s^{-1}$
Gas constant	R	$= 8.31$	$J\ mol^{-1}\ K^{-1}$
Plank constant	h	$= 6.62 \times 10^{-34}$	J s
		$= 4{:}13\ 10^{-15}$	eV s
Faraday constant	F	$= 96485.33$	$s\ A\ mol^{-1}$
Avogadro number	N_A	$= 6.02 \times 10^{-23}$	mol
Electron charge	e	$= 1.60 \times 10^{-19}$	C
Electric constant permittivity	ε_0	$= 8.84 \times 10^{-12}$	$C^2\ N^{-1}\ m^{-2}$
Magnetic constant permeability	μ_0	$= 12.56 \times 10^{-7}$	$m\ A^{-1}$
Boltzmann's constant	k	$= 1.38 \times 10^{-23}$	$J\ K^{-1}$

List of Symbols

P	Power	W (J s^{-1})
j	Current density	A m^{-2}
I	Current	A
E	Potential	V
C	Concentration	mol L^{-1}
V	Volume	L
T	Temperature	ºC
n	Number of charge carrier particles	
G	Gibbs energy	J
R	Resistance	Ω
A	Current	A
ω	Angular frequency	rad
γ	Activity coefficient	mol L^{-1}
η	Overpotential	V

1. Introduction

1.1 General Introduction

Over the last century the global electrical energy demands have grown exponentially due to the mechanisation and computerisation of every layer of modern society [1]. Usually, this electrical energy is generated through the combustion of oil or coal. This approach has two main issues. Firstly, the production and release of CO_2 in the atmosphere, which is the leading cause of climate change, and secondly the depletion of the limited reserves of these oil and coal resources[2], [3]. Because of this, a shift towards renewable energy sources such as wind, geothermal, hydroelectric and solar energy [4], [5] is required. Solar energy is one of the most promising renewable energy sources because of its availability everywhere in the world and massive abundance. However, it is an intermittent source of energy due to the day/night cycle, hourly and seasonal variation, and weather-related phenomena (e.g. clouds). Two challenges therefore exist: improving the conversion of the solar to electrical energy and storing this electrical energy for use when the solar energy flow is low.

The photovoltaic effect, discovered by the French scientist Edmond Becquerel, is the transfer of energy from a photon (light) to an electron. According to quantum mechanics, electrons bound to atoms occur in specific electronic configurations. The highest energy configuration (or energy band) that is generally occupied by electrons for a given material is known as the valence band, and the degree to which it is filled largely determines the electrical conductivity of the material. In a typical conductor (e.g metal), the valence band is about half-filled with electrons, which readily move from atom to atom, carrying a current. Semiconductors (like TiO_2) generally have their valence bands filled, but, unlike insulators, very little energy is required to excite an electron from the valence band to the next allowed energy band, because any electron excited to this higher energy level is relatively free. This is called the photovoltaic effect: a photon that has enough energy to excite an electron from the valence band to the conduction band, leaving behind holes in the valence band. It allows the semiconductor to convert the energy from the sunlight to electrical energy or chemical energy.

The photovoltaic solar cell is one of the direct applications of this effect. It consists of the use of two different semiconductor materials for creating an electron-hole pair at the contact area

and setting up a potential difference. However, this technology has to use a separate storage device for regulating electrical production over a full 24 hours of production. The photovoltaic panels require a battery to transform light to a storable chemical energy. Another method using the photoelectric effect is called the photo-electrochemical cell could directly transform the light into stored chemical energy. An electron-hole pair is generated in a semiconductor, with the electron sent through the electrical circuit, and the hole is driven to the surface of the semiconductor. The semiconductor is in contact with redox species, which is capable of exchanging an electron with the semiconductor. At the interface, the hole takes an electron from the redox species, thus oxidising the redox species. Simultaneously, the electron released into the electrical circuit (at a lower potential compared valence band hole) is transferred to another redox species in contact with a suitable negative electrode. [6]. The net effect is that a redox couple is oxidised at the semiconductor and another redox couple (with a more negative potential) is reduced at the negative electrode. These oxidised and reduced couples can be then stored, and later allowed to undergo their reverse (spontaneous) reactions to regenerate the stored energy.

1.2 Renewable energy market

Renewable energy is the future of global energy production. It is considered as a clean energy as it does not pollute the environment, release greenhouse gas and consumes fewer fossil resources. However, renewable energy has several barriers that significantly reduce its global usage. In 2000, the Collaborating Centre on Energy and Environment in Denmark [7] showed the two significant barriers including economic and institutional issues (GDP per capita, corruption, CO_2 emissions) . Even though renewable energy has started to be competitive on the energy market (PV module prices have declined around 80% since 2007: from US $4/W in 2007 to US $1.8/W in 2015 [8]), oil and coal are still the primary sources of electricity production. The first reason behind this phenomenon is the cost of electricity production in oil and coal power plants is less expensive comparing to others due to the lower price of the primary materials (especially since the gulf countries are artificially decreasing the oil price to less than 50 US$/Barrel [9]), cheap maritime transportation and the existence of widespread industrial infrastructure utilising oil and coal. The second reason is the associated lack of public and private investment in the renewable energy, due to the high investment required in infrastructure for integrated renewable energy.

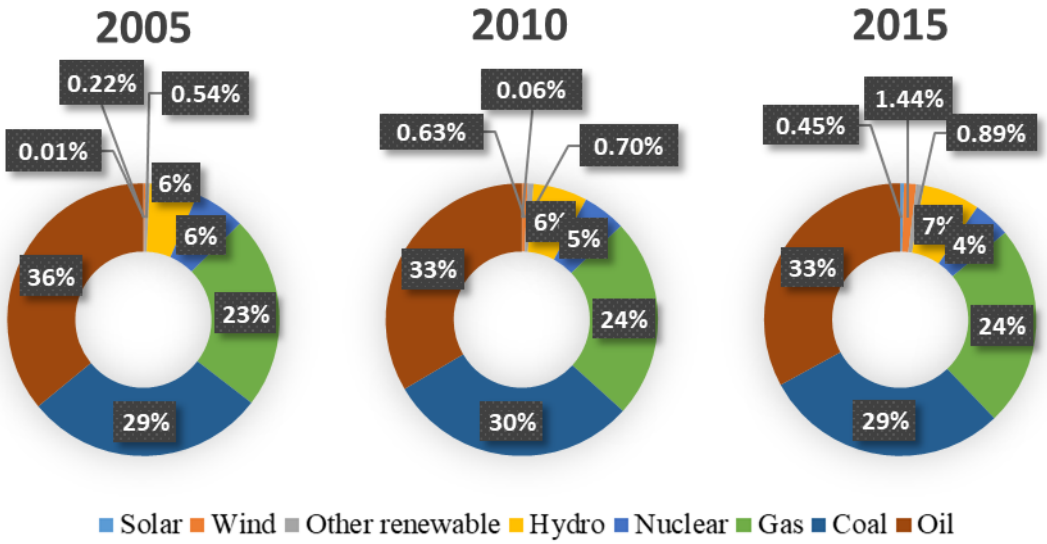

Figure 1: Comparative primary energy consumption over the past 15 years, based on BP Statistical Review of World Energy June 2016 data, which comprises commercially traded fuels for primary energy, including modern renewables used to generate electricity. Traditional biomass is excluded [8].

Fortunately, renewable energy generation is making inroads into the global energy market and many of the technical barriers are being solved. Significant research and development in renewable energy gives an excellent possibility to have less expensive electricity, which will lead to further investment and a global transformation of the worldwide energy mix. In this case, New Zealand has an essential advantage over the rest of the world, as its electricity generation is mostly sourced from hydroelectric and geothermal energy (Figure 2) [10], so the investment needed achieve 100% is lower than in many other countries.

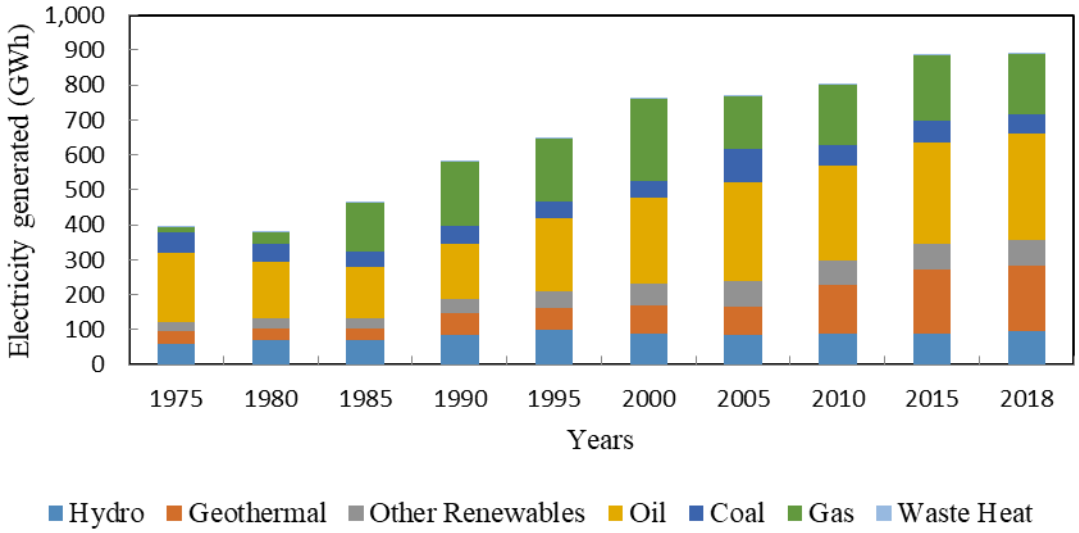

Figure 2: Electricity generation by fuel for the year 2017 in New Zealand [10]

1.3 Research objectives

The redox couple chosen is the V^{4+}/V^{5+} couple because it is one of the most known and used redox couples in a redox flow battery. The photoanode material chosen is TiO_2 since it has a suitable bandgap and energy levels compatible with the selected redox couple and is cheap and easy to deposit. The main objective of the overall project was to improve the photocatalytic efficiency of the photoanode. The first goal was to understand every aspect of the reaction at the photoanode: vanadium photo-oxidation, electrochemical reduction and water splitting. The second objective was to find a way to deposit the TiO_2 materials in a reproducible way and obtain a higher photocurrent by tuning the morphology of the film. The third objective is to improve the photocurrent of the photoanode by adding gold nanoparticles and nanoclusters on the film, to use the plasmonic effect of the gold particles. Finally, the last objective was to be able to propose a new redox couple that is more efficient than V^{4+} as the anodic electrolyte.

2. Background and general literature review

2.1 Redox flow batteries

2.1.1 General principle redox flow battery

The redox flow battery is a storage device which can store a large amount of energy. Unlike most other batteries, redox flow batteries store energy within a redox couple dissolved in a liquid electrolyte rather than storing energy within the electrodes themselves. The advantage of this system is the possibility to store the redox active electrolyte in external tanks, which can be changed, moved or enlarged for modulating the energy quantity stored in the battery. The battery is constituted of two parts, the positive half-cell and the negative half-cell, separated by an ion-exchange membrane. These half cells each have an electrode (often porous) and are connected to an electrolyte reservoir via a pump, which enables the electrolyte to be pumped through the porous electrode.

2.1.2 Redox flow battery cell diagram and reaction

The technology is based on the electrochemical oxidation and reduction of two redox couples (Figure 3) [11]. During the discharge process, the redox couple in the positive electrode is reduced from a high chemical potential state, an electron is released by the reduction and passes through an external circuit. The electron then reaches the negative electrode, where it is used to oxidise the redox couple in the negative electrolyte to a higher chemical potential state. During the charging process, the current and redox reactions are reversed. The general reactions are given as:

$$\text{Charge} = A^{n+} + xe^{-} \rightarrow A^{(n-x)+} \quad \text{Discharge} = A^{(n-x)+} \rightarrow A^{n+} + xe^{-} \qquad (1)$$

And

$$\text{Charge} = B^{n+} - xe^{-} \rightarrow A^{(n+x)+} \quad \text{Discharge} = B^{(n+x)+} \rightarrow B^{n+} - xe^{-} \qquad (2)$$

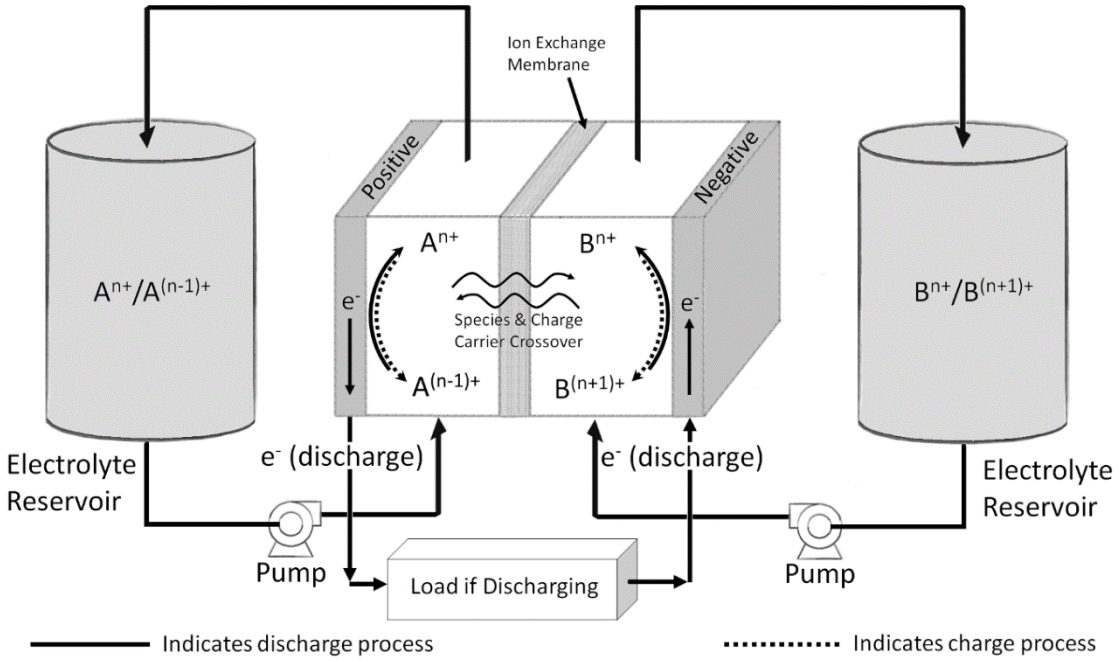

Figure 3: Cell diagram of a redox flow battery during charge and discharge

Redox flow batteries can use different redox couples and can distinguish it into three categories: redox couples in an aqueous electrolyte; redox couples in a non-aqueous electrolyte and half-solid redox battery. The dissolved redox couple in an aqueous electrolyte is the most common technology used industrially, because of its price and its stability. The most used and known redox couples dissolved in an aqueous electrolyte are:

- Iron/Chromium: $Fe^{2+} \leftrightharpoons Fe^{3+} + e^-$ E = 0.77 V *vs.* RHE
  $Cr^{2+} \leftrightharpoons Cr^{3+} + e^-$ E = -0.41 V *vs.* RHE
- Bromide/sulfide: $2Br^- \leftrightharpoons Br^{3-} + 2e^-$ E = 1.09 V *vs.* RHE
  $2S_2^{2-} \leftrightharpoons 2S_2^{4-} + 2e^-$ E = -0.26 V *vs.* RHE
- All vanadium: $VO_2^+ + 2H^+ + e^- \leftrightharpoons VO^{2+} + H_2O$ E = 1 V *vs.* RHE
  $V^{2+} \leftrightharpoons V^{3+} + e^-$ E = -0.26 V *vs.* RHE
- Vanadium/bromide: $ClBr^{2-} \leftrightharpoons Cl^{3-} + 2Br^{2-} + e^-$ E = 1.09 V *vs.* RHE
  $2VCl_2 + 2Cl^- \leftrightharpoons 2VCl_3 + 2e^-$ E = -0.26 V *vs.* RHE
- Hydrogen system: $H_2 \leftrightharpoons 2H^+ + 2e^-$ E = 0 V *vs.* RHE
  $H_2O \leftrightharpoons 4H^+ + O_2 + 4e^-$ E = 1.2 V *vs.* RHE

Table 1: Characteristics, advantages and drawbacks of several redox couples dissolved in an aqueous electrolyte [11].

Redox couple	Iron /chromium	Bromide /sulphide	All vanadium	Vanadium /bromide	Hydrogen system
Theoretical voltage	1.18V	1.35V	1.26V	1.35V	1.2V
Theoretical voltage	Highly reversible with electrolyte	Good Mixing efficiency	1. Good efficiency 2. Highly reversible	1. High energy density 2. Large solubility	1. Oxygen reaction 2. Very slow 3. Large overpotential
Drawbacks	1. Electro-catalysis required 2. Low efficiency	Contamination and precipitation of H_2S and Br_2	Energy density limited by precipitation of V_2O_5 (T or PH)	Production of toxic gas	1. Use of gas as the reactant 2. Need a large tank 3. Low efficiency

Table 1 gives the characteristics advantages and drawbacks of the different redox couple [11]. Using a redox couple in a non-aqueous electrolyte increases the operating voltage window, but the solvents are usually expensive and polluting. The most known redox couples dissolved in the non-aqueous electrolyte are:

- $[Ru(bpy)_2]^{3-}/[Ru(bpy)_2]^{2-}$: $[Ru(bpy)_2]^{3-} \leftrightharpoons [Ru(bpy)_2]^{2-} + e^-$
  $[Ru(bpy)_2]^{2-} \leftrightharpoons [Ru(bpy)_2]^{-} + e^-$
- $V(acac)_3/[V(acac)_3]^-$: $V(acac)_3 \leftrightharpoons [V(acac)_3]^+ + e^-$
  $[V(acac)_3]^- \leftrightharpoons V(acac)_3 + e^-$
- $Cr(acac)_3/[Cr(acac)_3]^-$: $Cr(acac)_3 \leftrightharpoons [Cr(acac)_3]^+ + e^-$
  $[Cr(acac)_3]^- \leftrightharpoons Cr(acac)_3 + e^-$

Table 2: Characteristics, advantages and drawbacks of several redox couples dissolved in a non-aqueous electrolyte [11].

Redox couple	$[Ru(bpy)_2]^{3-}$/ $[Ru(bpy)_2]^{2-}$	$V(acac)_3/[V(acac)_3]^-$	$Cr(acac)_3/[Cr(acac)_3]^-$
Theoretical voltage	2.6V	2.2V	3.4V
Theoretical voltage	1. No hydrogen formation 2. Large operating window	1. No hydrogen formation 2. Large operating window	1. No hydrogen formation 2. Large operating window
Drawbacks	High crossover	1. High crossover 2. High ohmic losses 3. A lot of side reactions	1. High crossover 2. High ohmic losses 3. A lot of side reactions

Table 2 gives the characteristics, advantages and drawbacks of the redox couples dissolved in a non-aqueous electrolyte [11].

Some technologies are a hybrid between a redox flow battery and a traditional battery. In these hybrid batteries, one half-cell uses a dissolved redox couple and the other uses a metal / dissolved metal couple. The most used and known redox couples for half-solid redox flow battery are:

- Zinc/bromine: $2Br^- \leftrightharpoons Br_2^- + e^-$ E = 1.09 V *vs.* RHE
  $Zn \leftrightharpoons Zn^{2+} + 2e^-$ E = -0.76 V *vs.* RHE
- Soluble lead acid: $Pb^- \leftrightharpoons Pb^{2+} + 2e^-$ E = -0.13V *vs.* RHE
  $Pb^{2+} + 2H_2O \leftrightharpoons PbO_2 + 4H^+ + 2e^-$ E = 1.49 V *vs.* RHE
- All iron: $Fe \leftrightharpoons Fe^{2+} + 2e^-$ E = -0.3 V *vs.* RHE
  $Fe^{2+} \leftrightharpoons Fe^{3+} + e^-$ E = 0.77V *vs.* RHE

gives the characteristics, the advantages and, drawbacks of some hybrid redox couples [11].

Lately few new type of electrolytes have been investigated: the organic [12]–[14]and polymers based electrolyte[15], [16]. The typical organic redox couples are 1,2-benzoquinone-3,5-disulfonic acid and anthraquinone-2-sulfonic acid or others organic materials or polymers of the quinone family , the advantage is their rapid kinetics of charge-transfer, and the possibility to tune the cell voltage by changing the substituent group. Being an aqueous battery, the voltage range for the electrolyte is limited by the oxygen evolution reaction at the positive electrode and the hydrogen evolution reaction at the negative electrode (*i.e.* water splitting). Consequently, a maximum cell voltage of 1.23 V is to be expected at room temperature.

Table 3: Characteristics, the advantages and, drawbacks of several half-solid redox flow battery technologies.

Redox couple	Zinc/bromine	Soluble lead acid	All iron
Theoretical voltage	2V	1.6V	1.07V
Kinetics	Good	Good	Good
Theoretical voltage	1. High energy density 2. High cell voltage 3. Good reversibility	1. Small tank	1. No dendrite 2. Low cost
Drawbacks	1. Corrosion of Zn electrode 2. Dendrite/short circuit 3. High self-discharge 4. Short cycle of life 5. Low energy efficiency	1. High crossover 2. High ohmic losses 3. A lot of side reactions	1. High crossover 2. High ohmic losses 3. A lot of side reactions

The most widely investigated material is the Vanadium Redox Flow Battery (VRFB), where VO_2^+/VO^{2+} and V^{3+}/V^{2+} redox couples are used as the positive and negative electrode respectively. VRFB was first shown to be a viable RFB system by Skyllas-Kazacos and Grossmith [17] where they used 1.5 M vanadium sulfate in 2 M H_2SO_4 as the electrolyte, carbon felts as the electrodes and a polystyrene sulfonic acid membrane as the cation-selective membrane. It gave an advantage over other mixed metal redox couples which were prone to cross-contamination through the ion-exchange membrane, as the vanadium redox species could continue to undergo the appropriate redox reactions even if cross-over occurred. The following reactions occur in a VRFB during the discharge process [18]:

Anode: $V^{2+} \rightarrow V^{3+} + e^{-} \quad E^0 = -0.26\ \text{V}\ vs.\ \text{RHE}$ (3)

Cathode: $VO_2^+ + 2H^+ + e^- \rightarrow VO^{2+} + H_2O \quad E^0 = 1.00\ \text{V}\ vs.\ \text{RHE}$ (4)

Overall Reaction: $V^{2+} + VO_2^+ + 2H^+ \rightarrow V^{3+} + VO^{2+} + H_2O \quad E^0 = 1.26\ \text{V}\ vs.\ \text{RHE}$ (5)

As shown above, the open-circuit voltage of an all-VRFB is 1.26 V *vs.* RHE which is considered relatively high. The energy density of VRFBs is around 19-38 Wh L^{-1} and is dependent on the concentration of vanadium ions dissolved in sulphuric acid with the average concentrations of $VOSO_4$ and H_2SO_4 being around 1.5-2.0 M and 2 M respectively. Given the higher energy densities of traditional storage batteries such as lithium-ion/polymer (250-730 Wh L^{-1}), nickel-metal-hydride (140-300 Wh L^{-1}) and lead-acid (60-110 Wh L^{-1}) systems, there has been significant research into increasing the energy densities of VRFBs. The problem exists due to vanadium ion instability in higher acid concentrations which can cause precipitation and loss of redox activity. Therefore, research has been conducted on stabilising vanadium-based electrolytes in concentrated acid solutions. A significant advantage of VRFBs is their very long cycle lifetimes which are on the order of 15000-20000 charge/discharge cycles vs solid-state batteries which have lifetimes of ~500-4500 charge/discharge cycles.

2.1.3 Vanadium redox flow battery components

Redox flow batteries consist of electrodes, ion-exchange membranes and electrolytes. Both electrodes must be stable in the electrolyte, have high oxygen and hydrogen overpotentials and a large specific area. A range of graphite and carbon rods, plates, felts and cloths have been investigated as anodes and cathodes [19]. These electrodes have good lifetime (several months) under regular charge/discharge cycling, but the oxygen evolution reaction during overcharging can corrode the positive electrode slowly. The negative electrode stays stable even after several months [19]–[21], in contrast to the positive electrode which reduces the lifetime of the battery. One solution is to coat the electrode with polyaniline [19] as protective layer. However, the electrode still degrades as the electrolyte slowly dissolves this polymer protection during the redox reaction. Some lead, gold, titanium, platinum, platinised titanium and iridium oxide electrodes were investigated alone or mixed [19]. Unfortunately, lead and titanium were passivated due to the potential range of the redox couple. Platinised titanium [20], gold, platinum and iridium oxide stay stable, but their cost is high compared to the other materials. Carbon felts has been chosen by the majority of scientists and commercial developers as the anode and cathode. Carbon felts are more protected against the overcharging

than the other carbon electrodes and can be designed to increase the chemical and the mechanical resistance.

The electrolyte must be cheap, contain a high concentration of vanadium species and be stable for a very long time. Therefore, research has been realised on the vanadium electrolyte at the positive electrode. The first work on the full vanadium battery used $VOSO_4$ dissolved in sulphuric acid [22], but the price of the $VOSO_4$ precursor was very high. Therefore, some use V_2O_5 as the initial precursor due to his lower price. The stability of the electrolyte shows a strong correlation with temperature and acid concentration [23]. Skyllas-kazacos *et al.* [24] have shown that above concentrations of 3 M sulfuric acid, V_2O_5 precipitates at temperatures above 40ºC. However, if the vanadium concentration is increased, the other vanadium compounds precipitate at less than 10ºC. Therefore, the operating temperature range is defined by 10 ºC / 40 ºC for a 2 M of vanadium electrolyte. The solubility data of vanadium in sulphuric acid at concentrations of 0 M to 9 M over the temperatures range of 10 ºC /50 ºC were generated by Rhaman and M. Skyllas-kazacos [25]. Recently, others have proposed adding hydrochloric acid to sulphuric acid based vanadium solutions to help stabilise the V^{4+} [26]. Consequently, the temperature range could be enlarged at -5 ºC / 50 ºC.

The ion exchange membrane must avoid vanadium and water transfer between the two compartments. If the vanadium passes through the membrane, the charge and discharge capacity is slowly decreased. If too much water goes through the membrane, the concentration in vanadium will be increased in the compartment which loses the water, which can lead to precipitation of the vanadium salt. The most commonly used membrane is a Nafion membrane [11], [27], [28], which is expensive but has excellent ion conduction and is stable in the acid electrolyte. Another option is the Selenion-AMV membrane, but it has poor stability [28], [29].

2.1.4 Redox battery performance: Thermodynamics

The first and easiest way to determine the redox battery performance will be to conduct thermodynamics studies on the redox reactions. For the electrochemical reaction, like in the full vanadium redox flow battery, the equilibrium potential at a single redox electrode could be:

$$E = E_0 + \frac{RT}{nF} \ln\left(\frac{c_{ox}}{c_{red}} . \frac{\gamma_{ox}}{\gamma_{red}}\right) \quad (6)$$

- E_{rev}: the potential difference of the reaction in V.
- E_0: standard reduction potential in V.

- R: universal gas constant.
- T: absolute temperature in K.
- n: number of electrons transferred per mole of species reduced or oxidized.
- F: Faraday's constant.
- c_{ox}: ionic concentration of oxidised species in mol L^{-1}.
- c_{red}: ionic concentration of reduced species in mol L^{-1}.
- γ_{ox}: activity coefficient of the oxidised species (deviation of an ion from ideal behaviour due to inter-ionic interactions within the solution) in mol L^{-1}.
- γ_{red}: activity coefficient of the reduced species in mol L^{-1}.

The Nernst equation is derived from the standard changes in the Gibbs free energy associated with a redox reaction. The actual free energy change G can be linked to the standard one $\Delta G_{standard}$ and the reaction coefficient Q, which corresponds in this case to $\frac{c_{ox}}{c_{red}} . \frac{\gamma_{ox}}{\gamma_{red}}$.

$$\Delta G = \Delta G_{standard} + RT\ln\left(\frac{c_{ox}}{c_{red}} . \frac{\gamma_{ox}}{\gamma_{red}}\right) \quad (7)$$

E is defined as the decrease in Gibbs free energy per coulomb of charge transferred: $\Delta G = -nFE$, so the potential difference is equal to $E_{rev} = \frac{-\Delta G}{nF}$. As the electrolyte is pumped the circulation of the species could be considered having enough for avoiding a yielding of the ions, so the γ_{ox} and γ_{red} could be regarded as equal to one. For example, for the all vanadium, redox flow battery and based on the half equation present sooner, the Nernst equation becomes:

$$E_{rev} = E^+ - E^- = E_0 + \frac{RT}{nF}\ln\left(\frac{c_{VO_2^+}}{c_{VO_2^{2+}}} . \frac{c_{V^{2+}}}{c_{V^{3+}}}\right) \quad (8)$$

- E^+: positive half-cell potential in V.
- E^-: negative half-cell potential in V.

The usual form of the Nernst equation does not take into consideration two phenomena, which are usually considered as negligible but have an influence on the result: the proton concentration at the positive electrode and the Donnan potential across the membrane [30]. The proton concentration proceeds to the positive electrode half-reaction of VO_2^+. The Donnan potential is caused by an unequal proton concentration between the two electrolytes and if all these parameters are taking in count, the Nernst equation becomes:

$$E_{rev} = E^+ - E^- = E_0 + \frac{RT}{nF}\ln\left(\frac{c_{VO_2^+} \cdot c_{V^{2+}} \cdot (c^+_{H^+})^3}{c_{VO_2^{2+}} \cdot c_{V^{3+}} \cdot c^-_{H^+}}\right) \quad (9)$$

- $c^+_{H^+}$: positive half-cell potential in V.
- $c^-_{H^+}$: negative half-cell potential in V.

2.1.5 Redox battery performance: actual cell performance

Unfortunately, a simple thermodynamic study does not include all the different phenomena occurring on the batteries. The total performance of the real cell is calculated for the charge of the battery as:

$$\text{charge: } E_{cell} = E_{rev} + |\eta_{cathode}| + |\eta_{anode}| + |\eta_{IR}| \quad (10)$$

- E_{cell} : the potential difference of the cell in V
- $|\eta_{cathode}|$: overpotential l at the cathode in V
- $|\eta_{anode}|$: overpotential at the anode in V
- $|\eta_{IR}|$: overpotential of the internal resistance of the cell in V

The different overpotential increases the energy required for fully charged the battery, but in the discharge the overpotential reduces the energy delivered by the battery:

$$\text{discharge: } E_{cell} = E_{rev} - |\eta_{cathode}| - |\eta_{anode}| - |\eta_{IR}| \quad (11)$$

This overpotential has a different origin: the activation energy required to initiate a charge transfer; the concentration, ohmic and ionic overpotential.

2.1.6 Redox battery performance: activation energy and kinetics

One of the significant overpotentials in cathode and anode comes from the rate of one or both of the redox reactions, *i.e.* the electron transfer rate between the electrode and the redox species, i.e. the kinetics of the electrochemical reaction. This kinetics is directly linked to the applied current and the redox species concentration in solution. The slower the kinetics is, the higher the applied potential should be, and the more concentrated the solution has to be. Therefore, a bigger overpotential for starting the reaction is required. In general, the solution is not in equilibrium and the activation energy in both half-cells is different. In this case, and if the mass transfer is considered negligible, the Butler-Volmer equation can be used:

$$I = I_0 \left[e^{\alpha \frac{nF}{RT} \eta_a} - e^{-1(1-\alpha)\frac{nF}{RT}\eta_a} \right] \quad (12)$$

- I: current in A
- I_0: standard current in A
- α: charge transfer coefficient
- η_a: overpotential due to the activation energy in V

Finally, the Tafel equation gives the values of the overpotential due to the activation energy:

$$\eta_a = \frac{RT}{\alpha F} ln(I) - \frac{RT}{\alpha F} ln(I_0) \quad (13)$$

2.1.7 Redox battery performance: mass transfer limitations

Concentration overpotentials are the overpotentials needed to overcome the energy losses associated with mass transport limitation effects on electroactive redox species, from the bulk electrolyte to the electrode surface and vice versa. The concentration overpotentials can be calculated by the following equation (14):

$$\eta_{conc} = \eta_{c,conc} + \eta_{a,conc} = E - E° + \frac{RT}{nF}\left|\frac{c_{surf}}{c_{bulk}}\right| \quad (14)$$

Where c_{surf} and c_{bulk} are the concentrations of electroactive species at the electrode surface and in the electrolyte respectively.

During RFB operation, when the electroactive species in each half cell undergo the appropriate redox reactions, the diffusion of reactants to and products from the electrode surface begin to change relative to the bulk concentration. Therefore, with sufficient electrolyte flow, the concentration of reactants can be maintained so that it resembles the initial concentration of reactants near the electrode surface, which somewhat mitigates concentration potentials. Besides, increasing the reactant concentration can also mitigate the concentration potentials by improving mass-transfer rates. At the electrode surface, however, the reactant and product concentrations form gradients that are characterised by diffusional fluxes (movement of species from the region of high concentration to low concentration) and the creation of the diffusion layer. The diffusion layer is where electrolyte concentration changes happen and where diffusion determines reactant and product mobility from the electrode surface. Low concentration of reactants at the surface of the half-cell electrodes can have negative effects on cell efficiency and power density. Fick's Law of Diffusion can be used to calculate the diffusion flux in the diffusion layer from the following equation:

$$J_i = D_i \frac{\Delta c_i}{\delta} = \kappa_i \Delta c_i \quad (15)$$

Where J_i is the diffusion flux (mol m^{-2} s^{-1}), D_i is the diffusion coefficient (m^2 s^{-1}), δ is the diffusion layer thickness (m), and κ_i the diffusion flux constant (m s^{-1}). Δc_i is obtained from $\Delta c_i = c_{bulk} - c_{surf}$ for reactants as they diffuse from the bulk electrolyte to the electrode surface and $\Delta c_i = c_{surf} - c_{bulk}$ for products as they diffuse from the electrode surface to bulk electrolyte.

2.1.8 Redox battery performance: ohmic and ionic loose

The last two overpotentials are the ionic and the ohmic due to the electrical charges: the electrical resistance of the different materials. The ohmic contribution is from resistance though

the electrode, current collector and the bipolar plate. The overpotential could be written by using the Ohm law as:

$$\eta_{ohmic} = \left(R_{electrode} + R_{collector} + R_{bipolar}\right)I \quad (16)$$

- η_{ohmic}: overpotential due to the ohmic loose
- $R_{electrode}$: Resistance of electrode
- $R_{collector}$: Resistance of the current collector
- $R_{bipolar}$: Resistance of the electrode bipolar plate

The electrolyte and the membrane also oppose the flow of ionic current, so the ionic over potential is:

$$\eta_{ohmic} = \left(R_{electrolyte} + R_{membrane}\right)I \quad (17)$$

- $R_{electrolyte}$: Resistance of the electrolyte
- $R_{membrane}$: Resistance of the membrane

2.2 Charging redox flow batteries by using solar energy

2.2.3 Photovoltaic solar panel coupled with redox flow battery

RFB can be used for storing renewable energy from wind, hydro or solar energy sources. Indeed, it is possible to purchase a commercial solar PV-battery package, PV solar panels are traditionally connected to either lead-acid of Li-ion batteries [31]. In comparison, the redox flow battery is more cost-effective, has a better life cycle and higher energy [11]. The first use of redox flow battery with solar energy sources was a 5 kW/12 kWh VRFB system installed in Thailand by Thai Gypsum Products Co., Ltd. in 1994. Two further zinc-bromine batteries of ZBB were installed in Australia (500 kWh) and the US (2x50 kWh) in 2002 and 2003, respectively [28]. Subsequently the technology has become common and is used around the world [32]. Whilst these PV coupled flow batteries are proving to be successful, new research is now exploring the direct photoelectrochemical charging of flow batteries [33].

2.2.4 Direct solar charging

In a solar flow battery, direct photoelectrochemical charging of at least one of the redox species occurs at a suitable photoelectrode (Figure 4). This could involve the use a photoanode to photoelectrochemically oxidise the positive electrolyte redox species, or a photocathode to photoelectrochemically reduce the negative electrolyte redox couple. In the case of a solar

flow battery using a photoanode, the negative electrode stays precisely like in a standard redox flow battery. Then the photoanode is present in the positive half-cell compartment which transforms the light into electron/hole pair, with this hole oxidising the redox couple in the electrolyte.

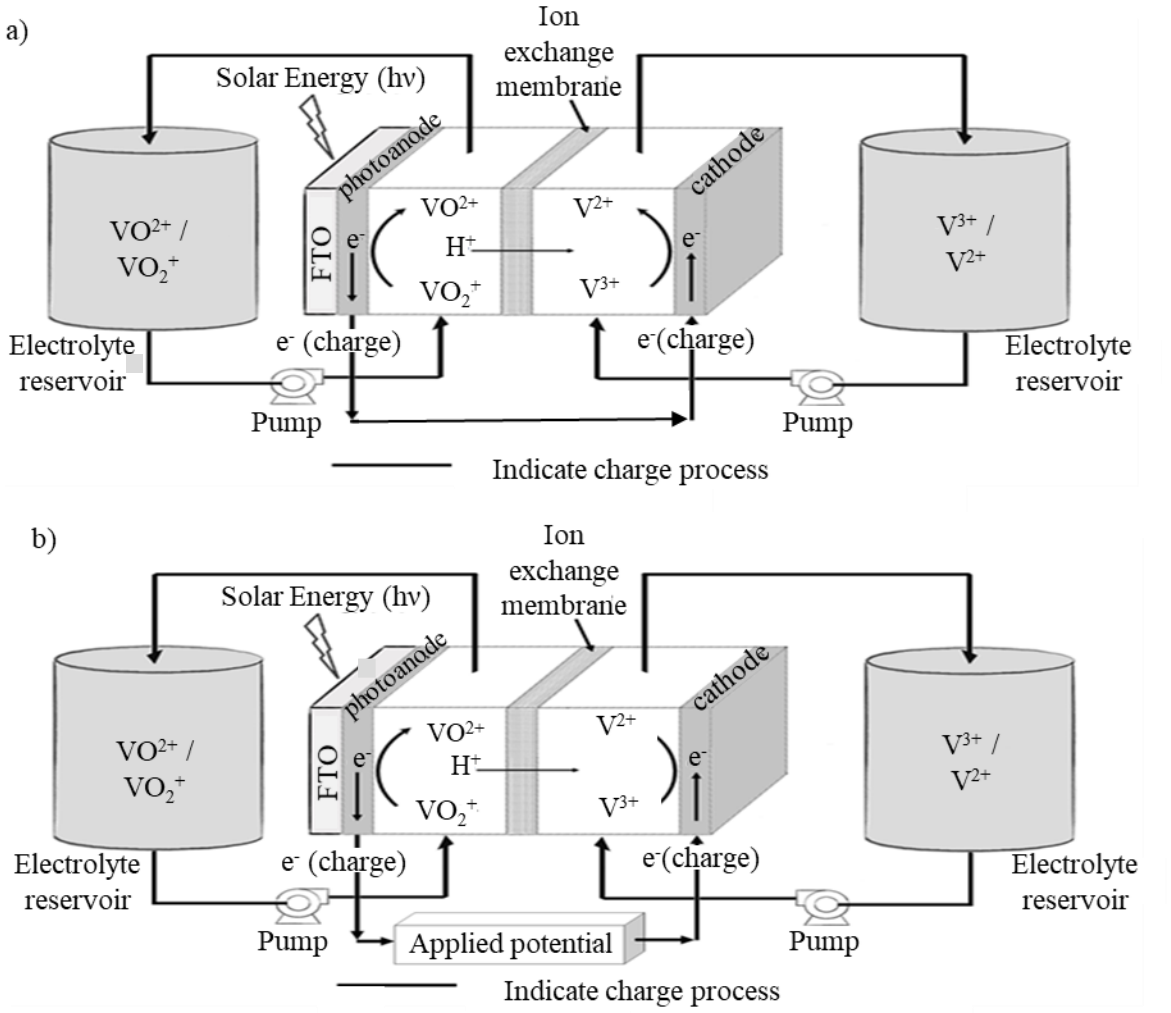

Figure 4: A schematic illustrating the operating principle of a solar redox battery in charging mode a) without external bias and b) with external bias.

The charge reaction of the example full vanadium redox flow battery can be written with the addition of the photoelectric reaction. The electron is not introduced by the generator but is provided by the light via the semiconductor:

electron: $h\nu + SE \leftrightharpoons SE + h^+ + e^-$ (18)

anode (electrode positive): $VO^{2+} + H_2O \leftrightharpoons VO_2^{+} + 2H^+ + e^-$ (19)

cathode (electrode negative): $V^{3+} + e^- \leftrightharpoons V^{2+}$ (20)

Historically the first device which could be described as a solar photoelectrochemical battery was generated by Hodes *et al.* in 1976 [34]. It was derivede from a photoelectrochemical cell (PEC), producing electricity from solar power by moving a chemical which is a shuttle for the

charge to flow. A third electrode was used to store the chemical in the solid form, then release it into the electrolyte during the discharge step. It was composed of an n-type CdSe photoelectrode in an $S^{2-/}S$ electrolyte, an Ag-Ag2S as storage electrode, and carbon felt as an anode. A three-electrode configuration and a two-electrode configuration has been tested with Ag-Ag_2S as storage electrode and anode but without any separator between the electrodes. The electrode was supposed to react with sulphide in solution to form a Ag_2S on the surface of the electrode and release them in the dark. This early photoelectrochemical storage cell had an open circuit potential (OCV) ~130 -150 mV, but with poor efficiency due to the lack of membrane to exclude S^{2-} ions that would recombine with the Ag-Ag_2S anode.

Further improvements were made to this solar photoelectrochemical storage cell (PESC) system by using $MoSe_2$ and GaAs as the semiconductor materials for the photoanode, with Nafion used as the membrane, resulting in higher solar conversion efficiencies, open-circuit voltage and current densities. Other metal couples in later works have replaced the anode: in 1987, Licht [35], [36] proposed a $Cd(Se_{0:65}Te_{0:35})$ semiconductor on a polysulfide electrolyte. It succeeded to reach a faradic efficiency (also called columbic efficiency) of 95% and an overall solar-to-electrical load conversion efficiency of 11.3%, but it was limited by the semiconductor due to its price and toxicity.

These early solar PESCs failed to attract much interest in research due to the relatively high cost of the semiconductor materials they used, the corrosion processes they underwent during cell operation, and low efficiencies. To overcome the problem of corrosion that broadband (low band-gap) light-absorbing semiconductors experience during redox processes, research began on using more low-cost and stable semiconductors, such as TiO_2, that were modified to overcome their high band gaps and increase light absorption at longer wavelengths i.e. the visible region. Then the concept of solar redox flow batteries appears, with the first true solar RFBs were developed in 2013 by the Gao group [33]. The first of these systems was a dye-sensitised solar cell (DSSC) in tandem with an RFB where the DSSC was made up of Ru based dye-sensitised TiO_2 deposited on FTO for the photoanode, Li^+ glass-ceramic separator (LiSICON), and platinised FTO as the cathode. The RFB utilised platinised electrodes as the anode and cathode with a LiSICON separator and I^-/I_3^- and $DMFc^+$/DMFc as the redox couple for the DSSC and I_3^- /I^- and DMFc/DMFc+ as the redox couple for the RFB.

Based on this work, the most commonly used catholyte couple (I_3^- /I^-) employed in solar batteries comes directly from the dye-sensitised solar cell [37]–[39]. In these batteries, the semiconductor (photoanode) is usually TiO_2, and the counter electrode is platinum or WO_3

[40]–[43]. The redox couple is kinetically fast because every photoelectron injected in the TiO_2 appears on the external circuit. The reaction is kinetically complex: I_3^- gives a mixture of I_2 and I^-; the I_2 can be reduced and becomes I_2^-. Finally, it can be again reduced to I_3^- and I^-, but the I_2 recombination process is slow because very few I_2 are absorbed. I_2 is highly volatile and corrosive for most metals, so platinum is used to accelerate the anode reaction and protect it. A lot of them used LiI in the electrolyte to accelerate the reaction. The test was realised by using another redox couple as negative electrolyte: using $[Fe(C_{10}H_{15})_2]^+/[Fe(C_{10}H_{15})_2]$ [43] couple, Li_2WO_4/Li_2+xWO_4 [41] or, $C_8H_6N_2/C_8H_6N_2^-$ [33] as anolyte. The main advantage of this anolyte is a higher working voltage, a lower cost and less toxic, however, the ion conductivity is quite low and limits the performances of the system.

Other solar batteries system have been investigated: like Keita and Nadjo [44] investigated a quinone-based solar battery in 2016. Sodium 9,10-anthraquinone-2,6-disulfonate/9,10-anthrahydroquinone-2,6-disulfonate (AQ/AQH_2), was used as catholyte and WSe_2 as the photoelectrode. The complete cell was n-$WSe_2|I_3^-/I^-|$salt bridge$|AQ/AQH_2|C$, which gave an OCV of 150 mV. Interestingly, a p-type WSe_2 as the photocathode in a p-$WSe_2|AQ/AQH_2|$salt bridge$|I_3^-/I^-|$Pt cell was successfully tested and presented a longer lifetime.

Betz and his colleagues study [44], realised a solar battery design with Cu_3PS_4 (n-type semiconductor, bandgap: 2.3 eV) as both the Photoelectrode and cathode. It can store and release energy through its reversible Cu intercalation and de-intercalation. A $Cu_{3+x}PS_4|CuCl/MeCN|Cu_{2-y}S$ cell was built, however, due to the severe recombination of Cu^+ at the electrode-electrolyte interface and poor visible-light absorption of the photoelectrode, the solar battery only achieved an OCV of 100 mV.

In 1990 Kaneko *et al.* [45] designed an all-solid-state device: n-CdS|iron(III) hexacyanoferrate(II)|Nafion separator|iron(III) hexacyanoferrate(II)|pt. Upon photocharging, the iron(III) hexacyanoferrate(II) on the cathode side was oxidised to iron(III) ferricyanide by holes. On the anode side, iron(III) hexacyanoferrate(II) was electrochemically reduced to iron(II) hexacyanoferrate(II). The device was able to use 65% of its theoretical capacity and had a coulombic efficiency of 36%.

Kanbara *et al.* [44] proposed an $Ag^+/Ag_xV_2O_5$ redox solar battery using p-Si as the photoelectrode. An ITO/(p-Si)/$SiO_x|Ag|Ag_6I_4WO_4|Ag_6I_4WO_4/AgxV_2O_5$ cell was built. $Ag_6I_4WO_4$ act as a solid electrolyte for Ag^+ ion conduction. The photocharging process was accomplished by reducing Ag^+ to Ag on the anode side and oxidising $Ag_xV_2O_5$ to $Ag_{x-d}V_2O_5$

on the cathode side. In the dark, the electric-energy-releasing process happened in the reverse direction. The solar battery showed an OCV of 0.55 V *vs.* SHE and excellent cycling performance over 900 cycles.

In 2001, Akuto and Sakurai [46] proposed a metal hydride/air solar battery design with $LaNi_{3.76}Al_{1.24}$, as an anode. The device has a gas-phase cathode of O_2/KOH and a photoelectrode of $SrTiO_3$. Upon photocharging, the cell's equilibrium voltage is determined by the Nernst potential difference between the $LaNi_{3.76}Al_{1.24}$/ $LaNi_{3.76}Al_{1.24}Hn$ and O_2/KOH redox couples. Their optimised solar battery had a photocharged OCP of 0.8 V *vs.* SHE and capacity of 950 mAh g^{-1} for at least 40 cycles. The device used a solid cathodic active electrode and a gas-phase anode. Therefore, the theoretical capacity of such a system should be much higher than conventional liquid-phase based solar batteries. However, the large bandgap of the semiconductor ($SrTiO_3$, Eg = 3.2 eV) led to limited utilisation of the visible light in the solar spectrum.

In 2015, Wu and colleagues [47] developed aqueous lithium–iodine (Li–I) solar redox flow battery. In their device, dye-sensitized TiO_2 and the I_3^-/I couple is used in the cathode chamber, and the Li^+/Li couple is used as the anode. Since the redox potential of the Li+/Li couple (i.e.--3.04 V *vs.* SHE) is more negative than the conduction band of TiO_2, an external voltage input is required for the charging process under illumination, make it a photoassisted battery with a total energy savings of 20 %. Then, in 2014, Wu and colleagues [46] applied the solar battery idea to the lithium-oxygen (Li–O_2) battery. They used an I_3^-/I^- redox couple to integrate a dye-sensitized TiO_2 photoelectrode with the air electrode. The solar energy was used to "pump" electrons to a higher energy level to reduce the battery's required charging potential. Their device was able to be photocharged at an external voltage of 2.8 V *vs.* SHE, much lower than that of a conventional Li–O_2 battery (ca. >4 V *vs.* SHE). This study introduced a new approach to address the overpotential issue in Li–O_2 batteries. However, similar to the Li–I solar battery, [48] these Li–O_2 solar batteries are not able to be fully photocharged.

Finally, one of the most promise solar batteries used the couples V^{2+}/V^{3+} and VO_2^+/VO^{2+}, which are based on the redox flow battery [49]–[51]. Their advantage is a significant difference of potential with TiO_2, no crossover between the species and well-known technology. Therefore, it is the couple which corresponds the most to the desired system for a solar redox flow battery. In the literature 44], [45], [47]–[49], the highest photocurrent obtained was 15 ± 0.5 µA cm^{-2} for a standard TiO_2 film of 3 mg, as shown in Table 4. However, by using micro channelling, Jiao *et al.* [52] succeeded to improve the photocurrent until 60 µA cm^{-2}.

Table 4: solar vanadium redox flow battery literature summary.

Photoanode composition	Photocurrent	Electrolyte	Counter electrode	Light source	Ref
compact TiO_2 then porous TiO_2 layer	60 µA cm^{-2}	0.1M VO_2^+/V^{3+}	Pt coated carbon fiber	100 mW cm^{-2}	[52]
0.5g TiO_2 P-25, 0.25 g ethyl cellulose, 0.062 g PVDF, and 2.15 g terpineol	0.1 mA in^{-2} so 15 µA cm^{-2}	0.1M VO_2^+/V^{3+}	Pt mesh	AM 1.5	[49]
0.5 g TiO_2 P-25 and 2.15 g terpineol	0.1 mA in^{-2} 15 µA cm^{-2}	0.01 M VO_2^+/V^{3+}	Carbon paper	AM 1.5	[53]
0.5 g TiO_2 P-25, 0.497 g ethylcellulose, 0.124 g PVDF and 2.501 g Terpineol	1 mA in^{-2} so 170 µA cm^{-2} with flow back to 0.3 mA in^{-2}: 46 µA cm^{-2} when the flow was cut	0.01 M VO_2^+/V^{3+}	Pt mesh	AM 1.5	[50]
6.45 cm^2: 1 g TiO_2 P-25 and 2.50 g Terpineol	60 µA in^{-2} 10 µA cm^{-2}	0.01 M VO_2^+/V^{3+}	Carbon paper	AM 1.5	[54]

2.3 Photoelectrochemical cell

2.3.1 General principle

The ability for a photoelectrode to operate in a solar RFB is based on the photoelectric effect phenomena, in semiconductor materials it is referred to as band-gap photoexcitation. In this process, when photons with greater energy than the semiconductors band-gap interact with a semiconductor, electrons (e^-) from the valence band are excited into the conduction band [6]. The holes (h^+) remaining in the valence band are then able to perform an oxidation reaction given the appropriate thermodynamic conditions, whereas the photoexcited electrons in the conduction band can perform a reduction reaction given the appropriate thermodynamic conditions or contribute to electrical conductivity.

For the reduction to occur the bottom of the conduction band must be at a potential more negative than the reaction reduction potential ($-E(V_{NHE})$), and the top of the valence band at a potential more positive than the reaction oxidation potential ($+E(V_{NHE})$). The redox potential value is also a determinant of the favourability of a reaction to occur where the possibility of more than one reaction occurring in a system exists. An example is that the oxidation of VO^{2+} to VO_2^+ occurs at 0.26 V vs SHE whereas the oxidation of H_2O occurs at 1.23 V vs SHE, so VO^{2+} oxidation occurs more readily than H_2O oxidation.

There are generally two types of photoelectrochemical cells. A tandem cell (Figure 5 a) consists of a photoanode in tandem with a photocathode, where the photooxidation occurring at the photoanode drives electron transfer to the photocathode combining with the photogenerated holes formed there to create a photocurrent. The photooxidation must occur a sufficiently positive potential and the photoreduction at a sufficiently negative potential to drive electron transfer. A single junction cell (Figure 5 b) [6] consists of a photoanode and a counter electrode where the photooxidation occurring at the photoanode drives electron transfer to the cathode where the redox species is reduced creating a photocurrent. The working principle is similar to each of these cells (Figure 5). As the photoanode absorbs photons, energy of photons absorbed dependent on band-gap, E_g, electrons (e^-) are promoted from the valence band to the conduction band leaving a hole (h^+). A depletion region which possesses an electrical field can separate these allowing the photogenerated electrons from the photoanode to reach the photocathode where they reach the semiconductor-electrolyte interface, increasing the quasi-Fermi potential of the photocathode, E^c_{QF}, to initiate the V^{3+}/V^{2+} redox couple reduction at a vanadium reduction catalysis (VRC) site. The corresponding process occurs in the photoanode cell where

photogenerated holes reach the semiconductor-electrolyte interface increasing the quasi-Fermi potential of the photocathode, E^{A}_{QF}, to initiate the VO^{2+}/VO_2^{2+} redox couple reduction at a vanadium oxidation catalysis (VOC) site. The quasi-Fermi potentials at each photoelectrode must be sufficiently positive to overcome the oxidation overpotential (η_O) and negative to overcome the reduction overpotential (η_R).

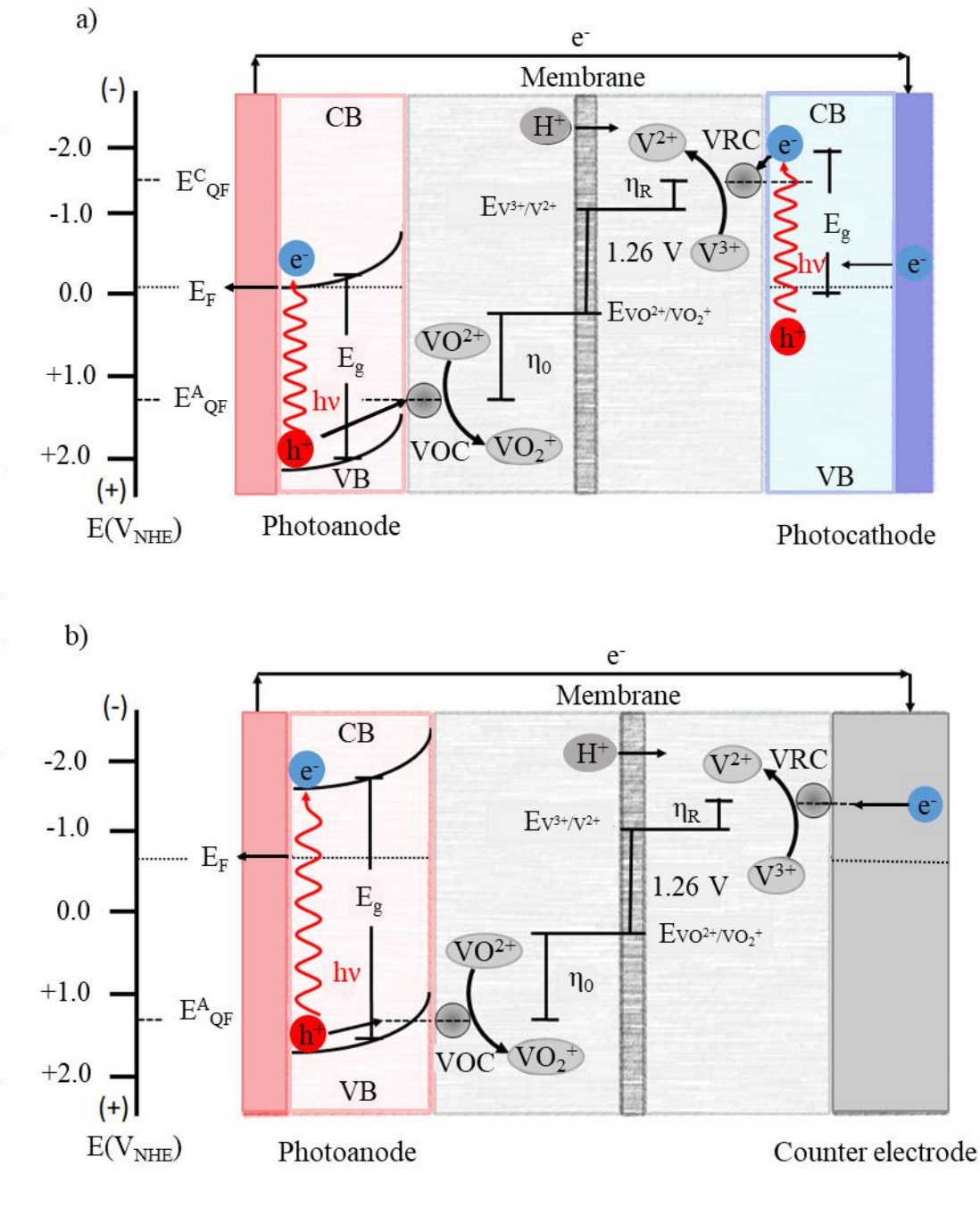

Figure 5: (a) tandem photoelectrochemical cell diagram (b) single junction photoelectrochemical cell diagram

The dye-sensitised solar cells (DSSC) is a specific photoelectrochemical cell [37]: the photoanode is composed of a semiconductor like photoelectrochemical cell. However, a

monolayer of charge transfer dye (usually a ruthenium complex) is attached to the semiconductor film.

Upon excitation, the dye injects electrons into the solid with a quantum yield of unity. The energy level of the excited state is matched to the lower bound of the conduction band of the oxide to minimize energetic losses during the electron transfer reaction. Finally, its redox potential should is sufficiently high that it can be regenerated via electron donation from the redox electrolyte or the hole conductor [37].

The electrolyte is regenerated in turn by its reduction at the counter electrode with the circuit being completed via electron migration through the external load. The voltage generated under illumination corresponds to the difference between the Fermi level of the electron in the solid and the redox potential of the electrolyte. Overall, the device generates electric power from light [55] without suffering any permanent chemical transformation.

The DSSC' even with the use of a dye, is similar to a solar redox flow battery for its photoanode. Indeed, DSSC research [55]–[58] has been conducted to increase the specific area, resulting in increased dye absorption on the film. These research projects are beneficial for the solar redox flow battery due to the increase of the active site for the oxidation reaction with the increase of the specific area. The addition of a metallic nanoparticles has been studied similar to the dye in DSSC.

2.3.2 Semiconductor Properties

The band-gap in a semiconductor is the void region between the top of the valence band and the bottom of the conduction band. It is created by the sum of ad infinitum repetition of molecular orbitals resulting from the hybridisation of atomic orbitals (cationic and anionic) from the individual atomic species in the material. An example of this is TiO_2 where the O 2p bonding (σ and π) orbitals mainly form the valence band and the Ti 3d anti-bonding (σ^* and π^*) orbitals mainly form the conduction band [59].

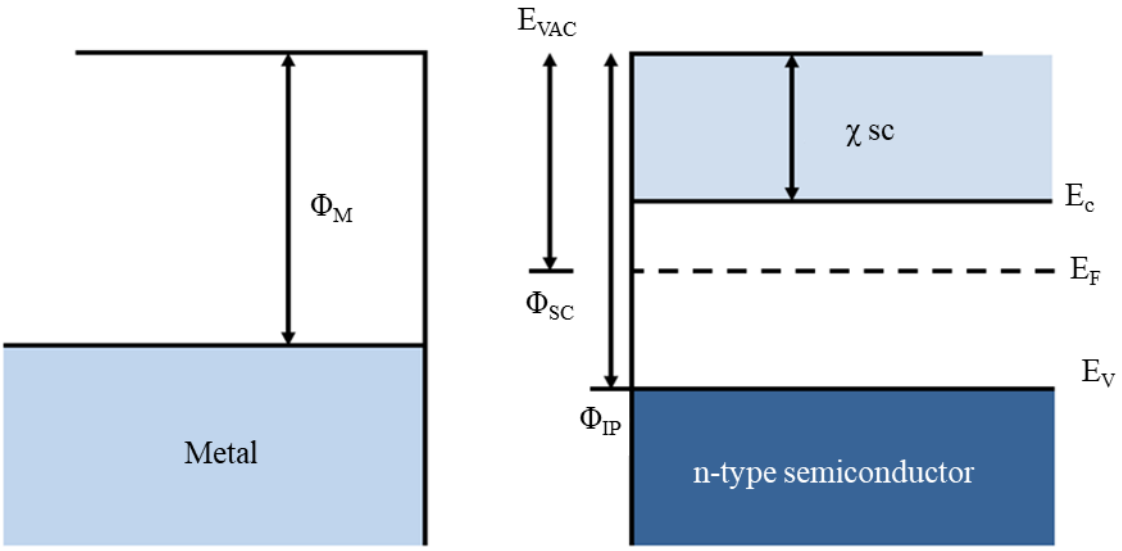

Figure 6: Band structures of metals (left) and an n-type semiconductor (right).

The Fermi level (E_F) (Figure 6), is a measure of the energy of the least tightly held electrons within a solid at 0 K. In n-type semiconductors the Fermi level exists closer to the conduction band (E_c) as there is a higher density of free electrons as the charge carriers and closer to the valence band (E_v) whereas in p-type semiconductors as there is a higher density of holes that act as charge carriers. The vacuum level of a material is the minimum energy at which a free electron can leave a material. The metal and semiconductor work-functions (Φ_M and Φ_{SC} respectively) are energies required to enable an electron to leave a solid form the highest filled electron state. The ionisation potential (Φ_{IP}) is the energy required to remove an electron from the highest filled state (in this case the valence band) to the vacuum level. The electron affinity (χ_{SC}) is the energy required to move an electron from the bottom of the conduction band to the vacuum level [60].

2.3.3 Semiconductor Interface

The band structure of a semiconductor (Figure 7) [6] is the typical band structure of the material at thermal and electronic equilibrium and will remain flat without the interference of outside forces, such as solar irradiance or applied electrical fields. In a photoelectrochemical cell where an interaction between the semiconductor material and electrolyte occurs, there are four outcomes to establish an electronic equilibrium due to the potential difference between the two. The first one is the establishment of a flat-band potential (Figure 7 a) as both semiconductor and electrolyte possess the same energy level, so the charge on each side of the semiconductor/electrolyte interface remains the same [61]. The second one is the formation of an accumulation layer (Figure 7 b) as electrons collect at the semiconductor surface when the

semiconductor has a lower E_f than the electrolytes redox potential. It creates a space charge (SC) region on the semiconductor side with the formation of a Helmholtz (H) layer on the electrolyte side with electrons accumulating in the semiconductor space charge region and an increase of free hole density at the semiconductor/electrolyte interface in the Helmholtz layer [61], [62]. The third one is the formation of a depletion layer (Figure 7 c) at the semiconductor surface as electrons move into the electrolyte when the semiconductor has a higher E_F than the electrolytes redox potential. The free hole density of SC region on the semiconductor side increases while electrons accumulate at the semiconductor/electrolyte interface in the H layer. If the depletion of electrons reaches a certain point below the intrinsic Fermi level of the semiconductor (Figure 7 d), then the space charge region of the semiconductor becomes that of a p-type semiconductor, inverting the semiconductor type.

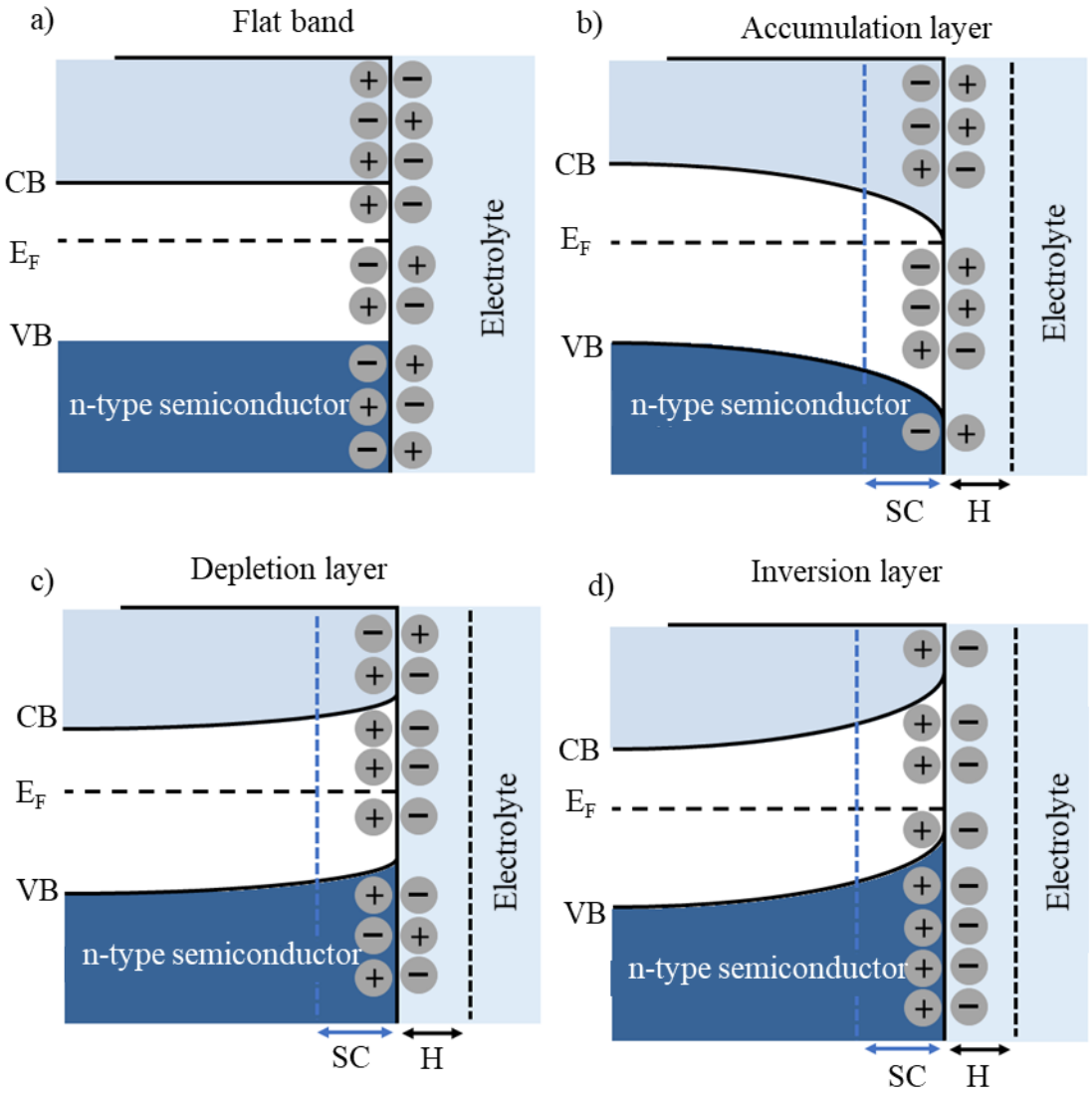

Figure 7: Charge and potential distribution at the semiconductor-electrolyte interface

The SC region allows the operation of photoelectrochemical cells to be possible when the E_F of an n-type semiconductor is higher than the redox potential of an electrolyte solution as

shown in Figure 5 a and Figure 7 b. Under these conditions, the electric field of the semiconductor is directed from the bulk to the semiconductor/electrolyte interface allowing electrons flow from the CB of the semiconductor to the electrolyte. As the semiconductor absorbs solar radiation the electron-hole pairs that are formed separate due to this field, the electrons move into the bulk while the holes move to the interface allowing them to oxidise the electrolyte species and have the electron transfer that will later generate electrical current.

Photocatalytic activity of semiconductor materials is driven by the transport property of photo-excited carriers from the interior to the surface of photoelectrode. When the light is turned on, the electron and hole separate and are driven on the surface to react with the redox couple in solution. However, when the light is turned off, the oxidative or reductive charge is trapped on the surface trap state and recombined with the others charge driven by the electric field produced by the charge trapped. It has been shown that the presence of the trap state can be seen by looking at the decrease in the potential in the dark [63]–[66]. If the change of potential is almost instantaneous, there is no charge flux and so no trapped charge. However, if the decrease is slight, it is corresponding to the slow recombination of the electron and holes.

Ozawa *et al.* [67] showed that the carrier dynamics were linked to space charge layer (SCL): an insulating region in the semiconductor material where the charge carriers have been diffused away or have been forced apart by an electric field. It could explain, according to the literature [68], [69],that the rapid decay of the anodic photocurrent is the sign of the presence of electron-hole surface recombination at the surface and band bending decrease. When the light was turned off, the conduction band electrons react with the holes trapped at the surface of the photogenerated species. In the literature of Tafalla *et al.* [68], the formation of OH radicals which led to the creation of oxygen evolution into alkaline media was observed. It is noticeable that an anodic were achieved right after the light was turned on and a cathodic peak right after the light was turned off. These two regions could be defined as, (I) the regions with the low band-bending when the recombination is important and (II) the high band bending region where only the accumulation of charge on the surface of the electrode influences the anodic peak. This electron-hole has to be minimised to be able to photogenerated a large amount of oxidised or reduced species.

2.4 Materials for photoactive electrode

The photoactive electrode has been studied for different applications e.g. water splitting, dye-sensitised solar cell and wastewater cleaning. All of these electrodes are composed of a n- or p-type semiconductor and they can be deposited onto a conductive and transparent substrate such as ITO, FTO or AZO coated glass.

2.4.1 Types of photoelectrodes

In order to fit the photoactive electrode to the application, it is crucial to determine if the desired reaction should be a photo-oxidation or a photo-reduction. As an example, the photo-oxidation is used in the dye-sensitized solar cell [6]. It is the hole which reacts with the redox couple into the anodic electrolyte. In this case, the semiconductor must be an n-type semiconductor as it has a more significant electron concentration than hole concentration. The photo-reduction can be used in the water reduction where the electron is driven into the solution by the electric field at the junction between the water and the semiconductor to reduced H^+ into H_2 [70]. In this situation, the semiconductor must be a p-type semiconductor because it has a more significant hole concentration than electron concentration. Different semiconductor materials are used depending on the application, their n or p-type, and their price.

2.4.2 Materials of interest

The semiconductor should be chosen by considering its specific characteristics while matching the semiconductor bandgap and the redox potential of the electrolyte (Figure 8) [5], [6], [71]–[74]. In the case of a p-type photoelectrode, the potential of the redox couple should be close to the conduction band. Conversely, the potential of the redox couple should be close to the valence band for n-type semiconductor. A huge amount of research into photoelectrodes has been conducted since the 1970s, with particular emphasis placed on adapting bandgap to the redox couple used while maximising the absorption of sunlight (Figure 9). The most used semiconductors for the water splitting are the transition metal oxides [75] such as TiO_2 (anatase: 3.3 eV [76], rutile: 2.95 eV [77], mix: 3.0 eV [78]) and ZnO (3.3eV [79]). Several other materials have been investigated like WO_3 (monoclinic: 2.5-2.6 eV [80], [81], orthorhombic: 2.9 eV [82]), $BiVO_4$ (2.45 eV [83]), Fe_2O_3 (2.1 eV [84]). These last materials

are used for water splitting as they have a large enough bandgap to react with a redox couple like VO_2^+/VO^{2+}. However, the conduction band might be too positive to reduce V^{3+} in V^{2+} in the counter electrode. In the dye-sensitized solar cell, the mostly used material is TiO_2, but ZnO [85], [86], SnO2 (3.62 eV) [86]–[88], Nb_2O_5 (3.2 eV) [89], [90] SrTiO3 (3.25 eV) [91], and Zn_2SnO_4 (3.25 eV) [92] have also been investigated. Overall, most parts of the solar redox flow battery published used TiO_2 [40]–[43], [93] since it is a known material, which has been largely studied in the literature.

A study has been conducted to understand the ion [94] and electron [95] diffusion through a TiO_2 film. Zerihun Kebede and Sten-Eric Lindquist [94] showed that the I_3^- ion diffusion was slower in a thin TiO_2 film than a thick one and the temperature drove the speed due to the viscosity of the solvent. Beside, Fei Cao *et al.* [95] have studied electron diffusion through a TiO_2 film. It was found that the photocurrent was composed of an active component, which corresponded to the injection of charge carriers close to the contact. However, the rest was quite slow: the movement of the electron proceeded to concentration gradients in the film to a steady-state value. This second part can be described by a diffusion model where the electron diffusion coefficient is dependent on light intensity. The bandgap and the photocurrent result of the TiO_2 layer could be altered by changing the macrostructure and the nanostructure of the TiO_2 depending on the deposition process.

One critical aspect of a photoelectrochemical cell is the interface between the semiconductor and the electrolyte. When this semiconductor is placed in contact with an electrolyte bulk containing a redox couple, an initial electrical current may flow for establishing an equilibrium between the Fermi level of the semiconductor and the redox potential of the redox couple in the electrolyte. This electron transfer leads to the formation of electric double layers in the bulk electrolyte. For the semiconductor, the effect depends on the initial Fermi level compared to the redox potential [6]. If the Fermi level is equal to the redox potential, a flat layer with no excess charge of each side will be obtained. On the other hand, if the Fermi level is lower than the redox potential, an accumulation of electron on the surface occurs. In the case that the Fermi level is higher than redox potential, a depletion of electron and the creation of positive charge at the interface occurs.

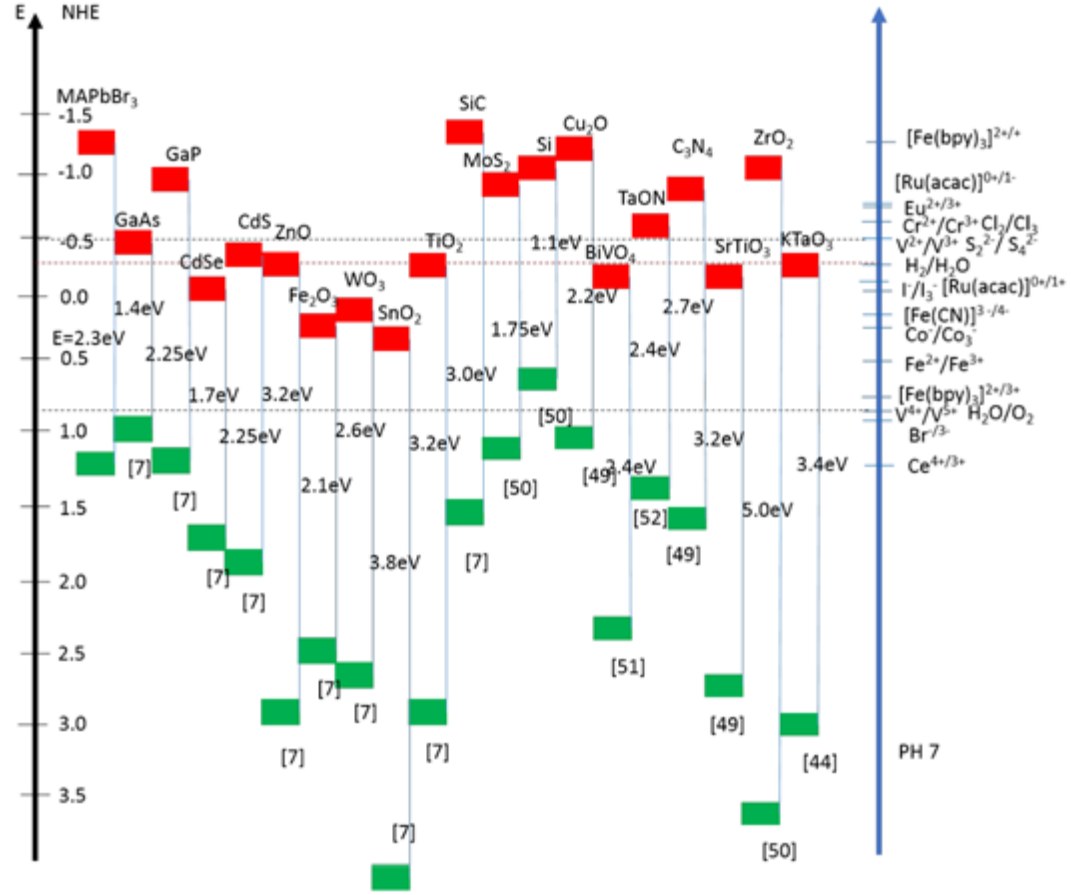

Figure 8: scheme of several semiconductor band gap with different redox couple and their redox potential at PH 7

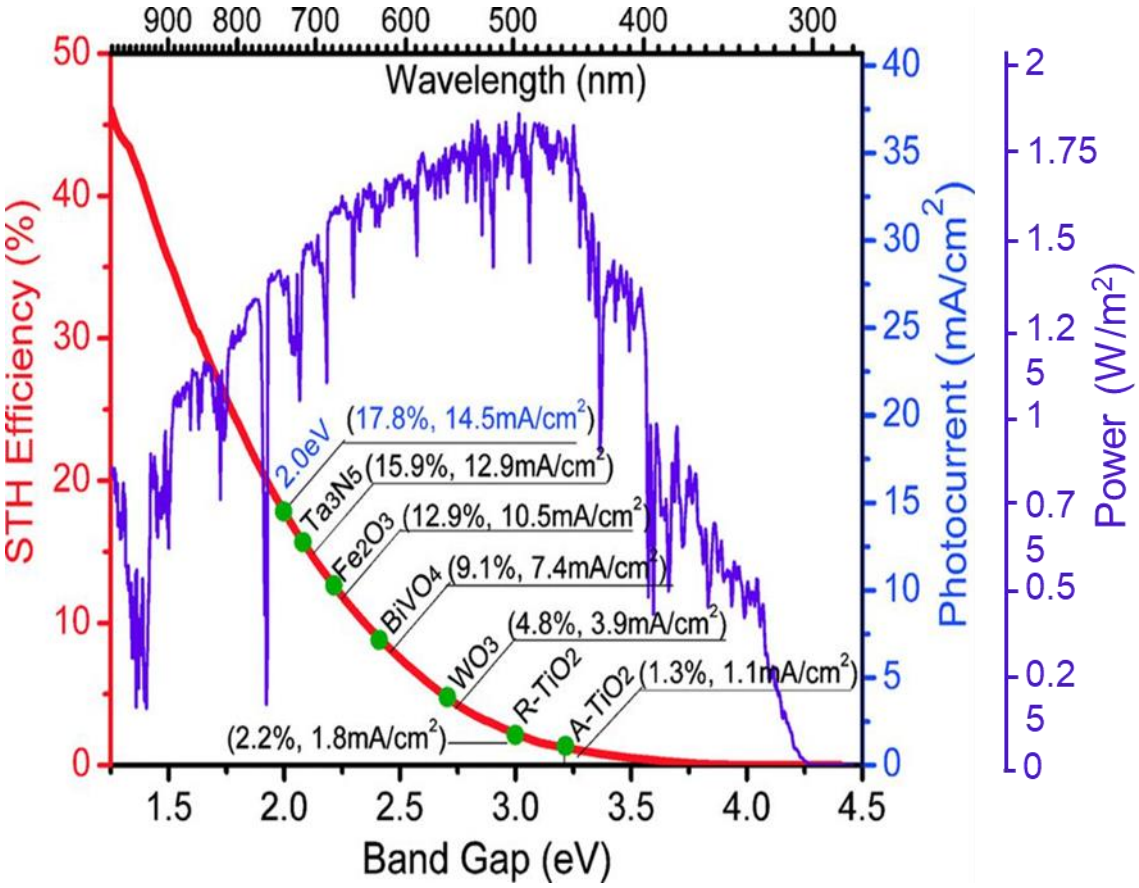

Figure 9: Solar spectra with some semiconductor with their photocurrent for hydrogen production [75]

2.4.3 Crystallographic structure of TiO_2

TiO_2 is the most common semiconductor used in photoelectrochemical cell and it is known that its semiconducting behaviour (as with many other semiconductors) depends on its crystal structure. TiO_2 can crystallise into three polymorphs: anatase, rutile and brookite (Figure 10): the anatase is a tetragonal structure ($P4_2/mnm$) formed by edge-sharing TiO_6 octahedra. Each Ti^{4+} ion is surrounded by an octahedron of six O^{2-} ions [96]. In anatase, the octahedron is distorted, so its symmetry is lower than the orthorhombic structure [97]. The titanium-titanium distances in this structure are 3.79, and 3.04 Å and the titanium-oxygen distances are 1.934 and 1.980 Å. Each atom is surrounding by eight other atoms (four sharing an edge and four sharing a corner). The crystal has a bandgap of 3.3 eV, a density of 3.894 g cm^{-3} and a free Gibbs energy of formation of -211.4 kcal mol^{-1} [97]. With this TiO_2 structure, some dye-sensitised solar cell has been built based on this powder and showed a photocurrent of 14 mA cm^{-2} [98].

Another crystallographic structure is the rutile with a tetragonal structure ($I4_1/amd$) formed by edge-sharing TiO_6 octahedra, and each Ti^{4+} ion is surrounded by an octahedron of six O^{2-} ions. The octahedron in rutile is not regular, showing a slight orthorhombic distortion [97]. The distance between two titanium atoms is lower than anatase (3.57 and 3.04 Å) but has a higher titanium oxygen distance (1.949 and 1.980 Å). Each atom is surrounded by ten other atoms (two sharing edge oxygen pairs and eight sharing corner oxygen atoms). The crystal has a bandgap of 3.1 eV, a density of 4.250 g cm^{-3} and a Gibbs energy of formation of -212.6 kcal mol^{-1} [97]. With this TiO_2 structure, some dye-sensitised solar cell has been built and give a photocurrent of 10.6 mA cm^{-2} [98].

Finally, some brookite structures have been studied. They are an orthorhombic (Pbca) structures formed by summit sharing TiO_6 octahedra: each Ti^{4+} ion is surrounded by an octahedron of six O^{2-} ions [96]. The distance between two titanium is similar to rutile (3.57 and 3.04 Å) as the titanium-oxygen distance (1.949 and 1.980 Å). Each atom is surrounded by eight other atoms. Unfortunately, this last phase is difficult to obtain due to the metastability of the brookite form [96].

A typical powder used for dye-sensitised solar cells is TiO_2 P-25, it is a nanopowder with particles of 25 nm diameter, composed of 75% anatase crystalline form and 25% of rutile. It is a cheap and easily processed powder, with a high surface area. The two phases are not interpenetrated but are still in contact, leading to a synergy effect [99]. However, the P-25

shows a lower device efficiency compared to the pure anatase. Although the literature has stated a disadvantage of the rutile for diminishing the photoelectrochemical efficiency of the P-25 photoanode, lately Kadhim Al-Attafi *et al.* [100] has shown that the issue comes from amorphous TiO_2 phase on the powder, which creates a network distortion, thereby creates some trap states close of conductive and valence band.

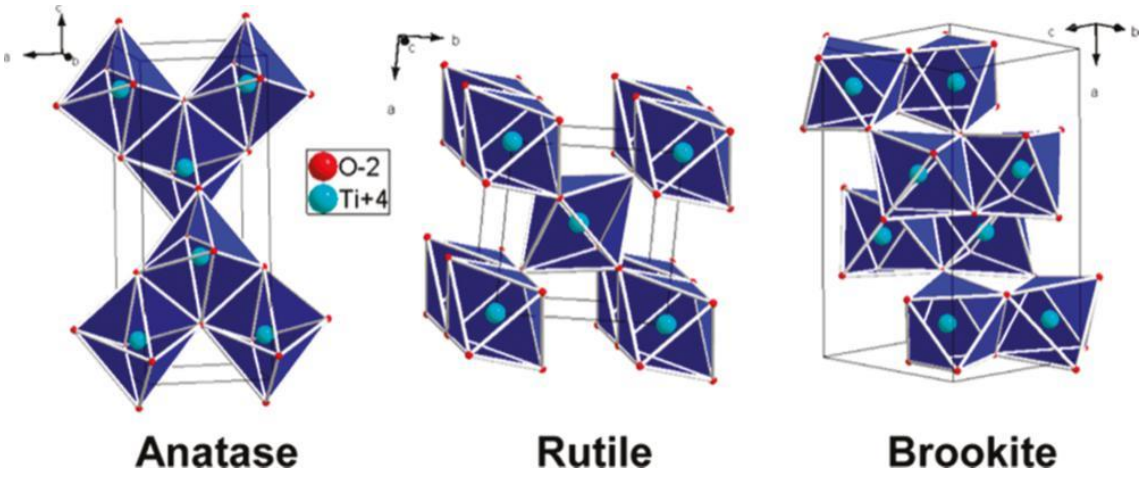

Figure 10: Representations of the TiO_2 anatase, rutile, and brookite forms [96]

2.4.4 Nanostructure of TiO_2

Another important parameter is the nanostructure of the TiO_2 film. The most used film in the dye-sensitised solar cell [101]–[103] and solar redox flow battery [40]–[43], [93] is a film composed of sintered nanoparticles. The film has a high mesoporosity, a good charge transfer, and a high specific area. The use of a nanoparticle film allows the tuning of the layer's morphology by changing the deposition process, the size of the nanoparticles and its porosity by adding polymers or other pore-forming agents. The porosity within the TiO_2 layer allows a better electrolyte penetration and therefore allows TiO_2 layers dye-sensitised solar cells to adsorb more dye. For example, Gratzel published the first dye-sensitised solar cell [104] with a photocurrent of 12 mA cm^{-2} by using a nanoparticle film. Dong Liu *et al.* [105] reported a photocurrent of 0.2 mA in^{-2} (31µA cm^{-2}) for a P-25 nanoparticle TiO_2 layer photoanode in a full vanadium solar redox flow battery.

However, nanoparticle films have a major drawback, an interfacial problem between the film and the conductive support, which affects the open-circuit voltage by decreasing the electron concentration in the conduction band [106]–[108] and the injection current [107]. Besides, the use of a concentrated electrolyte creates a prevent the formation of a macroscopic electrostatic potential gradient [101] (as any electrostatic gradients in an electrolyte are almost instantly removed due to ultra-fast ion movement). Another issue is the importance of the trapping process [109], which includes absorption and release of an electron with the light. It causes significant energy loss, especially as there are a large number of grain boundaries [110].

One solution for solving the problem of electron-hole recombination around a TiO_2 core [111], depositing nanoparticles on the TiO_2 powder before the film coating process [56] or decorating preformed TiO_2 films with nanoparticles [112]. The core-shell approach is intended to increase the physical separation of injected electrons and oxidised red-ox couple and thereby retarding the electron hole recombination reactions at the surface of the TiO_2(in the DSSC the core shell is used to improve the contact between dye and TiO_2 but it is not relevant in the case of solar redox flow battery). This core-shell could be composed of materials such as Nb_2O_5, ZnO, $SrTiO_3$, ZrO_2, Al_2O_3 or SnO_2 [56], [106], [108], [112] with a lower conduction band. The secondary materials are used as electronic shell between the electrolyte and the TiO_2 [112] and create an energy barrier at the interface between them. For dye-sensitised solar cells, Yishay Diamant *et al.* [84] showed an improvement of the photocurrent by 11% with Nb_2O_5 coating. Unfortunately, a lot of uncertainty on the real shell effect is presented in the

literature (formation of an energy barrier at the TiO_2 surface [104], [108] *vs*. a shift of the TiO_2 conduction band in the negative direction [56]) and the effect changes with the different core-shell materials.

A way to solve to the problem of contact between the substrate and TiO_2 the nanoparticles is to deposit a 1D TiO_2 structure. Like TiO_2 nanowire array [76], [82], [113]–[115], it consists of a wire of TiO_2 that grows vertically on titanium foil by anodisation or directly on the conductive glass [116]. As these nanowires are single crystals, they can provide direct pathways for electron transport and suppress charge recombination [84], [117]–[119]. Feng *et al.* [114] showed a photocurrent of 0.8 mA cm^{-2} for a TiO_2 nanowire array without dye in a 1 M KOH solution. The nanowire has a direct connection between the point of photo induced charge carrier generation with the conductive substrate, but the disposition of the porosity of the layer cannot be controlled [114] .

Another 1D TiO_2 structure is the TiO_2 nanotube [120]. It has a defined diameter, so films created from nanotubes have a defined mesoporosity. With these nanotubes, Wang *et al.* [120] have shown that a DSSC using these nanotube photoelectrodes can obtain a photocurrent of 13.5 mA cm^{-2}. A similar 1 D TiO_2 structure investigated is the nanorod [43], [121]. It is an array of TiO_2 single crystal of several hundred nanometers of thickness. The nanorods are usually bigger than nanowires and have a rectangular shape. The growing process parameters can control the diameter of the nanorod and the thickness of the layer.

Huang *et al.* [122] used a hydrothermal solution method to grow TiO_2 nanorod layers and showed that DSSCs using these TiO_2 nanorod electrodes gave a photocurrents between 0.94 mA cm^{-2} and 6.88 mA cm^{-2}, with these currents found to be a function of layer thickness and layer growth rate. Unfortunately, these nanorods layers are typically quite thin (maximum: 2 µm) which tends to limit the photocurrent. The same issue could be found in any 1D TiO_2 structure layer [122].

For improving the surface area, the addition of nanoparticles to the TiO_2 nanotubes or the nanowires array could be realised through mixing. If some nanowires are added to a TiO_2 powder, the layer has a better light absorption than a normal nanoparticle layer [123], [124]. For example, Morimoto *et al.* [100] showed a photocurrent of 12.89 mA cm^{-2} for dye with the addition of 20 wt% nanowires. This photocurrent is higher than the 12.11 mA cm^{-2} recorded without the nanowires on the film.

Finally, investigations have studied the influence of the 3D structure of the TiO_2 films [115], [125], [134], [126]–[133] to allow improved light-harvesting, and good charge transport within the high surface area film. The main advantage of these 3D structures is the creation of a continuous TiO_2 network, which could transport the charges carriers through the entire layer.

One example of 3D structured TiO_2 films are based on inverse opals. This approach uses a polymer or nanosphere (100 nm to 10 nm) close-packed framework with the gaps between these nanosphere filled with TiO_2 precursors such as titanium isopropoxide or butoxide solutions. The result is an inverse opal network, which allows better diffusion of the electrolyte in the layer. Eun *et al.* [134] reported a DSSC with a photocurrent of 6.42 mA cm^{-2} with a thickness of 12 µm and the use of 1 µm sphere diameter frame. However, due to the composition of the TiO_2 paste, the amount of TiO_2 incorporated in the cells was one third of the typical weight for a doctor blade film of the same thickness using the same TiO_2 paste. Another 3D structure is the forest like TiO_2 structure [127] (5.86 mA cm^{-2} with C101 dye and a thickness of 13 µm) with a large surface and a higher porosity allowing a good diffusion of electrolyte on the film and an increase of the charge lifetime. Finally, TiO_2 aggregates [125], [126] have been studied. The TiO_2 aggregate is based on the creation of the TiO_2 crystalline sphere at different orders: nanometer scale and micrometer scale. Micrometer-scale spheres are composed of several small nanocrystalline particles. It allows for better electrolyte diffusion between micrometer scales TiO_2 spheres, so it can diminish the distance required for the electrolyte to reach the nanocrystalline particles.

2.5 Photoelectrode preparation

2.5.1 1D structured TiO_2 film

To obtain a stable TiO_2 film on top of transparent and conductive substrates, the literature proposes several methods. They can be separated in three categories: 1D structure, randomly packed structure and 3D structure TiO_2 films.

Lately, a different deposition process has been used to create 1D structures TiO_2 layers, based on nanowire, nanotube or nanorod arrays. The first method is the use of a hydrothermal growth [76], [82], [113], [114], [135]. Nanowire array synthesis is

achieved using a nonpolar solvent and Ti^{4+} precursor. A small amount of polar water is added. With an increase in temperature, to minimise system energy, water will diffuse away from the high energy area to the interface phase and aggregates on the hydrophilic conductive glass surface. Simultaneously, the Ti^{4+} precursors will hydrolyse with water and create some nuclei on the conductive glass surface.

A method for obtaining a highly structured TiO_2 nanotube array is to grow it on a titanium foil by anodisation [116], [136]–[142]. The first step is to wash the titanium foil, removing impurities. This is followed by polishing, to create a flat layer that will reduce the number of cracks in the final film. The foil is then immersed in an electrolytic solution with a platinum counter electrode at 20 V *vs.* Ag|AgCl for 30 min [136]–[140]. The voltage and the time determine the thickness of the TiO_2 layer. The electrolyte is usually a hydrofluoric acid solution [116], [136]–[138], [142] or an ethylene glycol solution [139]–[141]. The advantage of HF is the incorporation of fluorine in the layer, but its safety and environmental issue are a limiting factor for using this electrolyte. After the growth of the nanotube on the titanium foil, the layers are annealed at around 500ºC [116], [136]–[138], [140] or can be detached from the titanium foil [139].

For separating the TiO_2 from the titanium foil, two methods have been investigated. The first one is to leave the foil in methanol overnight and let the methanol evaporate before detaching the TiO_2 layer. The other one is to use hydrochloric acid to dissolve the interface between the titanium foil and the TiO_2 [139], [141]. However, the TiO_2 layer is not on a proper substrate (FTO glass). It can be attached to the substrate by adding titanium isopropoxide and polymerising it into the TiO_2 (Figure 11 a). Finally, the layer is annealed at 500ºC to form a junction between the substrate and the nanotube array [139]. The easiest solution is to firstly deposit a titanium layer on the substrate, then grow the film directly onto it [116] (Figure 11 a b), but the thickness of the titanium deposition on the substrate will limit the resulting TiO_2 layer thickness. The use of a treatment with $TiCl_4$ [139] or decorating the nanotube array with CdS or CdSe nanoparticle [142] could be additional ways to improve the photocurrent. A novel post-treatment using a freeze-drying method has been published [143] and showed an improvement of the charge transport on the nanotube arrays.

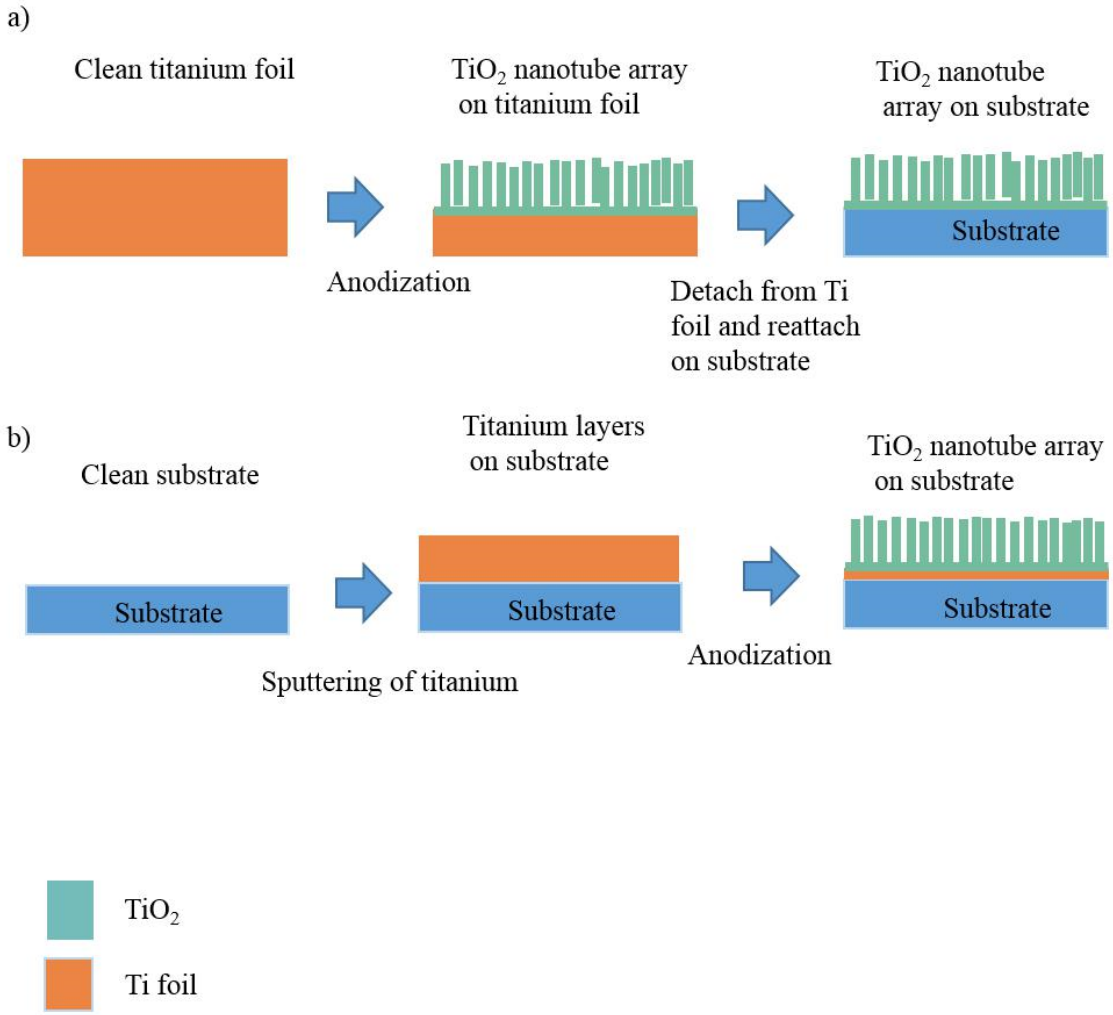

Figure 11: scheme of nanotube array formation a) on the titanium foil and b) directly on the substrate.

2.5.2 Doctor blading

For depositing TiO_2 nanoparticle-based films, one approach is to use a sol-gel deposition process. Consisting of the deposition of a TiO_2 nanoparticle slurry by different deposition processes. Several deposition processes were used in the literature for the deposition of the nanoparticle-based films: doctor blading [5], [38], [54], [95], [104], [144]–[147], screen printing [148]–[150] and airbrush spray deposition [151]. The first deposition method used was the deposition of a paste by doctor blading on conducting glass such as indium oxide doped tin oxide (ITO) or fluorine doped tin oxide (FTO) [5], [38], [54], [95], [104], [144]–[147]. The doctor blading consists of the deposition of a viscous slurry, which is spread on the conductive glass by a blade (Figure 12).

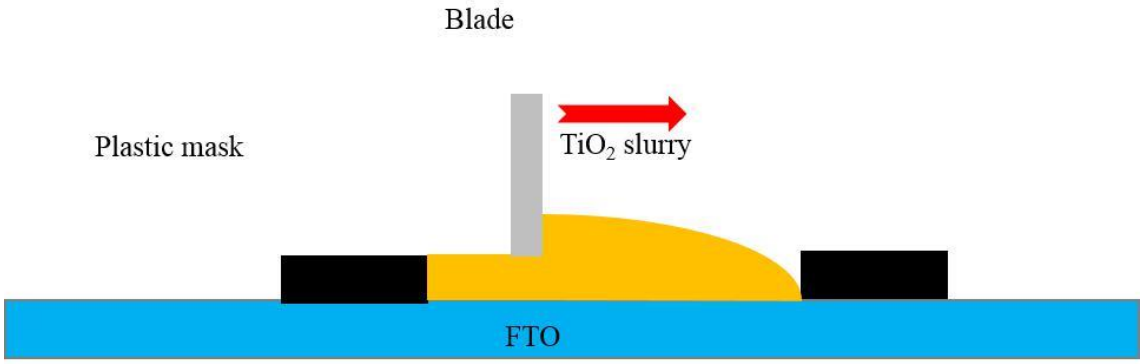

Figure 12: Scheme of doctor blading process

This method was used for the first time by Gratzel *et al.* [104], with the TiO_2 powder obtained by the hydrolysis of titanium isopropoxide. A viscous solution of TiO_2 was prepared and spread on the conductive glass and sintered at 450 ºC. The resulting layer had a high surface area and could absorb a ruthenium-based dye easily. The (short-circuit) photocurrent obtained for the first dye-sensitised solar cell (DSSC) was about 12 mA cm^{-2}.

Grunwald *et al.* [145] and Cao *et al.* [95] went into detail about the doctor blading deposition. A 10 µm silicon tape is used as the mask, and the slurry is bladed by a glass slide, the film is similar to the case of Gratzel *et al.* [104]. Yu and co-workers [144] even showed that this deposition process could be used with a solid electrolyte. Finally, Liu *et al.* [5], [54] reported results for some full vanadium solar batteries using a TiO_2 layer deposited by doctor blading. The photocurrent obtained with AM 1.5 filter and 100 mW cm^{-2} sun simulator reach the 80 µA cm^{-2}. The thickness of TiO_2 deposit is an important parameter and has a maximum effect

of around 10 µm for the dye absorption and for the TiO_2 photocurrent itself. The advantage of this deposition process is its ease of implementation and its speed of deposition. Still, the drawback is the use of a binding agent to obtain a viscous slurry which can diminish the electrical conductivity of the film and the difficulty to reproduce the same film precisely on a small surface [145], [151], [152].

2.5.3 Screen printing

The screen-printing method[148]–[150] is another prevalent deposition process: the slurry is deposited on a screen with a mask, and then a blade is passed on the screen (Figure 13). The slurry is dropped on the conductive glass under it through the screen, which gives a better porosity of the layer but the use of several successive layer deposition is needed for the thickness control [150].

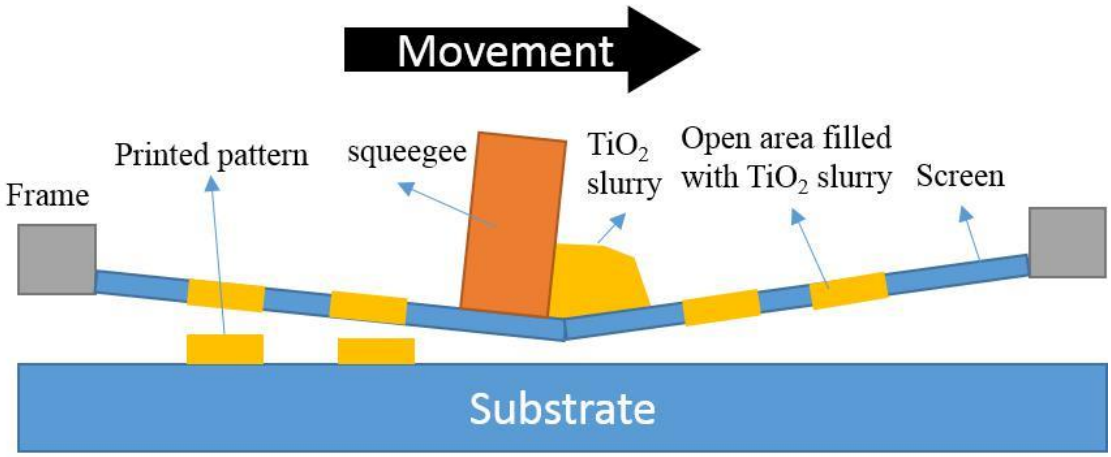

Figure 13: scheme of screen printing method for deposition of a TiO_2 layers composed of nanoparticles

In 2003, Wang *et al.* [153] used this deposition process for testing a new electrolyte. The FTO was inserted into a $TiCl_4$ solution before the deposition of the main layer to improve adhesion of the TiO_2 layer to the FTO. The photocurrent obtained was 10.4 mA cm^{-2}, which is lower than the doctor blading deposition process, but of the same order of magnitude. Feldt and his co-worker [149] used this deposition process for designing multiple organic dyes. Particles between 300 nm and 20 nm where used, with photocurrents between 11.31 mA cm^{-2} and 13.68 mA cm^{-2} recorded. Yum *et al.* [150] used this deposition process for testing a cobalt complex redox shuttle, the detected photocurrent was 13.01 mA cm^{-2}. Lastly, Hao *et al.* [148] deposited two different TiO_2 pastes to form the TiO_2 layer, by screen printing to obtain a dense TiO_2 film. The photocurrent reached 15.5 mA cm^{-2} by using a small electron donor in cobalt complex electrolyte.

The screen printing results shows the advantage of better porosity of the layer attained and the possibility to deposit thicker films a few micrometers thick of different materials. Still, its main drawback is that it requires the use of some FTO treatments, which are difficult to control for obtaining good adhesion of the layer.

2.5.4 Airbrush spraying

Lately, a new deposition process has been investigated: using an airbrush spray gun [151] for the deposition of the TiO_2 layer. The capacity of depositing the film in a specific area by the application of a spray mask is the main advantage of this method. Senevirathne *et al.* [151] published quasi-solid-state electrolyte based on γ-butyrolactone and tetrapropylammonium iodide dye-sensitized solar cells. A titanium colloidal solution was sprayed on an FTO glass heated at 150ºC on a hot plate. The film was sintered between 500 ºC and 450 ºC to create a homogenous film. The photocurrent obtained was 15.7 mA cm^{-2}, similar to the previous deposition process photocurrent.

2.5.5 Deposition parameters

In previous methods, the first is to prepare a colloidal slurry of TiO_2 nanoparticles. The first ingredient for realised a slurry is the TiO_2 powder. In the literature, some were prepared in the laboratory and were obtained by the hydrolysis of titanium isopropoxide [104]. The majority were purchased as pure anatase [55], [150], [153] or P-25 powder [5], [54], [95], [145].
The solvent used for the slurry depends of the viscosity required by the deposition process, for example the the doctor blading and screen printing techniques required a viscous paste. Not too viscous to spread, but not too liquid that the slurry is lost when the mask is removed. In contrast, the airbrush spray coating required a liquid slurry to be atomized. For the slurry of airbrush spray deposition process, Senevirathne *et al.* [151] used a mix of water and ethanol as the solvent (TiO_2 concentration about 20 wt%).

For the slurry used in doctor blading and screen printing, the solvents used were alcohol or water. Gratzel *et al.* [104], Grunwald *et al.* [145] and Cao *et al.* [95] used a water solvent with a TiO_2 concentration of 0.6 g ml^{-1}, terpineol [5], [54], [55], [144] were used as the solvent due to its high viscosity and boiling point [48] (paste between 10 to 30 wt% of TiO_2). However,

the viscosity of the slurry was challenging to control, so Zhang *et al.* [55] used an additional polymer (ethylcellulose) to bind the TiO_2 particle together. Other polymers could also be used to control the viscosity of the slurry [55]. Then polymers binders, like polyvinylidene fluoride (PVDF) [5] or ethyl cellulose [55], become a standard component of the slurry especially for screen printing (typically 5 wt%).

The slurry of TiO_2 in water could lead to agglomeration of the TiO_2 nanoparticles. Therefore, the use of a dispersive agent, acetylacetone [145] [151] was used to prevent agglomeration of the TiO_2 slurry. Commonly this dispersive agent makes up 1 % to 2 % of the volume of the slurry. Triton X [151] [145] [95], another dispersive agent, was used for dispersing the particle all over the substrate surface.

Early investigations into DSSC often focused on the properties and performance of various dyes and thus many used TiO_2 nanoparticle-based films following the method described by Gratzel *et al.*[104], Grunwald *et al.*[154].Oskam *et al.*[146] followed similar approaches but incorporated some polyethylene glycol to increasing the porosity of the layer. In 2006, Guo *et al.* [155]showed different and essential parameters relating to the TiO_2 layer. The use of polyethylene glycol with a bigger chain size could lead to better porosity by increasing the pore size, therefore, could improve the electrolyte path inside the layer.

The last step after deposited the slurry on the substrate was to annealed the TiO_2 film. The film was usually annealed at 450 °C [5], [38], [150], [153], [154], [54], [55], [95], [104], [144]–[147]. The sintering allows the TiO_2 particles to create interconnection, creating a network. Porosity of the thin films increased when the temperature is around 450 °C. The grain size increased, and the resistivity of the films decreased when the annealing temperature increased[156]. The heat treatment of TiO_2 photoelectrodes at this temperature result in enhanced electron transport. However, it was accompanied with a reduced specific surface area compared to lower sintering temperature[157]. Another critical parameter in the sintering step is the heating rate. John *et al.* [158] shown that the heating rate has an impact on the surface roughness of TiO_2 thin. The surfaces of the films prepared at low annealing rates (1°C/min) are more smooth and homogeneous due to enhanced mobility of molecules.in contrary, annealing directly from room temperature to the sintering temperature led decreased the particle coalescence and agglomeration of the islands and so to an increase of the roughness of the film.

2.5.6 Other randomly packed structure

The spray pyrolysis [159] process is a basic method used to growing a TiO_2 layer on the conductive glass, providing better contact with the substrate and a more compact layer [160]–[163]. The principle is to prepare a solution of a suitable titanium precursor (titanium (IV) oxy acetylacetonate [160] or butoxide [161]). This solution is atomised by a nebuliser and deposited on a substrate at 400ºC-500ºC. Okuya *et al.* [160] published a method of forming a TiO_2 layer based on titanium (IV) oxy acetylacetonate and aluminium (III) acetylacetonate dissolved in butanol. The solution is atomised by a nozzle and some compressed air and deposited on a conductive glass heated at between 300ºC and 500ºC. The film is composed of anatase TiO_2, and some dye is absorbed on it. It gives a photocurrent of 7.2 mA cm^{-2} for a thickness of 10 µm.

Abou-helal *et al.* [161] have built a similar spray pyrolysis chamber with a solution of titanium (IV) isobutoxide dissolved in a mixture of HNO_3 and methanol (1:9). A 350 L h^{-1} air volume, 1.0 mL min^{-1} solution rate, 450-600ºC deposition temperature range and 5-30 min spray time range. Finally, Li and his colleagues published two papers [162], [163] for doping TiO_2 layer with fluorine, nitrogen and carbon. The solution is composed of $TiCl_4$ and NH_4F aqueous solution.

A dry deposition process, the vacuum cold spraying, has been investigated for several years. It consists of spraying dry powder by using an accelerating gas to project the powder on the FTO substrate under vacuum [38], [164], [165]. The advantage of this technique is a more precise deposition without solvent and surfactant use. Fan *et al.* published three papers in 2006 and 2007 [38], [164], [165] on the vacuum cold spraying TiO_2. This vacuum cold spraying is composed of an aerosol room contained in a sealed beaker with a P-25 TiO_2 powder. This powder is transported by a helium gas until the film deposition chamber under vacuum. The gas with the aerosol passes through a nozzle and is deposited on the substrate hold on an adjustable holder. The photocurrent obtained was 7.3 mA cm^{-2} for a thickness of 15 µm.

In 2001, Lee *et al.* [166] modified a non-crystalline TiO_2 layer by using a solution of $TiCl_3$ with NaCl (pH 2-3) and driven the titanium oxidation by photocatalysis of the solution. This method gave a better layer coherence and a similar photocurrent (18.8 mA cm^{-2} with the use of dye). This result in a new TiO_2 deposition method the electrodeposition. These several studies have confirmed that it is possible to deposit some TiO_2 by using a mix of $TiCl_3$ [166]–

[168] in acidic electrolytes driven by the appliance of a current. Lokhande *et al.* [148] used a mixture of $TiCl_3$ in concentrated HCl (1:2 ratio). Its pH was adjusted by using $NaHCO_3$ solution (7% $NaHCO_3$). An anodic potential of 1 V *vs.* Ag|AgCl was applied for 10 min. The film formed is deposited on CD-SE semiconductor and a current of 200 µA. cm^{-2} is recorded against 1M NaOH. Wessels *et al.* [167] succeeded to deposit a TiO_2 film with dye on a single-step process using a 50 mM aqueous acidic solution of $TiCl_3$ at 80ºC with the addition of a solution containing the dye. The film is anodized at a potential of 0.13 V *vs.* Ag|AgCl for 30 min. Leading to a decrease of the preparation time of a photoelectrode for dye sensitised solar cell. Finally, Endrodi *et al.* determined the effect of the temperature and the voltage on the electrodeposition of TiO_2 using an HCl stabilised solution of $TiCl_3$ (12%) with Na_2SO_3. They received a photocurrent of 2 mA cm^{-2} without dye for a 50 mM $TiCl_3$ solution at pH = 2.0 and room temperature (j = 100 µA cm^{-2}, Σ = 200 mC cm^{-2}). The formation of the TiO_2 layer was directly grown on the surface, and the current offered the possibility to control the thickness of the final layer. These methods can be used for forming ruthenium/TiO_2 [169], or silicone oxide/TiO_2 [170] composite.

2.5.7 3D structure TiO_2 film

The most popular way to create a 3D network is the creation of an inverse opal TiO_2 structure: a highly ordered and porous TiO_2 layer with tuneable pore size. The literature has shown the use of this inverse opal for DSSC to increase the photocurrent [131], [134]. The preparation method is easy but can take a long time.

The first step is to prepare a sacrificial framework composed of a microsphere of polymers [115], [128]–[134], [171] or silicate [172]. The most commonly used polymer is polystyrene [115], [128], [129], [131]–[134], [171], but polymethyl methacrylate (PMMA) [130] has also be used. The polystyrene microspheres can be synthesized by using a polymerization of styrene controlled by temperature [171] or obtained commercially [128], [129], [131]–[133], [171], [173]. The first step is to make a suspension of polymer microspheres in proper solvent (water is usually used [128]–[133], [171], [173]), then ultrasonicates it to break the agglomerated particles.

For depositing these microspheres on the substrate (FTO, quartz or simple glass slide), several methods are used. The first one is dip coating[115]: the substrate is immersed in the microsphere dispersion liquid lifted out of the solution at a preset speed controlled by a

continuous motor. This is a fast technique but needs to have a very low speed in order to obtain a proper coverage of the substrate [130].

The vertical deposition method (Figure 14 a). the substrate was left immersed in the solution for a long time [129], [130], [132], [133], [171]. Then the solution evaporates and the nanosphere is concentrated in the meniscus, thereby the interface slowly decreases down the slide and deposit nanosphere on the substrate [129], [130], [132], [133], [171] The immersion time and temperature are the two parameters used to control the thickness of the opal layers and should be carefully monitored.

The gravity sedimentation [130] consist in a time-dependent deposition of particles due to gravity, the substrate is left on the bottom of a beaker into the microsphere dispersion and is left a long time to let the sphere fall on the bottom of the beaker on the substrate, but this is a slow technique [130]. To diminish the preparation time, the centrifugation technique [130] (rotating the sample at high speed which separates the solids suspended in a liquid) produced the same quality of template, but only takes 24 hours instead of five weeks.

Finally, they use a specific doctor blading deposition method, like microfluidic doctor blading [131], [173] (Figure 14 b) have been studied. The method consists of the deposition through a microfluidic glass canal of polymer dispersion solution between a glass slide and the substrate, separated by a tape with a thickness of several micrometres. The top part is moved slowly over the substrate to evaporate only the solvent in contact with air. This method allows the formation of a well-ordered layer in a few hours, and as the top of the layers dries faster than the bottom, the top will be more concentrated with microspheres, which increases the future TiO_2 contact with the substrate. This method allows depositing a binary mixture of TiO_2 and polystyrene microspheres and dries it with a warm airflow for a faster deposition of TiO_2.

The polymer on the substrate is maintained at around 80ºC-90ºC for a specified time to removing all of the water. A solution containing isopropoxide in ethanol or other alcohols and a trifluoroacetic or hydrochloric acid can be used. The solution is deposited as small droplets [130], [132], [133], [171], [172] by immersing the template in the solution [115], [129] or by centrifugation [131]. The titanium solution infiltrates the framework until covering all the interstices. Finally, the layers are heated at around 400ºC-500ºC to calcine the polymer and form the porous inverse opal structure (Figure 15).

The opal structure has several advantages, the first one is its highly structured periodicity, which helps have a good exchange between the electrolyte and the TiO_2 with a better interconnection of the particles between them, due to the use of isopropoxide. The second benefit is the fact that it can be doped with nitrogen and fluorine [172] or loaded with gold and fluorine [133]. The only drawback of the structure is an increase in reflectance under the visible light, leading to a diminution of the film absorption and of the photocatalytic efficiency [133].

Another 3D structure is the forest-like structure. This TiO_2 film is grown on FTO-coated glass substrate and is prepared with a pulsed laser deposition method, following a procedure published by Sauvage and al [127]. It consisted of the use of a laser to ablate a titanium target in a background O_2 atmosphere. The thickness was driven by the deposition time. Finally, the layer was sintered at 500ºC in air. The film consisted of assemblies of 10 nm nanocrystalline particles of anatase TiO_2, morphologically resembling a tree with branches approximately 40 nm in diameter and 500 nm in length. The photocurrent obtained with C101 dye was 8.99 mA cm^{-2} [127].

Finally, the last investigated 3D structure is the TiO_2 aggregate. Sub-micrometre-sized TiO_2 spheres have often been prepared by sol-gel methods controlling the hydrolysis and condensation reactions followed by a calcination step. Kim *et al.* [125] used relatively low concentration of titanium (IV) isopropoxide and water solution for forming a highly monodispersed and well-defined spherical TiO_2 and higher titanium (IV) isopropoxide, and water solution for form deformed spherical structure with diverse sizes and shapes. The photocurrent of 14.57 mA cm^{-2} was achieved for a dye-sensitised solar cell.

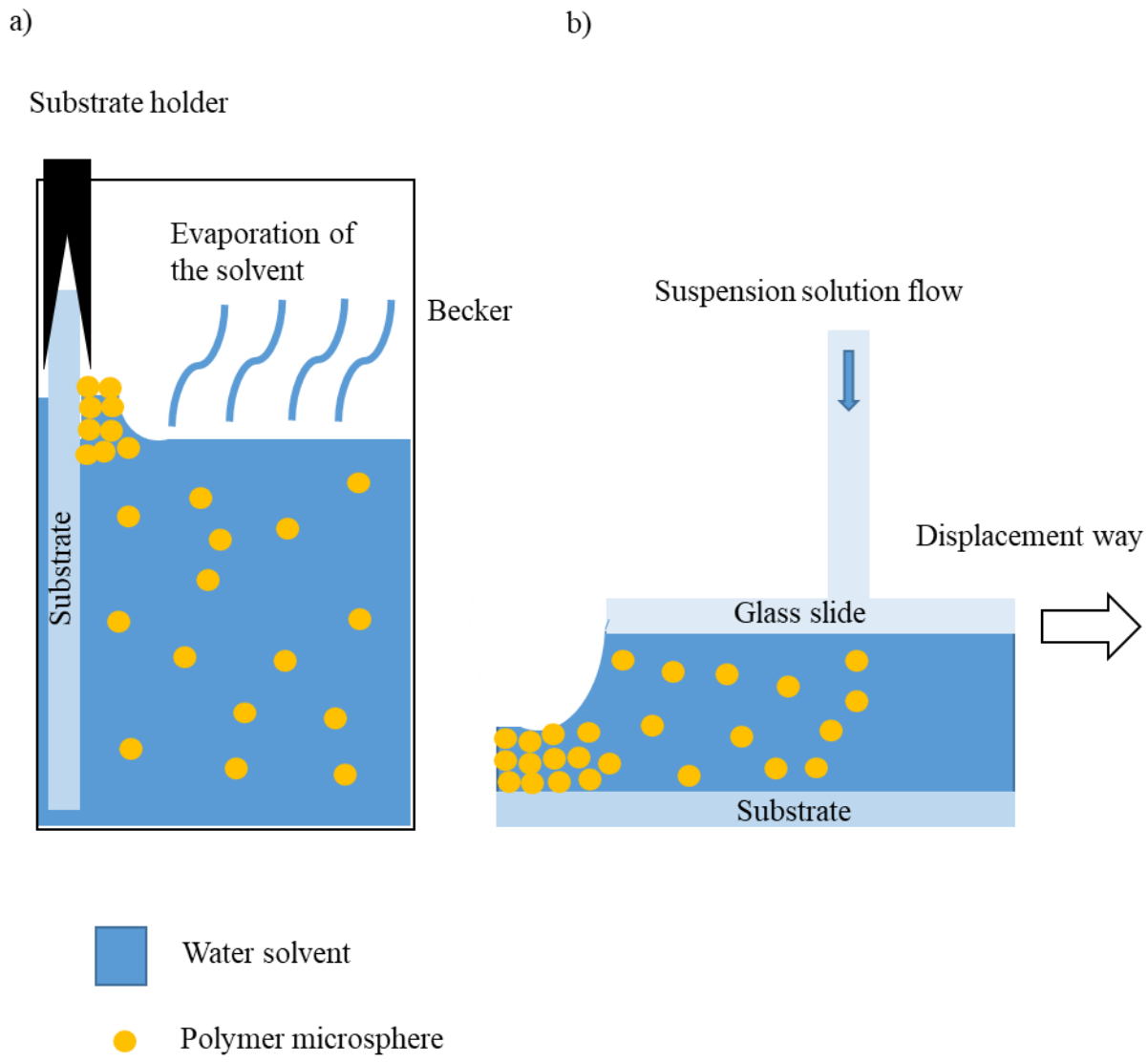

Figure 14: deposition method of polystyrene micro-sphere a) vertical deposition method b) microfluidic doctor blading.

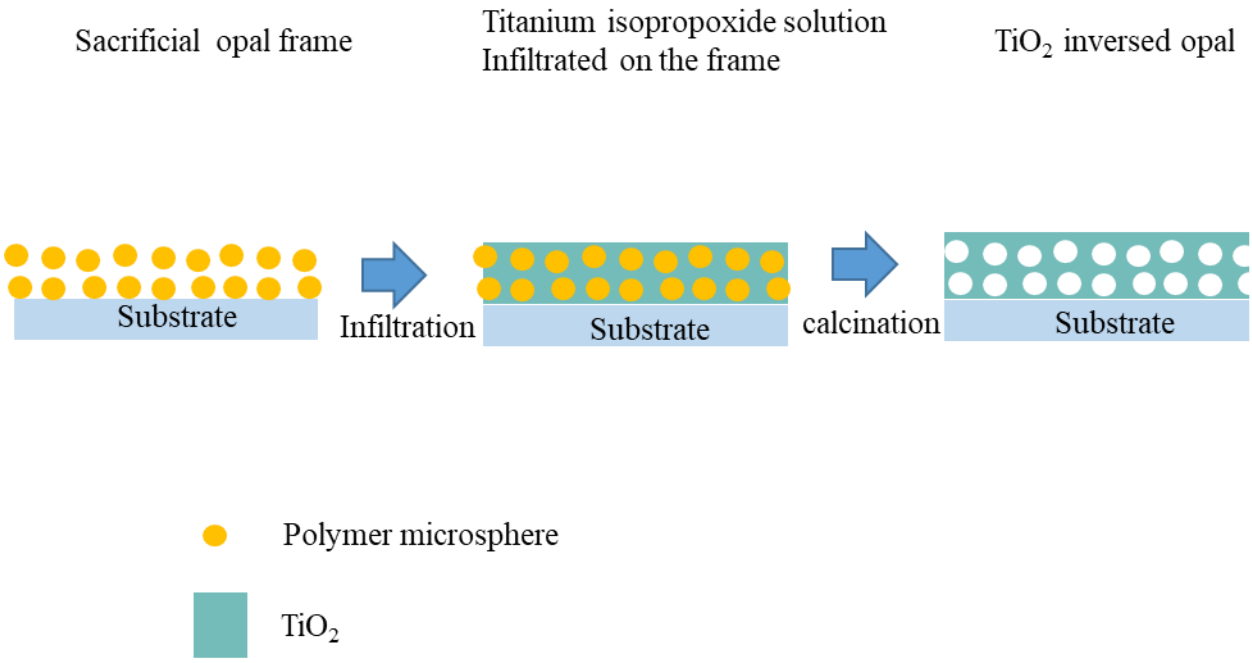

Figure 15: process of the inverse opal formation.

2.5.8 Photoelectrode preparation: Porous film

Solvothermal and hydrothermal reactions were favoured when specific complex morphologies were desired [174]. These processes involve the use of a solvent under high temperature between 100°C and 1000°C and high pressure, typically between 1 atm and 10,000 atm. If water was used as a solvent, the method was called hydrothermal synthesis and solvothermal synthesis if a non-aqueous solvent was used.

Microwave methods use high-frequency electromagnetic waves to induce hydrolysis of the titania precursor to form larger ordered structures [174]. Microwave methods are a bottom-up approach, whereby titania is synthesised by evaporation following by vapour deposition in a cool environment [175]. Combinations of different processes, such as sol-gel processing combined with microwave treatment of the resulting powder, allow for the conversion of a nanoparticulate sol-gel product with particle sizes of around 9 nm and specific surface areas of larger than 550 m^2 g^{-1} to nanocrystalline anatase titania tubes with a diameter of about 5 nm.

Hu *et al.* [176] prepared spherical and monodisperse nanoparticles from the titanium sulphate precursors by the microwave method. The study showed that the power output of microwaves affected the particle size. Indeed, the small particles were obtained by a high power while a low power led to large particles. Microwave synthesis could allow for better control of particle size and morphology [177].

2.6 TiO_2 photoelectrode improvement

The primary problem with TiO_2 based photoelectrodes comes from its absorption band. As pure TiO_2 P-25 has a bandgap of 3.2 eV [97], it can only absorb photons, which have energy greater than 3.2 eV. The conversion between eV and wavelength is given by:

$$E = \frac{hc}{\lambda} \qquad (21)$$

Where E is the energy of the photon (eV), h is Plank's constant (4.135667516 x 10^{15} eV s), c is the speed of light (299792458 m s^{-1}), and λ is the wavelength of the photon (m). From this, it can be seen that only photons with wavelengths below 387 nm will have sufficient energy to generate an electron-hole pair. Unfortunately, the majority of light from the sun has much longer wavelengths (Figure 16).

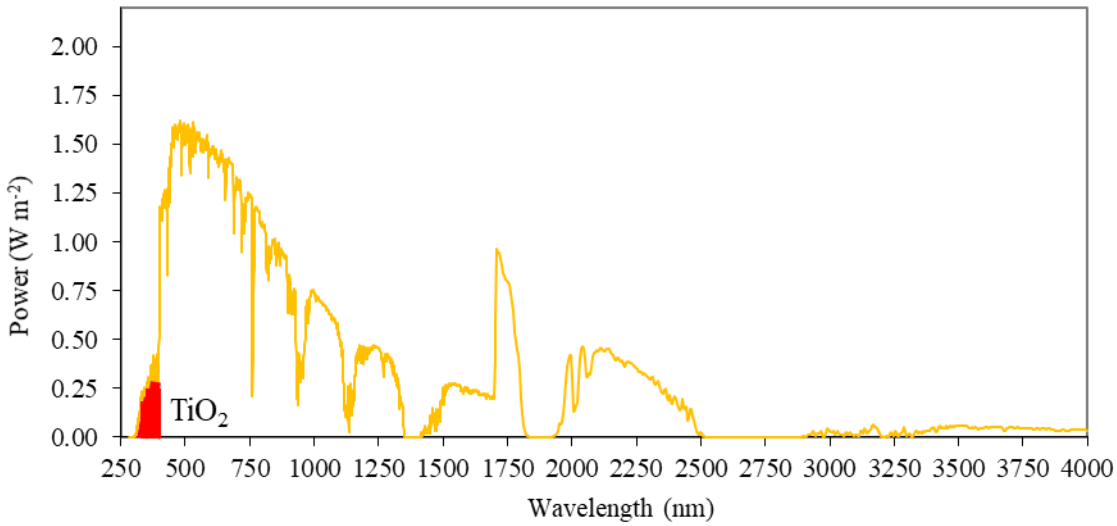

Figure 16: The standard solar spectra (AM 1.5) used for photovoltaic performance evaluation. This spectrum represents the light power (W m^{-2}) which reaches the earth at an angle of 48.2 in Toledo (latitude: 41.6639 N).

To determine the light intensity of relevance for TiO_2 photoanodes, the total power of light between 280 nm and 400 nm is calculated by integrating the area under the sun spectra between those two wavelengths. This integration was performed numerically using the trapezoidal method and yielded a power of 47.24 W m^{-2}. Dividing this value by the total power from the AM1.5 spectrum (1000.37 W m^{-2}), shows that pure TiO_2 will only absorb 4.72 % of the solar spectrum. Therefore, the TiO_2 layer should be altered to absorb a larger fraction of visible light.

2.6.1 TiO_2 doping

Doping metal oxides (like TiO_2) with metallic elements is one way of improving photoelectrochemical activity by harnessing the beneficial properties of such elements, together with improving the atom economy and reducing costs [178].

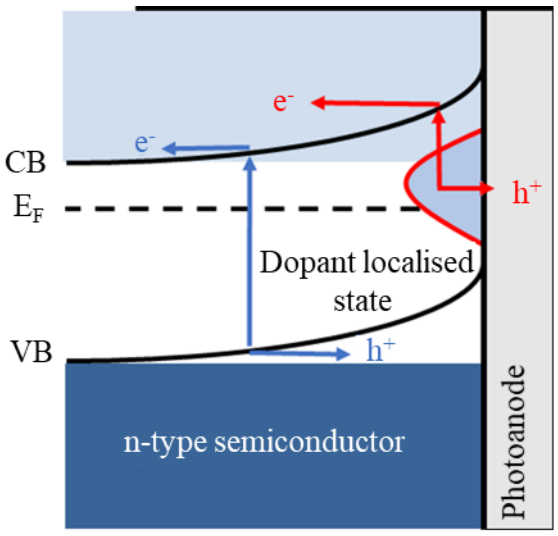

Figure 17: Diagram of band level created by dopant in a semiconductor

There are two purposes of doping, either to introduce localised surface states (*i.e.* trapped) (Figure 17) or delocalised electrons for improving conductivity. The localised states occur due to electrons from dopants not acting as charge carriers *i.e.* not being ionised into the conduction band, thus allowing an increase in light absorption at higher wavelengths. Delocalised electrons can be found throughout a bulk material to increase charge carrier mobility and as a consequence, the Fermi level of a semiconductor will increase proportionally to the number of free charge carriers, as more accessible energy levels to excited electrons are added in between the valence and conduction bands resulting in a decreased bandgap [179].

The photocatalytic activity is the ability of a material to create an electron–hole pair as a result of exposure to UV (which can also be improved by doping if the oxidative or reductive potentials of excited charge carriers are reduced). In the degeneration of n-type semiconductors, however, the bandgap is widened as accessible states are added above the conduction band minimum as carrier concentrations are increased with increasing metal dopant concentration. This indicates that lower light energy (*i.e.* higher wavelength) could excite electrons from the valence to conduction band [180]. The layer can be co-doped with nitrogen and fluorine [172]: the TiO_2 layer is prepared by the inverse opal method with a mixture of

titanium isopropoxide, trifluoroacetic acid and HNO_3 as the precursor. The layer has a reduction of the electronic bandgap due to N–F co-doping: 3.2 eV (387 nm) to 2.56 eV (484 nm) [172].

The TiO_2 could be loaded with gold and doped with fluorine by using a single precursor [133]. This time the precursor was a mixture of titanium isopropoxide, trifluoroacetic acid, tetrachloroauric acid and HCl, with the TiO_2 film prepared by the inverse opal method. The layer has a reduction of the electronic bandgap due to gold and fluorine doping: 3.2 eV (387 nm) to 3.01 eV (412 nm). In the paper of Xu *et al.* [172], they used it for hydrogen production: the photocurrent I–t responded at a potential bias of 0.3 V *vs.* Ag|AgCl electrode in 0.1 M Na_2SO_4 solution showed a maximum photocurrent of 2 μA cm^{-2}.

Photoanode design must take into account how the stability and activity of the photoanodes are affected by the environment, typically the photoanode is operated under alkaline and acidic electrolytes. While research is conducted into solid oxide and ion exchange electrolytes and inorganic/organic electrolytes, alkaline and acidic electrolytes are still the most commonly used. While highly abundant non-noble metals such as Cu, Ni, and Fe can be employed as photoanode materials in alkaline operating environments, less abundant noble and early transition metals, such as Ru, Ir, and Ta, show higher resistances in acidic mediums.
Research into photoanodes is increasingly moving towards the incorporation of multiple semiconductor materials into the design of devices, with multiple phase catalysts showing more promising results than single-phase semiconductor [181], [182]. Like the electronic equilibrium that is established at the semiconductor-electrolyte interface, an equilibrium will form at the interface of different semiconductor materials, commonly called a hetero or phase junction. By carefully considering the valence and conduction band level positions of semiconductors or tuning them in such a way, heterojunction composites (Figure 18) can improve charge carrier transfer and charge separation across phase junctions between multiple semiconductors, enhancing photoanode activity and efficiency. This is due to the system moving to minimise the potential energy of the phase junction, and as a result, electrons will tend towards points or increasingly positive potentials (higher to lower Fermi level) in contrast with holes towards points of increasingly negative potentials (lower to higher Fermi level) in relation to the position of the conduction and valence bands [183].

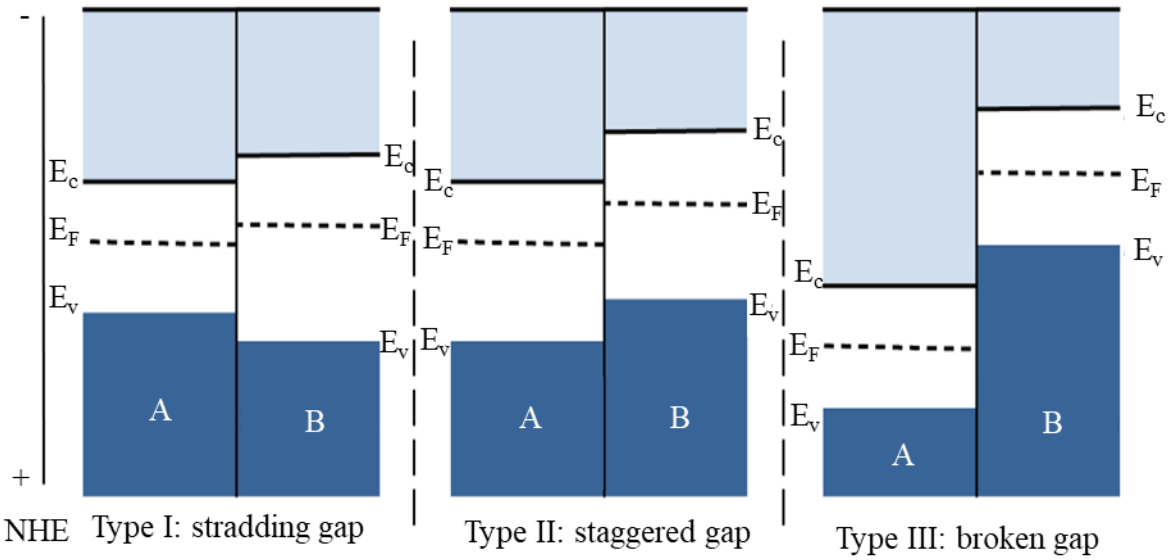

Figure 18: Types of semiconductor heterojunctions

2.6.2 Nanoparticles *vs.* nanoclusters

Gold nanoparticles are typically gold particles of a size between 1 and 100 nm. They have shown unique chemical properties which depends on their size, shape and protective shell. They can have a crystalline phase which can be observed in bulk gold with defined edge transitions to others faces. As nanoparticles, the high surface area to volume ratio leads to surface atoms with different chemical properties than the central atoms of the nanoparticle. On the other hand, clusters are small assemblies of atoms with precisely defined stoichiometries and structures that are less than 1 nm. These properties lead to a completely different chemical configuration than bulk gold. The clusters show property changes with only the addition of a single gold atom (vide infra)[184], [185]. As with Au nanoparticles, the high surface area to volume ratio leads to a unique chemical environment for Au clusters, although in clusters nearly all of the atoms are at the surface and might have lower coordination numbers compared to their larger nanoparticle counterparts.

2.6.3 Gold nanoparticles on TiO_2

As pure TiO_2 has band-gap of 3.2 eV [50], it can only absorb photons which have energy greater than 3.2 eV. So only photons with wavelengths below 387 nm will have sufficient energy to generate an electron-hole pair. To improve the absorption range of the TiO_2 photoelectrode, Koichi Awazu and co-workers [186] developed plasmonic photocatalysts based on silver nanoparticles embedded in titanium dioxide. The photocatalytic activity of TiO_2

was improved ca. seven-fold by a locally enhanced electromagnetic field induced by surface plasmon resonance (SPR) of Ag Nanoparticles.

Many studies have investigated the metal nanoparticles effect on a semiconductor [57], [187]–[191]. Nanoparticles such as Ag and Au have the capability to store a few electrons captured from photoexcited semiconductor nanoparticles [192], [193]. The double-layer charge inside of these nanoparticles leads to a stabilisation of the electron stored inside the metal nanoparticles [194]–[196]. This then leads to a charge equilibration and therefore to a decrease in the Fermi level.[193]. Another effect was the reduction of the charge recombination at the surface of the photoelectrode [197]

In parallel a lot of studies have been conducted on gold catalysis for organics reactions [9]. It has been shown that Au plasmon resonances come from the oscillations of the electrons close to the surface of the nanocrystals [198], [199]. The plasmon-excited hot electrons in the noble metal nanocrystals can be transferred to the conduction band of TiO_2 [198], [199]. Finally, in the last few years, the plasmonic resonance of Au nanoparticles have used to obtain better photoelectrode performance and enhance the absorption range of TiO_2 in the visible region [200], [201], [210], [202]–[209],

In addition, Au nanoparticles show another interesting effect, due to their electronic and optical properties. They show semiconductor properties when the particles size becomes small enough. This effect is due to a loss of overlapping electronics bands, usually present in the bulk metal, which explains their conductor properties. Instead the gold nanoparticles give rise to discrete electronic energy levels [211]. Studies have shown that this transition from conducting to semiconducting behaviour occurs at a size below 1.5 nm to 4 nm, as a function of the support and the surface coverage [212], [213]. Okazaki et al have shown that with a particle size below 0.4nm deposited on TiO_2 rutile surface, the semiconducting effect was observable with a change of adsorption energies and charge transfer based on the stoichiometry of the surface [214].

2.6.4 Gold nanoclusters

The use of ligand stabilised Au clusters yields a better particle size control compared to the Au nanoparticles. Au nanoclusters were developed in 1970 [215] to enable better control of the

number atoms in the cluster core. These types of Au clusters usually required treatment to remove the ligand [216]. Indeed, the ligand that was used for protecting the gold clusters was usually detrimental for catalysis, blocking access to light and reactants. However, the removal of the ligand can lead to an aggregation of clusters, thus formating of Au nanoparticles. Reducing the chance of agglomeration can be done by reducing the cluster density and using a high surface area support [215].

Alvino *et al.* characterised a collection of ligand-stabilised gold clusters, which were found to yield better particle size control compared with top-down approaches, which broke down the structure of bulk material [217]. The gold clusters including: Au_6, Au_8, Au_9, Au_{11}, Au_6Pd and Au_7Pt were comprehensively characterised. The study concluded that the binding energy increased as the number of gold atoms were increased, the acidic pre-treatment and the form of the titanium dioxide support have a strong impact on the degree of agglomeration and ligand loss, charge transfer from the gold clusters to titania and the introduction of numerous occupied gold states at the valence band edge that extend into the bandgap.

Similarly, Anderson *et al.* conducted synthesis and characterisation of Au_8, Au_9, Au_{11} and Au_{101} clusters. The synthesised clusters were doped on P-25 titania support. One of the main factors that influenced the reactivity of supported titania systems was the loading of the metal clusters. Anderson *et al.* used a relatively low loading of 0.5 wt% in an attempt to minimise particle sintering compared to the typical loading of 3 to 10 wt% [218]. The gold clusters were observed to be sensitive to ambient light, leading to the sintering of the gold particles. Acid washing of the titania was used in an attempt to control this photosensitivity, in addition to wrapping the titania in foil. It was noted that the gold-infused titania nanoparticles had a light purple colour that deepened after activation. A range of activation procedures was investigated and briefly characterised by electron microscopy, but was limited by the ability to identify the ultra-small gold clusters, which were less than 1.4 nm. The photocatalytic and electrochemical characterisation could aid in distinguishing between synthesised samples.

2.7 Photoelectrochemical measurement

The first test concerning the photoelectrochemical cell is the measurement of the open circuit potential (maximum potential difference when there is no current). Realising this test with and without illumination showed the effect of the light on the semiconductor layer, in steady light the potential corresponds to the increase of the quasi-Fermi level of the semiconductor and by calculation the band gap could be determined [219]. It gives information on the properties of the electron hole recombination process and on the charges lifetime (if switched between light and dark).

The photo-electrochemical measurement requires some analysis to determine the photocurrent of the cell. The classic approach consists of doing chronoamperometry at 0 V *vs.* the counter electrode on the semiconductor layer, with a platinum counter electrode and recording the current when the light is on and off. This measurement approach gives information on the photocurrent created by the photoelectrochemical cell and its time-related behaviour. Unfortunately, Hodes *et al.* [220] showed that two-electrode measurements can be dependent on the counter electrodes performance. However, another test could be conducted using a three-electrode measurement by adding a reference electrode. This measurement gives photoelectrode efficiencies, without contributions or limitations from the counter electrode.

The result of one test can be simultaneously affected by many parameters, which leads to difficulty in measuring the impact of each variable.For example, the composition of thecounter electrode or its position could change the photocurrent result between two measurements. So, for only determining the impact on the semiconductor electrode, another method is needed. This process is the plot of the polarisation curve in dark and light of the semiconductor electrode and of the counter electrode separately with a three-electrode measurement for being able to analyse them independently.

The polarization curves (Figure 19) show a piece of important information. The plot of the inverse of the counter electrode curve creates a cross between itself and the working electrode curves. It enables determination of the voltage (E) and current (A) of the photoanode in the dark and in the light. However, it does not give the cell voltage, but only an indication of if the semiconductor electrode has a higher current than the previous one. This plot will give an accurate overview of the effect of the parameters of the semiconductor electrode and will be

dissociated from the counter electrode effect. The example shows a high current pair in dark and light (A_a and A_b). The photocurrent must logically be higher than the other electrode measurements. In the second case, either photoanode (A_c and A_d) or counter electrode (A_e and A_f) is the poor one. In the last case, both are poor, so the photocurrent is very low (A_g and A_h). It is shown in an example that the proper electrode is better than the poor one. Based on this test, it can be used to determine parameters influencing the photocurrent. Finally, intensity-modulated photocurrent spectroscopy, which provides the electron transport time in the device coupled with intensity-modulated photovoltage spectroscopy providing the electron recombination time and using for showing the quantity of electron-hole recombination in a photoelectrochemical cell.

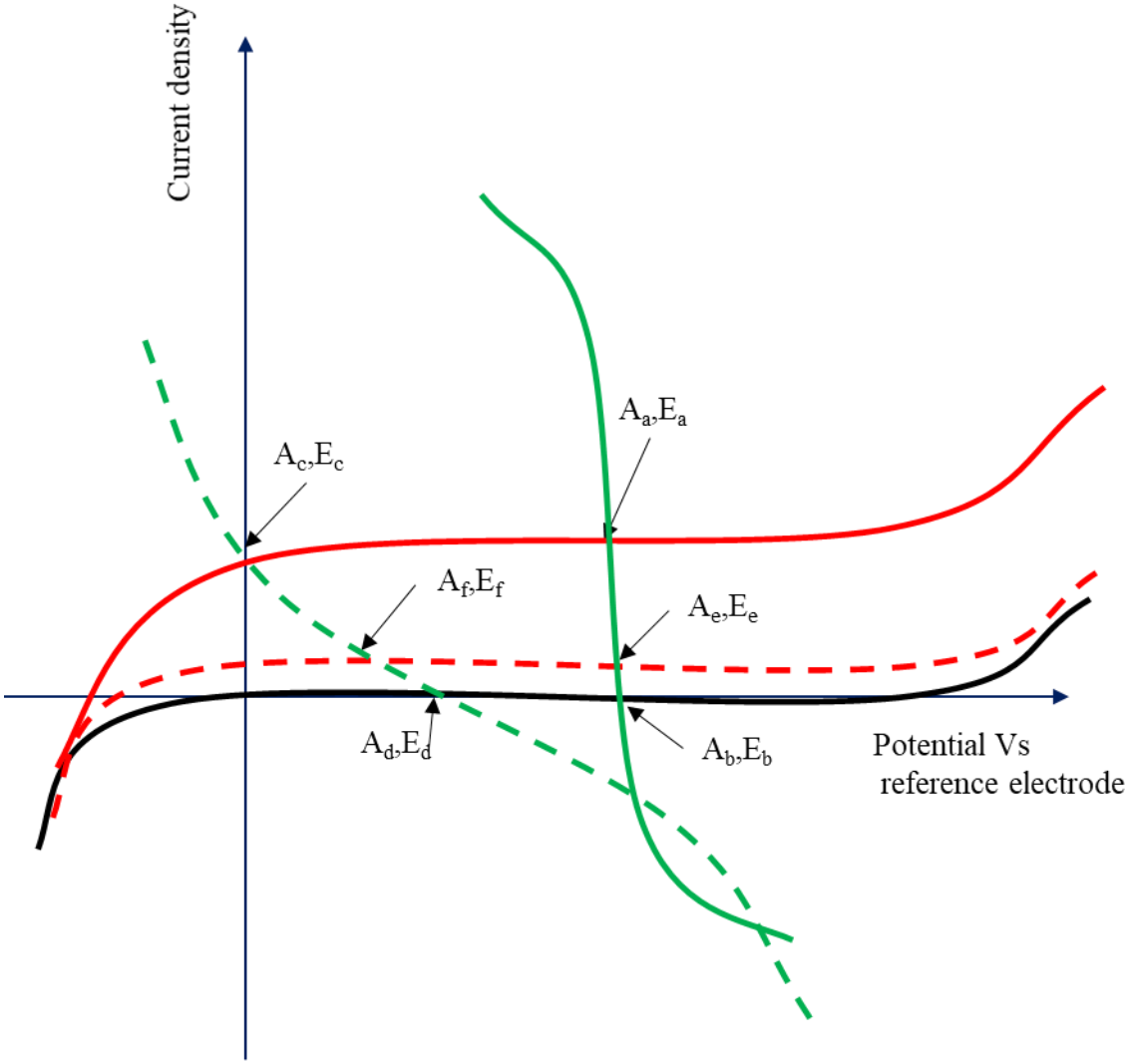

Figure 19: scheme of hypothetical polarization curve: the black and red line represents a hypothetical photo-electrode in dark (black line) and light (red line) and the dotted line a poor photo-electrode. The solid green line represents the inverse of the value of good counter electrode and the dashed green the poor one. As the current at the counter electrode will be the same absolute magnitude as the photoelectrode but the opposite sign, to determine the operating point of these photoelectrode – counter electrode combinations, the currents for the counter electrode curves are inverted, and the operating points are the intersections between the photo-electrode and counter electrode curves. The couple A_a,E_a; A_b,E_b; A_c,E_c;A_d,E_d; A_e,E_e; A_f,E_f are the y and x coordinate of respectively the good photo-electrode and the good counter electrode in light and dark, the good photo-electrode and the poor counter electrode in light and Dark, the poor photo-electrode and the good counter electrode in Light, the poor photo-electrode and the poor counter electrode in Light.

2.8 Materials characterisation

2.8.1 Scanning Electron Microscopy

Scanning electron microscopy (SEM) is an excellent characterisation technique for imaging surfaces and nanostructured materials, using a focused beam of electrons to scan over a sample and provide details of its topography, morphology and composition. In a conventional SEM (Figure 20), the electron source (commonly referred to as an electron gun) is responsible for producing a stable electron beam. It is formed from the application of a strong electric field between an anode and a Wehnelt cylinder which contains, most commonly, a tungsten filament or wire which acts as the cathode. The negative potential used to produce and accelerate the electrons is on the order of 0.1-30 keV, but it requires further focusing given the wide diameter of the beam to allow for high-resolution imaging. High vacuum conditions are required to allow the electron beam to reach the desired target without being scattered by interaction with air molecules. This focusing is achieved through the combination of condenser and objective lenses which allow the collimation convergence of the electron beam through the implementation of a controlled magnetic field which gives a small, well-defined and focused spot size. The condenser lenses can affect the number of electrons that interact with the sample through the manipulation of the aperture diameter. Most SEM setups utilise two condenser lenses to allow the best demagnification of the electron beam. The objective lens is used to alter the position of the point where the electrons are focused on the sample by controlling the distance between the objective lens and point at which the electron beam interacts with the surface, commonly referred to as the working distance. The x and y scan coils allow the high precision rastering of the electron beam as it passes through to give it a defined resolution by controlling the current supplied [221].

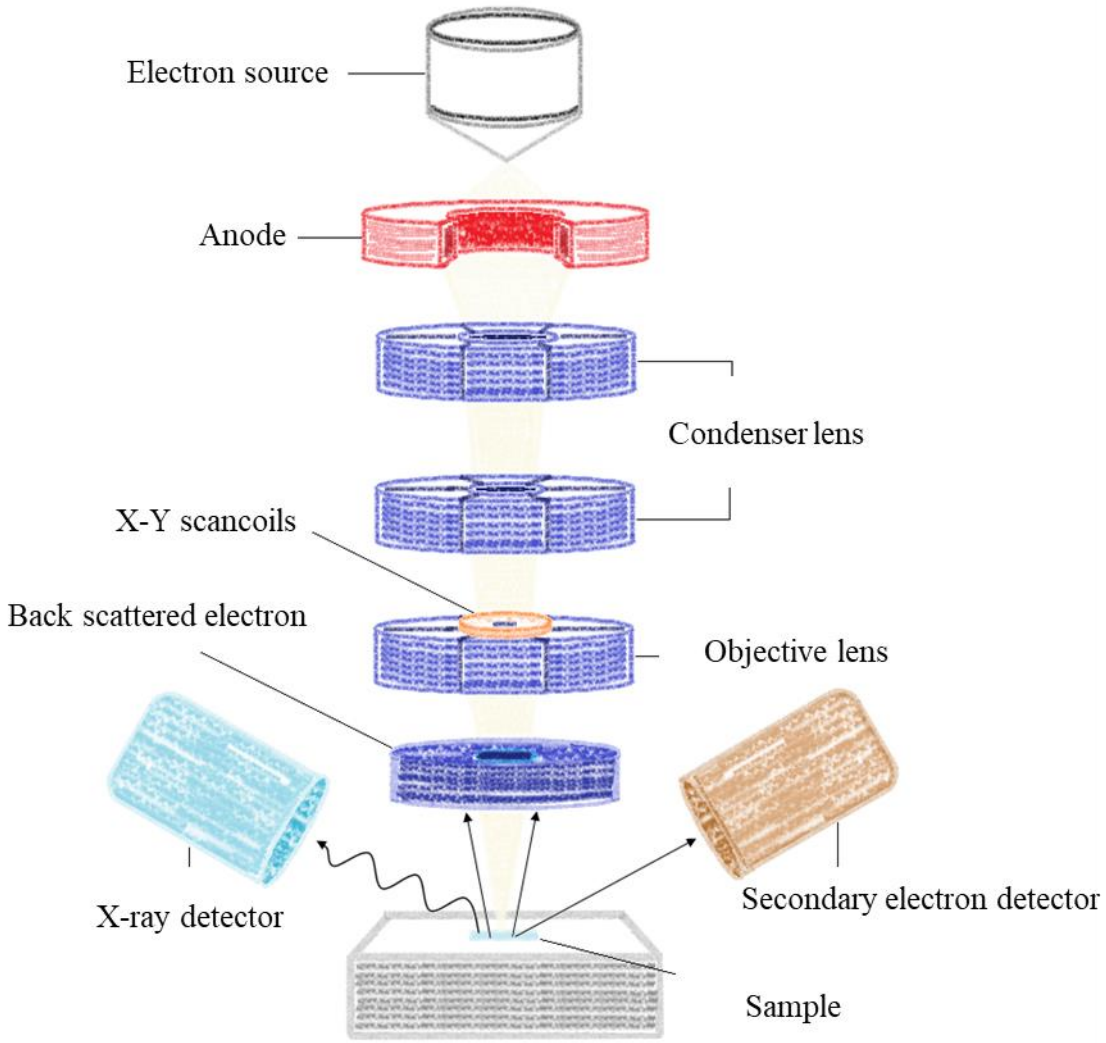

Figure 20: Diagram of the components in an SEM.

The electrons are captured by a number of detectors depending on the nature of their interaction with a sample and will produce either secondary electrons, backscattered electrons or characteristic X-rays, which are then processed into an image. The penetration depth of the electron beam is dependent on the accelerating voltage of the beam, the composition and density of the sample. Secondary electron scattering is the most commonly used method in sample imaging, where a secondary electron detector captures the inelastic scattering of low energy secondary electrons from conduction or valence bands of atoms located up to a few nanometres in depth. Backscattered electron detection is a less common method, where the elastic scattering of high energy electrons occurs from the interaction of the electron beam with heavier elements and can provide information by contrasting areas with different chemical compositions as lighter elements are more prone to inelastic scattering. The characteristic X-rays produced from the interaction of the electron beam with a sample are used for energy

dispersive X-ray spectroscopy (EDS), which are useful for mapping individual element abundance and distribution within a sample.

2.8.2 Powder X-Ray Diffraction

Powder X-ray diffraction (PXRD) is a method used for characterising polycrystalline materials. It is considered as a bulk characterisation method that provides information on the phase (polymorph), preferred crystal orientation and crystallinity of material as well as other structural details such as particle size, internal strain, and defects. It differs from single-crystal XRD, which is used for absolute structure determination of a single crystal from the bulk of a material, as it can provide exact atomic positions in a sample and thus interatomic distances and angles.

In XRD, a Cu or Mo source located in an X-Ray tube is generally used to produce a monochromatic (single-wavelength) X-ray beam, which is electromagnetic radiation of a short-wavelength. At ~0.1-100 Å, these short-wavelengths are around the same order of magnitude as the spacing between the atomic planes in a sample, which will allow the generation of a diffraction pattern. A collimator is used to focus the X-ray beam directed at the sample. Diffraction in XRD occurs from the elastic scattering of X-ray photons, which is primarily caused by the interaction with an atom's electrons, with the atoms themselves forming a periodic lattice. Using Braggs relationship (Equation 22), the derivation of lattice spacing is possible in from the coherent and incoherent scattering (which gives constructive and destructive interference respectively) of X-rays as they interact with the lattice planes in a sample.

$$n\lambda = 2dsin\theta \tag{22}$$

In single-crystal XRD, the diffractive X-ray gives the angle of maximum intensity of 2θ when the incident X-ray interacts with an atom electron density in a crystal. Although the process of PXRD is the same as in single-crystal XRD; however, the maximum intensities of diffractive X-ray are measured as a function of the angle 2θ, which exists between the beam axis and the diffractive X-ray (Figure 21). In a polycrystalline powder sample, the X-rays interact with a small fraction of the powder particles, which are orientated in random directions. Because of this random orientation of powder particles, there is a requirement that an atomic plane must be at a certain angle in relation to the beam axis for constructive interference to be observed. Rotation of the sample during data collection increases the likelihood of this condition being met, meaning a higher percentage of particles can contribute to diffraction. This diffraction

leads to the formation of a circular diffraction pattern which is processed to give a 2-dimensional powder plot [222].

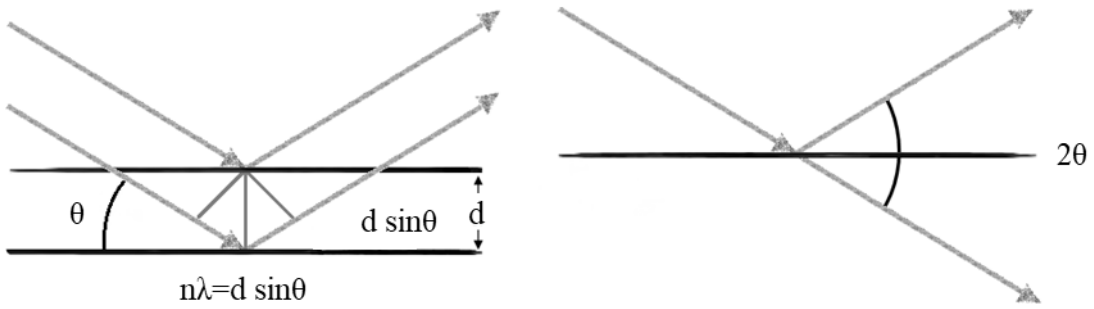

Figure 21:Diffraction in Single-crystal XRD (Left) and Powder XRD (Right) where: λ is x-ray wavelength, d is the distance between two lattice planes, θ the incident angle and n is the order of reflection.

PXRD patterns of samples deposited on FTO slides in this work were collected at room temperature on a Rigaku Smartlab diffractometer. General data collecting was conducted in Bragg-Brentano focusing mode utilising Cu Kα (1.5418 Å) radiation, operating at a tube voltage of 40 kV and tube current of 30 mA passing through a Cu Kβ filter, with a Cross Beam Optics Bragg-Brentano selection slit, 10-mm length limiting slit, 5.0° Soller incident and receiving parallel slit. The detector was a Rigaku D/tex Ultra 250 1D. The data collected was in the 10- 90 2θ range conducted at 5°/min.

3. Photo electrochemistry and electrochemistry of the vanadium solar redox flow battery

3.1 Introduction

The most used catholyte couple employed in solar batteries comes directly from the dye-sensitised solar cell, the I_3^-/I^- [6], [38], [39]. The semiconductor used was typically a form of TiO_2 and the counter electrode was eiter platinum or WO_3 [40], [42], [43], [93], [223].This couple has been studied through kinetics and electrochemical study to understand the photo electrochemical reactions at the photo electrode [40], [42], [43], [93], [223]. The redox couple was kinetically slow, because every photo-electron injected in the TiO_2 appears on the external circuit. The reaction was kinetically complex, and create a I_2 ion wich is highly volatile and corrosive for metal.

Two of the most promising couples are the V^{2+}/V^{3+} and VO_2^+/VO^{2+} couples, which were based on the vanadium redox flow battery. Their main advantages are a large difference of potential with TiO_2,no crossover between the species and a well-known technology [49], [50], [54]. While all-vanadium photoelectrochemical batteries have been investigated previously [3,5–7] and displayed ability to produce a photocurrent, there has been limited studies focused on understanding the photoelectrochemical reactions at the photoanodes and the subsequent limitations. Therefore, this work investigates the factors of the photoelectrodes which limit the photocurrent, their origins and the issues which need to be solved to increase the vanadium photoelectrochemical redox batteries performance.

3.2 Experimental

3.2.1 TiO_2 deposition process

Sixteen TiO_2 coated FTO slides were prepared simultaneously. The FTO glasses (FTO type: NSG TEC 10, size: 1.1mm x 20 mm x 15 mm, FTO thickness 750 nm, resistance: 9.39 ± 0.38 Ω FTO work function: 4.4 eV - 4.7 eV, transmission 83.4%, Provider: Ossila) were first cleaned by ultrasonication in DI water and isopropanol (UNIVAR, analytical grade). The slides were then further treated under a UV-ozone cleaner (MTI corporation, compact UV-ozone cleaner, with 55 W UV lamp of 254 nm and 185 nm maxima of irradiation with peak UV intensity of 4.6 $mW \cdot cm^{-2}$) for 20 min.

The FTO slides were then placed on a temperature-controlled plate at 90°C and covered with an aluminium mask with a 1.13 cm diameter opening (A=1 cm^2) over each slide. These slides were then spray coated with ink containing 20 mg mL^{-1} TiO_2 P25 (Degussa) and 71 mg mL^{-1} titanium isopropoxide (Aldrich 97%) in isopropanol. The spray process was conducted using an ultrasonic atomiser (Sonozap) at 60 kHz mounted on a microprocessor-controlled X-Y carriage and fed by a syringe pump at 1 mL min^{-1}. Once coated, the TiO_2 coated FTO slides were sintered in air at 450°C for 30 min with a heating and cooling rate of 7 ºC/min.

The completed TiO_2 coated FTO slides had a TiO_2 loading of 0.7 ± 0.1 mg/cm^2.

3.2.2 Photoelectrochemical measurements

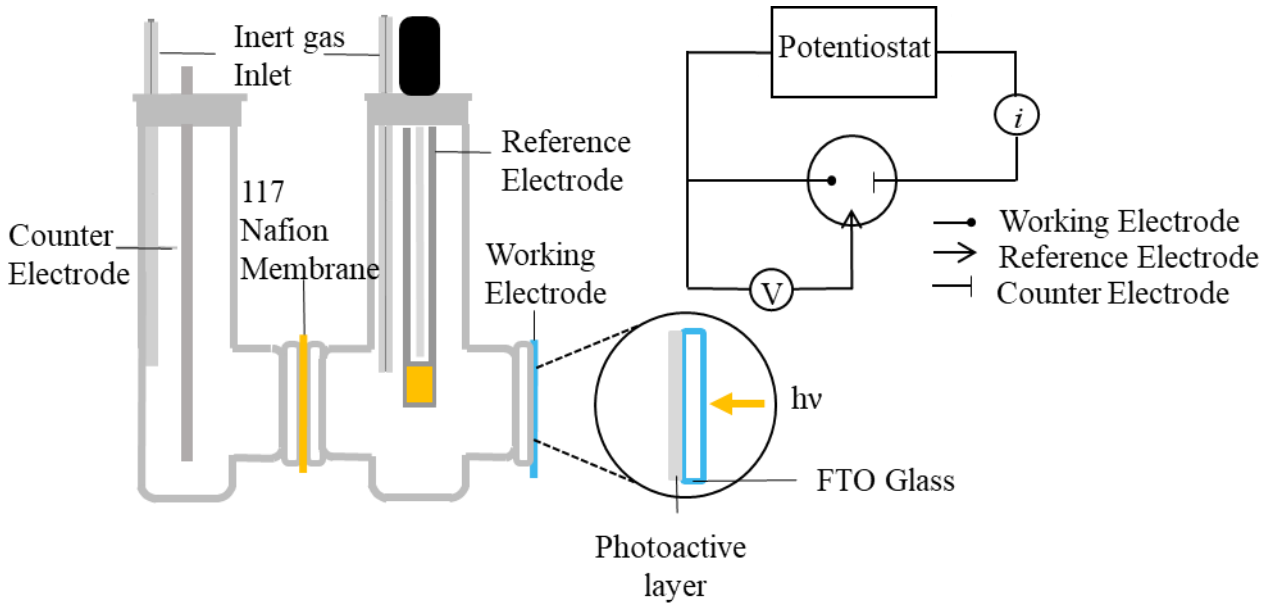

Figure 22: Experimental setup used to perform the different photoelectrochemical measurements reported in this work.

The photoelectrochemical performance of TiO_2 photoanodes was measured by mounting the TiO_2 coated FTO slides in a custom made glass cell (Figure 22). This cell had two chambers separated by a 117 Nafion membrane, with a platinum wire used a counter electrode in one chamber, and the TiO_2 coated FTO slide (working electrode) as well as Ag|AgCl used in the other chamber. The cell was illuminated through an electro-mechanical shutter with either a xenon arc lamp (SLS401, Thorlabs) equipped 1.5 AM filter or a 365 nm LED lamp (M365LP1, Thorlabs), with the light intensity measured using a thermal power meter (S401C, Thorlabs). The system was configured so that the TiO_2 was illuminated through the backside of the FTO glass to minimise absorption of the light by the strongly adsorbing vanadium electrolytes.

Both two and three-electrode photoelectrochemical measurements were performed using a Gamry Reference 3000 potentiostat, which was also configured to control the light shutter via the potentiostats I/O connector. For the two-electrode measurements, the cell potential (*i.e.* between the TiO_2/FTO working and Pt counter electrodes) was controlled at 0 V *vs.* Pt counter electrode and the cell current measured as the under chopped light conditions (20 s light / 20 s dark). The two-electrode measurements simulate the charging of the photoelectrochemical battery under zero-bias conditions. During these measurements, the potential of the TiO_2/FTO

working electrode (and counter electrode) was measured between photoelectrode and the Ag|AgCl reference electrode.

Linear sweep voltammetry and chronoamperometry at the TiO_2/FTO photoelectrode in three-electrode measurement mode were made under constant illumination, chopped illumination and dark conditions. The concentration and speciation of the vanadium in the working electrode chamber was determined before and after chronoamperometry measurements using UV-Vis spectrophotometry (VWR, UV-1600PC).

3.3 Results and discussion

3.3.1 Two-electrode measurements

Under chopped illumination with the cell controlled under a zero-bias condition (*i.e.* two-electrode mode, with the cell potential between the photoelectrode and the counter electrode set to 0 V *vs.* pt counter electrode) a photoanodic current is observed during the light periods and approx. zero currents is found during the dark periods (Figure 23). This indicates that the light is driving the oxidation of some species at the TiO_2/FTO photoelectrode.

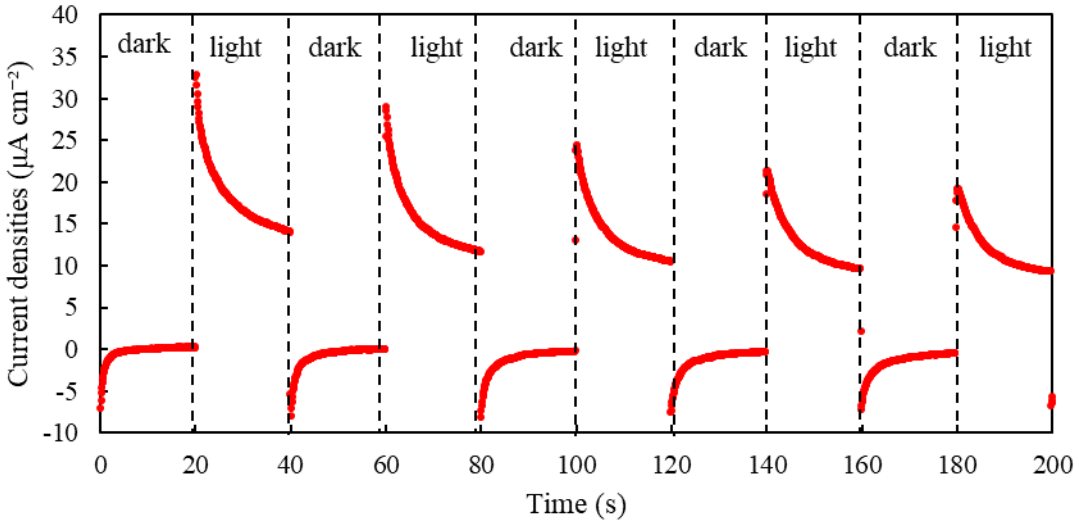

Figure 23: Two electrode current densities measurement in the dark and under AM 1.5, 1 sun light of anodic and cathodic electrolyte 0.1 M $VOSO_4$ in 0.5 M H_2SO_4.

As the potential of the photoelectrode and the counter electrode are identical during these measurements, the potential of the counter electrode must be such to enable the reduction of some species at the same absolute current as observed at the photoelectrode. In these measurements, it is not possible to determine if the current is thus limited by the photoelectrode

or the counter electrode (three-electrode measurements are needed to address this). Despite this, two-electrode measurements are often conducted as a proof-of-concept for photoelectrochemical systems [49], [50], [53], [54].

A series of measurements were conducted using a TiO_2/FTO photoelectrode in 0.1 M $VOSO_4$ -0.5 M H_2SO_4 (pH = 0) and the counter electrode in either H_2SO_4, $VOSO_4$ or VCl_3 electrolytes (pH = 0), to illustrate how the counter electrode reaction influences the two-electrode measurements. As oxygen reduction could occur at the Pt counter electrode, measurements were made with air-saturated and deaerated (Ar was bubbling through the electrolytes prior to the measurements). As the cell voltage (between the TiO_2/FTO and Pt counter electrode) was set at 0 V *vs.* Pt counter electrode by the potentiostat. The potential of the photoelectrodes was measured in the same time against an Ag|AgCl electrode placed in the working photoelectrode chamber using the auxiliary analogue input on the potentiostat.

When $VOSO_4$ is used in the counter electrode chamber, the photoanodic current under illumination was approximately 10 μA cm^{-2} and 4 μA cm^{-2}, when the counter electrode-electrolyte was saturated with air or deaerated respectively (Figure 24 a). This difference can be explained by the difference in electrode potential, which was significantly lower when the electrolyte was deaerated (Figure 24 b). When O_2 is present in the counter electrode chamber, the O_2 reduction reaction can occur at potentials below 1.03 V *vs.* Ag|AgCl [6], and on the platinum counter electrode, this reaction is expected to occur quite readily. In contrast to this, the V^{4+} present in the counter electrode is unable to be reduced to V^{3+} as the potential at the counter electrode (approx. 0.28-0.35 V *vs.* Ag|AgCl) is more positive compared to the standard reduction potential of V^{4+} to V^{3+} (E^o=0.143 V *vs.* Ag|AgCl). When this solution is deaerated, as the O_2 reduction reaction can no longer occur, the potential decreases to just below the standard reduction potential of V^{4+}, and thus the counter electrode reaction is now the reduction of V^{4+} to V^{3+}, and the kinetics of this reaction are slow [224]. The photocurrent is lower than when the O_2 reduction reaction can occur. Interestingly, it is observed that the deaeration of the counter electrode-electrolyte results in a rapid increase in the current, followed by a slow decrease when the photoelectrode is first illuminated. This phenomenon will be investigated later in this study. It is also observed that when the photoanode is illuminated the potential decreases in an exponential fashion (Figure 24 b), which may correspond to the presence of trap sites [63]–[66], that not participate in the charge transport any more (*i.e.* the photocurrent decays).

With VCl_3 in counter electrode chamber electrolyte, when this is saturated with air, the potential of the electrodes (Figure 24 d) is more negative compared with the case of the counter electrode chamber containing $VOSO_4$. The potential will be lower as the VCl_3 reduction is much more negative than the O_2 reduction reaction and thus the potential is a mixed potential between the V^{3+} reduction and O_2 reduction reactions. As the air saturated electrolyte in the counter electrode will facilitate O_2 reduction, as discussed above, the photocurrent (Figure 24 c) in this situation is almost the same as when $VOSO_4$ is in the counter electrode chamber. The photocurrent drops significantly to approximately 1.2 μA cm^{-2} when the VCl_3 solution is deaerated, as the potential (approx. 0.12 V *vs.* Ag|AgCl, Figure 24 d) is not negative enough to reduce V^{3+} to V^{2+} (Eo=-0.457 V *vs.* Ag|AgCl [225]). As a small photocurrent is still measured during this test, suggesting that a small quantity of either O_2 or V^{4+} may be present in the counter electrode chamber to facilitate the reduction process which must happen at the counter electrode.

Finally, when only 0.5 M H_2SO_4 is used in the counter electrode, in the presence of dissolved O_2, the photocurrent (Figure 24 e) was equal to 7 μA cm^{-2} and approx. 0 μA cm^{-2} without O_2 (Figure 24 e). It confirms that O_2 reduction is indeed a significant reaction to consider when performing two-electrode measurements. Furthermore, as the potential (Figure 24 f) is generally more positive when dissolved O_2 is present in the counter electrode chamber, it also means that the potential is more positive on the photoanode. As more positive potentials on photoanodes will improve charge separation (and thus photocurrents) [226], care must be taken when interpreting the significance of two-electrode measurements.

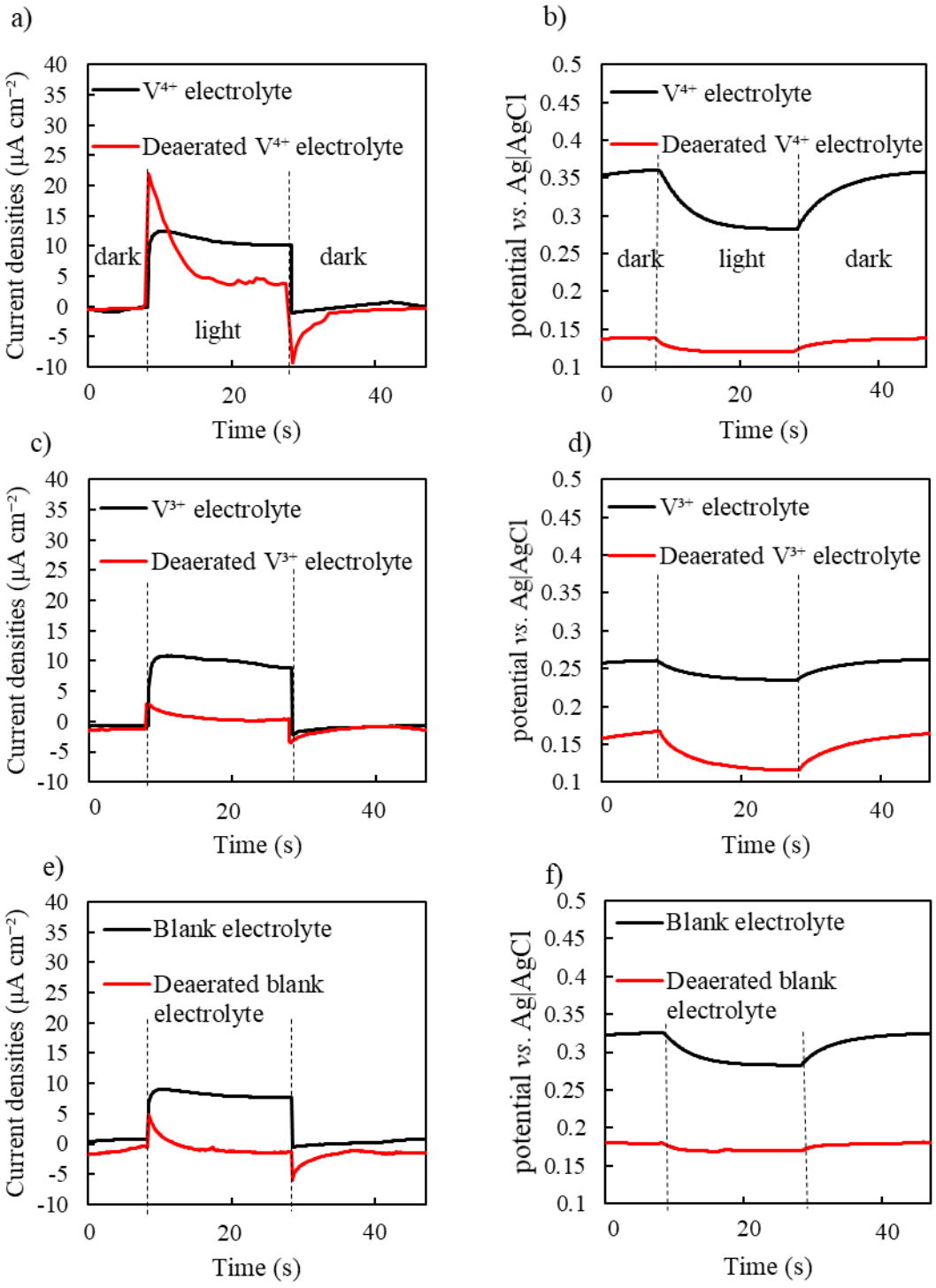

Figure 24: Two electrode current densities and working electrode potential measurement in the dark and under AM 1.5 1 sun light of different cathodic electrolyte with and without deaerated the electrolyte. Cathodic electrolyte 0.1 M $VOSO_4$ in 0.5 M H_2SO_4 (V^{4+} electrolyte) a) current densities, and b) working electrode potential. Cathodic electrolyte 0.1 M VCl_3 in 0.5 M H_2SO_4 (V^{3+} electrolyte) c) current densities, and d) working electrode potential. Cathodic electrolyte 0.5 M H_2SO_4 (blank electrolyte) e) current densities, and f) working electrode potential.

3.3.2 Polarisation curve of the photoelectrode

To further understand the two-electrode measurements, the polarisation curves for the TiO_2 photoelectrode (in light and dark) and the Pt counter electrode were measured in a conventional three-electrode mode. Theoretically, the two-electrode potential and current are defined by the intersection of these polarisation curves [226]. – *i.e.* the potentials and absolute currents must be equal. Under illumination, as the current from the photoelectrode is positive, the current at the counter electrode will be the same magnitude but negative.

Polarisation curves for TiO_2 in the dark were measured between -0.3 V *vs.* Ag|AgCl to 1.1 V *vs.* Ag|AgCl (Figure 25 a). Below 0.23 V *vs.* Ag|AgCl, the negative current suggests that V^{4+} is reduced to V^{3+}. This is consistent with the standard reduction potential of this reaction being 0.143 V vs Ag|AgCl (the standard potential is corresponding to the state where V^{4+} and V^{3+} are at equal activities). Thus, assuming ideal solution behaviour, at 0.23 V vs Ag|AgCl, according to the Nernst equation, the molar ratio of V^{4+} to V^{3+} at equilibrium would be around 30:1. As the solution used in the test contained only V^{4+}, it should be expected that an oxidation current would only occur once the potential was high enough to drive either the $V^{4+} \rightarrow V^{5+}$ reaction (E_0=0.8 V vs Ag|AgCl) or oxygen evolution reaction (E_0=1.0 V vs Ag|AgCl). However, as the potential in this measurement was swept from -0.3 V *vs.* Ag|AgCl to 1.1 V *vs.* Ag|AgCl, above 0.23 V *vs.* Ag|AgCl the V^{3+} generated at lower potentials is oxidised to form V^{4+}, giving rise to a small but positive current above 0.23 V. Above 1 V *vs.* Ag|AgCl the oxidation current increases more rapidly, most likely due to the $V^{4+} \rightarrow V^{5+}$ or oxygen evolution reactions.

For the TiO_2 polarisation curve under illumination (Figure 25 a), the light-induced electron-hole separation should drive the photooxidation of V^{4+} to V^{5+} at potentials above the flat band potential (the potential required to bring back the semiconductor band edges to their flat band position from the bending position at the semiconductor/electrolyte junction [227]). For rutile and anatase the flat band potential at pH = 0 are reported to be -0.155 V *vs.* Ag|AgCl and -0.355 V *vs* Ag|AgCl [228]. Thus, over the potential range examined here, it is expected that anodic currents will be observed as the valence band potential will be significantly more positive than the standard potential for the $V^{4+} \rightarrow V^{5+}$ reaction (E_0=1.0 V vs Ag|AgCl). Indeed, this is what occurs with an almost constant oxidation current observed above approximately 0.1 V *vs.* Ag|AgCl. Below this potential, a cathodic current is found, suggesting that the electrochemical reduction of V^{4+} to V^{3+} still occurs.

On Pt, as expected between 0 V *vs.* Ag|AgCl and 1.0 V *vs.* Ag|AgCl, the current in V^{4+} is almost zero (Figure 25 b). This curve also indicates that the electrochemical reduction of V^{4+} to V^{3+} between -0.2 V *vs.* Ag|AgCl and 0.2 V *vs.* Ag|AgCl is very slow on Pt, which is consistent with literature reports [224]. Below -0.2 V *vs.* Ag|AgCl, the cathodic current increases rapidly, which would be consistent with either the electrochemical formation of V^{2+} from V^{3+} or V^{4+} or the hydrogen evolution reaction. As the performance of a zero-bias solar redox flow battery will depend on both the photoanode and the negative electrode, more active negative electrodes for the reduction of vanadium species will be required.

The intersection between the platinum curves and the TiO_2 polarisations curves (Figure ***25*** c) should correspond to the previous two-electrode experiments. There is good agreement with the observation that the potential of the system decreases when the photoanode is illuminated. The potentials correspond to the value found in the two-electrode measurements without deaeration (in dark: intersection value = 0.4 ± 0.01 V *vs.* Ag|AgCl / two-electrode value = 0.36 ± 0.01 V *vs.* Ag|AgCl, in light: intersection value = 0.24 ± 0.01 V *vs.* Ag|AgCl / two-electrode value = 0.26 ± 0.01 V *vs.* Ag|AgCl).

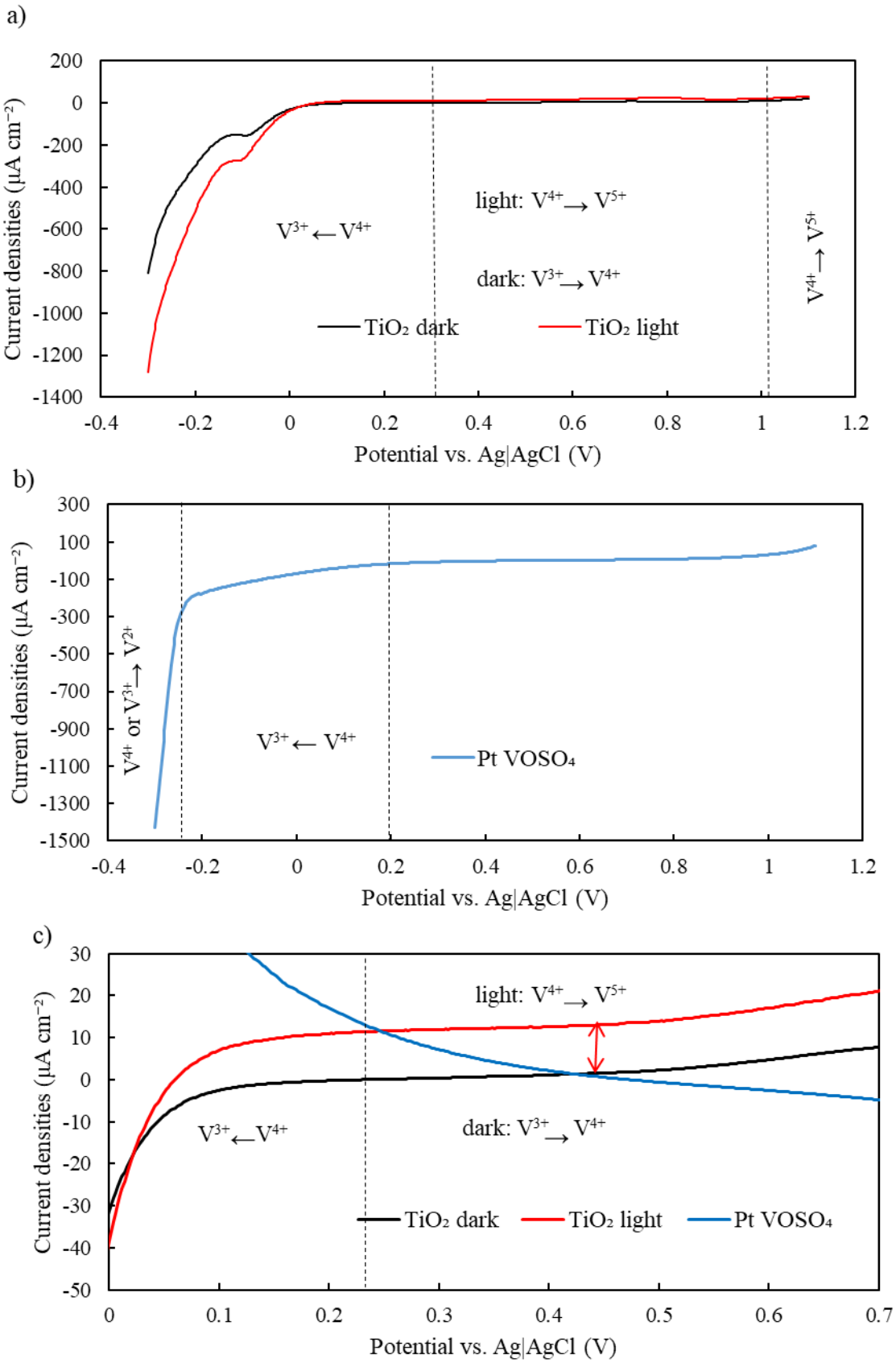

Figure 25:a) Polarisation curves of the TiO_2 photoanodes in dark and light and in the presence of 0.1 M $VOSO_4$ between -0.3 V *vs.* Ag|AgCl to 1.1 V vs. Ag|AgCl. b) Pt counter electrode in the presence of 0.1 M $VOSO_4$ between -0.3 V *vs.* Ag|AgCl to 1.1 V vs. Ag|AgCl. c) Polarisation curves of the TiO_2 photoanodes in dark and

light and the inverse current of the Pt counter electrode in the presence of 0.1 M $VOSO_4$ 0 V *vs.* Ag|AgCl and 0.7 V *vs.* Ag|AgCl.

3.3.3 Polarisation curves of TiO_2 photoelectrodes under chopped illumination

Linear sweep voltammetry was measured between 0 V *vs.* Ag|AgCl to 0.7 V *vs.* Ag|AgCl in different electrolytes containing different concentrations of V^{4+} under chopped illumination (20 s dark, 20 s light, AM1.5 illumination at 1 sun). The measurements performed in 0.1 M V^{4+} (Figure 26 a) show two regions. Between, 0 V *vs.* Ag|AgCl to 0.15 V *vs.* Ag|AgCl a reducing current is observed in the dark. This reducing current is attributed to the reduction of V^{4+} to $V^{3+,}$ which is thermodynamically possible below approx. 0.143 V vs. Ag|AgCl. [225] Above 0.15 V *vs.* Ag|AgCl, as the electrolyte contains no species which can be readily oxidised (other than the small amount of V^{3+} produced by the reduction occurring below 0.15 V *vs.* Ag|AgCl) the pseudo-steady-state current is close to zero in the dark. Under illumination and above 0.15 V *vs.* Ag|AgCl, it is found that an oxidation current is observed which is either due to V^{4+} or water oxidation.

As the band-gap for TiO_2 is approximately 3.2 eV [50], the effective potential of the valence band (where the oxidation reaction occurs) will be 0.15 + 3.2 = 3.35 V *vs.* Ag|AgCl which is easily high enough to drive both of these oxidation reactions. Below 0.15 *vs.* Ag|AgCl, the potential of the valence band is still above the thermodynamic requirement for V^{4+} and water oxidation, but now the potential of the conduction band (which is almost the energy level controlled by the potentiostats) is low enough to reduce V^{4+}. The sum of these processes is the net current measured, and as the V^{4+} reduction to V^{3+} increases as the potential decreases from 0.15 V *vs.* Ag|AgCl, once the potential is low enough (approx. < 0.08 V *vs.* Ag|AgCl), the net current under illumination becomes negative.

Similar observations were found at 0.01 M V^{4+} (Figure 26 b), but with much smaller currents. When the concentration of V^{4+} is decreased further to 0.001 M (Figure 26 c) the photooxidation current is almost the same as found at 0.01 M, although no significant reduction current is found below 0.15 V *vs.* Ag|AgCl in the dark. This suggests that almost no V^{4+} reduction to V^{3+} occurs, possibly because of mass transfer limitations. The fact that the photooxidation current is essentially unaffected when the V^{4+} concentration is decreased from 0.01 M to 0.001 M suggests that at these concentrations the dominant reaction contributing to the photooxidation current is water oxidation (oxygen evolution). This is confirmed by performing the same experiment in only 0.5 M H_2SO_4 (Figure 26 d). In this experiment, as there are no vanadium

species to oxidise or reduce, the only reactions which can occur are water splitting processes (*i.e*. hydrogen and/or oxygen evolution) [229].

Assuming that the presence of vanadium will not influence the water-splitting reaction, the fraction of current contributing to V^{4+} oxidation has been calculated by subtracting the oxidation current in (Figure 26 d) from those in (Figure 26 a-c). This shows that the V^{4+} oxidation is constant at around 85% across the potential range (Figure 27) for 0.1 M. This decreases to 55-60 % and 35-40% for V^{4+} concentrations of 0.01 M and 0.001 M respectively. However, according to the Nernst equation and the vanadium oxidation should be 9% for a V^{4+} concentration of 0.01 M and 0.9% for a V^{4+} concentration of 0.001 M. This difference could be explained by a lack of reproducibility in 0.5 M H_2SO_4, indeed a slight change of the photocurrent could lead to completely different results. So unfortunately, no conclusion on the percentage of water splitting in the reaction can be made at this point.

The presence of the water-splitting reaction means that some energy from the photon will be lost (to gas evolution reactions) and not be retrieved during the discharge of the battery. Furthermore, the water-splitting reaction could form bubbles in the TiO_2 film, blocking some pores and preventing the diffusion of the V^{4+} species inside the film. The linear sweep voltammetry could be separated into two regions, one beside 0.4 V *vs.* Ag|AgCl where there was no sharp peak and the photocurrent was constant and one below 0.4 V *vs.* Ag|AgCl where a reductive current occurs in the dark and some sharp peaks occurred when the light was switched on or off. These two regions were investigated to explain the different phenomena happening at the photoelectrode.

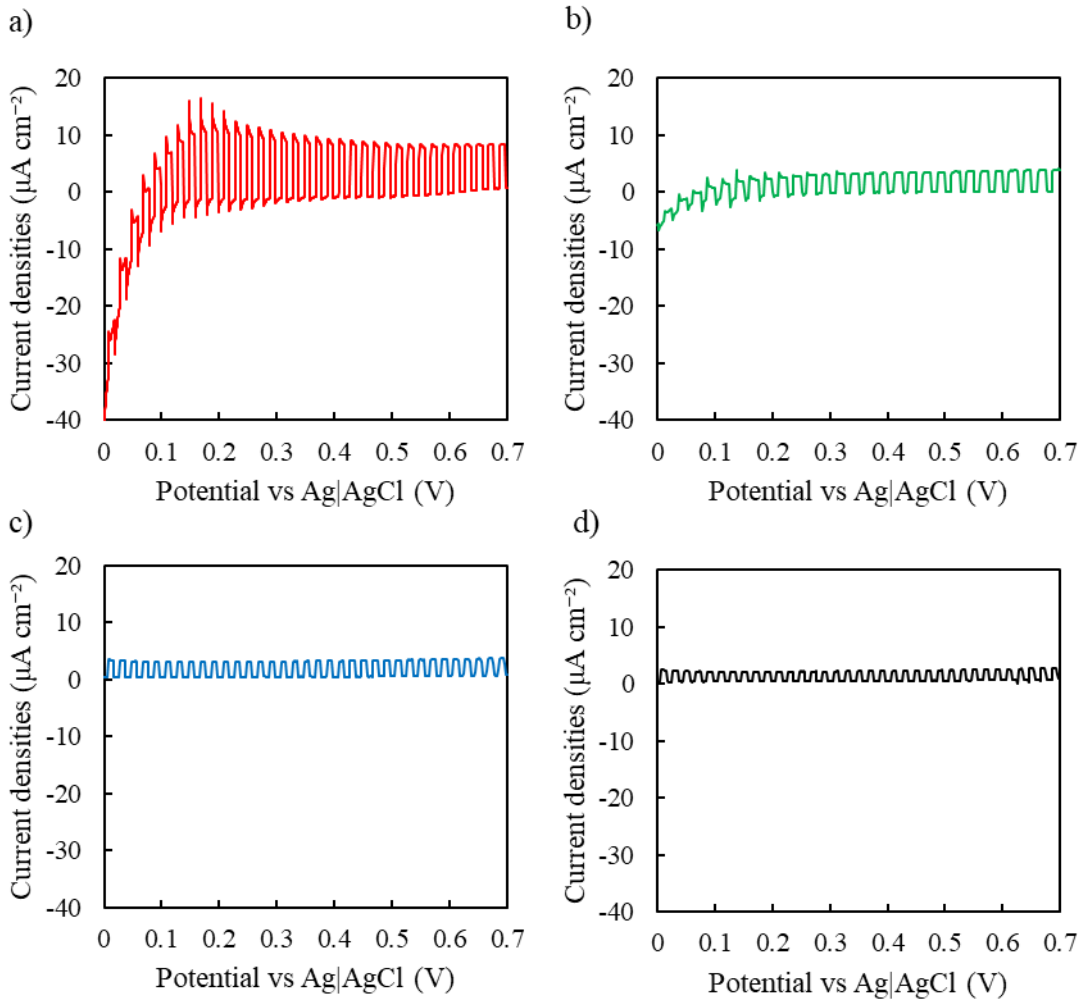

Figure 26: polarization curves between 0 V *vs.* Ag|AgCl and 0.7 V *vs.* Ag|AgCl realised on a 0.7 mg TiO_2 film with an electrolyte of: a) 0.1 M $VOSO_4$ in 0.5 M H_2SO_4, b) 0.01 M $VOSO_4$ in 0.5 M H_2SO_4 c) 0.001 M $VOSO_4$ in 0.5 M H_2SO_4 and, d) 0.5 M H_2SO_4

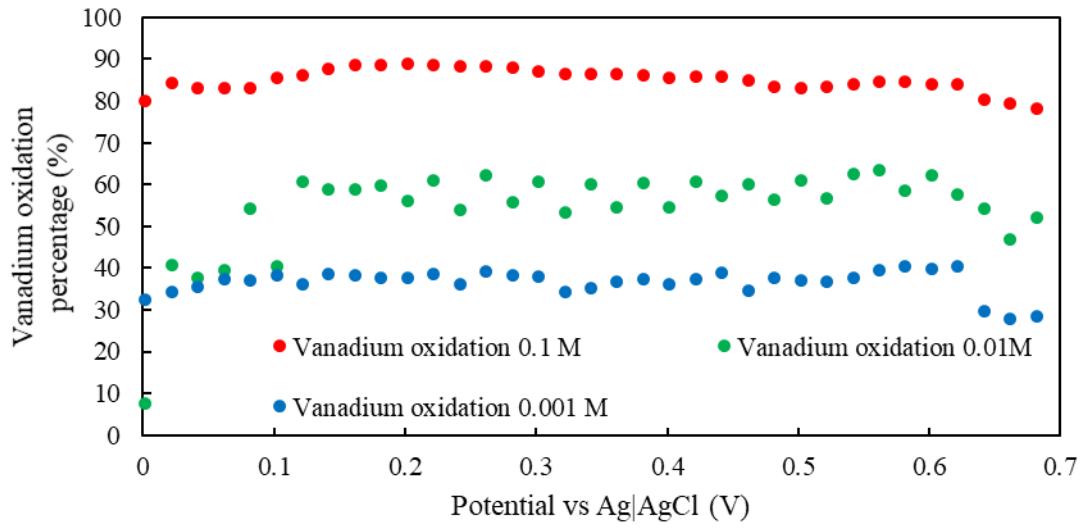

Figure 27: Percentage of charge used for vanadium oxidation with different $VOSO_4$ concentration of the electrolyte, assuming that the vanadium concentration does not influence the water-splitting reaction.

3.3.4 UV-Vis spectroscopy to confirm the oxidation and reduction of vanadium species

UV-Vis spectroscopy was used to confirm that V^{4+} oxidation does contribute to the photocurrents around 0.15 V *vs.* Ag|AgCl. In these measurements, both the photoanode chamber and the counter electrode chamber were filled with 0.01 M $VOSO_4$ in 0.5 M H_2SO_4 to avoid concentration changes in the photoanode chamber caused by diffusion across the membrane separator. In order to increase the rate of oxidation and to minimise experimental duration, the photoanode was illuminated with a 365 nm LED at a power density of 130 mW cm^{-2}. Initially, the current was found to be > 400 $\mu A\ cm^{-2}$ and slowly decreased to an almost steady-state current of 150 $\mu A\ cm^{-2}$. Based on the changes to the UV-Vis spectrum (Figure 28 b), the V^{4+} (peak at 780 nm [230]) concentration was calculated to decrease by 12%. By integrating the charge measured and assuming 100% of this charge results in V^{4+} oxidation, the concentration of V^{4+} in the photoanode chamber should decrease by 15% ± 1%, implying that in these experiments, the water oxidation reaction consumes approximatively 20% of the current. Comparing this with the data measured in 0.01 M $VOSO_4$ + 0.5 M H_2SO_4 *vs.* only 0.5 M H_2SO_4 (Figure 26 and 27) suggests that the assumption that the V^{4+} and water oxidation reactions occur independently from each other is most likely wrong – *i.e.* the presence of VO_2^+ can suppress (but not completely remove) the water oxidation reaction, possibly by competing for the same active sites on the TiO_2 surface.

The slow decrease in the photocurrent during this measurement could be due to several possible effects. Some of the initially high currents may be due to double-layer charging (as the potential is stepped from an open circuit potential of ~ 0.3 V *vs.* Ag|AgCl to 0.5 V *vs.* Ag|AgCl) [231], although normally such charging currents decay within the order of a few seconds. The second hypothesis could be the competition between water splitting and vanadium oxidation taking place inside the porous layer. Initially, when the photoelectrode is illuminated, the active porous layer will contain V^{4+} at the same concentration as a bulk solution. This would be readily oxidised without significant diffusion limitation (as the path length within the porous layer is small). As this V^{4+} in the layer is oxidised, the concentration in the layer will decrease, and the concentration of the V^{4+} in the layer will increase. To balance these changes in concentration, V^{4+} from the bulk will diffuse into the porous layer, and the newly generated V^{5+} within the layer will diffuse into the bulk solution. Concentration gradients are therefore, established within the layer and at the layer-bulk solution interface. If the mass transport of

vanadium species is insufficient, the current density will decrease over time until it reaches a pseudo-steady state based on the mass transport characteristics. In parallel with this, as water splitting also occurs in these pores, the bubbles formed may partially block pores off, impeding the transport of vanadium species either within the porous layer or between the porous layer and the bulk solution.

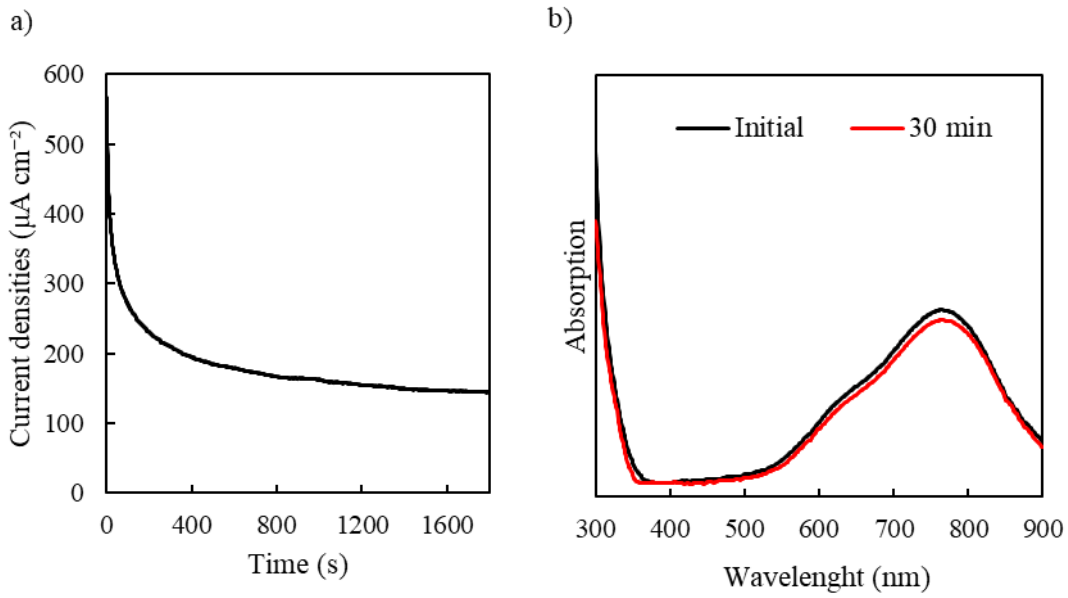

Figure 28: a) Current density over time and b) initial, and after 30 min in light, UV VIS spectrum of the 0.01 M vanadium (IV) electrolyte in photoanode wherein the photoanode is held at 0.5V vs. Ag|AgCl, while illuminated by a 365 nm, LED at 130 mW cm^{-2}.

A third option to explain the slow decay in the photooxidation current is related to the changing light adsorption profile of the photoactive layer. As V^{4+} and V^{5+} absorb different wavelengths of light (300 to 350 nm and 780 nm for V^{4+} and 300 to 400 nm for V^{5+} [230]), as the V^{4+} in the layer is oxidised to V^{5+} the light adsorbed by the vanadium species within the layer will change over time. This will alter the light reaching the TiO_2 and thus the photooxidation current. To estimate the magnitude of these possible effects, a simplified model was considered (Figure 29). This model is based on the assumption that the porous photoactive layer is 10 µm thick with 50% porosity, giving an effective TiO_2 thickness of 5 µm and an electrolyte layer thickness of 5 µm. Using the absorption behaviour of TiO_2, 0.1 M V^{4+} and 0.1 M V^{5+}, the fraction of light with wavelengths between 280 - 405 nm could be estimated. Based on these calculations, the FTO glass adsorbs 12% of the light illuminated onto the photoelectrode. A further 45% of the light will be absorbed by an equivalent 5 µm thick layer of 0.1 M V^{4+} electrolyte. If this electrolyte is converted to V^{5+} the fraction of light (which transmits through

the FTO glass) adsorbed by the electrolyte increases to 92% (as V^{5+} adsorbs significant more UV light than V^{4+}). While this suggests that the electrolyte will adsorb significant amounts of UV light, similar calculations have been conducted on the TiO_2 film as a function of the thickness using literature the absorption coefficient at 405 nm [232]. This calculation (Figure 29 b) shows that almost all of the light at 405 nm is adsorbed by the 200 nm thick TiO_2 film. The maximum absorption of the visible light by TiO_2 is only 10%, so the visible light passes through the film whatever the thickness. In conclusion, the absorbed light by the electrolyte is negligible relative to that by TiO_2 in the film.

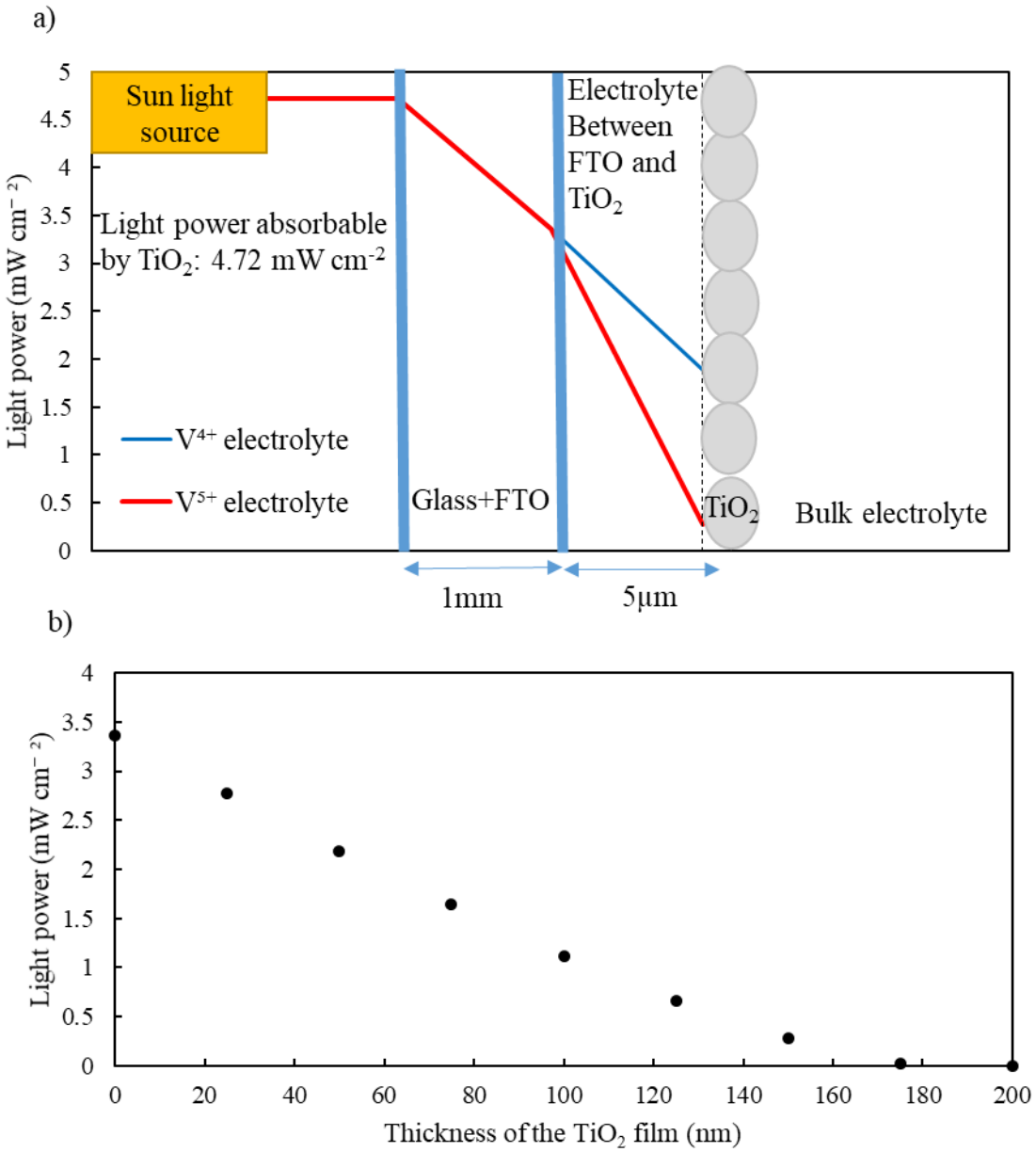

Figure 29: a) Model of light power densities changes when passing through the photoelectrode. The TiO_2 film was considered a surface at 5 µm of the FTO surface with 0.1M $VOSO_4$ electrolyte between the FTO and the TiO_2 surface. b) Absorption of the light of the TiO_2 film at 405nm wavelength.

Similar UV-Vis spectroscopy was performed to confirm that V^{4+} reduction occurs at potentials below 0.15 V *vs.* Ag|AgCl. In these measurements the potential was set at 0 V *vs.* Ag|AgCl for 20 h in the dark. During this measurement, an almost constant reduction current of 10 µA cm^{-2} was found over the entire 20 h experiment (Figure 30 a). The UV-Vis spectra measured before and after this experiment (Figure 30 b) shows a decrease of 8.78 % in the concentration in V^{4+} (740 nm peak) and an increase of 7% for the V^{3+} (400 nm) peak. The small difference between these values most likely occurs due to diffusion across the membrane (separating the photoelectrode and counter electrode chambers) and experimental uncertainties. Based on the

charge passed over the 20 h experiments (0.72 C) one would expect the concentration of V^{4+} in the photoelectrode chamber to decrease by 7.84%, which is consistent with the measured decrease, confirming that the reduction current below 0.15 V *vs.* Ag|AgCl is entirely due to the reduction of V^{4+} to V^{3+}.

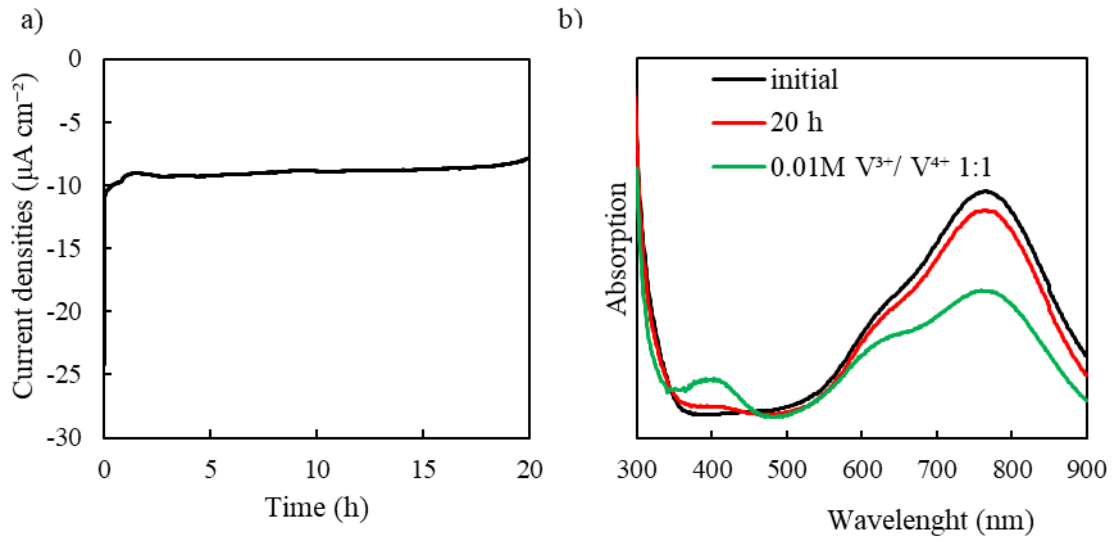

Figure 30: UV VIS spectrum of 0.01 M V^{4+} electrolyte in the photoelectrode chamber in the dark at 0V *vs.* Ag|AgCl over 20 hours. 0.01 M $VOSO_4$ was used as the cathodic electrolyte. For comparison a spectrum of a solution of 0.01M $VOSO_4$ mixed with 0.01 M VCl_3 1:1 were realised.

3.3.5 Understanding the current peak upon illumination

In many experiments, it was observed that the current exhibited a sharp peak or spike immediately following illumination (e.g. Figures 24, 25, 27 and 29). Following this spike, the current is seen to slowly decrease, with this proposed in the previous section to be due to double-layer charging or concentration gradients within the porous photoelectrode layer. The effects of a concentration gradient within the photoelectrode layer could reduce the photocurrents due to the accumulation of oxidised species within the layer. When the photoanode is illuminated the V^{4+} inside the TiO_2 film is rapidly oxidised to V^{5+} leading to an accumulation of V^{5+} within the film. The diffusion of V^{4+} species back into the film is slow due to the porosity of the film and diffusion layer at the outside surface of the photoanode. The low concentration of V^{4+} within the film would then result in V^{4+} oxidation only occurring on the outer-most surface of the TiO_2 film.

To test this hypothesis, experiments were performed wherein the photoanode was illuminated with chopped light with different lengths of dark periods. During the dark periods oxidation of V^{4+} does not occur and V^{4+} will diffuse back into the film, with a longer dark period allowing a higher percentage of the film to receive a fresh solution. These measurements were performed at multiple light intensities and V^{4+} concentrations.

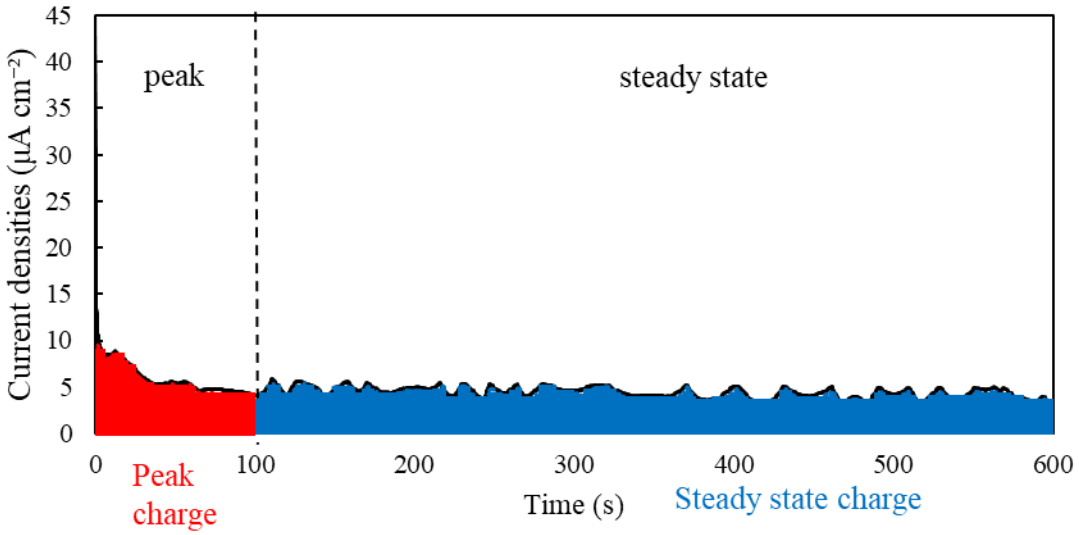

Figure 31: Constant light chronoamperometry of 600 s with A.M 1.5 at 1 sun with a 0.1 M $VOSO_4$ electrolyte. the red area represents the calculated charge of the peak in comparison of the rest of the chronoamperometry acting as steady-state current density

During the tests with constant light we observe a large peak (Figure 31) which increases as a function of the light power (Figure 32 a) (Increasing from 1 mC cm^{-2} to 20.5 mC cm^{-2} for an increase from 3.3 mW cm^{-2} to 100 mWcm^{-2} in UV light intensity for a 0.1 M electrolyte) and the concentration of the electrolyte (Increasing from 13 mC cm^{-2} for a 0.5 M H_2SO_4 / blank electrolyte to 20.5 mC cm^{-2} for 0.1 M $VOSO_4$ for a UV light of 100 mW cm^{-2}). The increase of the peak with light power could be linked to the creation of higher diffusion layer or higher potential photoinduced (ie- higher double layer charging). The increase of the peak with a concentration of the electrolyte could be linked to the creation of higher concentrated blocking layer or higher concentration for the formation of a double layer [233].

When the light from the solar simulator (Figure 32 b) is chopped no trends occur except a difference between with and without chopping light. The charge densities jump from for constant light to for a dark period of one second with a 0.1 M $VOSO_4$ electrolyte. However, the increase of the dark periods has no effect (plateau around from 2 s to 40 s). The difference between with and without chopping light was due to a charge pumping difference [234]–[236]:

when the light is turned on some photoinduced charge carrier with a lifetime of few seconds were created (similar but with a longer lifetime than the one record with time-resolved terahertz spectroscopy [235]: about few picoseconds). Besides the different concentration (Figure 32 b) of the electrolyte show that the blank electrolyte did not seem to be affected by the photoinduced charge carrier with a lifetime of few seconds, due to the difficulty of water splitting compared to V^{4+} oxidation. Allowing more time for the V^{4+} to diffuse back into the film and removing the hypothetical V^{5+} blocking layer, do not affect the overall charge densities. In conclusion, the hypothesis seems to show a lack of evidential support. However, it is possible that the solar simulator is not powerful enough (ie- not creating a thick blocking V^{5+} layer, which will take more than 1 second to remove) for being able to see any change in the charge densities.

Therefore, the test was repeated with four different UV light intensities (3.3 $mWcm^{-2}$, 10 $mWcm^{-2}$. 50 $mWcm^{-2}$, and 100 $mWcm^{-2}$) (Figure 32 c-f). The same phenomena (ie- no trends occurs except a difference between with and without chopping light) occurs for each UV light intensity. Even increasing the photocurrent and charge densities had no effect asthe blocking layer refill could not be observed. In conclusion, the hypothesis was false: the peak is not due to the layer concentration effects, but is due to the double layer charging.

To further test this option, a series of measurements were performed wherein the length of light / dark periods was varied (Figure 33). In some cases (e.g. Figure 24), the sharp spike immediately following illumination could be a direct result of photochemistry or due to the photoinduced change in electrode potential. To separate these effects, the potential was stepped from the open circuit potential (OCP, approx. 0.3 V *vs.* Ag|AgCl) to 0.5 V *vs.* Ag|AgCl under dark conditions. This results in a sharp peak in the measured current which is attributed to only double layer charging effects as at 0.5 V *vs.* Ag|AgCl in the dark. No other significant effect can occur (the exception being the oxidation of the small quantity of V^{3+} present in $VOSO_4$ electrolyte as shown previously). Once the potential is held at 0.5 V *vs.* Ag|AgCl, upon illumination, while the current rapidly increases (*i.e.* a photoanodic current is generated) and slower decreases, the very sharp spike in current observed in Figure 24 does not occur. This behaviour is also seen during chopped illumination LSV measurements above approx. 0.3 V vs. Ag|AgCl (Figure 26).

The fact that at 0.5V vs Ag|AgCl a double layer is observed is not a critical effect in the case of the experimentation (even if the tests is realised at 0 bias when the light is switched off the

potential between the photoelectrode and the counter electrode is 0 V vs Ag|AgCl). However, in the case of a real battery will be at OCP, thus when the light is turned on again the possibility to have a double layer is high.

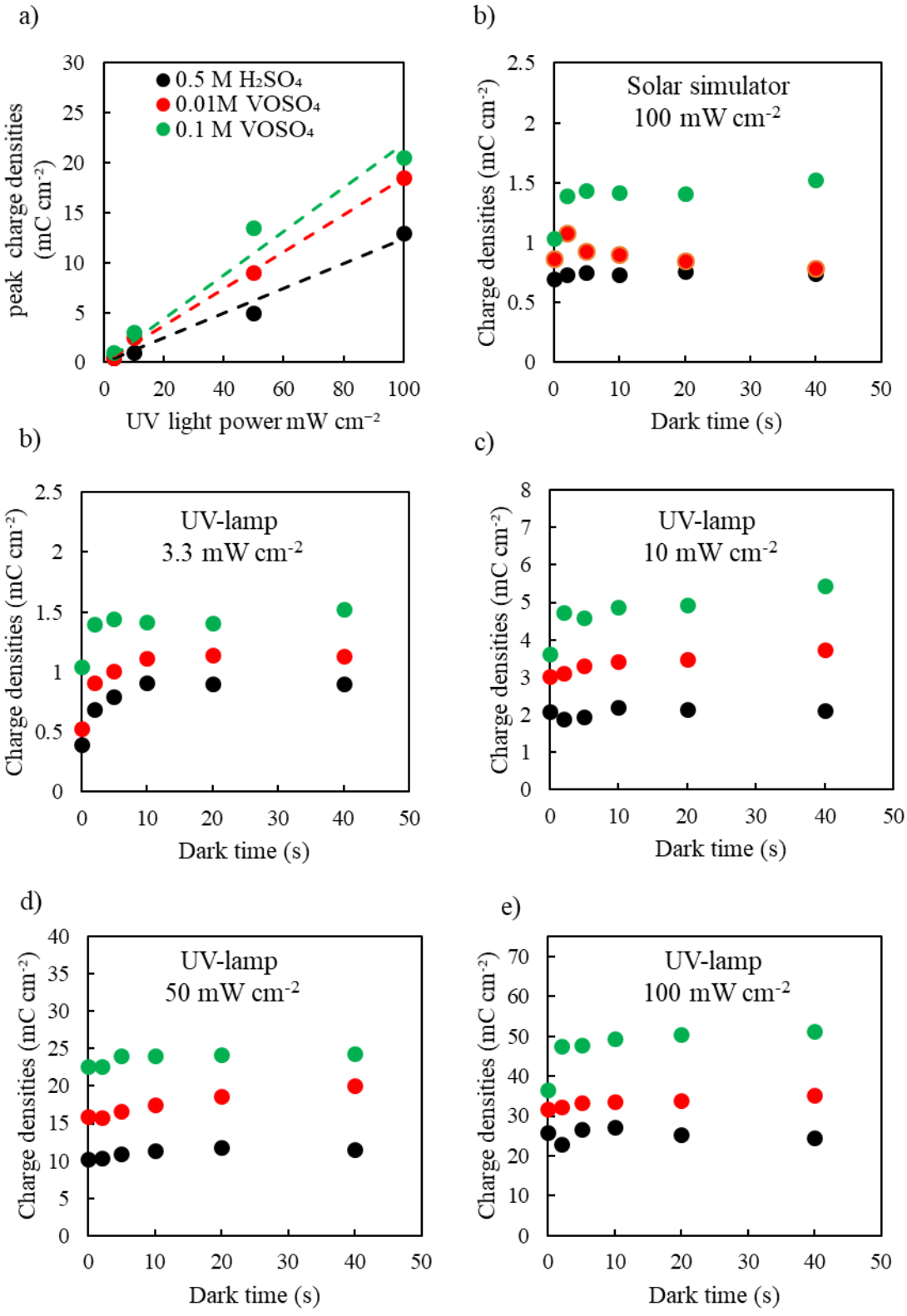

Figure *32*: a) Double layer charge densities in function of the light power density. Charge densities in function of the dark pulse time of a TiO_2 film at 0.5V *vs.* Ag|AgCl under b) A.M 1.5, 1 sun or 365 nm UV LED illumination at c) 3.3 mW cm^{-2}, d) 10 mW cm^{-2}, e) 50 mW cm^{-2}, f) 100 mW cm^{-2} with different electrolyte (0.1 M $VOSO_4$, 0.01 M $VOSO_4$, 0.5M H_2SO_4).

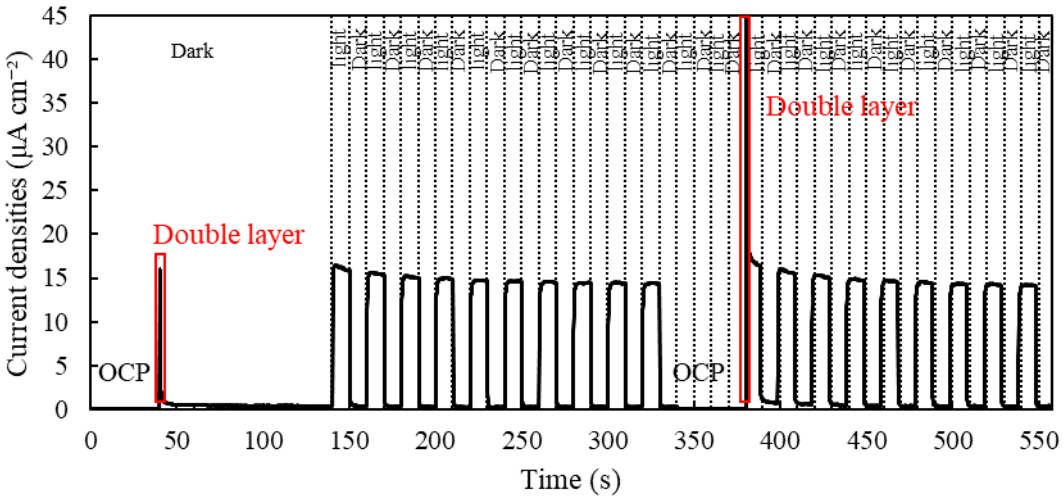

Figure *33*:Current densities in the function of time: Open Circuit Potential test of 40 second, a chronoamperometry at 0.5 V *vs.* Ag|AgCl during 300 seconds (100s in dark then 200s in chopped light), an Open Circuit Potential test of 40 second, another chronoamperometry at 0.5 V *vs.* Ag|AgCl of 200 seconds. The test was realised under chopped light (10 seconds dark, 10 seconds under sun simulator light). The cathodic electrolyte used was 0.5 M H_2SO_4, and the photoanode electrolyte was 0.01 M $VOSO_4$ (in 0.5 M H_2SO_4. The red box highlights the current spikes attributed to double-layer charging

3.3.6 Explanation of the peak in dark and light in the linear sweep voltammetry below 0.3 V *vs.* Ag|AgCl

To be able to determine what the phenomenon is occurring below 0.3 V *vs.* Ag|AgCl, which gave a sharp peak when the light is turned on or off was, a series of chronoamperometry and OCP tests were recorded (Figure 34). After the first OCP, we observed a sharp peak. Like previously, as the photoelectrode was still in the dark, this peak was due to the formation of a double layer at the surface of the electrode, as a result of the change in potential between the OCP voltage (0.3 V *vs.* Ag|AgCl) and the 0.15 V *vs.* Ag|AgCl of the experiment. Additionally, a negative current appears in the dark and reduces over time, due to the reduction of the V^{5+} present in the $VOSO_4$ solution.

When the light was turned on, a cathodic peak (ie- a positive peak) occurs and when the light was turned off an anodic peak appears (ie- a negative peak). According to the literature [68], [69], the rapid decay of the anodic photocurrent is a sign of the presence of electron-hole surface recombination and a decrease in band bending. These two phenomena occur on the active site of the film (ie- the site of contact between the TiO_2 and the electrolyte). When the

light was turned off the conduction band electrons react with the holes trapped at the surface of the photogenerated species. In the literature [68], Aplicada *et al.* study the formation of $OH^{\cdot}$ radical which leads to the creation of oxygen evolution in alkaline media. However, in the case of $VOSO_4$ in H_2SO_4 the photogenerated species where mostly V^{5+}.

If the electron-hole recombination process was occurring in this study, an increase of the steady state current should be observed when the potential was increased, until the steady state current is equal to the anodic peak value. However, as the polarization curves (Figure 26) show, the steady state current was unchanged and only the double layer charging peak disappeared. Therefore, the most probable explanation is that V^{3+} species form in the dark, which are then oxidised instantly in the light by the photocurrent and then reduced back to V^{3+} in the dark. The peak appears until 0.3 V, which is consistent with a small amount (V^{3+} to V^{4+} = 1:1000) of V^{3+} present in the solution.

The test has been repeated with different vanadium concentrations (Figure 35 a). Firstly, the increase of vanadium concentration leads to a higher stationary photocurrent and to a higher reductive current in the dark. As shown by the comparison between the linear sweep voltammetry and the dark polarisation curve of 0.1 M $VOSO_4$, the reductive current was linked to the reduction of V^{4+}. The use of only H_2SO_4 as electrolyte leads to a small anodic peak and an almost non-existent cathodic peak. Tafalla *et al* [68] have shown that this small anodic peak is only due to the accumulation of positive charge on the surface, which is used to split the water. The cathodic peak for 0.1 M $VOSO_4$ has a similar charge density to the one from 0.01 M $VOSO_4$ (Figure 35 b). It is shown that the number of V^{3+} generated in the dark are similar. The anodic peak behaviour was different: the anodic peak for 0.01 M $VOSO_4$ was higher than the one for 0.1 M $VOSO_4$ (Figure 35 b). The reason could be that in the 0.01 M $VOSO_4$ the majority of the V^{4+} have been electrochemically reduced to V^{3+}, so when the light is turned on all the V3+ are oxidized in V4+ and very few V5+ species are photogenerated.

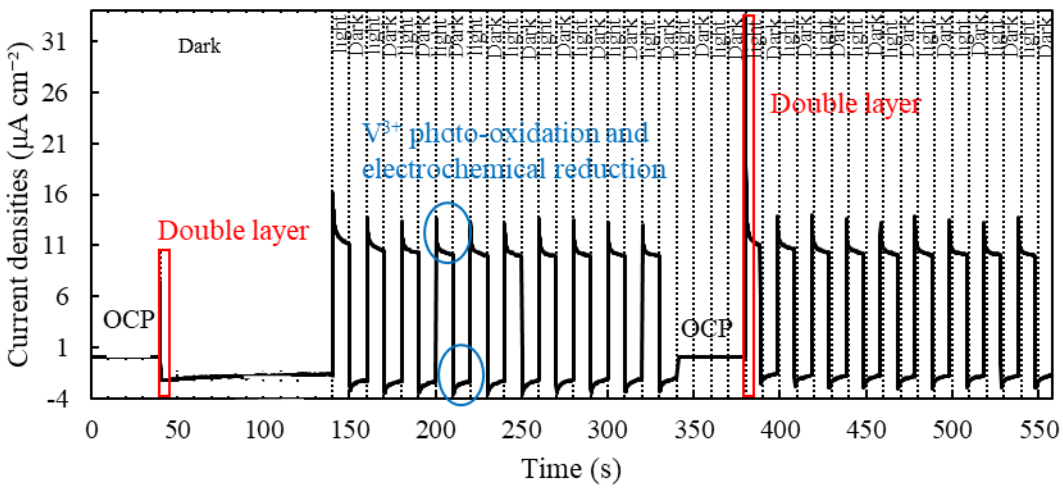

Figure 34: Current densities in the function of time: Open Circuit Potential test of 40 seconds, a chronoamperometry at 0.15 V *vs.* Ag|AgCl during 300 seconds (100s in the dark then 200s in chopped light), an Open Circuit Potential test of 40 seconds, another chronoamperometry at 0.5 V *vs.* Ag|AgCl of 200 seconds. The test was realised under chopped light (10 seconds dark, 10 seconds under sun simulator light). The cathodic electrolyte used was 0.5 M H_2SO_4, and the photoanode electrolyte was 0.01 M $VOSO_4$ (Alfa Aesar 99.9%) in 0.5 M H_2SO_4.

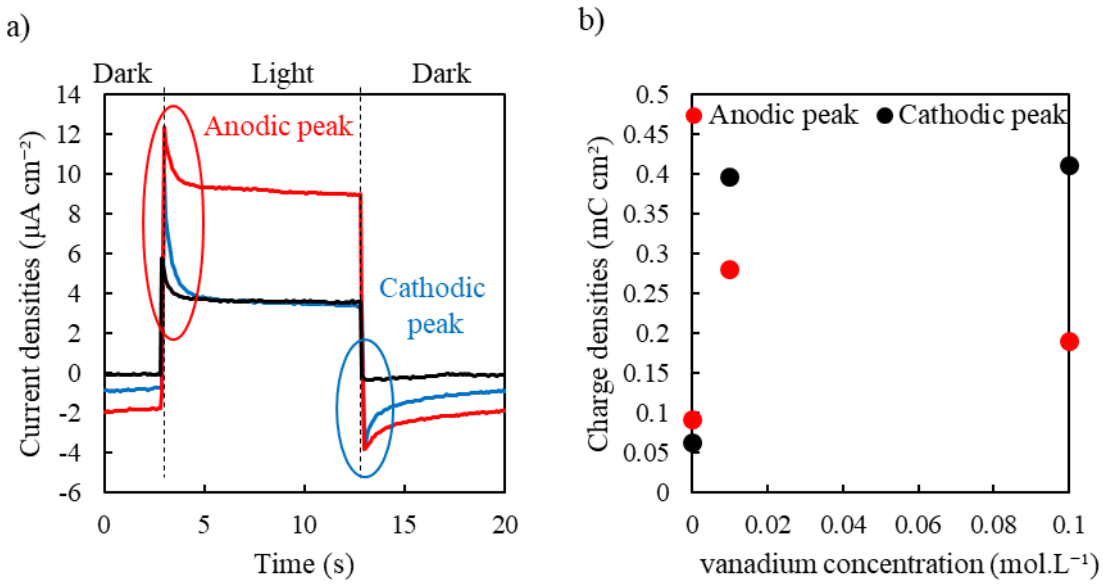

Figure 35: Single light-dark step at 0.15 V *vs.* Ag|AgCl with 0.1 M $VOSO_4$, 0.01 M $VOSO_4$ and 0.5 M H_2SO_4 electrolyte. Charge densities of the anodic and cathodic peak in the function of the electrolyte concentration.

3.4 Conclusion

This study allows a better understanding of all the reactions which could occur at the photoelectrode of a full vanadium solar battery (Figure 36). So, in the hypothesis where the device was measured with a 0 bias. Firstly, in the counter electrode chamber, the presence of oxygen will shift the working potential and induce an oxygen reduction instead of V^{4+} or V^{3+} reductions. In the photoelectrode when the light was off the potential is at 0.35 V *vs.* Ag|AgCl (when $VOSO_4$ is used in the non-deaerated counter electrode chamber without) or 0.3 V *vs.* Ag|AgCl (when VCl_3 is used in the non-deaerated counter electrode chamber. When the light was turned on two phenomena, occur, firstly the formation of a double layer due to the change between the open circuit potential to the light-induced potential. This double layer vanished in a few minutes. The second phenomena were an anodic peak due to the electron-hole recombination by the reduction of the photogenerated V^{5+} species at the surface of the electrode. However, after a few seconds, the photooxidation reaches an equilibrium and the photocurrent a stationary state. Some water splitting was also observed and led to a release of gas into the system. Finally, when the light was turned off again, a cathodic current occurs due to the recombination of the hole at the surface of the V^{5+} with the electron still in the surface of the semiconductor occurs, and so more V^{5+} were reduced.

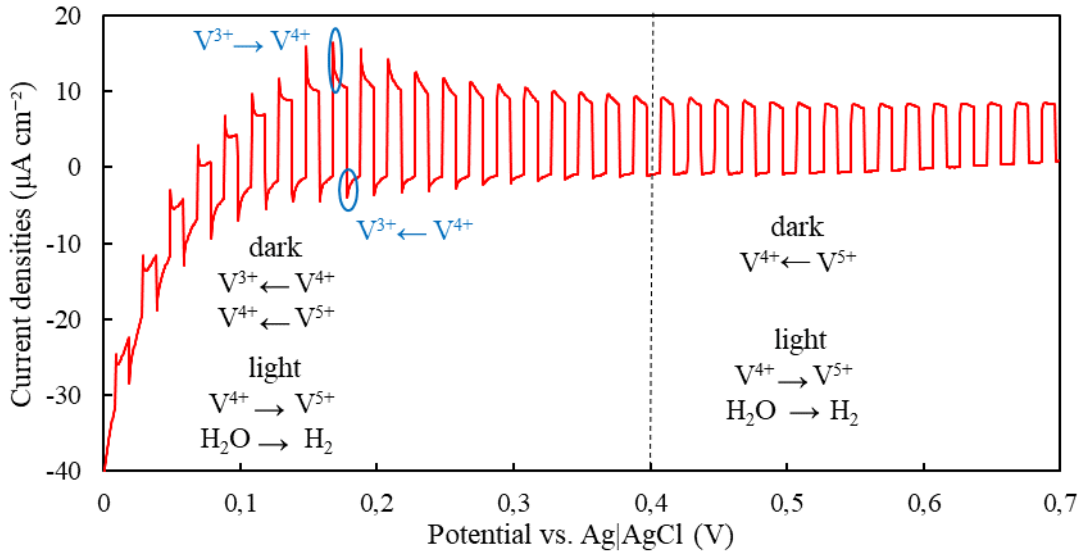

Figure 36: polarisation curves between 0V *vs.* Ag|AgCl and 0.7V realised on a 0.7 mg TiO_2 film with an electrolyte of 0.1M $VOSO_4$ in 0.5 M H_2SO_4.

In the hypothesis of bias of 0.5 V *vs.* Ag|AgCl as an example: in the dark, the V^{3+} present in the $VOSO_4$ solution was oxidised very slowly in V^{4+}. When the light was on the V^{4+} photooxidation takes place, and only the double layer was formed during the process. When the light was turned off, the oxidation of V^{3+} still takes place if it was not totally consumed. All of these phenomena can influence the design of a solar vanadium redox flow battery, and the tests need to be carried out to identify the efficiency.

4.Tuning photoactivity of TiO_2 film by changing its macroscopic structure

4.1 Introduction

Several methods have been developed to create TiO_2 thin films, mostly for dye-sensitised solar cells. The most commonly utilised method was the deposition of a titania paste by doctor blading on conducting glass - indium oxide doped tin oxide (ITO) or fluorine-doped tin oxide (FTO) [38], [95], [153], [164], [165], [237] The first step was to prepare a slurry of TiO_2 nanoparticles. Some TiO_2 particles were dispersed in a solvent, such as water, or in a slurry of terpineol and ethanol [38], [94], [95], [237]. Some surfactant may be added to increase the stability of the suspension. Addition of some polyethylene glycol can also increase the porosity of the TiO_2 film: the porosity of the layer is proportional to the molecular weights of the ethylene glycol used [38], [155], [165]. The slurry is finally deposited on the substrate on an area delimited by a tape mask with a defined thickness. The surplus of slurry is removed with a blade. Another way to deposit the same slurry is to use the screen printing method [153]. The slurry is put on a screen with a mask few centimetres above the substrate with a mask, and a blade is passed on the screen: the slurry passes through the pore of the screen to land on the FTO under it. This method gives a better porosity of the film, but to control the thickness one needs to use several successive layer depositions [153]. Another of the investigated methods was vacuum cold spraying. It involves spraying dry powder by an accelerating gas onto the FTO substrate under vacuum [38], [164], [165], [237]. Unfortunately, all these different deposition methods have limitations. The macroscopic morphology of the TiO_2 films deposited using these techniques are of low quality: the vacuum cold spraying does not use solvent, so the morphology of the TiO_2 films cannot be changed by controlling evaporation temperature [38], [164], [165], [237]. The doctor blading method uses different solvents. However, the solvent is typically limited to ethanol-terpineol mixture or water due to the need of a viscous slurry limiting film morphology tuning by solvent evaporation temperature [38], [94], [95], [237].

Presented here study investigates a way to tune the TiO_2 films by using the wet spray deposition technique based on the work of Halme *et al*. [238] and a new deposition method the ultrasonic spray technique to control the TiO_2 film macrostructure. The effects of the nature of the solvent

and evaporation temperature have been studied for the ultrasonic spray coating. The goal is to obtain an improved photocurrent for the TiO_2 photoanode by controlling the morphology structure of the film. To achieve control of the morphology different deposition methods of the TiO_2 film have been used and the performance of obtained films have been systematically tested.

4.2 Experimental

4.2.1 Commercial film

The commercially available TiO_2 film has been purchased to the company Solaronix. The photoelectrodes were composed of: a soda-lime glass slide of size 50 x 50 x 2 mm, an FTO (fluorine-doped tin oxide, SnO_2:F) film with a resistivity of 7 Ω and a transmission >70% from 470 to 1100 nm, an active area of 40 x 40 mm composed of Ti-Nanoxide D/SP TiO_2 paste (15 - 20 nm anatase particles with terpineol and organic binders; concentration in TiO_2 of the film: 18 wt%) which has been screen-printed and fired at 500 °C for 30 min. The films were broken into four pieces of roughly 25 x 25 mm. Before being tested the films were cleaned by UV-ozone for 20 min (MTI corporation, compact UV-ozone cleaner, with 55 W UV lamp of 254 nm and 185 nm maxima of irradiation with peak UV intensity of 4.6 $mW \cdot cm^{-2}$).

4.2.2 Preparation of suspensions

Suspensions of TiO_2 P-25 (Degussa) with a concentration of 20 $mg \cdot mL^{-1}$ of TiO_2 were prepared in different solvents: methanol (Fisher) absolute ethanol (Fisher), propan-2-ol (UNIVAR, analytical grade), butan-2-ol (UNIVAR), butan-1-ol (UNIVAR) and Milli-Q water. For the doctor blading deposition, a viscous slurry was prepared by dispersing 0.3 g of titanium oxide P-25 (Degussa) in 7 mL of ethanol, followed by the addition of 1 mL of terpineol and the evaporation of the ethanol by heating the slurry at 90 ºC on a hotplate (referred to as terpineol slurry).

In addition, two other slurries were prepared to determine the effect of the organic binders in the doctor blading deposition method. First, two test tubes were filled with 8 mL of water each; then 0.035 g of **C**arboxyl **M**ethyl **C**ellulose (CMC) was added to the first tube (CMC/Water),

0.035 g of CMC + 1 mL of **S**tyrene **B**utadiene **R**ubber (SBR, MTI corporation, 50 wt% water suspension, Viscosity: 100 ~ 350 mPa.S) to the second (CMC/SBR/Water). The two tubes were ultrasonicated for two hours. In parallel, two glass vials were prepared with the same solution compositions, but this time they were stirred at 80 ºC during 1 hour. Titania-containing CMC and CMC /SBR slurries were obtained by the addition of powder of TiO_2 P-25 (Degussa) (320 mg of TiO_2) to achieve final concentrations of 40 $mg \cdot mL^{-1}$ in these vials. However, as the slurries turned out to be not suitable for doctor-blading an extra slurry has been made with 38 wt% of CMC (38%CMC): 0.2 g of CMC was added to 8 mL of the previously sonicated 40 $mg \cdot mL^{-1}$ aqueous TiO_2 dispersion (320 mg of TiO_2 P-25 in 8 mL of water), and the resulting mixture was stirred at 80 ºC for 1 hour. Finally, an additional slurry has been obtained with a 7:3 CMC/SBR ratio at 38 wt% (38%CMC/SBR).

Suspensions of the titanium isopropoxide (TTIP) and the TiO_2 powder were prepared as follow: TiO_2 P-25 (Degussa) was dispersed in propan-2-ol to give 20 $mg \cdot mL^{-1}$ mixture. Then titanium isopropoxide (TTIP, Aldrich 97%) was diluted in propan-2-ol to obtain a mixture with a concentration of 71 $mg \cdot mL^{-1}$. This concentration would be equivalent to a TiO_2 concentration of 20 $mg \cdot mL^{-1}$, under the hypothesis that all of the TTIP is transformed into TiO_2. Finally, the two solutions were mixed (at various ratios tested) and put on a sealed test tube to avoid hydrolysis of TTIP by ambient moisture before the deposition.

4.2.3 FTO cleaning

FTO glasses (FTO type: NSG TEC 10, size: 1.1mm x 20 mm x 15 mm, FTO thickness 750 nm, resistance: 9.39 ± 0.38 Ω FTO work function: 4.4 eV - 4.7 eV, transmission 83.4%, Provider: Ossila) were cleaned by immersion in Milli-Q water and ultrasonication for 30 min followed by ultrasonication in propan-2-ol for 30 min. Finally, they were treated in a UV-ozone cleaner (MTI corporation, compact UV-ozone cleaner, with 55 W UV lamp of 254 nm and 185 nm maxima of irradiation with peak UV intensity of 4.6 $mW \cdot cm^{-2}$) for 20 min.

4.2.4 Preparation of underlayer

An underlayer could be deposited before the deposition of the main film. The first type of the underlayer was made by dipping the FTO glass for 30 min in 40 mM $TiCl_4$ aqueous solution maintained at 70 ºC according to the literature [239], [240].

Alternatively, mesoporous thin films have been realized by our collaborators (Paula C. Angelomé , Gerencia Química & Instituto de Nanociencia y Nanotecnología, Centro Atómico Constituyentes,CNEA-CONICET, Buenos Aires, Argentina). It was produced by spin-coating taking advantage of the evaporation-induced self-assembly (EISA) strategy [241], [242] using an inorganic precursor (titanium(IV) ethoxide $Ti(OEt)_4$, Sigma Aldrich), a template (Pluronic P123, Sigma Aldrich) and an inhibitor (HCl, 37 % w/w concentration, Merck) in 1-butanol (Panreac). The preparation of titania sol was performed adapting a procedure reported elsewhere [243]. Firstly, 1.6 g of HCl_{conc} was slowly added to 2.1 g of $Ti(OEt)_4$ at room temperature under vigorous stirring. Separately, 0.65 g of Pluronic P123 was dissolved in 12 g 1-butanol, and then added to the HCl/$Ti(OEt)_4$ mixture, under stirring. The molar composition of the final mixture was 1 $Ti(OEt)_4$:1.8 HCl:0.012 P123:6.1 H_2O:17.6 1-butanol. This mixture was subsequently aged with stirring at room temperature for 3 h before film casting. Films were prepared by spin-coating 75 µl of the solution onto an FTO substrate at 8000 rpm. Immediately after the deposition procedure, a 1 mm wide area was removed from one of the film edges using a cotton swab dipped in ethanol, to create a film-free FTO contact area. The as-prepared film was aged for 48 hrs in a chamber at 80 % relative humidity (obtained using a saturated KNO_3 solution). Finally, the films were calcined in air using a two-step procedure: first, they were heated at 17 °C min^{-1} until 200 ºC and then, were heated at 1°C min^{-1} until 450 °C, holding the chosen temperature for 2 hrs.

The third alternative underlayer was fabricated by my colleague Sam Nesbitt (chemical and process engineering department, university of Canterbury, Christchurch, New Zealand) using the hydrothermal growth method. The slides were placed on a Teflon base (6 mm high) in a custom-made Teflon liner at an angle with the conductive side facing down. Toluene (11 mL) and concentrated HCl (1.0 mL) were added into the liner, and the liner was transferred to a glovebox where $Ti(iOPr)_4$ (1.0 mL) was added. The liner was then sealed in the stainless steel autoclave and placed in an oven that had been preheated to 180 °C. Total heating time was 2 hrs 20 mins before cooling naturally in the oven (baffle closed) to room temperature. Slides were washed twice with EtOH, dried in air and then calcined in a tube furnace under static air at 450 °C for 2 hrs with a ramp rate of 4 °C/min and cooled naturally in the furnace at the end.

For spraying, the samples were placed on the heater support (hotplate) and a stainless steel mask with an opening of 1 cm^2 over each slide was placed on top of them.

4.2.5 Deposition process

In this study, two deposition processes have been investigated: the airbrush spray coating and the ultrasonic spray coating. The first one involves spraying the suspension with an airbrush. The suspension was put in a small tank on the top of the airbrush; then it drops on a chamber swept by an airflow. The solution is propelling through a nozzle of 0.2 mm, forming a cone of a fine mist. This mist of droplets hits the pre-heated FTO glass, and the solvent was evaporated under various temperatures studied. This method was improved further using the airbrush spray robot, with airbrush mounted on an x-y stage and programmed to follow a repeatable pattern over the mask and, thus, capable of depositing the desired amount of suspension onto the FTO. The second method utilised an ultrasonic atomiser (Sonozap) operating at 60 kHz with titania suspension fed by a syringe pump (New Era Pump System Inc.) at 1 $mL \cdot min^{-1}$. This method also gave rise to a fine mist being deposited onto FTO. This ultrasonic spray-gun was mounted on the x-y robotic stage and followed a pre-programmed pattern over the top of the mask placed over FTO slides. To compare with the most frequently used deposition method, doctor blading, TiO_2 films have been deposited by doctor blading using a 10 µm thick tape mask attached to FTO glass. Some TiO_2 slurry prepared as described above was dropped on FTO covered by the mask, and the excess of the slurry was removed using a scalpel blade. Finally, the TiO_2 films were sintered: heating ramp of 7 $°C \cdot min^{-1}$, to the target temperature of 450 °C at which samples were kept for 30 min in static air then the temperature was ramped down at 5 $°C \cdot min^{-1}$.

4.2.6 Photoelectrochemical tests

The TiO_2 films were placed in contact with a 0.1 M $VOSO_4$ (Alfa Aesar 99.9%) electrolyte in 0.5 M H_2SO_4: the films were clipped to a glass cell with the TiO_2 film inside the electrolyte chamber as described in the previous chapter (Figure 22). Redox couple V^{4+} / V^{5+} was used for a model redox reaction. This choice is motivated by its potential (E_0 = 1 V *vs.* RHE) close to the thermodynamic potential matching band gap of TiO_2 photoanodes (3.0 eV. In addition, it is a widely used redox couple in the field of solar photoelectrochemical storage cell [33], [49], [50], [244], [245] A the Ag|AgCl reference electrode was placed in this electrolyte. The second

half cell was formed by a platinum wire, acting as the counter electrode, dipped inside a 0.5 M H_2SO_4 solution. The cell was sealed by using a Nafion 117 membrane to separate the two half-cells (Figure 22). Polarisation curves were recorded by linear sweep voltammetry using Gamry 600 potentiostat with scanning between 0 V *vs.* Ag|AgCl and 0.7 V *vs.* Ag|AgCl at a scan rate of 0.5 mV s^{-1}.

The light source was furnished by a solar simulator (Xenon lamp) at 100 $mW.cm^{-2}$ with a 1.5 AM filter placed 35.5 cm from the cell, and a shutter was placed between the light source and the cell. This shutter was controlled by the potentiostat: it was closed for 20 seconds and then opened for 20 seconds repeatedly. The curve obtained in this way was showing current densities corresponding to the periods of no illumination ("the dark") and followed by the periods under illumination ("the light") superimposed within the function of the potential of the photoelectrode on a single curve. The photocurrent was calculated at 0.5 V *vs.* Ag|AgCl, in the previous chapter it had been shown that this value (> 0.4 V *vs.* Ag|AgCl) is on a plateau where there is almost no electrochemical oxidation or reduction in the dark (the current recorded will be only due to the exposure of the photoelectrocatalyst to the light. Besides at 0.5V vs Ag|AgCl the phenomenon of anodic peak (peak of current of few seconds when the light is turned on) and cathodic peak (peak of negative current of few seconds when the light is turned off) does not occurs: the photocurrent stays constant during illumination (Figure 36). This potential allows a reproducibility of ± 0.2 µA between two consecutive linear sweep voltammetry tests.

In this way, it was possible to obtain information about the electron-hole recombination as shown as was discussed in the previous chapter.

4.2.7 Error studies

For the commercial film samples, the photocurrents at 0.5 V *vs.* Ag|AgCl were calculated for each film by averaging the value recorded on two consecutive linear sweep voltammetry tests. The potential of 0.5 V *vs.* Ag|AgCl has been chosen because the linear sweep voltammetry shows a constant current without any peaks due to the electron-hole recombination and due to the absence of reductive current in the dark (see the previous chapter). The error bars were calculated as 95 % confidence intervals for the same sample (*i.e.* same film) on two consecutive

linear sweep voltammetry tests. Then the average of the ten film samples was calculated, and the error bar was given as the 95 % confidence interval for all the film samples.

The films deposited by doctor blading, airbrush spray coating and ultrasonic spray coating were deposited by batches of three. The photocurrent plot shows the average photocurrent of the three TiO_2 films measured with two consecutive linear sweep voltammetry test per film at 0.5V *vs*. Ag|AgCl and the error bars were the 95 % confidence intervals of these three layers with two consecutive linear sweep voltammetry tests per each film.

4.2.8 Surface analysis

Surface analysis was carried out using an SEM microscope (JEOL 7000F FE-SEM, parameters: magnification x1000, 15 kV) on the TiO_2 film after the photoelectrochemical test. These SEM images were processed by Image J to obtain a 3D surface plot: the luminance of an image is interpreted as height for the plot. Internally the image is scaled to a square image using nearest neighbour sampling. The distances were calculated by using the Image J measurement tool. PXRD patterns of samples deposited on FTO slides in this work were collected at room temperature on a Rigaku Smartlab diffractometer. General data collecting was conducted in Bragg-Brentano focusing mode utilising Cu Kα (1.5418 Å) radiation operating at a tube voltage of 40 kV and tube current of 30 mA passing through a Cu Kβ filter, with a Cross Beam Optics Bragg-Brentano selection slit, 10 mm length limiting slit, 5.0° Soller incident and receiving parallel slit. The detector was a Rigaku D/tex Ultra 250 1D. The data collected was in the 10 - 90 2θ range conducted at 5°/min.

4.3 Results and Discussion

4.3.1 Commercial films

The use of a commercial film was motivated by the need to have an independent film standard for comparison with the performance of the samples made using different deposition methods.

These films have been deposited by screen printing using a paste composed of terpineol, organic binders and TiO_2. The advantage of the screen printing method (Figure 13) is that it gives a high porosity of the film; however, the use of several successive layer depositions is

often needed for the thickness control [150]. This deposition method has been widely used for dye-sensitized solar cells [148]–[150].

The high magnification SEM images show some agglomerates (diameter 32 to 56 µm) dispersed on the surface of the film (Figure 37 a). However, at medium magnification (Figure 37 b) the film has some TiO_2 particles inside its matrix (some agglomerates of 1.3 µm, but the majority of particles are smaller than 100 nm). There are also visible zones looking like drop silhouettes (diameter 2.3 to 11 µm). These drop silhouette zones when the image is zoomed in (Figure 37 c) again are formed of TiO_2 particles (about 100 nm in size) under the surface, which pushes the top layer up and forms a half-sphere (diameter *ca*. 40 nm). Some even break the top surface layer. According to the literature, examples of screen printed films without binders [246] do not show such smooth surface, but a rougher surface composed of merged particles. Therefore, the top layer is probably formed of a binder-rich layer which is on top of a dense TiO_2 film.

The plot of the surface in 3D at the low magnification shows (Figure 37 d) low roughness: Ra = 5 greyscale. Ra is the arithmetic average value of the deviation of the trace above and below the center line of the film surface. The greyscale corresponds to a measure of the brightness of pixels from black to white. The scale goes from 0 (black) to 255 (white), the 3D plot is in colour for a higher clarity but correspond to this scale. Unfortunately, it is difficult to transform this scale in distance, but it is sufficient to be able to compare the roughness of the different films. When the magnification is increased (Figure 37 e), the magnified local roughness of the layer becomes more visible, but overall, it stays low. However, only when we focus and zoom even further (Figure 37 f) on the drop silhouette, some high peaks appear. Yet, such features are relatively small since the highest magnification is required to discern them. These observations suggest that the top layer of the film surface is overall smooth, which results in a flat surface being in contact with the electrolyte (an important reference point for comparison with more structured films made in this study).

The linear sweep voltammetry on these commercial samples (Figure 37 g) is similar to the one discussed in the previous chapter (Figure 36). However, a small difference could be seen: there is no anodic peak (but a cathodic one is present) even below 0.15 V *vs*. Ag|AgCl. It could be due to the fact than the binders shield the TiO_2 particles and so provide fast surface recombination under illumination. Besides, The TiO_2 powder is different compared to the one used in the previous chapter. Unfortunately, without complete information on the composition of the TiO_2 paste used, it is impossible to make a solid conclusion regarding surface electron-hole recombination.

The commercial films show a reproducibility of 70 % with only three samples giving values outside of the 95 % confidence interval (Figure 37 h). This 30 % of samples out the range could be due to a small variation of the thickness of the "as purchased" Solaronix film samples. However, it was possible to determine the TiO_2 loading of each sample by weighting the sample then carefully removed the TiO_2 thin film by scratching the surface and weight the sample again. Then as the TiO_2 paste used by Solarnix contains 18 wt% of TiO_2, it was possible to determine the approximate TiO_2 loading of each sample

The average photocurrent is 8 ± 1 µA cm^{-2} mg^{-1}, in comparison the usual photocurrents for the full redox flow batteries reported in the literature [49], [53], [54] were 15 µA cm^{-2} for a 3 mg film, giving normalised by weight photocurrent of 5 µA cm^{-2}·mg^{-1}. The photocurrent for commercial films observed in this study is slightly higher than the literature values. Still, it is in a similar magnitude range so that these films could be considered as a proper standard for this study.

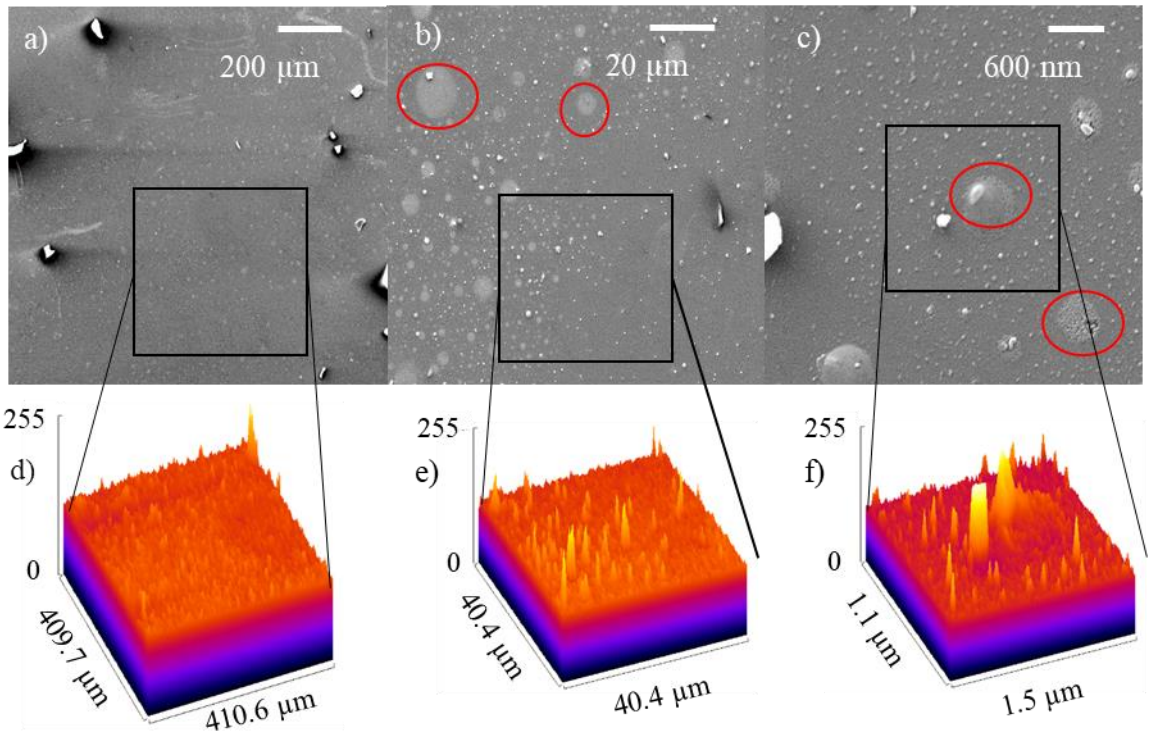

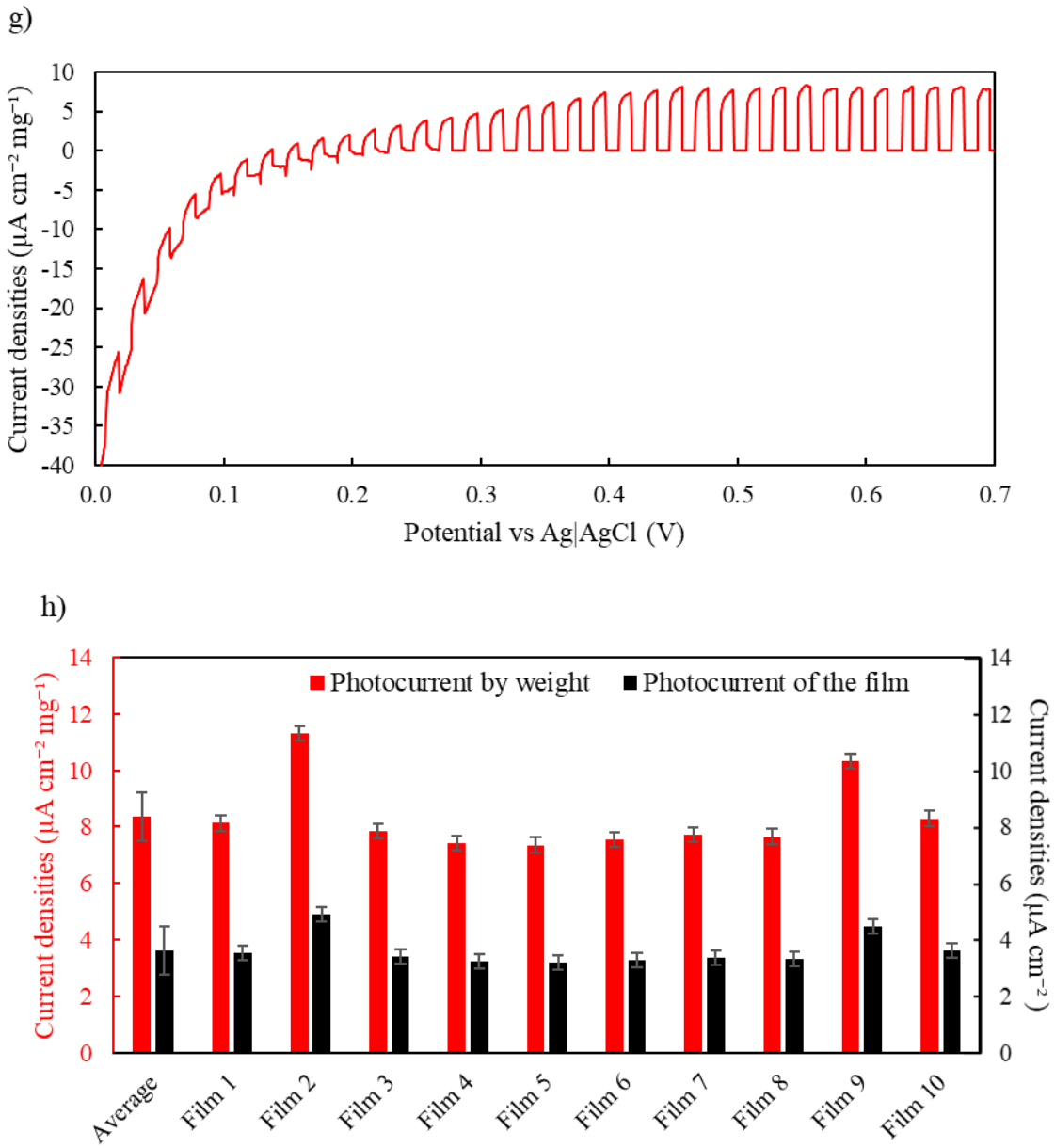

Figure 37: SEM images of commercial TiO_2 films at various magnifications. Scale bars: a) 200µm, b) 20µm, and c) 600 nm. Surface roughness analysis of the commercial TiO_2 films on a surface of d) 168.2 x 10^3 µm^2, e) 1620.4 µm^2, and f) 1.98 µm^2.

g) linear sweep voltammetry (scan rate 0.5 mV s^{-1} between 0 V *vs.* Ag|AgCl and 0.7 V *vs.* Ag|AgCl) of a commercial TiO_2 films

h) Photocurrent densities at 0.5 V vs. Ag|AgCl of 10 commercial TiO_2 films and the average photocurrent.

4.3.2 Doctor blading

Doctor blading method is the most common method used in the literature [5], [38], [54], [95], [104], [144]–[147].The method was used for the first time by Gratzel *et al.* [94]. A viscous slurry of TiO_2 in water was prepared by evaporation and spread on the conductive glass and sintered at 450 ºC. In their respective publications, Grunwald *et al.* [128] and Cao *et al.* [85] provided more details on the doctor blading deposition method. The TiO_2 P-25 powder was suspended in water (12 g TiO_2 in 4 mL of water) with 0.4 mL of acetylacetone added to avoid aggregation. 0.2 mL Triton X was added to help the nanocrystals to disperse on the substrate. A tape mask was used, and the slurry was bladed by a glass slide. The film was similar to the case of Gratzel *et al.*; lately, the better solvent mixtures have been used to disperse TiO_2 in the slurry: some polymers in water [5] or terpineol [48], [126], [127], similarly to the case of commercial samples studied here, are used for forming the slurry.
Based on this slurry recipe, films made using a doctor blading method have been prepared for the comparison of their performance with that of the commercial ones. The initial experiments were performed with an aim to find the best way of obtaining a good titania slurry, with first screening experiments aimed at establishing the best slurry matrix without actually using TiO_2. One alcohol and two polymers were tested: the terpineol was chosen because it used for several TiO_2 films preparations in the literature [48], [126], [127]; The SBR and the CMC have been chosen because they have been previously investigated as binding agents (*i.e.* polymer which binds the TiO_2 particles together) for nanocrystalline anatase TiO_2 anode in Li-ion battery electrode [247].

Unfortunately, the slurry matrix was too liquid (it would wash off when the mask was removed) in the case of CMC/Water and CMC/SBR/Water. Nevertheless, CMC and CMC/SBR slurries were investigated further. After an additional 1 hour of stirring no significant visible changes to the consistency of these slurries occurred. An extra CMC (0.5 g) was added to the CMC slurry and this time the slurry became too solid.

According to the literature for lithium-ion batteries, to obtain a proper slurry, a weight ratio of CMC/SBR of 7:3 is required, and the binders should represent 10 wt% of the slurry [247]. However, as there is only CMC, no carbon black and that the support is different, the quantity of binders (*i.e.* CMC + SBR) was increased to 38 wt% of the slurry. The slurry obtained in this

way was deemed to have acceptable consistency (it was possible to deposit it on the FTO glass without forming a solid half-sphere on the surface and without spreading out when the mask was removed) and thus this wt% of binders was used in the follow-up experiments. However, because the as CMC is a rather stiff and brittle binder [247] (*i.e.* polymer which binds the TiO_2 particles together), the addition of a more flexible and elastomeric binder, such as SBR, was required to obtain a homogenous film [247], so the 38%CMC/SBR slurry has been made with the same wt% of binders and it has shown an acceptable consistency too.

Three FTO glasses were covered by doctor blading with 38%CMC slurry, 38%CMC/SBR slurry, and terpineol slurry for comparison. The slurry made using CMC alone did not adhere efficiently enough to the FTO after sintering, but for the one made with CMC/SBR, the adhesion and the homogeneity were better.
The SEM images show very homogenous top layer with particle size below 1 µm, but with a large, round half drop shape going out of the surface (diameter of 22 µm, 1 per image) and some cracks (maximum width of 2.3 µm, 3 per image) on the surface for the film made using slurry with terpineol (Figure 38 a). The cracking could arise due to the difference in thermal expansion between TiO_2 and FTO film [267].

The film of CMC/SBR (Figure 38 b) is composed of large TiO_2 particle agglomerates (from 1.6 to 3.8 µm in diameter) and show lack in homogeneity and variability of thickness. The commercial sample had a very homogenous top layer with particle size about 100 nm (Figure 38 c). The surface in 3D show a large difference of roughness: the use of terpineol results in (Figure 38 d) a low roughness of the layer if we exclude the half-sphere protruding out of the surface and cracks (Ra = 6 greyscale) (Figure 38 e). The use of CMC/SBR as binders leads to higher roughness (Ra = 18.6 greyscale). Use of the terpineol as a solvent yields a film with the high homogeneity in terms of roughness at the small scale: the particles are all the same size, and not a lot of agglomerates were formed in comparison to the commercial sample, which shows a few big agglomerates but still has a majority of tiny particles on the surface (Figure 38 f).

Comparison of the photocurrents at 0.5 V *vs.* Ag|AgCl (Figure 38 g) shows that the titania film made using terpineol-containing slurry has a higher photocurrent when normalized by weight (6.0 ± 0.2 µA $cm^{-2} \cdot mg^{-1}$) than the film made using CMC/SBR slurry (1.6 ± 0.2 µA $cm^{-2} \cdot mg^{-1}$).

The terpineol-based film shows a photocurrent of 18 ± 0.8 µA cm^{-2} and a photocurrent normalized by weight of 6 ± 0.2 µA cm^{-2} mg^{-1}. In comparison, the commercial films show a lower photocurrent of 3.6 ± 0.8 µA cm^{-2}, but a higher photocurrent by weight (8.3 ± 0.2 µA cm^{-2} mg^{-1}). In the literature [53], the photocurrents of a TiO_2 film deposited by doctor blading with a terpineol slurry were 15 ± 1 µA cm^{-2} for a 3 mg film (5 ± 1 µA cm^{-2} mg^{-1}). It confirms the choice of terpineol as a good solvent for the doctor blading deposition.

The use of polymer binders was not effective at improving the photocurrent of the photoanode. It could be explained by the partial coverage of TiO_2 particles by these polymers and especially SBR, which has some insulating properties [248], prohibiting the charge to pass from one TiO_2 particle to another. The reproducibility of the doctor blading could be low and is based on the capability of the person depositing the film (required two failed slides before three acceptable films which can be tested have been obtained). Besides, the use of a slurry limits the possibility to change the deposition parameters (limited to viscosity and TiO_2 loading in terpineol) to obtain TiO_2 films with different macrostructure. Hence, a more reproducible, automated and more tuneable with respect to deposition parameters deposition method was required.

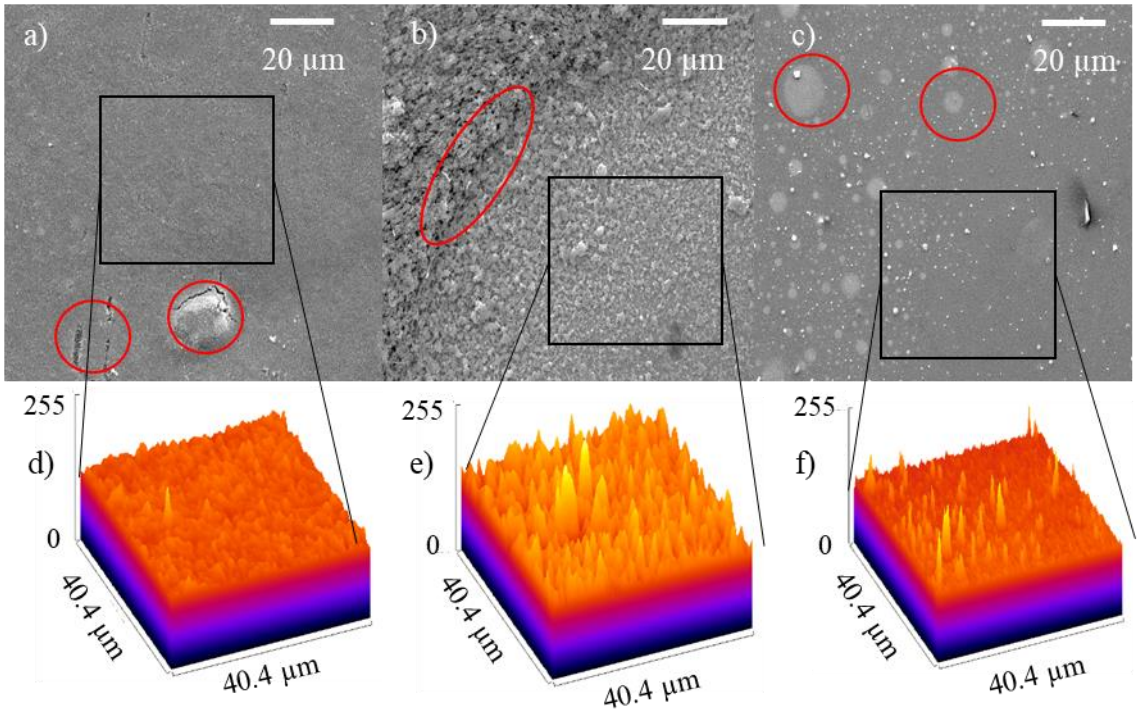

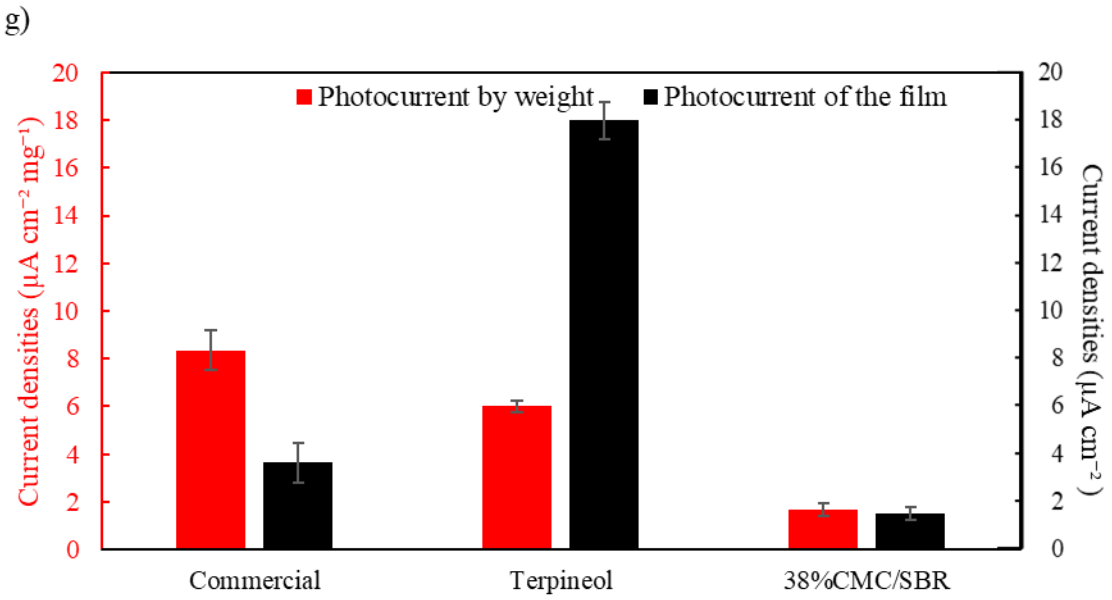

Figure 38. SEM images at x1000 magnification (scale bars of 20 µm) of a) terpineol-based doctor bladed TiO_2 film, b) 38 % CMC/SBR slurry-based doctor bladed TiO_2 film, and c) commercial TiO_2 film. Corresponding 3D surface plots: d) terpineol, e) 38 % CMC/SBR, and f) commercial. g) photocurrent densities at 0.5 V *vs.* Ag|AgCl of the different TiO_2 films.

4.3.3 Spray coating

As the doctor blading method shows a lack of reproducibility and tuneability, two other deposition processes were investigated: the airbrush spray and the ultrasonic spray. The airbrush spray has been used by Senevirathne *et al.* for deposition a TiO_2 film for dye-sensitized solar cells with success [151]. The capacity of depositing the films in a specific area by the application of a spray mask and the possibility to control the films morphology including aggregation domain size [249] are the main advantages of this method. Senevirathne *et al.* [151] used a mixture of titania colloidal solution (20 mL, 20.5 % by volume of TiO_2 in water), acetic acid (5.5 mL), Triton X-100 (5 mL), and ethanol (20 mL) which was sprayed on an FTO glass heated at 150 ºC on a hot plate.

The ultrasonic spray method is a small variation of the airbrush spray method which employs a different source of propulsion for the TiO_2 colloidal solution. In the airbrush spray, the mist was formed at the nozzle by using a compressed airflow. The colloidal solution mist was projected by the same airflow on the mask and the FTO glass. In the ultrasonic spray, the creation of the mist is realized by an ultrasonication (60 kHz) of the solution at the nozzle, and airflow is projected around the nozzle not to propelled but to focus the mist to the desired

surface by creating a boundary that the mist ca not pass. Overall the ultrasonic spray shows better control over the area of deposition (0.5 cm^2 minimum deposition spot size with ultrasonic spray over 1.2 cm^2 with an airbrush spray) and removed parameters which could lead to a decrease of the film reproducibility and external contamination (*i.e*. the compressed air used by the airbrush spray). However, to be able to obtain a reproducible film, both devices were mounted on an x-y robotic stage controlled by computer, which allows a precise definition of the desired deposition area.

To investigate the effect of the solvents used in the common TiO_2 film preparation, water and a selection of alcohols with different boiling points was studied. Indeed ethanol (boiling point temperature: $T_{b.p}$ = 78 ºC [250]) and water ($T_{b.p}$ = 100 ºC [250]) have been widely used for dispersing the TiO_2 particles in the slurry for the doctor blading [85], [94], [128]. Propan-2-ol ($T_{b.p}$ = 80 ºC [250]) has a boiling point close to that of the ethanol. However, the TiO_2 dispersion was more stable over a long time in propan-2-ol (could be still used after three days instead of 1 day in ethanol and a few hours in case of water). Besides, as the goal was to obtain a liquid suspension suitable for spraying, thus, the concentration in TiO_2 particles has been set at 20 mg mL^{-1} (a lower TiO_2 concentration than the 40 mg·mL^{-1} used for doctor blading). Photoanodes were prepared from TiO_2 P-25 with these three different solvents using the two different deposition processes (Table 5).

Table 5. Summary of the titania suspension compositions used for the depositions and different deposition processes used in this study.

Deposition method	Suspension composition	Short name
Doctor blading	0.3 g mL^{-1} in 1 mL of terpineol Doctor blading TiO_2 P-25 slurry. Hot plate temperature: 90 ºC	D B
Airbrush spray coating with 1.2 $m \cdot s^{-1}$ airflow	20 mg mL^{-1} of TiO_2 P-25 in ethanol as a solvent. Hot plate temperature: 90 ºC	eth/LAF
Airbrush spray coating with 1.2 m s^{-1} airflow	20 mg mL^{-1} of TiO_2 P-25 in propan-2-ol as a solvent. Hot plate temperature: 90 ºC	iso/LAF
Airbrush spray coating with 1.2 m s^{-1} airflow	20 mg mL^{-1} of TiO_2 P-25 in water as a solvent. Hot plate temperature: 120 ºC	wa/LAF
Airbrush spray coating with 3 m s^{-1} airflow	20 mg mL^{-1} of TiO_2 P-25 in ethanol as a solvent. Hot plate temperature: 90 ºC	eth/HAF
Airbrush spray coating with 3 m s^{-1} airflow	20 mg mL^{-1} of TiO_2 P-25 in propan-2-ol as a solvent. Hot plate temperature: 90 ºC	iso/HAF
Airbrush spray coating with 3 m s^{-1} airflow	20 mg mL^{-1} of TiO_2 P-25 in water as a solvent. Hot plate temperature: 120 ºC	wa/HAF
Ultrasonic spray coating	20 mg mL^{-1} of TiO_2 P-25 in ethanol as a solvent. Hot plate temperature: 90 ºC	eth/sonic
Ultrasonic spray coating	20 mg mL^{-1} of TiO_2 P-25 in propan-2-ol as a solvent. Hot plate temperature: 90 ºC	iso/sonic
Ultrasonic spray coating	20 mg mL^{-1} of TiO_2 P-25 with water as a solvent. Hot plate temperature: 120 ºC	water/sonic

Surface analysis was carried out using an SEM microscope on the different TiO_2 films obtained. These films were compared with the TiO_2 films deposited using doctor blading approach and the commercial films. The TiO_2 films obtained using titania suspensions in selected three solvents and the various deposition processes (Figure 39) show a vast diversity of morphology.

The eth/LAF (Figure 39 a) formed a homogenous layer (no extra-large agglomerates on the surface, but large particles 2 to 1 μm merged together) without any deep cracks but quite a rough surface. In comparison, the iso/LAF film (Figure 39 b) present a large number (16 on

this image) of agglomerates (diameter of agglomerate from 4.7 to 8.5 µm, made of small particles below 100 nm merged together) on the top of a homogenous layer. The formation of agglomerate on any TiO_2 film is due to high surface area and interfacial energies of TiO_2 particles [251], in the case of iso/LAF the lower surface tension (propan-2-ol 21.7 $mN \cdot m^{-1}$ < ethanol 22.3 $mN \cdot m^{-1}$) can explain the formation of numerous agglomerate (lower surface tension so faster evaporation linking to a larger chance to form agglomerate [252]). Finally, when the water is used as the solvent (wa/LAF) (Figure 39 c) the film shows two larger agglomerates (diameter of agglomerates *ca*. 12 µm compared to the 4.7 to 8.5 µm in iso/LAF), the rest of the film was composed of small agglomerate of 1 µm.
On the 3D surface plot, the roughness of the eth/LAF (Figure 39 d) is evident (Ra = 22.41 greyscale). However, the distribution of the particles is homogenous. The iso/LAF (Figure 39 e) film shows a much lower roughness of the layer over the agglomerate (Ra =15.17 greyscale). However, it is still rougher than the film deposited using doctor blading (Ra =6 greyscale) (Figure 38 d). Finally, the 3D surface plot analysis of wa/LAF (Figure 39 f) film shows that it is rougher than the SEM picture was showing: the surface is full of high peaks with a small diameter.

The solvent has an effect on the aggregation domain size and the overall film morphology because of the difference in surface tension (water 72.75 $mN \cdot m^{-1}$> ethanol 22.30 $mN \cdot m^{-1}$> propan-2-ol 21.7 $mN \cdot m^{-1}$ [250]). When a droplet is about to be formed, two force occurs the Bernoulli pressure, which is the internal pressure of the droplet and the surface tension of the solution, which is opposite to the internal pressure. The droplets are finally formed when these two forces reached an equilibrium. In the initial stage, large droplets will be broken into smaller ones with decreased surface tension [253]. When Bernoulli pressure equals to surface tension, droplets remain at the equilibrium state and do not break. The choice of the solvent will lead to a difference in the equilibrium size of the droplets and finally when the droplets dry will result in a difference in morphology of the film. In the deposition process, the droplets will spread out into a spherical cup shape specified by the contact angle with the substrate [254], [255], and form laminar spot mark after drying. A significant number of spots accumulate as cascade and turn into a thin film ultimately. The morphology of the film is dependent on the size of droplets and thickness difference between the center and edge of the spot mark [254], [255].

When airbrush spraying was used with airflow of 3 m s^{-1} eth/HAF film (Figure 39 g), a large network of cracks was found (from 2.3 µm to 12.0 µm width and more than 112 µm in length)

all other the surface of the film with agglomerates (diameter 1 to 5 µm, 20 per image) the rest of the film is composed of particles smaller than 100 nm. In the case of iso/HAF, the film is crack-free with some agglomerates (11 per image with a diameter from 7 to 10µm) and a surface composed of 500 nm particles, however, compared to the eth/LAF (Figure 39 h) the agglomerates are much more integrated within the top layer. Finally, the (Figure 39 i) wa/HAF shows a homogenous film (fine grain surface features smaller than 100 nm) surface with small cracks spread over the surface (20 per image, 1 µm maximum width and 30 µm maximum length).

The 3D surface plot (Figure 39 j) shows correctly the cracks going deep inside the eth/HAF film, while the rest of the surface is quite rough (Ra =27.3 greyscale with the cracks). The iso/HAF 3D surface plot (Figure 39 k) confirm the roughness of the surface and the presence of agglomerate particles (Ra =21.5 greyscale). Finally, the wa/HAF (Figure 39 l) is looking very flat, but due to the presence of the cracks, overall, it has a similar roughness as the iso/HAF (Ra =22.6 greyscale).

It is noteworthy that cracking is more pronounced in the case of eth/HAF film sample. Which could be explained by the hypothesis that the droplets reach the surface faster without losing as much solvent, as in the case of lower flow rate and hence the growing film at the surface is oversaturated with solvent, fast evaporation of which results in cracking. The cracking could arise due to rather vigorous evaporation of residual ethanol (lowest $T_{b.p.}$ in series) from the film during deposition resulting in the build-up of the capillary pressure and hence rupturing of the surface [256], [257]. In the case of water, the airflow did not dry the droplet as much as in the case of alcohols with lower boiling points ($T_{b.p.}$: water 100 ºC *cf.* isopropanol 82.5 ºC and ethanol 78.37 ºC [250]) and enthalpy of vaporization ($\Delta_{vap}H^o$: water 44.0 kJ/mol *cf.* isopropanol 45 ± 3 kJ/mol and ethanol 42.3 ± 0.4kJ/mol [258]). Therefore, the large droplets were landing onto the surface, losing the individual droplet shape by merging with slurry-like TiO_2 film which dried much slower (*cf.* alcohol-based formulations) on the FTO. This hypothesised process could explain the formation of the smoother and more ordered TiO_2 films. It is noteworthy that films obtained at higher flow rate of air are smoother, implying that the growing films were more rich in water allowing more even distribution of titania particles and resulting in some minor cracking (1 µm maximum width and 30 µm maximum length) upon evaporation of the solvent from within the film.

In the case of the ultrasonic deposition using titania suspension in ethanol eth/sonic (Figure 39 m), SEM image shows the homogenous TiO_2 film covered with numerous agglomerated

particles (4 to 8 µm diameter, 30 per image). In the case of the iso/soni (Figure 39 n), the TiO_2 film was rough with agglomerated particles (4 to 24 µm diameter, 20 per image) and pronounced cracks (1 to 4 µm width, up to 86 µm long) can be observed. The mechanism of formation of such features should be similar to the case of eth/HAF (fine grain below 100 nm size). The capillary pressure increase inside the film and when sintered create some cracks in the film. Finally, the wat/soni (Figure 39 o) shows soft (fine grain below 100 nm size) but wavy-like top surface with intermingled flat-looking wave-tops punctuated by shallow and wide crack-like (1 µm width, 4 µm long) features (unlike in any other sample in these series). The morphology is due to the same effect that the wa/HAF, however, this time the saturation of the surface in solvent has been higher (more liquid concentrated on a smaller surface). So the suspension finally has formed a single layer across all surface which had been evaporated slowly.

The 3D plots show a rough layer (Ra =27.34 greyscale) for eth/soni (Figure 39 p). The cracks were observed for the iso/soni film (Figure 39 q), leading to more irregular film (Ra =28 grayscale) overall. Finally, the wa/soni (Figure 39 r) show a smoother top layer (Ra =20 greyscale) with cracks (57 µm of length and 1 µm width) quite visible on the 3D surface plot. Compared to the film deposited by doctor blading (Figure 38 a) and the commercial one (Figure 38 c), all the films made by spraying were rougher and so, potentially could present higher surface area to the electrolyte. Besides, the absence of polymer binders leads to direct intrinsic contact between the TiO_2 particles and between the particles and the liquid electrolyte.

Thus, by changing the deposition procedure, the macroscopic morphology of the TiO_2 film could be changed, which could, eventually, lead to a better tunability of the surface morphology. The cracks allow a higher surface area and provide high diffusion pathways penetrating deep inside the film which could be useful in helping the transport of the electrolyte within the film in contrast to the case of a continuous layer [259]. The solvent is an additional parameter which can be tuned to change the morphology of the film. The solvent can be changed, creating different dispersion, mist droplet size and evaporation/wetting behaviour [260], [261], which results in different deposition behaviour as discussed above. The tunability of the TiO_2 films has been realized in the order of micrometres. However, some photoelectrochemical tests are required to determine if this TiO_2 films tuning have an impact on the photoelectrode efficiency.

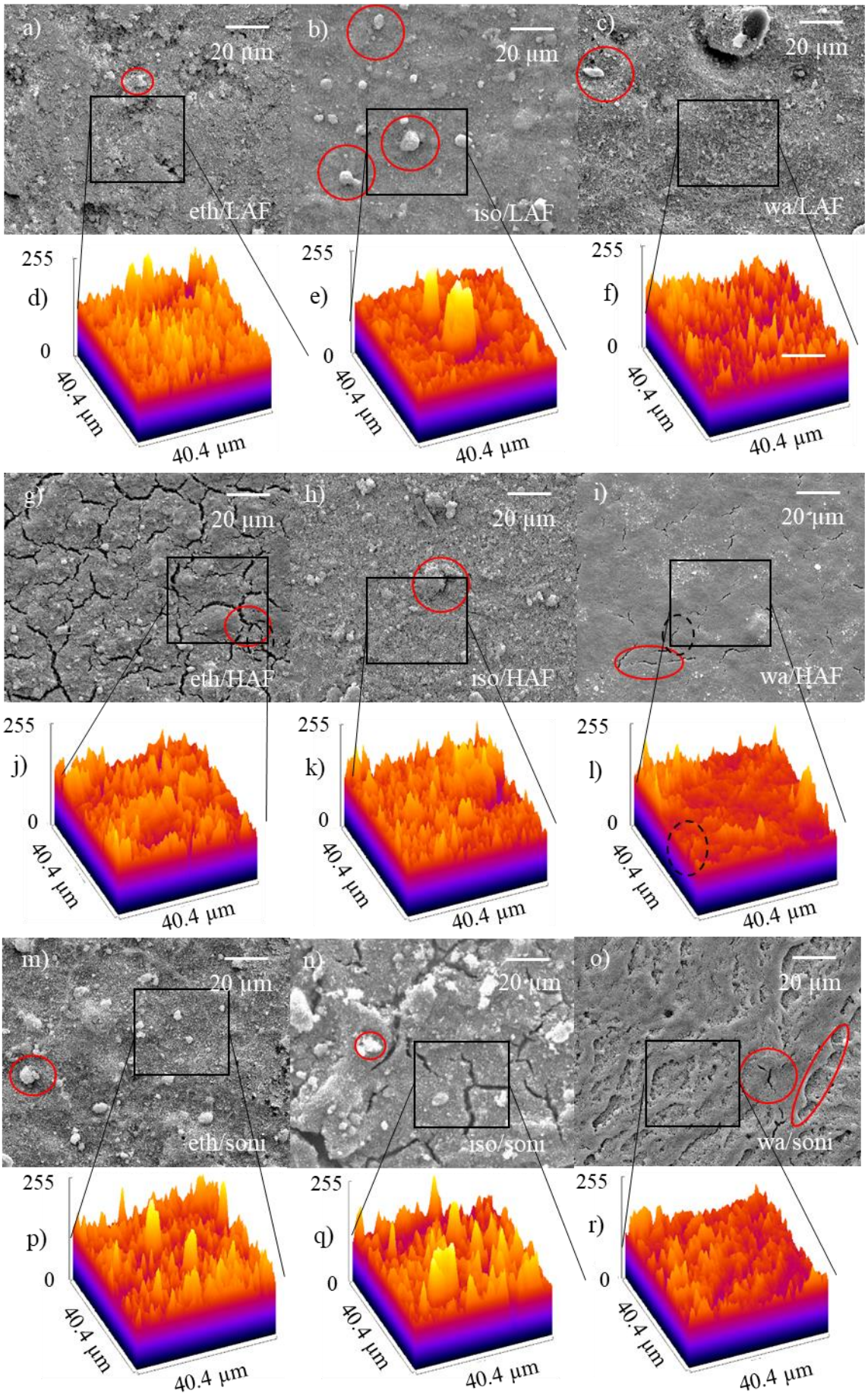
a)
20 µm
eth/LAF
b)
20 µm
iso/LAF
c)
20 µm
wa/LAF
255
d)
0
40.4 µm
40.4 µm
255
e)
0
40.4 µm
40.4 µm
255
f)
0
40.4 µm
40.4 µm
g)
20 µm
eth/HAF
h)
20 µm
iso/HAF
i)
20 µm
wa/HAF
255
j)
0
40.4 µm
40.4 µm
255
k)
0
40.4 µm
40.4 µm
255
l)
0
40.4 µm
40.4 µm
m)
20 µm
eth/soni
n)
20 µm
iso/soni
o)
20 µm
wa/soni
255
p)
0
40.4 µm
40.4 µm
255
q)
0
40.4 µm
40.4 µm
255
r)
0
40.4 µm
40.4 µm

Figure 39: SEM images x1000 magnification (scale bars of 20 µm) and surface 3D plot of the films made using TiO_2 P-25 suspensions with a concentration of 20 mg mL^{-1} dispersed in different solvents and deposited using the different deposition processes. SEM images: a) eth/LAF, b) iso/ LAF, c) wa/ LAF, g) eth/HAF, h) iso/ HAF, i) wa/ HAF.m) eth/sonic, n) iso/sonic and o) water/sonic. Surface 3D plots: d) eth/LAF, e) iso/ LAF, f) wa/ LAF, j) eth/HAF, k) iso/ HAF, l) wa/ HAF, p) eth/sonic, q) iso/sonic and r) water/sonic.

The photoelectrochemical tests have been conducted on these TiO_2 films (Figure 40). It is important to mention here that the photocurrents (Figure 40) are normalized by the weight of the titania film. Changing the morphology of the TiO_2 films affects the result of the photoelectrochemical test. Surprisingly, in the case of eth/HAF, the appearance of cracks and the increase of the roughness seems to have decreased the photocurrent. It may be due to a loose of contact with the substrate at the bottom of the film (the cracks seems to be deeper than the water-based one) however no clear conclusion could be made. For the propan-2-ol-based suspensions, the variations in the deposition process had no significant effect on the morphology of the TiO_2 films surface and the photocurrent. The water-based suspensions deposited by ultrasonic spraying show the maximum of photocurrent in the studied series: 10. ± 1 µA cm^{-2} mg^{-1}. The current is twice the one published in the literature, 5 ± 1 µA cm^{-2} mg^{-1} [49], [53], [54], but only 2 µA cm^{-2} mg^{-1} higher than that for the commercial films. Interestingly, in the case, water-based suspensions differences in film morphology between the different samples imply the importance of film structuring, with the smoothest film (wa/LAF) showing worst performance, which is in line with the literature [262]. Performance improves with the appearance of narrow cracks (wa/HAF) and reaches a maximum for the series for the highly corrugated top surface with wide and shallow crack-like features (ultrasonic spraying). In conclusion, it seems that the water solvent is a good candidate to obtain a high photocurrent, but the water must be used with care: any small change on the deposition process could lead to a drastic change of efficiency of the TiO_2 film. Propan-2-ol was the solvent which gave rise to the least variation in the surface morphology of the TiO_2 films, which correlated well with very similar photocurrents observed for all the films made using this solvent. Indeed, photocurrent of 6 ± 1 µA cm^{-2} mg^{-1} was observed for airbrush sprayed film using 1.2 m s^{-1} airflow rate, 6.1 ± 0.1 µA cm^{-2} mg^{-1} for a 3 m s^{-1} airflow deposition and finally 5.6 ± 0.3 µA cm^{-2} mg^{-1} for ultrasonic deposition (similar to the one published in the literature: 5 ± 1 µA cm^{-2} mg^{-1} [49], [53], [54])

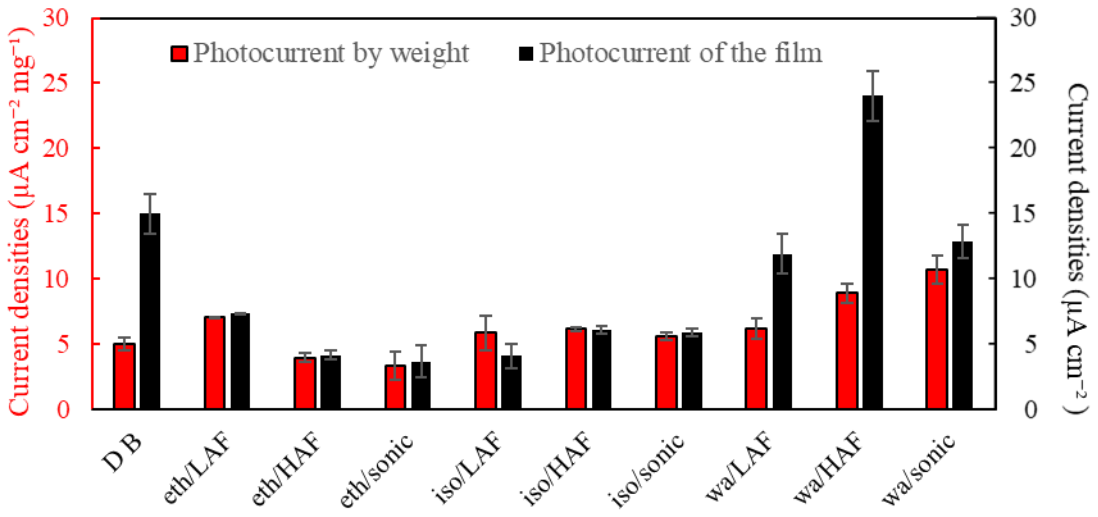

Figure 40: Summary of the photocurrents (black – total per sample, red – normalised by weight of titania) of TiO_2 films deposited by different methods and using different solvents at 0.5 V *vs.* Ag|AgCl.

The effect of the solvent on the photocatalytic activity of the TiO_2 thin films could be due to the difference in the dispersion of TiO_2 particles and different structure of the film surface and other films properties resulting at least in part due to varying rates of evaporation of solvents. Hence, it was decided to explore the effect of solvent evaporation efficiency during film deposition by using solvents with different boiling points and by changing the temperature of the hotplate.

4.3.4 Tuning by changing the molecular structures of alcohol solvent

The influence of the molecular structures of alcohol solvent in relation to evaporation conditions has been studied. The goal is to determine how the evaporation conditions (droplets size and shape and solvent evaporation speed) will affect the TiO_2 film macroscopic structure. The different solvents (alcohols) have been chosen for their availability and their broad range of structure, boiling point temperatures, surface tension and polarity (Table 6). For the deposition process, the ultrasonic spray coating was used due to better control of the deposition area. Finally, the substrate was heated at 120 °C, which is a temperature high enough to evaporate butan-1-ol – solvent with the highest boiling point within the selected solvent range. The important characteristics of the different alcohols are presented in Table 6.

Table 6: Summary of evaporation temperatures, enthalpies of evaporation, surface tensions and polarities of alcohols used in this study.

Solvent	Boiling point temperature (ºC) [250]	Enthalpy of vaporization ($kJ\ mol^{-1}$) [258]	Surface tension ($mN \cdot m^{-1}$) [250]	Polarity (water 100) [250]
Methanol	64	37.6 ± 0.5	22.6	76.2
Ethanol	78	42.3 ± 0.4	22.3	65.4
Propan-2-ol	80	45.0 ± 3	21.7	54.6
Butan-2-ol	108	48.0 ± 5	22.8	55.2
Butan-1-ol	118	52.0 ± 3	24.6	60.2

The boiling point temperature and the enthalpy of vaporization will affect the surface morphology by changing the speed of evaporation of the solvent. Indeed, a solvent with a low boiling point and a low enthalpy of evaporation will evaporate very quickly compared to a higher boiling point and low enthalpy alcohol.

The surface tension and polarity of the alcohol will affect the surface morphology by changing the drop shape when landing on the substrate. Indeed, a solvent with a low surface tension will form small droplets [263] and a low contact angle [254], [255], [260] with the substrate. Besides the high polarity of a solvent could lead, on a hydrophilic surface like FTO [263] or TiO_2 films, to a low contact angle with the substrate [264]–[266].

These four parameters could affect the deposition process at two moments. First, when the droplet is sputtered on the surface, it can start to evaporate before landing Kebarle *et al* [263] have shown that the solvent evaporation in the air reduces the volume of the droplets and leads to fission of the droplets. It will change the size of the droplets landing on the substrate, and so influence the formation of agglomerates [252] (Figure 41 a). In this case, the surface tension, the boiling point temperature and the enthalpy of vaporization are an important factor: the boiling point temperature and the enthalpy of vaporization will determine if the droplets can be evaporated in the air (probably it will occur for methanol, ethanol and propan-2-ol) [263], the surface tension will determine the size of the droplets forming at the nozzle and the one landing at the substrate [263].

Then, when the droplets land on the substrate. In the literature [254], [255], [260] it' have been shown that the droplet when landing will first spread out and form a cuvette shape before eventually come back to a half-sphere shape. However, if the evaporation speed is fast, the droplet will not have time to return to a half-sphere shape. Accumulation of nanoparticle in the edge of the droplets will occur and dried slower than the centre resulting in the slight excess accumulation of nanoparticle were the edge of the droplet were, leaving a mark behind (Figure 41 b). In this case, the four parameters are essential: the boiling point temperature and the enthalpy of vaporization will determine if the droplets evaporate fast enough to form the accumulation of particles on the substrate [254], [255], [260], the surface tension [254], [255], [260] and the polarity [264]–[266] of the alcohol will determine the size of the droplets silhouette left behind.

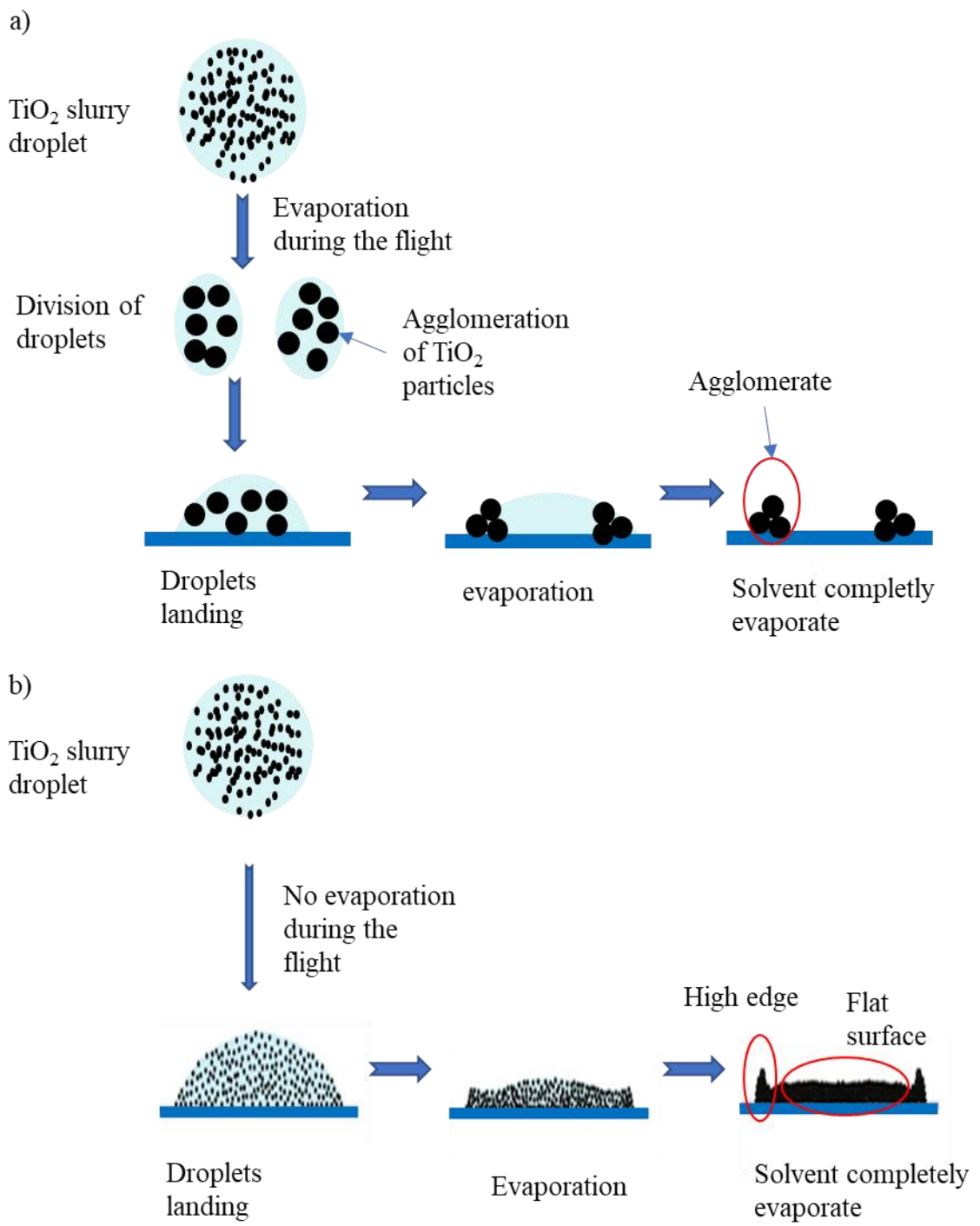

Figure 41: droplet landing and evaporation process leading to: a) the formation of TiO_2 agglomerate on the substrate , b) the formation of droplets silhouette on the substrate.

The SEM micrograph images (Figure 42) show a diversity of surface morphology of the samples in these series. The TiO_2 particles dispersed in methanol (Figure 42 a) solvent formed a TiO_2 film (~500 nm fine grain) with some agglomerated particles (1 to 3 µm of diameter, 20 agglomerate per image) and some droplet silhouettes at the surface (57 µm of diameter) formed of fine-grain below 500 nm size. Methanol has a low boiling point temperature (64 ºC for a hot plate temperature set at 120 ºC), a low enthalpy of vaporization (37.6 ± 0.5 kJ mol^{-1}), a

relatively medium surface tension (22.6 $mN \cdot m^{-1}$) but a high polarity (76.2). Therefore, according to the previous hypothesis, the droplets have been probably evaporated in air, and so the droplets have diminished in size compared to the one in the nozzle. Some droplets have a high TiO_2 particle concentration resulting in the formation of agglomerates. However, the majorities are still dispersed correctly: when the drop landed on the substrate, the solvent evaporates and form the drop silhouette observed on the SEM. In comparison, the previous experiment with different deposition process does not show that drop silhouette due to a lower temperature of the hot plate in case of ethanol and propan-2-ol leading to much slower

The SEM image of the sample obtained with ethanol (Figure 42 b) shows a homogenous film with agglomerated particles (1 µm of diameter, 20 agglomerate per image). A silhouette of the droplet shape is visible on the surface (calculated diameter of the droplet silhouette of 52 µm for the largest, 8 µm for the smallest). Propan-2-ol-based film (Figure 42 c) has a similar morphology. However, a qualitative comparison of the size of droplet silhouette shows that these are larger in the case of propan-2-ol as a solvent: 61.25 µm for the propan-2-ol > 57 µm for methanol > 51.8 µm and 23.8 µm for the ethanol. However, based on the surface tension values shown in Table 6, it could be inferred that the mist of small droplets was formed in the case of propan-2-ol due to its lower surface tension: propan-2-ol 21.7 $mN \cdot m^{-1}$ < ethanol 22.3 $mN \cdot m^{-1}$ < methanol 22.6 $mN \cdot m^{-1}$. However as the boiling point temperature and the enthalpy of vaporization are higher than methanol and ethanol (T_{bp} propan-2-ol: 80 ºC > T_{bp} ethanol: 78 ºC > T_{bp} methanol: 64 ºC , $\Delta_{vap}H^o$ propan-2-ol: 45.0 ± 3 kJ mol^{-1} > $\Delta_{vap}H^o$ ethanol: 42.3 ± 0.4 kJ mol^{-1} > $\Delta_{vap}H^o$ methanol: 37.6 ± 0.5 kJ mol^{-1}) the droplets will be less evaporate in the air, and the size of the droplets will stay bigger than the methanol and ethanol one.

The 3D plot confirm the previous observation for the sample made using methanol (Figure 42 d): a droplet silhouette with a rough surface (Ra =22 greyscale). Compared to an ethanol-based film (Figure 42 e), methanol-based one as a higher roughness (Ra =17 greyscale for ethanol < Ra = 22 greyscale for methanol). However, the sample made using propan-2-ol as a solvent (Figure 42 f) shows a rougher film than the two previous ones (Ra =24 greyscale).

The surface tension of the solvent explains the fact that samples made using ethanol as a solvent have the smallest droplet silhouettes amoung theseries studied here. The methanol due to its highest surface tension should form bigger droplets in air and on the substrate. However, due to its lower evaporation boiling point temperature and the enthalpy of vaporization, it should

have an inverse effect than propan-2-ol and splitting the large drop into smaller one. However, methanol has a high polarity (methanol 76.2 > ethanol 65.4 > propan-2-ol 54.6). As seen previously, the FTO and TiO_2 film are hydrophilic (formed a low contact angle with polar solvents), so the drops when landing on the substrate will spread on the surface and formed a large cuvette shape in comparison of its size droplets [264]–[266].

In comparison, the previous experiment with different deposition process does not show that drop silhouette. It is due to a lower temperature of the hot plate in case of ethanol and propan-2-ol (90 ºC for the previous experiment against 120 ºC for this experiment) leading to much slower evaporation and the formation of agglomerate on the surface (Figure 39 a, b, g, h, m, and n), and some cracks (Figure 39 g and n). For the water, the hydrophilic of the FTO and TiO_2 film leads to the formation of a liquid thin film which has been evaporated slowly forming a smooth surface (Figure 39 c, i, and o).

The butan-2-ol film (Figure 42 g) shows surface morphology composed of large droplet silhouettes (diameter: 66 µm) and some holes (diameter: 38-10 µm) on an otherwise flat surface (fine grain size of less than 100 nm). The butan-2-ol has similar polarity value than propan-2-ol (propan-2-ol 54.6, butan-2-ol 55.2) with higher surface tension (24.6 $mN \cdot m^{-1}$) than all the previous alcohol tested. Its boiling point temperature (T_{bp} butan-2-ol: 108 ºC , $\Delta_{vap}H^o$ butan-2-ol: 48.0 ± 5 kJ mol^{-1}) and its enthalpy of vaporization ($\Delta_{vap}H^o$ butan-2-ol: 48.0 ± 5 kJ mol^{-1}) are too high to affect the size of the droplets in the air so it's resulting in a big droplet size which land on the substrate create a large cuvette shape and dried.

The creation of the hole could be explained by shrinkage of the film during the annealing step due to remaining solvents on the surface: Golobostanfard *et al* [267] show some similar shape for a mixed solvent of propan-2-ol and propan-1-ol solvent (even if in their publication the crystallisation of the TiO_2 particle happens in the same time that their deposition process).

Finally, the butan-1-ol (Figure 42 h) TiO_2 film shows a similar shape that butan-2-ol: larger droplet silhouette (72 µm diameter) and some massive cracks (3 -10 µm width, length > 100 µm). The butan-1-ol has a higher polarity value than butan-2-ol (butan-1-ol 60.2, butan-2-ol 55.2) with the highest surface tension (22.8 $mN \cdot m^{-1}$). Its boiling point temperature (T_{bp} butan-2-ol: 118 ºC) and its enthalpy of vaporization ($\Delta_{vap}H^o$ butan-2-ol: 52.0 ± 3 kJ mol^{-1}) are the highest of the series. The butan-1-ol will formed the larger droplets of the alcohol series (larger drop silhouette). The increase of saturation in solvents of the film (higher boiling point means

a longer time of evaporation, so higher amount of solvent in the film [268]) leading to a high capillary pressure which in turn leads to the formation of cracks

Butan-2-ol-based films (**Erreur ! Source du renvoi introuvable.** i) do not show a flat surface without agglomerate (Ra =10 greyscale). The holes are clearly visible in 3D plots: they have significant depth (81 greyscale) and an elevation of the edge probably due to the shrinking of the film. Butan-1-ol-based film (Figure 42 j) shows a smooth surface (Ra =12 greyscale) with the presence of the drop silhouette and deep cracks which seems to be lifted on their edges.

The photoelectrochemical tests have been conducted on deposited TiO_2 films deposited using different alcohols (Figure 43). Changing the alcohol molecular structure, affected the morphology of the TiO_2 film, which in turn should affect the photocurrent of the photoanode. The photocurrent by weight decreased in the following order: methanol (6.2 ± 0.7 µA cm^{-2} mg^{-1}) < propan-2-ol (5.6 ± 0.3 µA cm^{-2} mg^{-1}) < ethanol (4 ± 1 µA cm^{-2} mg^{-1}) < butan-2-ol (3.5 ± 0.3 µA cm^{-2} mg^{-1}) < butan-1-ol (3.1 ± 0.4 µA cm^{-2} mg^{-1}). The value for methanol propan-1 ol , propan2-ol and ethanol stays very close to the one reported in the literature (5 ± 1 µA cm^{-2} mg^{-1}) [49], [53], [54] and in the order of the commercial films (8.3 ± 0.2 µA cm^{-2} mg^{-1}). Except for ethanol, the photocurrent by weight decreased when the boiling point temperature increased (consistent with the decrease in the overall roughness (Ra) of the film with an increase of the boiling point temperature). The lower photocurrent by weight of ethanol could be linked to the small number of agglomerates at the surface. The diminution of the film surface presented to the bulk electrolyte can explain the decrease of photocurrent with the increase of solvent evaporating temperature. However, the cracks, which should help the electrolyte to circulate better into the film, were not beneficial in the case of butan-2-ol: the shrinking of the film during the creation of the crack could lead to a loss of contact between the TiO_2 particles and the FTO film around these cracks [269].

In conclusion, the best solvents for a maximum photocurrent was methanol and propan-2-ol due to their low boiling point temperature (films with the roughest surface). Hence, the example of butan-2-ol has shown the importance of proper contact between the substrate and the film. One way to improve the contact between the FTO and the TiO_2 film is to use a TiO_2 precursor instead of using an already formed powder. The precursor will form TiO_2 directly on the substrate surface and will establish better contacts between pre-formed TiO_2 particles within the film and with the FTO substrate [270].

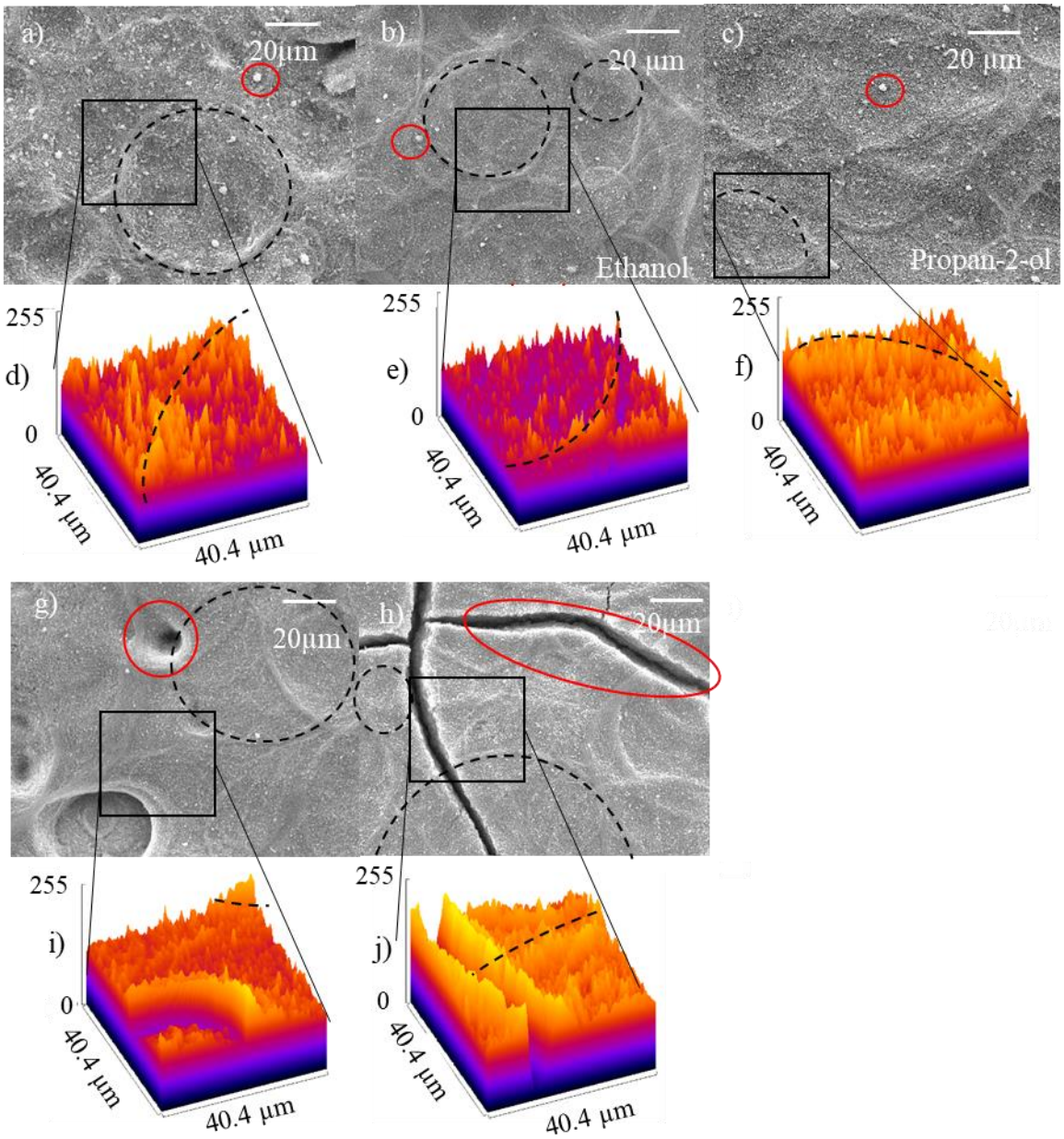

Figure 42: SEM images x1000 magnification (scale bars of 20 µm) of TiO_2 films prepared by ultrasonic spray deposition at 120 ºC with different solvents: a) methanol, b) ethanol, c) propan-2-ol, g) butan-2-ol and, h) butan-1-ol. Corresponding 3D surface plots: d) methanol, e) ethanol, f) propan-2-ol, i) butan-2-ol and, j) butan-1-ol.

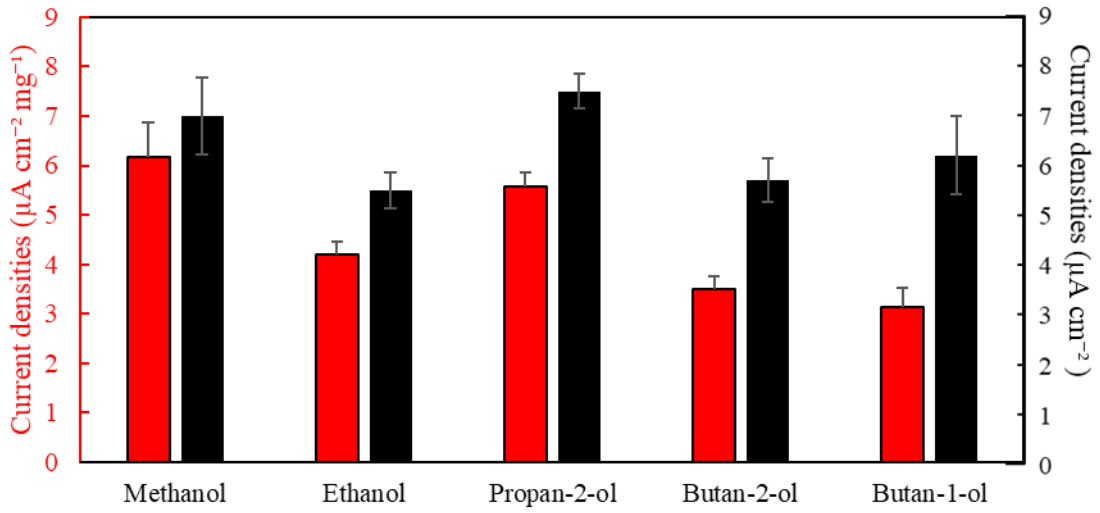

Figure 43: Photocurrent (black – total per sample, red – normalised by weight of titania) of TiO_2 films deposited with different alcohol solvent at 0.5 V *vs*. Ag|AgCl.

4.3.5 Tuning by addition of titanium isopropoxide

To provide better contact between the substrate, growing a TiO_2 film from a titania precursor could be a solution [270].

The titanium tetra-isopropoxide (TTIP) has been used in literature to produce TiO_2 powder [271]–[274] and TiO_2 films [270]. The titanium isopropoxide reacts with water to form TiO_2 and propan-2-ol:

$$Ti(OCH(CH_3)_2)_4(l) + 2\ H_2O \rightarrow TiO_2(s) + 4\ (CH_3)_2CHOH\ (l) \qquad (24)$$

A mixture between the TTIP and P-25 in propan-2-ol as a solvent should form a TiO_2 film upon exposure to ambient water from air (according to the reaction equation 24) comparable to the previous films studied here, but with better connection with the substrate and between particles.

PXRD diffractograms (Figure 44) have been obtained for pure P-25 and for films made using a mixture of the TTIP and the P-25 in propan-2-ol. The TiO_2 formed by hydrolysing TTIP during film growth and subsequent heat treatment of the films has an anatase crystalline structure. Indeed, the intensity of the peaks corresponding to anatase is higher in the presence of TTIP than with only P-25.

Surface analysis on TiO_2 films deposited by ultrasonic airbrush at 90 °C hotplate temperature with a propan-2-ol as a solvent with different amounts of P-25 and TTIP was carried out using SEM micrographs (Figure 45). The images of the film made using titanium isopropoxide alone (0% P-25 / 100% TTIP) (Figure 45 a) film shows an interesting macrostructure: the film was composed of independent flakes or TiO_2 islands (3600 μm^2 and below in area, with flakes separated by 20 to 40 µm, 4 per image). This morphology is typical of titania films grown *via* titanium isopropoxide hydrolysis [156], [275].

The flakes could be formed due to a Volmer–Weber growth [269]. It occurs when the smallest stable TiO_2 clusters (*i.e.* small particles) nucleate on the FTO surface and then grow in three dimensions. It happens because the newly formed TiO_2 building blocks have a higher affinity to the existing TiO_2 nuclei than to the FTO substrate [269]. Besides, the large gap between the flakes could be due to tensile stress from the capillary pressure of solvent evaporation and film densification before the step of crystallization of the amorphous film [268] during the sintering of the film at 450 ºC. Unfortunately, the film was not mechanically stable and often disintegrated when it was placed in contact with the electrolyte.

The film made using 5 % of P-25 and 95% TTIP mixture (Figure 45 b) shows (similar flake sizes, spaces between them and flake numbers per image as for the film made using pure TTIP. The mechanical stability was similarly unsatisfactory as in the case of the film made using pure TTIP.

The use of 15% P-25 and 85% TTIP mixture (Figure 45 c) increased the mechanical stability of the TiO_2 film. The size of the flakes diminished (1800 μm^2) their number increased to 5 per image, and the space between them stayed constant.

The 3D plot of the film made using pure TTIP (Figure 45 d) shows a high and homogenous layer representing the top surface of the flake then a cliff representing the side of the flakes, and in the bottom another very smooth layer of FTO. Similar structural motifs were even more pronounced in the 3D plot of the samples made using 5% P-25 and 95% TTIP (Figure 45 e) and 15% P-25 with 85% TTIP (Figure 45 f).

The films made using 25% P-25 and 75% TTIP films (Figure 45 g) show a diminution of the size of the flakes (1700 μm^2), an increase of their numbers (10 per image), and a diminution of the gaps between them (20 µm in average). An increase in the percentage of P-25 powder seems

to decrease the size of the flakes and the gap. It could be due to an increase of the nucleation site with more TiO_2 P-25 particle creating crystallization point. However, as the TTIP hydrolyse and crystallization is not perfectly homogenous, the Sem image could represent a specific region which has more island than the previous SEM picture.

The samples made using 50% P-25 and 50% TTIP mixture (Figure 45 h) show usual flakes (1700 μm^2, 8 per image, 20 µm between the flakes) and a large number (>100) of particles on the FTO between the flakes. The film made using 65% P-25 and 35% TTIP mixture (Figure 45 i) shows a notable shift in the morphology: the flake surface morphology has been changed to a fine grain film (sub-100 nm) like in the case of the film obtained using pure P-25 (Figure 45 u). There is still deep cracks and a separation between the flakes, but it has significantly decreased (5 to 10 µm). The surface looks more like the film perforated with cracks, rather than a collection of flakes as in the case of lower P-25 loadings. Such-morphology have been observed previously in the case of film eth/HAF (Figure 39 g). or deposited with butan-1-ol solvent and P-25 powder (Figure 42 i).

The 3D plot of the surface of the film made using 25% of P-25 and 75% TTIP mixture (Figure 45 j) shows a similar cliff as in the case of the previous film (Figure 45 f). However, its boundaries are lifted compared to the surface of the flakes. This could be due to the shrinking of the flake during heat treatment [268]. The surface plot of the film made using 50 % P-25 and 50 % TTIP mixture (Figure 45 k), and that of the sample made using 65% P-25 and 35% TTIP mixture (Figure 45 l) show the same phenomenon – lifted up edges of the flakes. Moreover, these surface plots confirm the decrease in the distance between the flakes.

The film made using 75% of P-25 and 25% TTIP mixture (Figure 45 m) shows similar morphology to that of the sample made using 65 % P-25 and 35% TTIP mixture (Figure 45 i) - fine grains are now better visible at the top surface of the densely packed flakes (or a film perforated with numerous cracks). Grains appear to be coarser in the case of (Figure 45 i) However, they were more grouped: the distance between them decreases (3 to 10 µm, with some at only 1 µm). For the film made using 80 % P-25 and 20% TTIP mixture (Figure 45 n), the TiO_2 film shows a morphology close of the pure P-25 morphology obtained earlier. In essence, the flakes are not separated anymore and merge on a continuous film perforated by cracks. The separation was transformed in cracks of maximum 4 µm width (12 per image). Besides, small agglomerates (up to 1 µm in diameter) now occur at the top surface. The sample made using 85% P-25 and 15% TTIP mixture (Figure 45 o) shows smoother top surface

morphology without pronounced aggregates protruding above the surface as in the previous case (Figure 45 n). There are only a few wide cracks with film visibly peeling off FTO around these cracks (which previously was deemed to reduce photocatalytic performance –TiO_2 film made with butan-1-ol solvent and P-25 powder, p 116) and a significant number of small cracks perforating the flat areas of the film. As was suggested earlier, such cracks could facilitate diffusion of the electrolyte through the bulk of the film. To summarize, there are two categories of cracks in this film which can be grouped by their size: micrometre scale cracks (1 to 10 µm wide) and nanometre-scale cracks (sub-500 nm wide). Importantly, the overall number of the cracks significantly increased (> 100 per image) in comparison with the samples discussed above.

As explained previously, the increases in capillary pressure within the film could lead to the formation of the cracks. However, like shown in literature Henkel *et al* [276] another phenomenon could be responsible for the nanoscale cracks: after the sintering treatment, the TiO_2 thin film is cooled down and the TiO_2 particles of different crystallographic phase contract differently (P-25 particles 85 wt% rutile $\alpha_a = 7.0 \times 10^{-6}\ K^{-1}$ [277] 15 wt% anatase crystals $\alpha_a = 4.4 \times 10^{-6}\ K^{-1}$ [277], in the addition of the anatase crystals formed *via* hydrolysis of TTIP followed by crystallization $\alpha_a = 4.4 \times 10^{-6}\ K^{-1}$ [277]). The compressive stress is gradually removed, and the cooled down TiO_2 thin film is under tensile stress creating the nanocracks into the film.
However, it is hard to explain why this phenomenon would manifest itself only in the case of the film made using 85% P-25 and 15% TTIP mixture, while samples with 5% less or more of the P-25 do not show so many nano-cracks despite having very close precursor mixture compositions.

The 3D surface plot of the sample made using 75% P-25 and 25% TTIP mixture showed a continuous film with cracks (Figure 45 p). For the sample made using 80% P-25 and 20% TTIP mixture (Figure 45 q), the presence of cracks (area with small cracks within the square area sampled) was more pronounced in SEM image, but less visible on the surface plot. Finally, the 3D surface plot of the sample made using 85% P-25 and 15% TTIP mixture (Figure 45 r) shows a homogenous film (in the area sampled, with no obvious large cracks) with a lot of small nano-cracks clearly visible in SEM image, but hardly discernible in the 3-D plot.

The film made using 90% P-25 and 10% TTIP mixture (Figure 45 s) shows cracks. However, their size is larger, and their number much lower than in the case of the film made using 85%

P-25 and 15% TTIP mixture. Besides, the droplet silhouette (42.8 µm diameter) and depression (17 to 40 µm diameter) can be observed. The formation mechanism of droplet silhouette and depression surface features has been explained previously. The film made using 95% P-25 and 5% TTIP mixture (Figure 45 t) shows a similar surface morphology to the film made using only pure TiO_2 P-25 (100% P-25 and 0% TTIP) (Figure 45 u). However, the agglomerates of TiO_2 protruding above the surface were bigger (1 to 4 µm). The 3D plot confirms the droplet silhouette on top of the TiO_2 film made using 90% P-25 and 10% TTIP mixture (Figure 45 v) as well as in the case of the pure P-25 film (100% P-25 and 0% TTIP) (Figure 45 x). The film made using 95% P-25 and 5% TTIP mixture shows a moderate rough homogenous film (Figure 45 w).

In conclusion, it is evident that increase the percentage of P-25 in the precursor mixture affects the morphology of the film drastically. Due to the crystallization reaction, the film made with high TTIP content in the precursor mixture will form well-separated islands or flakes of titania. However, when the percentage of P-25 reached 65%, the titania made *via* hydrolysis of TTIP acts as a binder and not as the main component of the matrix anymore, and a cracked film morphology appears. These cracks diminish in size but increase in number when more P-25 where added. Numerous nano-cracks and just a few remaining macro-cracks are observed for the sample made using 85% P-25 and 15% TTIP precursor mixture. Finally, after 90% of P-25, a film with very few cracks is formed, and the agglomerated titania particles protruding above the surface could be observed. The TTIP percentage is so low that the cracks could only be due to the vigorous evaporation of the isopropanol solvent, and as discussed in the previous section (p. 106), this solvent has a too low boiling point temperature for creating a large number of cracks.

The photocurrents obtained as a function of the composition of the film precursor mixture and hence resulting film structure (Figure 46) were plotted on the same graph. It shows a stagnation of photocurrent normalised by TiO_2 weight when P-25 were added to TTIP (from 5% to 50%), until a composition of 75% of P-25 is reached. Then, the value increases until a maximum photocurrent normalised by weight of 11.2 ± 0.6 µA cm^{-2} mg^{-1} for the composition of the film precursor mixture of 85% of TiO_2 P-25 and 15% TTIP. This is more than twice the value of 5 ± 1 µA cm^{-2} mg^{-1} for titania films reported in the literature [49], [53], [54] and still higher than 8.3 ± 0.2 µA cm^{-2} mg^{-1} obtained using for commercial films in this study. The 5% of TiO_2 P-25 and 15% TTIP sample also demonstrated the highest total current without normalisation by

weight. Finally, the photocurrent by weight decreases when more than 85% of TiO_2 P-25 was added to TTIP until reaching 5 ± 1 µA cm^{-2} mg^{-1} for a pure P-25.

The best composition to obtain a high total photocurrent and photocurrent normalised by TiO_2 weight was 85% of TiO_2 P-25 and 15% of TiO_2 from TTIP. It formed a layer with many small nano-cracks which likely facilitated diffusion of the electrolyte through the bulk of the porous film without loss of a good interconnection between the TiO_2 particles. Importantly, the titania obtained *via* hydrolysis of TTIP could form a connection between the particles of TiO_2 at the bottom of the porous titania film and the FTO substrate allowing better transmission of the electrons to the external circuit. Absence of a large number of wider cracks with titania film peeling of the FTO substrate around such cracks in this sample also indirectly confirms the importance of a good connection of the titania layer to FTO.

By adding the optimal quantity of TTIP, the morphology of TiO_2 films have been successfully optimised, and the photocurrent has been improved. However, the catalyst design and fabrication could be investigated further: instead of using a single process to deposit all the TiO_2 film in one step, a compact and well connected to the FTO substrate thin TiO_2 underlayer could be made first using the appropriate method and the bulk of the porous titania film could be deposited on the top using an optimised 85% P-25 and 15% TTIP film precursor mixture. This approach could allow improvement in the connection between the porous titania film and the FTO substrate while maintaining an optimal morphology of the titania film, allowing the facile diffusion of the electrolyte.

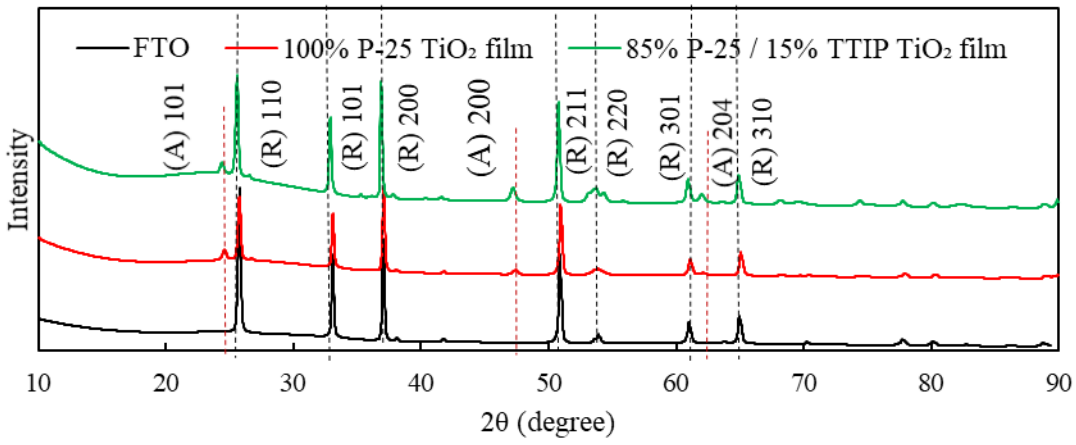

Figure 44: X-ray diffractograms (with K-beta filter edge and background removed) of: FTO (black line)., TiO_2 film with 100% P-25 (red line) and TiO_2 film made using 85% P-25 and 15% TTIP solution (green line).

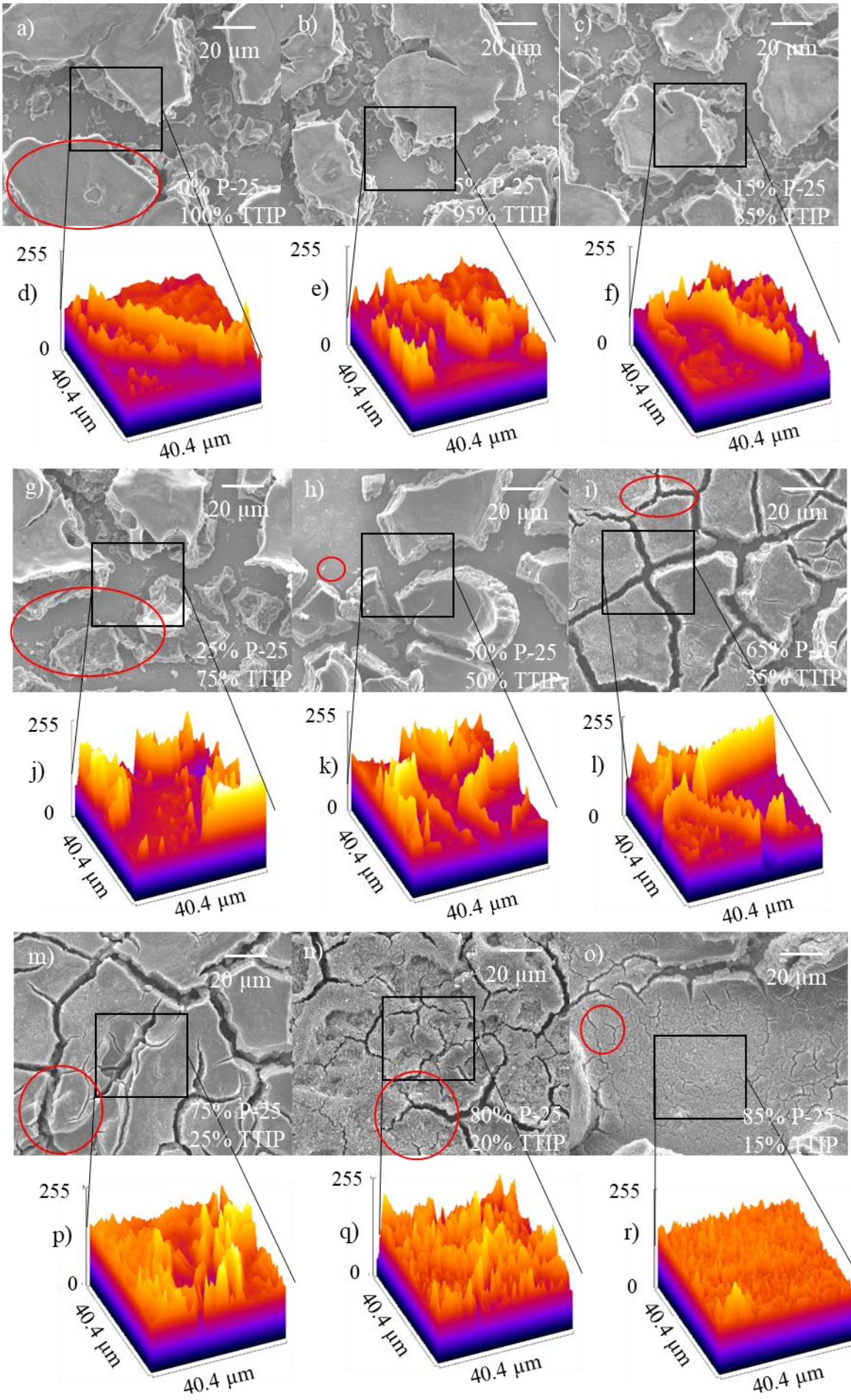
a)
20 µm
0% P-25
100% TTIP
b)
20 µm
5% P-25
95% TTIP
c)
20 µm
15% P-25
85% TTIP
255
d)
0
40.4 µm
40.4 µm
255
e)
0
40.4 µm
40.4 µm
255
f)
0
40.4 µm
40.4 µm
g)
20 µm
25% P-25
75% TTIP
h)
20 µm
50% P-25
50% TTIP
i)
20 µm
65% P-25
35% TTIP
255
j)
0
40.4 µm
40.4 µm
255
k)
0
40.4 µm
40.4 µm
255
l)
0
40.4 µm
40.4 µm
m)
20 µm
75% P-25
25% TTIP
n)
20 µm
80% P-25
20% TTIP
o)
20 µm
85% P-25
15% TTIP
255
p)
0
40.4 µm
40.4 µm
255
q)
0
40.4 µm
40.4 µm
255
r)
0
40.4 µm
40.4 µm

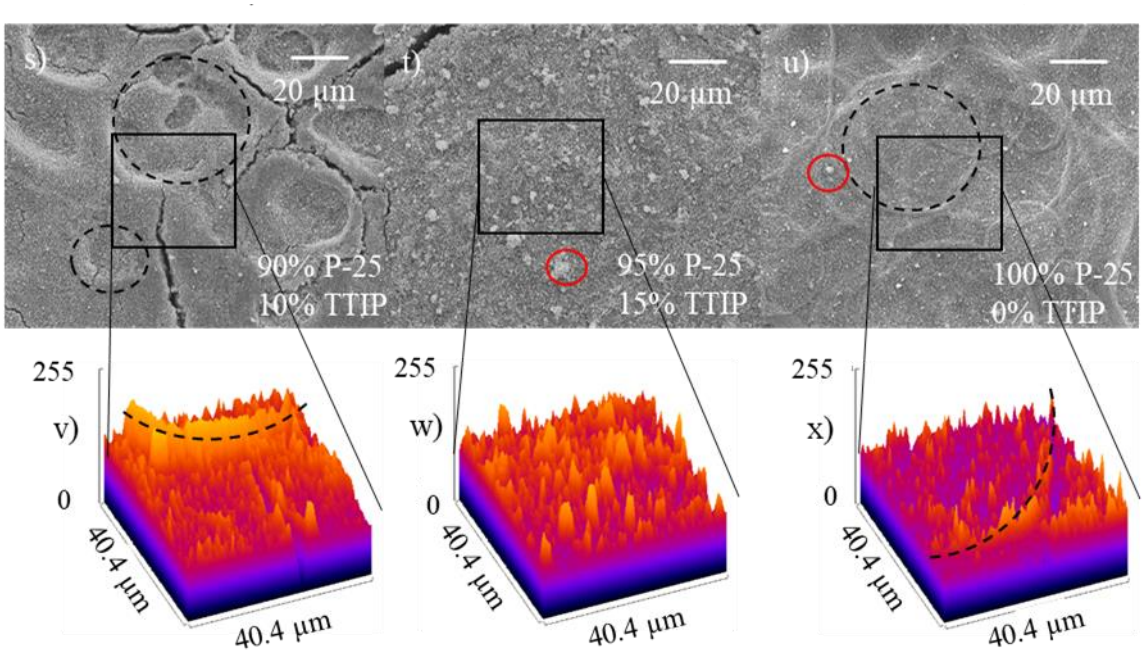

Figure 45: SEM images x1000 magnification (scale bars of 20 µm) of TiO_2 films prepared by spraying mixtures of TiO_2 P-25 nanoparticles and TTIP with different loading percentages: a) 0% P-25 100% TTIP, b) 5% P-25 95% TTIP, c) 15% P-25 85% TTIP, g) 25% P-25 75% TTIP, h) 50% P-25 50% TTIP, i) 65% P-25 35% TTIP, m) 75% P-25 25% TTIP, n) 80% P-25 20% TTIP, o) 85% P-25 15% TTIP, s) 90% P-25 10% TTIP, t) 95% P-25 5% TTIP, u) 100% P-25 0% TTIP. And corresponding 3D surface plots: d) 0% P-25 100% TTIP, e) 5% P-25 95% TTIP, f) 15% P-25 85% TTIP, j) 25% P-25 75% TTIP, k) 50% P-25 50% TTIP, l) 65% P-25 35% TTIP, p) 75% P-25 25% TTIP, q) 80% P-25 20% TTIP, r) 85% P-25 15% TTIP, u) 90% P-25 10% TTIP, v) 95% P-25 5% TTIP, w) 100% P-25 0% TTIP.

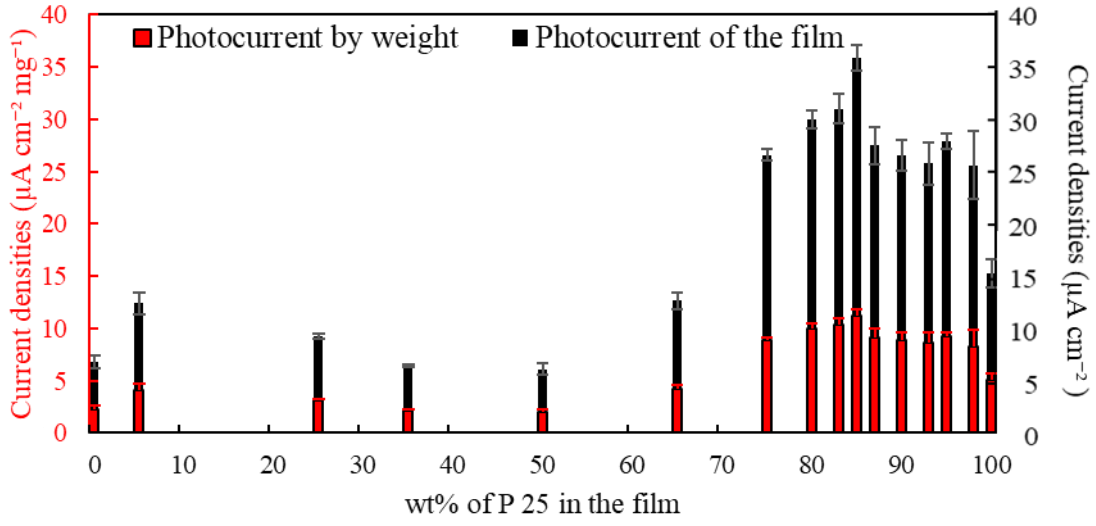

Figure 46: Photocurrents (black – total per sample, red – normalised by weight of titania) of TiO_2 films made using film precursor mixtures of different compositions (X-axis) at 0.5 V *vs*. Ag|AgCl.

4.3.6 Addition of an underlayer

Several underlayers have been deposited onto the FTO before spraying a porous titania layer by ultrasonic spray using the previously optimised 85% P-25 15% TTIP precursor solution with an aim to improve the connection between TiO_2 film and FTO substrate. In the literature [278], pre-treatment of FTO by an aqueous solution of $TiCl_4$ has been tested to increase the connection between the substrate and the film. Following this idea, three so-called underlayers (thin TiO_2 layer between the FTO substrate and the main porous titania film) were tested.

First, an FTO glass has been dipped in $TiCl_4$ aqueous solution (30 min in 40 mM $TiCl_4$ aqueous solution maintained at 70 ºC) following procedures reported in the literature [239], [240], [278]. Compared to a not treated FTO substrate (Figure 47 a) The SEM images of the $TiCl_4$ under layer (Figure 47 b) have shown that the underlayer is composed of spherical titania particles (*ca*. 100 to 200 nm diameter) spread other the FTO surface with the minimal interconnection between the particles (Figure 47 b). The 3D plot (Figure 47 c) confirms the presence of independent particles (independent peaks on the surface). The roughness was not calculated due to the presence of FTO underlayer and TiO_2 in the same image, which can lead to a misinterpretation. Based on size and surface coverage/density of the titania particles, the loading of TiO_2 on FTO has been estimated at 0.001 mg cm^{-2}.

The second TiO_2 underlayer was a deposited by evaporation-induced self-assembly (EISA) by our collaborators (Paula C. Angelomé , Gerencia Química & Instituto de Nanociencia y Nanotecnología, Centro Atómico Constituyentes,CNEA-CONICET, Buenos Aires, Argentina). SEM imaging was carried out using a Carl-Zeiss SUPRA 40 microscope. The FTO wafers were cut in small pieces (around 0.5 ✕ 0.5 cm^2) and attached to the sample holder with conductive carbon tape. The SEM images of the surface of the sample indicate that an ordered array of mesopores is present, as expected. The pores are interconnected on the surface, forming slits, due to the contraction and crystallization of titania walls occurring during the thermal treatment (Figure 47 d). Pore ordering was confirmed by means of Small Angle X-ray Scattering using a Xenocs - Xeuss 2.0 instrument operating in transmission mode. Samples were fixed onto a coverslip to allow the measurements. The sample-detector distance (determined using silver behenate as standard) was 1192.13 cm. The SAXS pattern indicates that the array is compatible to the one expected: *Fm3m* face-centred cubic array of pores oriented with the [111] plane parallel to the substrate, contracted in this direction [279], [280]. X-ray reflectometry (XRR) studies from raw small-angle X-ray scattering (SAXS, Figure 48)

allowed determination of the film thickness and porosity. Measurements were performed on a Panalytical Empyrean X-ray diffractometer with an incident beam of Cu Kα radiation at 1.54 Å, and an incident angle of 1°. A divergence slit of 0.38 mm and a mask of 10 mm were used for the measurements. Electronic density was obtained from the critical angle, and film thickness was determined from the Kiessig fringes in the reflectogram. Film porosity was estimated by measuring the shift in the critical angle when the relative humidity was changed from <5% (*i.e*. the pores are full of air) to >90% (*i.e*. the pores are filled with water). More details about these calculations can be found elsewhere [281], [282]. The films treated at 450 ºC were 112 nm thick, with a porosity of 56%. The critical angle of the film measured at low RH was 0.18º. From this data, a TiO_2 loading of 0.019 ± 0.002 mg cm^{-2} can be estimated [283], [284]. The 3D plot of the surface shows a homogenous and well-ordered film (Figure 47 f).

Finally, the hydrothermal film (realized by Sam Nesbitt, chemical and process engineering department, university of Canterbury, Christchurch , New Zealand) have been made using a mixture of 11 mL toluene, 1.0 mL concentrated HCl and 1.0 mL of titanium isopropoxide during 2 hrs 20 mins hydrothermal treatment at 180 °C in Teflon-lined stainless steel pressure vessel had a TiO_2 loading of 0.2 mg cm^{-2}. The idea was to crystalize a titania film under controlled conditions with a controlled water content [285].
The SEM images (Figure 47 e) have shown a dense carpet composed of crystallite-like structures (*ca*. 0.1 μm^2 each) interconnected together completely covering FTO substrate. The films are well ordered and uniform. The 3D plot (Figure 47 g) of the surface shows a homogenous and well-ordered film with notable roughness (Ra = 19.7 greyscale).

The underlayers tested by themselves were very photoactive except for the one made using $TiCl_4$ (Figure 49): 5 ± 1 µA cm^2 mg^{-1} for $TiCl_4$, 110 ± 0.5 µA cm^2 mg^{-1} for mesoporous film, and 360 ± 8 µA cm^2 mg^{-1} for a hydrothermal film. Hydrothermal and mesoporous films were dense and very well connected to the FTO substrate, which explains the high photocurrent by weight compared to the $TiCl_4$ film. The mesoporous film was porous (56% porosity) with a high active surface area available for V^{4+} oxidation. However, the hydrothermal film has a better photocurrent by weight with a thicker film. The underlayer may have some porosity, but it also appears as a much more some crystalline structure grown directly on FTO. However, it is challenging to grow a thick film using this approach. That is the reason for the investigation of the use of such films as an underlayer.

An optimised porous titania film was deposit has been deposited top of the underlayer. With the $TiCl_4$ underlayer, the total photocurrent per sample and normalised by weight (Figure 49) of were similar to the optimised porous titania film (12 ± 0.5 µA cm^2 mg^{-1} with $TiCl_4$ and 11.5 ± 0.5 µA cm^2 mg^{-1} without $TiCl_4$).

However, the used of the mesoporous underlayer shown a large increase of the photocurrent per sample and normalised by weight (Figure 49): 25 ± 0.5 µA cm^2 mg^{-1} with mesoporous underlayer for 11.5 ± 0.5 µA cm^2 mg^{-1} without.

The use of the hydrothermal under layer shown an even larger increase of the photocurrent per sample and normalised by weight (Figure 49): 105 ± 3 µA cm^2 mg^{-1} with hydrothermal underlayer for 11.5 ± 0.5 µA cm^2 mg^{-1} without. However, The hydrothermally grown underlayer shown a unique trend: the photocurrent per sample and by weight (Figure 49) is diminished with the addition of the optimised film (79 ± 2 µA cm^2 underlayer alone against 47 ± 3 µA cm^2 with the 85% P-25 and 15% TTIP based film). This observation suggests that the hydrothermal growth of a TiO_2 film is sufficient by itself to obtain a photoactive film even with a low titania loading of 0.2 mg cm^{-2}. Thus, the hydrothermally grown film is the best material within samples studied here, showing high photoactivity.

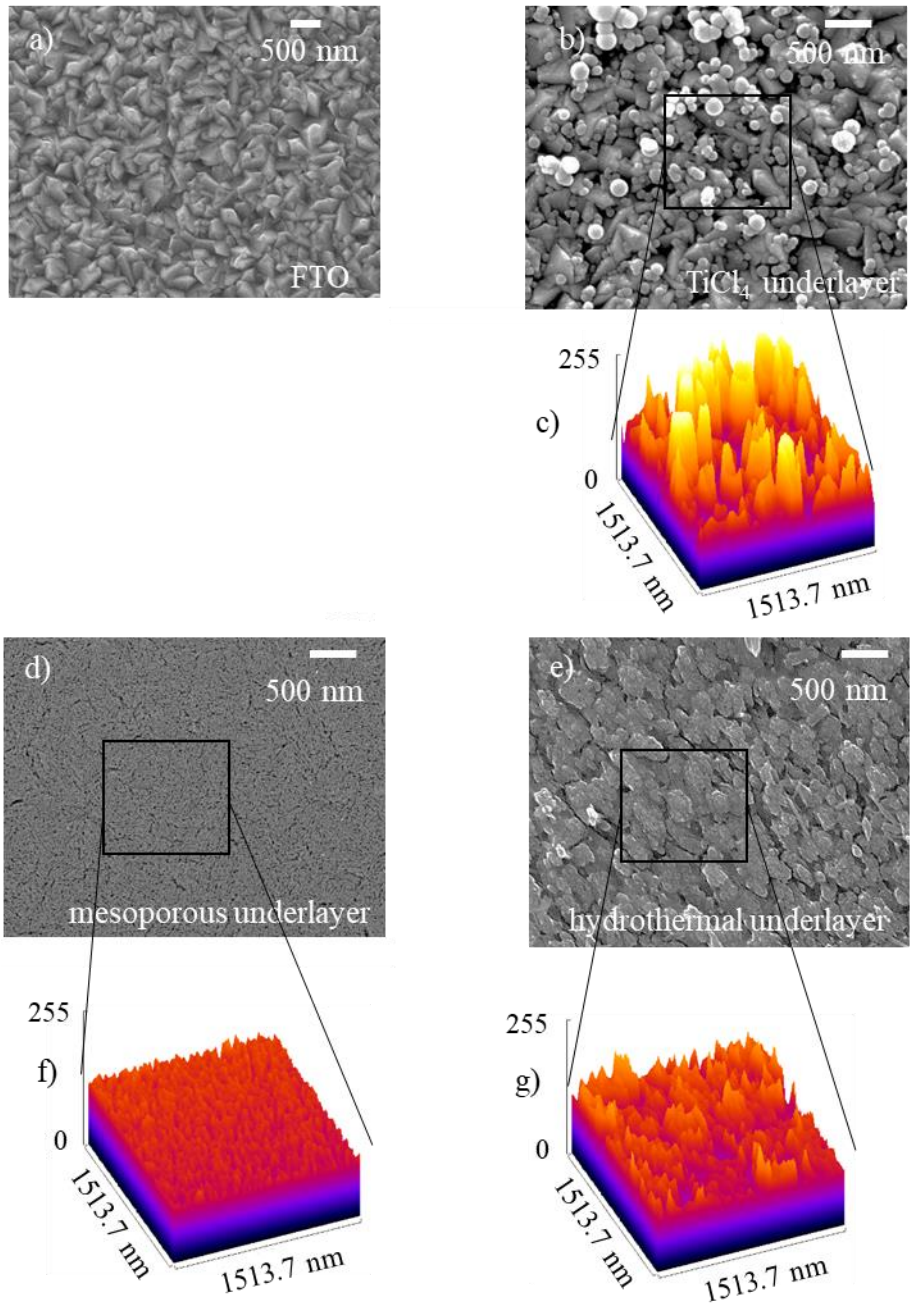

Figure 47: SEM images of TiO_2 underlayer prepared by a) dipping the FTO slide in $TiCl_4$, b) by growing a mesoporous film, c) and growing titania by hydrothermal method. 3D surface plots of d) $TiCl_4$ underlayer, e) mesoporous underlayer, f) hydrothermal underlayer.

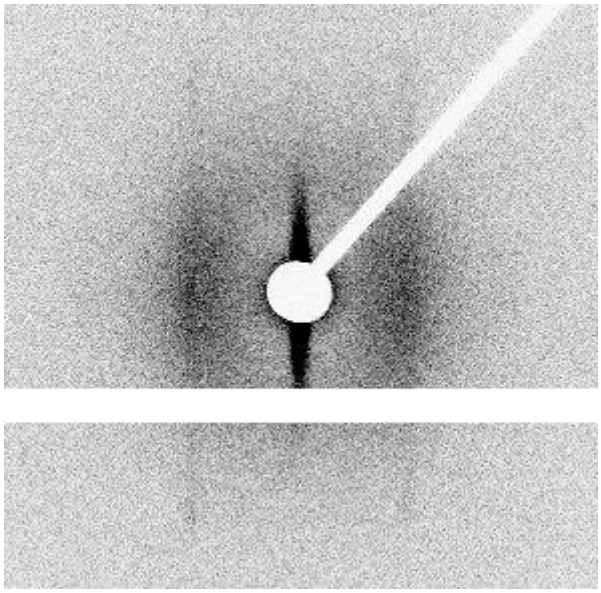

Figure 48: Raw SAXS pattern for the mesoporous underlayer obtained in transmission mode.

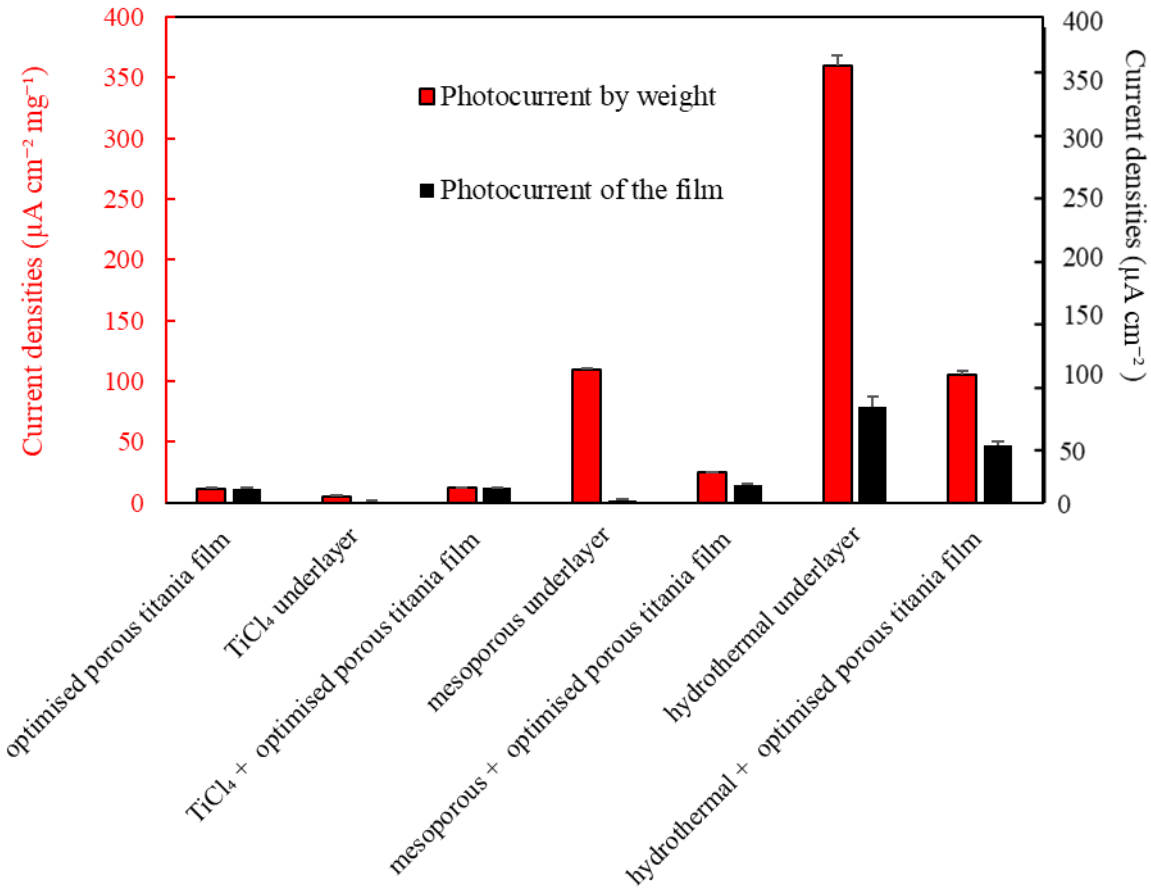

Figure 49: Photocurrents (black – total per sample, red – normalised by weight of TiO_2) of underlayers and underlayers with the optimised 85% P-25 / 15% TTIP TiO_2 films at 0.5 V *vs.* Ag|AgCl.

4.4 Conclusions

In summary, the use of different deposition processes and solvents allowed tuning of the TiO_2 film morphology on the order of ten-micrometre scale. This was achieved by changing the deposition processes: using an airbrush process or ultrasonic spray process, achieving better control of the drying parameters with results contrasted with the usual doctor blading. Indeed, the morphology can be tuned by changing the solvent. The surface roughness of the layer can be increased by using a solvent with low boiling point temperature and high airflow rate in case of airbrush spray deposition.

The appearance of the cracks in the titania film can be controlled by choosing a solvent with a low boiling point temperature. These cracks could act as a diffusion channel for the electrolyte of the photoelectrochemical cell. By changing the film morphology, it is possible to improve the photoactivity of the films slightly. As an example, the use of water as solvent shows a high photocurrent (11 ± 1 µA cm^{-2} mg^{-1}) in the case of an ultrasonic spray, but it is difficult to reproduce. The films deposited using propan-2-ol as a solvent appear not to be sensitive to the nature of the deposition process and show the best uniformity and reproducibility. Another way to change the morphology and to improve the photoactivity is by improving the connection of the TiO_2 film with the FTO substrate; it was first achieved by the addition of titanium isopropoxide to the film precursor mixture. The P-25 particles are interconnected by TiO_2 formed *via* the hydrolysis of TTIP creating a network within the film and improving contact with FTO, but optimisation of the precursor mixture composition proved to be critical. The morphology of the TiO_2 film impacts the photoelectrochemical performance: a maximum current was obtained when the precursor mixture composition was 85% P-25 and 15% TTIP (optimised TiO_2 film): 11.2 ± 0.6 µA cm^{-2} mg^{-1}, twice the value reported for titania films in the literature [49], [53], [54].

The use of an intermediate compact TiO_2 layer (*i.e.* underlayer) between the substrate and the film deposited by ultrasonic spray coating has been studied and show a major improvement. On the three methods to grow underlayer (dipping into a concentrated $TiCl_4$ solution, growing a thin mesoporous layer by EISA or growing a TiO_2 film by hydrothermal method) only two has shown a high photoactivity on their own: 110 ± 0.5 µA cm^2 mg^{-1} for the mesoporous underlayer, and 360 ± 8 µA cm^2 mg^{-1} for the hydrothermal underlayer. However, these

underlayers by their own have a small loading (0.019 ± 0.002 mg cm^{-2} and 0.2 ± 0.02 mg cm^{-2} respectively). Then an optimised TiO_2 film has been deposited on top and shown a large improvement of the photoactivity of the anode compared to the optimised TiO_2 film: 25.0 ± 0.5 µA cm^2 mg^{-1} with a mesoporous underlayer, and 105.0 ± 3.4 µA cm^2 mg^{-1} with hydrothermal underlayer compared to the 11.2 ± 0.6 µA cm^{-2} mg^{-1} of the optimised TiO_2 film by itself.

The hydrothermally grown underlayer shown a higher photoactivity per sample and by weight without optimised film (79 ± 2 µA cm^2 underlayer alone against 47 ± 3 µA cm^2 with the 85% P-25 and 15% TTIP based film). It is sufficient by itself to obtain a photoactive film even with a low titania loading of 0.2 mg cm^{-2}. Thus, the hydrothermally grown film is the best material within samples studied here, showing high photoactivity. It is suggested that the hydrothermal growth deposition process is a promising way to obtain a high photoactive anode. However, it required a systematic study of the effect of the different deposition parameters to obtain the maximum photoactive TiO_2 film for a full vanadium solar redox flow batteries.

5.Photocurrent improvement of a full vanadium solar redox flow battery by using atomically precise gold clusters.

5.1 Introduction

The photoelectrochemical performance of the vanadium solar redox battery was found to be limited by the used of TiO_2 at the photoanode due to its the small absorption range of the solar spectrum. As pure TiO_2 has band-gap of 3.2 eV [50] it can only absorb photons which have energy greater than 3.2 eV. Therefore, only photons with wavelengths below 400 nm will have sufficient energy to generate an electron-hole pair. Therefore, to improve the absorption range of the TiO_2 photoelectrode Awazu *et al*. [186] realised what they call plasmonic photocatalysts based on silver nanoparticles embedded in titanium dioxide. The photocatalytic activity of TiO_2 was improved ca. seven-fold by a locally enhanced electromagnetic field induced by surface plasmon resonance (SPR) of silver nanoparticles.

Many studies have been conducted to investigate the metal nanoparticles effect on a semiconductor [57], [187]–[191]. Nanoparticles such as Ag and Au have the capability to store a few electrons captured from photoexcited semiconductor nanoparticles [192], [193]. In addition, the double-layer charge inside these nanoparticle leads to a stabilisation of the electron stored inside the metal nanoparticles [194]–[196]. This then leads to a charge equilibration and therefore, to a decrease in the Fermi level [193]. Another significant effect was the reduction of the charge recombination at the surface of the photoelectrode [197]. In parallel, a lot of studies have been conducted on gold catalysis for organics reactions [9]. Au plasmon resonances come from the oscillations of the electrons close to the surface of the nanocrystals [198], [199]. The plasmon-excited hot electrons in the noble metal nanocrystals can be transferred to the conduction band of TiO_2 [198], [199]. Finally, in the last few years, the plasmonic resonance of Au nanoparticles have used to obtain better photoelectrodes and enhance the absorption range of TiO_2 into the visible region [200], [201], [210], [202]–[209].

As an example, Shi *et al.* [201] succeeded in increasing the photocurrent of water oxidation when TiO_2 was illuminated by light with a wavelength of 650 nm. This was achieved by depositing gold nanoparticles of 20 nm on a commercial TiO_2 film. In fact, the photo driven water oxidation was higher when the material was illuminated with wavelengths of 650 nm compared than with 550 nm. These nanoparticles can be formed in many ways [205], for example, Tanaka *et al.* [209] used a calcination method, and succeeded in the preparation of

partially spherical gold particles supported on TiO_2 exhibiting photo-absorption due to surface plasmon resonance at around 620 nm for the selective oxidation of benzyl alcohol to benzaldehyde. For the full vanadium battery, the gold has been proved as a good electrode for V^{4+} / V^{5+} oxidation and reduction [286], [287], when deposited on carbon felt and used as a positive electrode (*i.e*. the gold is electrocatalytically active for the V^{4+} / V^{5+} redox reaction).

As Au nanoparticles have interesting and useful plasmonic and catalytic properties, it is also worth considering the use of nanoclusters (NCs) in this application. NCs are ultra-small nanoparticles with atomically precise chemical composition, which have geometrical, electronic, magnetic and optical properties which are strongly dependent on their size. Thus, these materials have attracted massive interest in catalysis as the catalytic activity or selectivity of a chemical reaction which can be fine-tuned via a minor change in the composition of the catalyst [288], [289]. These metallic cluster could be based on gold, silver or copper. Au nanoclusters have a large range of size and optical properties. In summary, the clusters were promising materials for photoelectrochemical oxidation. This project will study the effect of Au nanoparticle deposit on TiO_2 at different loading and the effect of gold nanoclusters of different size deposit on TiO_2 at different loading against a 0.1 M V^{4+} electrolyte.

5.2 Experimental

5.2.1 Au nanoparticles

Citrate-stabilized Au nanoparticles were prepared according to the procedure detailed by Turkevich *et al.* with modifications [290]. $HAuCl_4$ (0.08 g, 0.2 mmol) was dissolved in 200 mL of milli-Q water. The Au solution was heated while stirring at 1000 rpm until vigorous boiling. The solution of sodium citrate (0.15 g, 0.6 mmol in 10 mL of Milli-Q water) was added into the $HAuCl_4$ solution. The resultant blue-purple solution was stirred with heating for 10 seconds to obtain a colourless solution then deep red solution after ten more seconds. The mixture was further stirred for 10 minutes to obtain the red wine solution. The resulting solution was cooled down in an ice bath for 10-20 minutes before analysing by UV-vis spectroscopy technique. The UV-vis spectrum showed one peak at the wavelength of 524 nm corresponding to Au colloid with an approximate particle size of 12 nm [291].

5.2.2 Au nanoclusters

$[Au_6(dppp)_4]$ $(NO_3)_2$, $[Au_9(PPh_3)_8]$ $(NO_3)_3$, $[Au_{11}(PPh_3)_8]$ NO_3Cl_2, $[Au_{13}(dppe)_5Cl_2]$ Cl_3 $[Au_{20}(PP_3)_4]$ Cl_4 and $Au_{101}(PPPh_3)_{21}$ Cl_5 (referred as Au6, Au9, Au11, Au13, Au20 and Au101 in this study) were synthesised by the different techniques (detailed in the Appendix D) and deposited on TiO_2 films. These clusters have been chosen for their absorption properties. Au6 shows a strong absorption peak at 600 nm (Figure A1). The Au9 and Au11 clusters absorb light in the UV range (Figure A2 A3). The Au13 clusters shown a high absorption peak at 400 nm (Figure A4). The Au20 clusters show an absorption peak at 500 nm and below 400 nm (Figure A5). Finally, the Au101 clusters show an absorption from 400 to 600 nm (Figure A6).

5.2.3 TiO_2 deposition and gold process

Sixteen TiO_2 coated FTO slides were prepared simultaneously. These FTO glasses (Ossila TEC-10) were first cleaned by ultrasonication in DI water and isopropanol (UNIVAR, analytical grade). The slides were then further treated under a UV lamp (MTI corporation, compact UV-ozone cleaner, with 55 W UV lamp of 254 nm and 185 nm maxima of irradiation with peak UV intensity of 4.6 $mW \cdot cm^{-2}$) for 20 min.

The FTO slides were then placed on a temperature-controlled plate at 90°C and covered with an aluminium mask with a 1.13 cm diameter opening (A=1 cm^2) over each slide. These slides were then spray coated with ink containing 85% of 20 mg mL^{-1} TiO_2 P25 (Degussa) and 15% of 71 mg mL^{-1} titanium isopropoxide (Aldrich 97%) in isopropanol. The spray process was conducted using an ultrasonic atomiser (Sonozap) at 60 kHz mounted on a microprocessor-controlled X-Y carriage, and fed by a syringe pump at 1 mL min^{-1}. Once coated, the TiO_2 coated FTO slides were sintered in air at 450°C for 30 min with a heating and cooling rate of 7 ºC/min.

The completed TiO_2 coated FTO slides a TiO_2 loading of 0.7 ± 0.1 mg cm^{-2}. This film will be called standard TiO_2 films in this study.

5.2.4 Gold nanoclusters deposition process

Au was added to the TiO_2 photoelectrodes in three ways: between the FTO and TiO_2 film, mixed into the TiO_2 film and drop cast on top of the TiO_2 film (Figure 50). In these three cases, the Au loading was fixed at 5 wt% relative to the TiO_2 film. A second series of electrodes were also prepared by the drop cast method in which the Au loading was varied (Figure 50). For the drop cast electrodes, once prepared the electrodes heated at 200 ºC for 1

hour to remove the ligand (Figure 50 c). The films were all test by a standard linear sweep-voltammetry test.

Table **7**: Au nanoparticles solution dropped on TiO_2 films

Number of drops	wt% Au loading	Solution used
1	0.085	citrate gold nanoparticle dilute 10 times
2	0.17	citrate gold nanoparticle dilute 10 times
6	0.45	citrate gold nanoparticle dilute 10 times
1	0.85	citrate gold nanoparticle 0.32 mg ml^{-1}
3	1.7	citrate gold nanoparticle 0.32 mg ml^{-1}
6	3.4	citrate gold nanoparticle 0.32 mg ml^{-1}
9	5.1	citrate gold nanoparticle 0.32 mg ml^{-1}
12	6.8	citrate gold nanoparticle 0.32 mg ml^{-1}
15	8.5	citrate gold nanoparticle 0.32 mg ml^{-1}
17	10.2	citrate gold nanoparticle 0.32 mg ml^{-1}
20	11.9	citrate gold nanoparticle 0.32 mg ml^{-1}

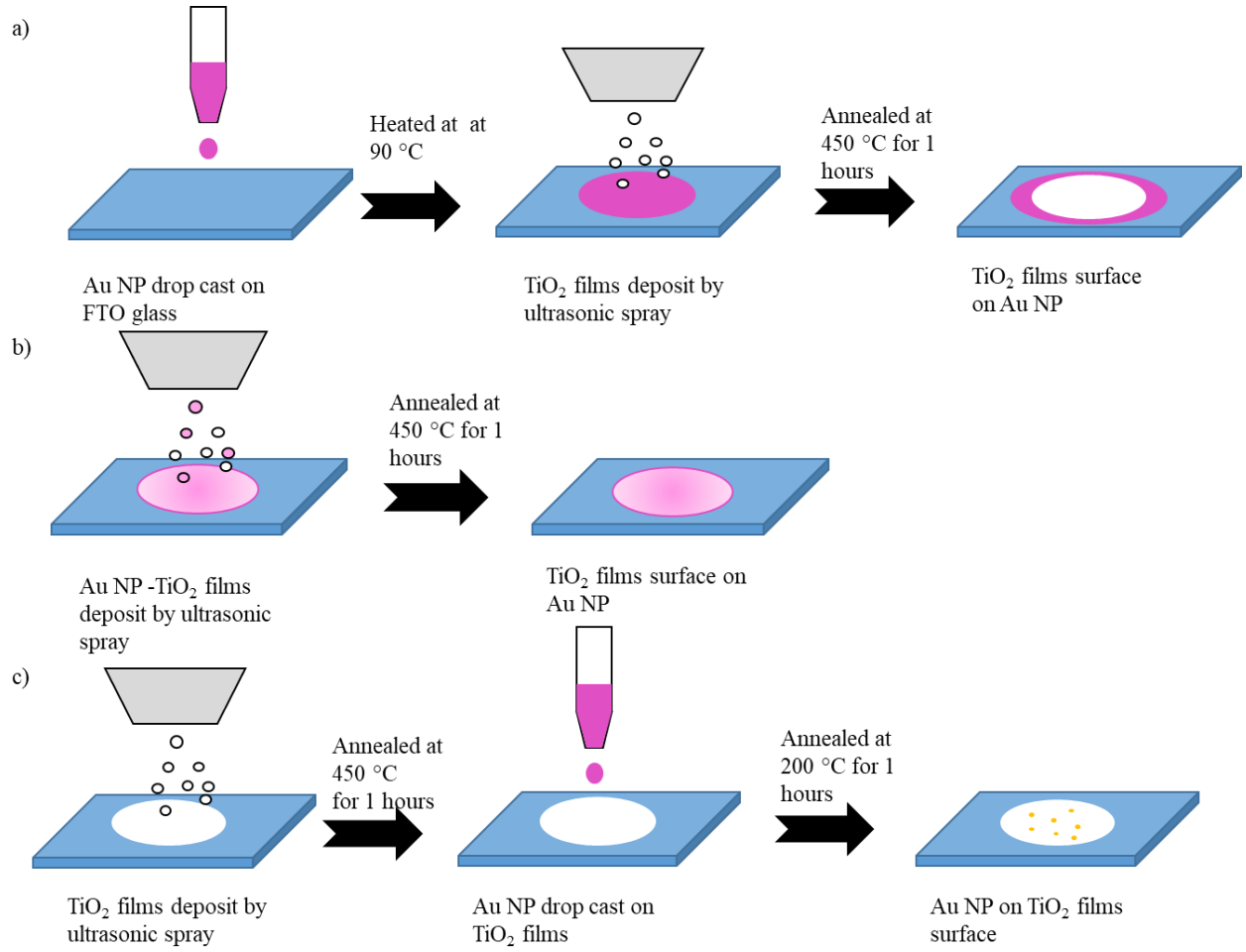

Figure 50: Deposition process of the Au nanoparticles a) between the FTO and the TiO_2 film, b) mixed with TiO_2 solution, c) and on top of the TiO_2 film

5.2.5 Au nanoclusters deposition process

The Au nanoclusters were deposited on the TiO_2 film by absorption of a solution of Au nanoclusters on the TiO_2 films, using a solution of 0.01 mg ml^{-1} of Au nanocluster dispersed in dichloromethane. The TiO_2 films were immersed in a 0.5 M H_2SO_4 for 12 hours. Then, washed for 30 min in Milli Q water, and then 30 min in methanol (repeated four times). This pre-treatment step allows a better connection between the Au nanoparticles and the TiO_2 support, as shown by Ruzicka et al [292]. Finally, the nanoclusters were deposited by dropping 50 µL / 100 µL / 250 µL / 500 µL / 1 ml / 3 ml of the Au nanocluster solution for a loading of 0.085 % / 0.17 % / 0.85 % / 0.45 % / 0.85 % / 1.7 % and 5 wt% respectively. For Au_6 a solution of 0.1 mg ml^{-1} was prepared and dropped on TiO_2 films by dropping 50 µL / 100 µL / 150 µL / 200 µL / 250 µL / 300 µL and 350 µL of the solution given a loading of 1.7 % / 3.4% / 5.1 % / 6.8 % / 8.5 % / 10.2 % and 11.9 % respectively. Finally, the TiO_2 film with nanoclusters was heated at 200 ºC for 1 hour to remove the ligand.

5.2.6 Photoelectrochemical analysis

The photoelectrochemical performance of TiO_2 photoanodes was measured by mounting the TiO_2 coated FTO slides in a custom made glass cell (Figure 22). This cell had two chambers separated by a 117 Nafion membrane, with a platinum wire used a counter electrode dipped into 0.5 M H_2SO_4 in one chamber, and the TiO_2 coated FTO slide (working electrode), and Ag|AgCl dipped into a 0.1 M $VOSO_4$ in 0.5 M H_2SO_4 electrolyte used in the other chamber. The cell was illuminated through an electro-mechanical shutter with either a xenon arc lamp (SLS401, Thorlabs) equipped 1.5 AM filter, a 365 nm (M365LP1, Thorlabs), 385 nm (M385LP1, Thorlabs), 405 nm (M405LP1, Thorlabs), and 420 nm LED lamp (M420LP1, Thorlabs), with the light intensity measured using a thermal power meter (S401C, Thorlabs). The system was configured so that the TiO_2 was illuminated through the backside of the FTO glass to minimise absorption of the light by the strongly adsorbing vanadium electrolytes.

Three-electrode photoelectrochemical measurements were performed using a Gamry Reference 300 potentiostat, which was also configured to control the light shutter, via the potentiostats I/O connector. The curve obtained in this way show the current densities corresponding to the periods of no illumination (“dark”) and followed by the periods under illumination (“light”) as a function of the potential of the photoelectrode on a single curve. The

photocurrent at 0.5 V vs Ag|AgCl was then used to compared the electrodes as in the previous chapter it had been shown that this value, there is almost no electrochemical oxidation or reduction in the dark, and there is no anodic and cathodic peak when the light is turned on or off. Two consecutive linear sweep voltammograms were measured to assess the stability of the film over time.

For the nanoparticles, a batch of 16 films was prepared, and the Au nanoparticles at different loadings were deposited. Each loading was deposited on two different films for reproducibility, and two films were left without any Au. First, the blank films (without Au) were averaged, and the blank photocurrent range was calculated as the 95 % confidence interval of these two films with two consecutive linear sweep voltammetry per film.

The photocurrent of the two TiO_2 films with the same Au loading measured with two consecutive linear sweep voltammetry per film at 0.5V vs Ag|AgCl were averaged, and the error bar based on the 95 % confidence interval of these two films with two consecutive linear sweep voltammetry per film. The blank average photocurrent was finally removed from the average photocurrent of the different Au loading to obtain the photocurrent improvement compare to the blank films.

To improve the statistics when testing the influence of the Au nanoclusters, each batch of 16 TiO_2 films were used to as substrates for each nanocluster loading. *i.e*. for a nanocluster loading of 0.085 wt% Au, Au6, Au9, Au11, Au13, Au20 and Au101 were each loaded onto 2 TiO_2 electrodes from the batch of 16 films. Then another batch of 16 TiO_2 films was prepared with a new value of Wt% Au loading. Over the entire group, a total of 12 blank (*i.e*. only TiO_2) electrodes were used as a control (taken over 6x lots of 16 spray deposition), with the blank photocurrent range taken as the 95 % confidence interval over these 12 electrodes. While this widens the range of photocurrents for the blanks, it also helps confirm any Au induced improvements as the variability of the spray process is now accounted for by the statistics.

5.2.7 Others Analysis

Reflectance spectrum was recorded by using UV-DRS, PXRD patterns of samples deposited on FTO slides in this work were collected at room temperature on a Rigaku Smartlab diffractometer. General data collecting was conducted in Bragg-Brentano focusing mode

utilising Cu Kα (1.5418 Å) radiation operating at a tube voltage of 40 kV and tube current of 30 mA passing through a Cu Kβ filter, with a Cross Beam Optics Bragg-Brentano selection slit, 10 mm length limiting slit, 5.0° Soller incident and receiving parallel slit. The detector was a Rigaku D/tex Ultra 250 1D. The data collected was in the 10 - 90 2θ range conducted at 5°/min.

5.3 Results and discussion

5.3.1 Effect of the placement of the Au particle

The Au nanoparticles have been chosen for three main reasons. Au is a common metal used to obtain a plasmonic effect which will decrease the semiconductor bandgap [57], [187]–[191]. Au nanoparticles were stable in acidic solution so in the photoanode electrolyte and could be compared to a large number of Au nanoclusters [288], [289].

The first step is to determine where the deposition of Au nanoparticles is the most effective. Indeed, three placement are possible: the most common is to deposit the Au nanoparticles along with the TiO_2 powder so as to disperse it everywhere into the film [293], [294]. The film is essentially doped by Au, and a low number of triple junction point were created with the electrolyte-electrode interface. The nanoparticles could be also deposited on the surface of the film [295], allowing a higher number of the triple junction at the interface but decreasing the Au doping of the film. Finally, the Au nanoparticles could be deposited between the FTO and the TiO_2 film [187], helping the transition of the electron from the TiO_2 film to the FTO.

When the Au nanoparticle was deposited between the FTO and the TiO_2 film, the photocurrent obtain was very low (1.9 ± 0.2 µA cm^{-2} mg^{-1} *vs.* 13.4 ± 0.4 µA cm^{-2} mg^{-1} at 0.5 V *vs.* Ag|AgCl) and under 0.4 V *vs.* Ag|AgCl act as a photocathode (Figure 51 a). above 0.4 V *vs.* Ag|AgCl , Even if theoretically the Au nanoparticles should attract the electron to the surface of the FTO [192], [193], [294], they absorb all the light before it reaches the TiO_2 (Au strongly absorbs light between 300 nm to 550 nm, Figure 55 a) and so is counterproductive. Under 0.4 V *vs.* Ag|AgCl the photoreduction of the vanadium could be explain by the relation between FTO and gold. FTO could act as photoanode, however this absorption range (Figure 29 a) is too low for sunlight. However, the use of Au nanoparticle improved the absorption of FTO and creates photoreduction of V^{4+}.

When the Au nanoparticles were mixed with TiO_2 powder, a small improvement could be noticed in the photocurrent (16.3 ± 0.4 µA cm^{-2} mg^{-1} *vs.* 13.4 ± 0.4 µA cm^{-2} mg^{-1} at 0.5 V vs. Ag|AgCl) (Figure 51 b). In case of the gold nanoparticles deposited on the surface of the film (Figure 51 c), a larger photocurrent improvement could be observed. Indeed, for a deposition of 1.7 wt% Au nanoparticle the photocurrent is improved (20.4 ± 0.4 µA cm^{-2} mg^{-1} against 13.4 ± 0.4 µA cm^{-2} mg^{-1} at 0.5 V vs. Ag|AgCl). The difference between the Au nanoparticles deposited on TiO_2 powder and those deposited on the surface of the TiO_2 film can be explained by the higher percentage of Au nanoparticles in contact with the electrolyte and the TiO_2 particles suppressing the charge recombination by facilitating hole transfer to the redox couple in the electrolyte.[294], [296].

Due to the above findings, the remainder of this study investigates the influence of the Au nanoparticles or nanoclusters by depositing them onto the surface of pre-formed TiO_2 electrodes to maximising the number of Au particles in contact with TiO_2 and the electrolyte.

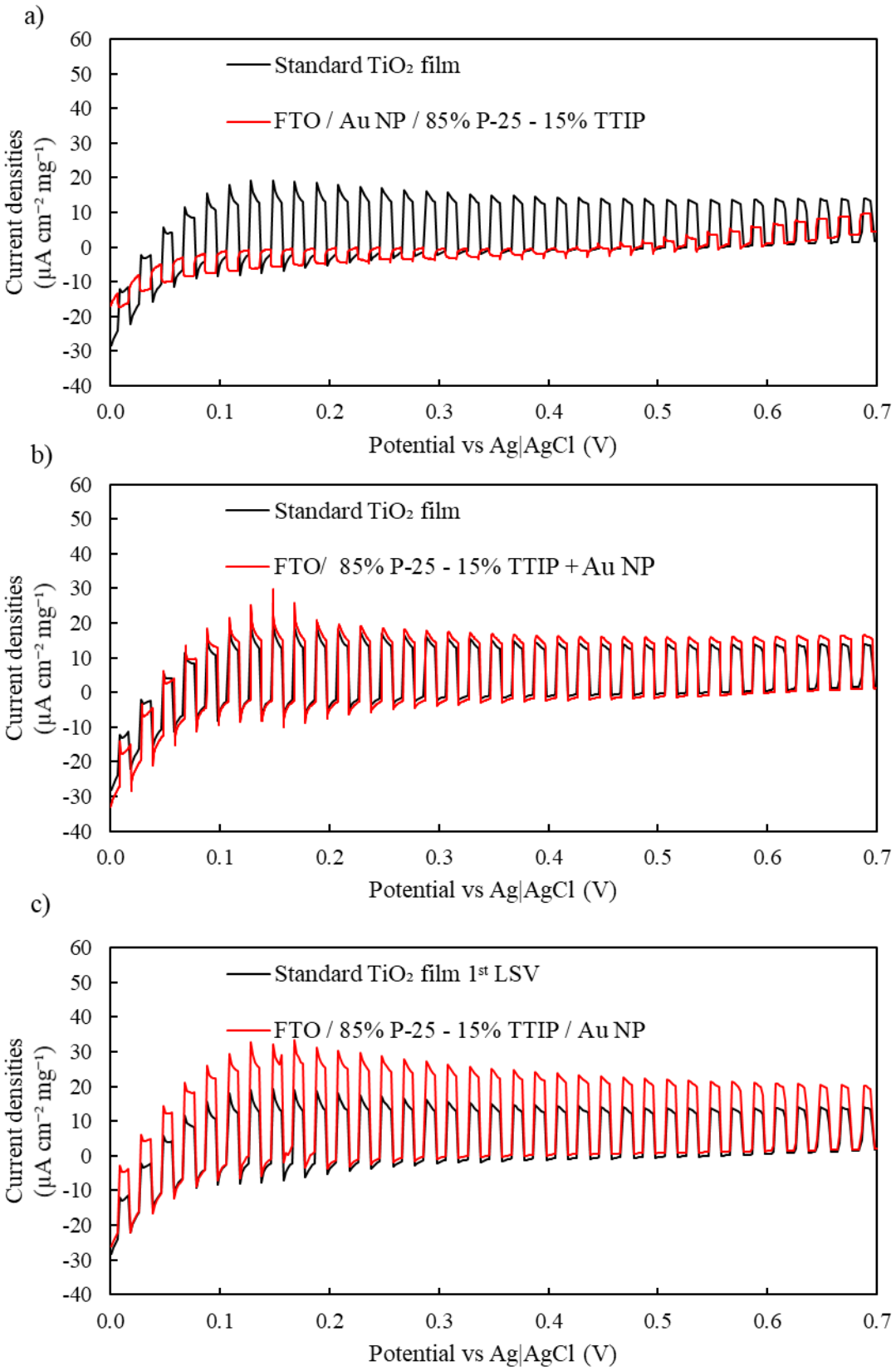

Figure 51: linear sweep voltammetry of Au nanoparticles deposited at different places a) between the FTO and the TiO_2 film, b) mixed with TiO_2 solution, c) and on the top of the TiO_2 film

5.3.2 Au nanoparticles and nanoclusters

The next step focused on determining the best Au nanoclusters to be able to obtain an improvement of the photocurrent. A large range of Au nanoclusters size have been tested: Au 101 (almost a gold nanoparticle), Au20, Au13, Au11, Au9, and Au6. The photocurrent of the films with different gold nanoclusters and gold nanoparticles with loadings between 0.085 wt% Au and 5 wt% Au were recorded, and the photocurrent of the blank of the same batch (*i.e.* films without Au) was removed from them.

The photocurrent obtained with Au nanoparticles (Figure 52 a) deposited on TiO_2 at different Au loadings shows an increase in the photocurrent when the gold loading on the TiO_2 surface increases. The value of the improvement of the photocurrent at 1.7 wt% of Au nanoparticle (4.8 ± 0.6 µA cm^{-2} mg^{-1}) and 5 wt% (4.3 ± 0.6 µA cm^{-2} mg^{-1}) was higher than the improvement of the film with less Au nanoparticle loading. The loading of nanoparticles has a strong effect on the photocurrent: the photocurrent increase when the loading of Au increase. This increase of photocurrent seems to be logical, as more Au loading means more suppressing the charge recombination. However, the fact that the addition of 5 wt% appears to decrease the photocurrent could be the sign of the presence of a maximum loading. After this maximum, the addition of Au was ineffective or even counterproductive. However, with only this small difference of photocurrent between 1.7 wt% and 5 wt%, no clear conclusion could be made. That is why an additional screening of higher loadings of Au nanoparticles was required.

The photocurrent improvement has been calculated for Au nanoclusters differently at different Au loading to determine which one leads to the most significant increase. The photocurrent improvements obtained for the TiO_2 films with the different Au nanoclusters shows an interesting result. Firstly, the use of Au_{101} gold clusters (Figure 52 b), which are the closest of the clusters in size to the nanoparticles show no improvement compared to the TiO_2 film without Au nanoclusters (blank) at loadings. It may be the result of excess dispersion on the film, thus a failure to induce any plasmonic effect.

Au20, Au13, Au11 also do not show any photocurrent improvement. The reason is linked to the light absorption of these nanoclusters: the Au20 absorb light from 300 to 400 nm with a small peak around 550 nm like Au nanoparticles [297] (Annexe 2, Figure A5), Au13 absorb at 306, 366 nm and 486 nm (Annexe 2, Figure A4 c), and Au11 at 320 nm and 450 nm (Annexe 2, Figure A3). None of them absorbs the light on the visible region, so the plasmonic effect and the injection of hot electron should not occur [187].

Au9 (Figure 52 b) show an improvement of the photocurrent but do not exceed the blank photocurrent range (*i.e.* the improvement is unlikely to be statistically significant). The Au9 nanoclusters absorbed light at 442 nm, 424 nm, 354 nm and 316 nm (Annexe 2, Figure A2). No peak occurs in visible range so the improvement could be only due to better coverage by smaller clusters or due to the TiO_2 films itself. Therefore, the improvement could not be considered conclusive.

Finally, the addition of Au_6 (Figure 52 g) shows a significant increase of the photocurrent at 5 wt% Au loading (7 ± 1 µA cm^{-2} mg^{-1} higher than the average blank value). This nanocluster has an absorption peak at 600 nm (Appendix D, Figure A1). However, as only one point is out of the blank range. An additional test with a more extensive range of Au loading is required to confirm this trend.

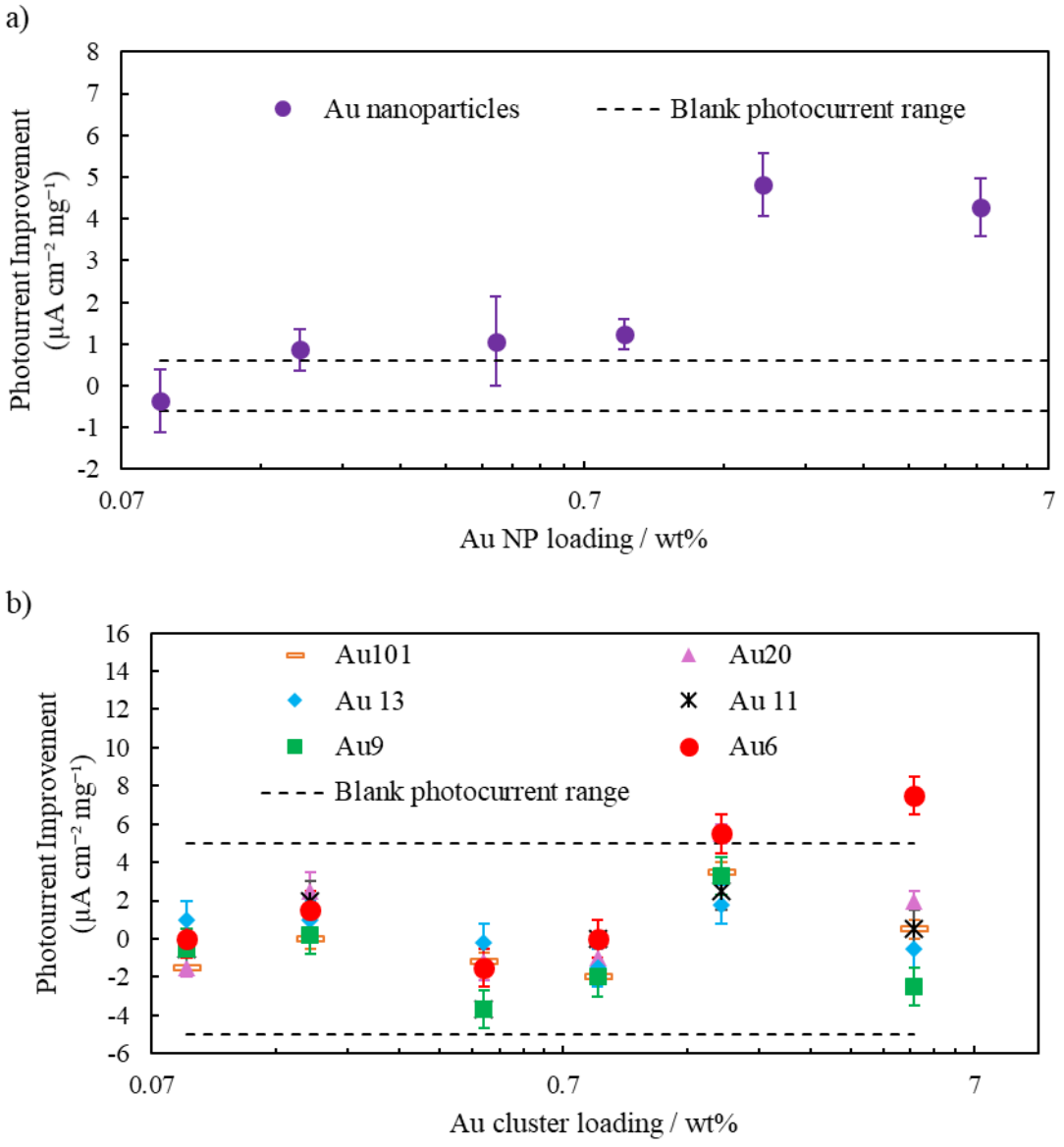

Figure 52: Photocurrent obtains with different Au nanoclusters at different loadings on 85% P-25 and 15% TTIP layer at 0.5 V vs. Ag|AgCl. a) Au nanoparticle and b) different Au nanoclusters.

5.3.3 Au nanoparticles and Au6 nanoclusters

A series of measurements were conducted by depositing a range of higher Au_6 and Au nanoparticles loadings to further examine the findings from the previous section. The photocurrent at 0.5 V *vs.* Ag|AgCl were calculated and compared to the blank sample (Figure 53). In the case of the Au nanoparticles, the photocurrent improvement increases right after 0.17 wt% Au loading. It reaches a maximum of 4.8 ± 0.6 µA cm^{-2} mg^{-1} photocurrent improvement at 1.7 wt% Au then decreases after this maximum and reaches a plateau at 1.8 ± 0.6 µA cm^{-2} mg^{-1} photocurrent improvement. This observation may be due to the Au nanoparticles deposited on the TiO_2 film having a plasmonic effect, thus storing electrons and injecting hot electrons which increase the number of holes on the surrounding TiO_2 which favour the oxidation of V^{4+} to V^{5+} [296]. However, two hypotheses could explain the decrease of the photo activity after 1.7 wt% Au loading. The excesses nanoparticle will cover the active site on TiO_2 (*i.e.* fewer actives available for the oxidation) [298] and/or it can be the recombination centres of photo-induced electrons and holes [299]. Therefore, the plateau can be explained by a saturation of the film with Au nanoparticles which will not have any further effect.

For Au_6 nanoclusters, the addition of Au from 0.085 wt% to 3.1 wt% Au did not improve the photocurrent significantly. However, at 5 wt% Au the photocurrent increases until reaching a maximum at 8.5 wt% Au with an improvement of the photocurrent of 8 ± 1 µA cm^{-2} $mg^{-1}$and then decreases reaching the same plateau value that the Au nanoparticles photocurrent improvement achieves. The Au6, by their small size, allows a higher loading on the TiO_2 film: the clusters are dispersed more widely over the surface, and their small size provides the coverage of the actives sites. It seems that Au6 show a bigger improvement of the photocurrent (almost the double) than the Au nanoparticles, probably due to the absorption peak in visible light at 600 nm compared to the Au nanoparticles peak at 550nm (more sunlight intensity at this wavelength). However, these experiments are a summary at 0.5 V vs Ag|AgCl of the linear sweep voltammetry. A more in-depth analysis of these linear sweep voltammetry was required.

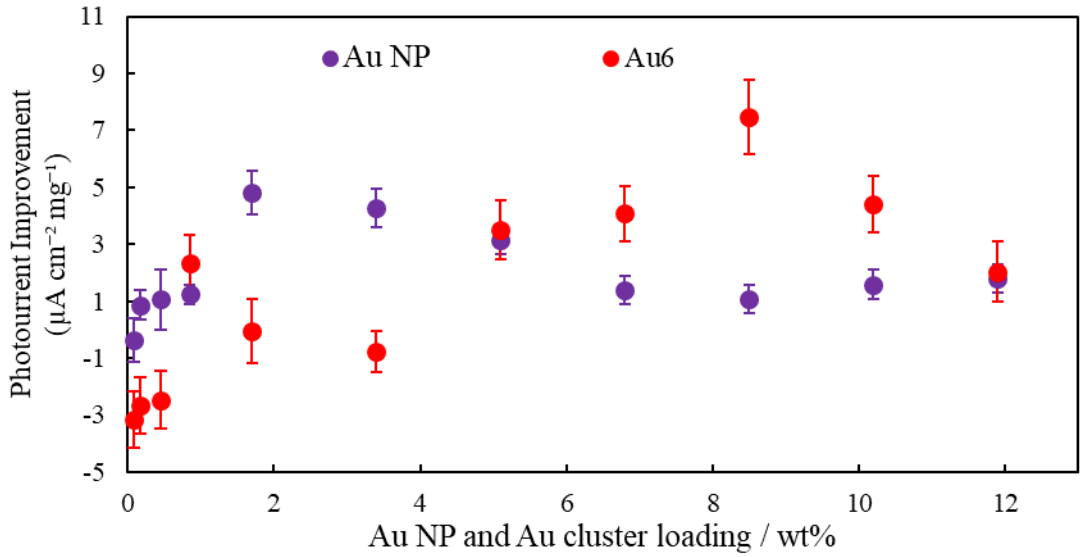

Figure 53: Photocurrent improvement compared to the standard TiO_2 films of the TiO_2 films with Au nanoparticle and Au6 nanoclusters at different wt% Au loading.

The analysis of the linear sweep plot of the best Au nanoparticles and Au_6 nanoclusters based photoelectrodes leads to a more unobstructed view of the real impact of the Au on the performance of the photoelectrode. The linear sweep voltammetry with 1.7 wt% Au loading of Au nanoparticles (Figure 54 a) shows an improvement of the photocurrent at each potential. However, when the experiment was repeated, a large reduction of the photocurrent occurs, ultimately reaching a photocurrent similar to that recorded on the bare TiO_2 film. A second test after a few days showed no improvement. The most likely explanation is that the stability of the gold nanoparticles is low on the TiO_2 film: the Au nanoparticle are deactivated by sintering of these nanoparticle [300]

The linear sweep voltammetry with 8.5 wt% Au loading of Au_6 nanoclusters (Figure 54 b) showed an improvement of the photocurrent at each potential. However, if there was a fading of the photocurrent with time, the fading was much smaller compare with the Au nanoparticles (5 µA cm^{-2} mg^{-1} against 10 µA cm^{-2} mg^{-1}). Due to the capability of nanoclusters to be deposited on the favourable site in TiO_2 surface and form a stronger bond that gold nanoparticle [301]. with Au_6 nanoclusters an increase of the electron-hole recombination can be observed. The anodic and cathodic peak were superior in case of 8.5 wt% Au Au_6 loading than without any gold. It seems to suggest then for the Au_6 nanoclusters there was more creation of electron-hole pairs and that the Au nanoclusters do not provide surface recombination of the electron and the holes [299].

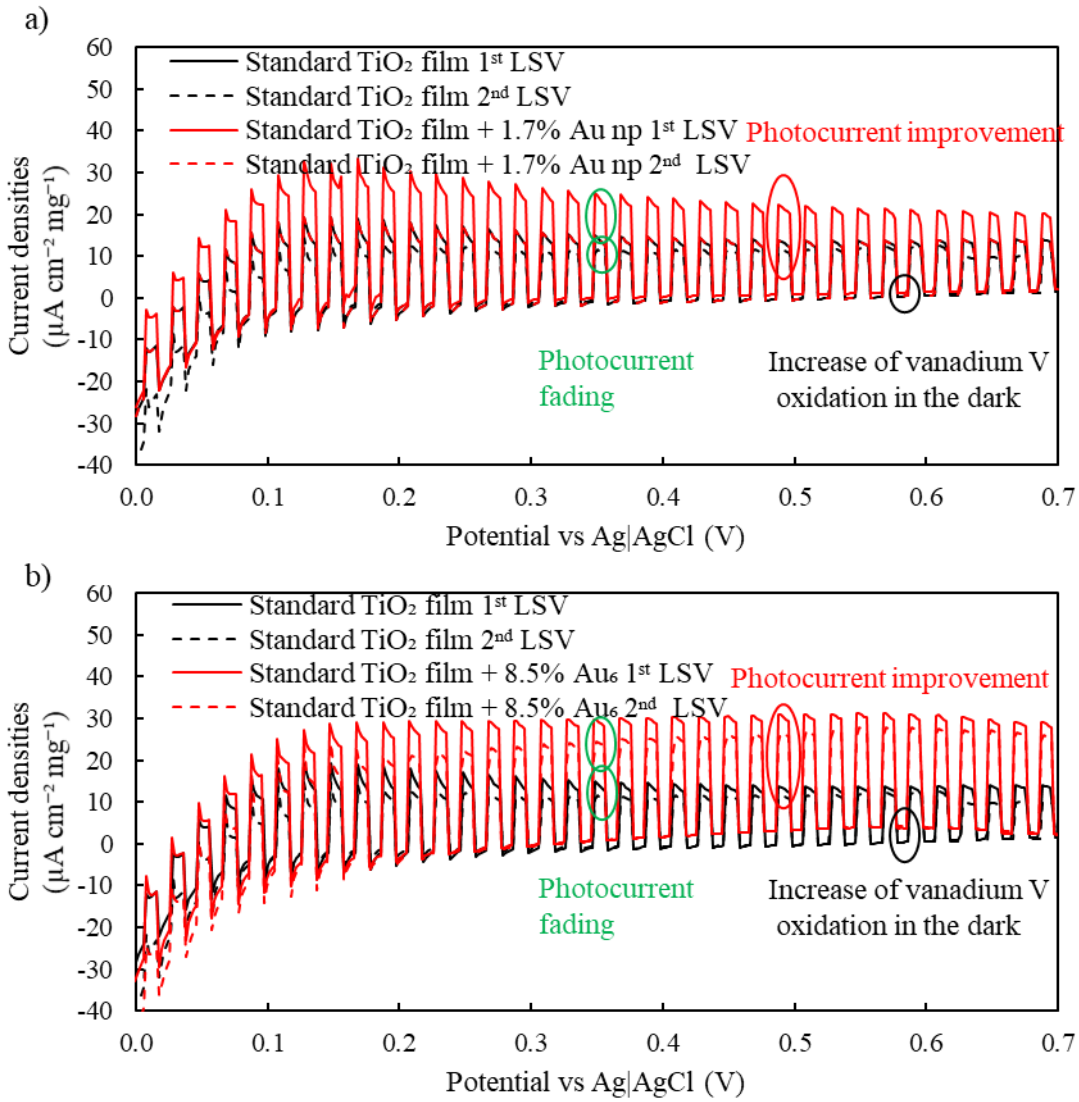

Figure 54: a) Linear sweep voltammetry at 5 wt% of Au nanoparticles. b) Photocurrent obtains with different Au nanoparticles of 25 nm at different loading on 85% P-25 and 15% TTIP layer at 0.5 V vs. Ag|AgCl.

An optical study of the TiO_2 films with the Au nanoparticles and Au_6 nanoclusters was conducted to prove the Au effect on the photoanode absorption band increase.

The absorption spectrum has been recorded, and the Kulbeka Munk plot has been calculated to determine the effect of the gold loading on the bandgap. The TiO_2 films with Au nanoparticle absorption spectrum (Figure 55 a) showed a clear absorption peak at 550 nm, which correspond to the Au plasmonic peak [297]. The peak absorption increases when more nanoparticles where added on the TiO_2 film. The Kulbeka Munk plot (Figure 55 b) shows a bandgap at 3.05 eV. These plots show that Au nanoparticle improve the photocurrent by plasmonic effect

In contrast, the TiO_2 films with Au_6 nanoclusters absorption spectrum did not show any plasmonic gold absorption peak even at 11.9 wt% Au. It could prove that the improvement of photocurrent is due to the quantized semiconductor like characteristics of Au6 and that the nanoclusters do not sinter into nanoparticles when the photoelectrodes were prepared. The Kulbeka Munk plot still shows the same bandgap (3.05 eV).

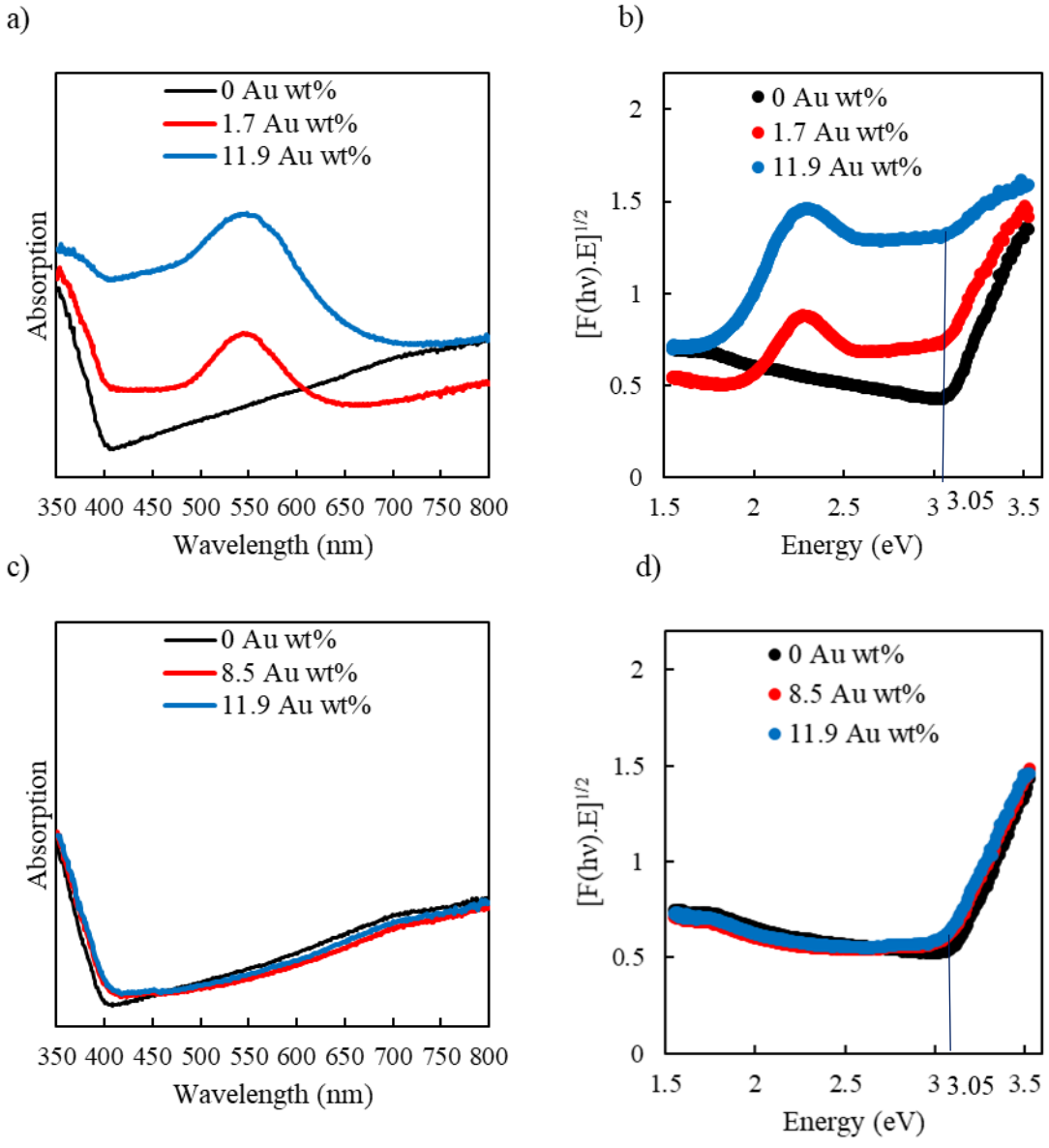

Figure 55: a) Absorption spectra and b) Kulbeka Munk plot for TiO_2 film with Au nanoparticles with a gold loading of 0 wt%, 1.7 wt% and 11.9 wt% Au. a) Absorption spectra and b) Kulbeka Munk plot for TiO_2 film with Au_6 nanoclusters with a gold loading of 0 wt%, 8.5 wt% and 11.9 wt% Au.

With the naked eye, no pink colourisation due to the merging of the nanoclusters, and by the absence of absorption peak at 550 nm, the Au_6 nanoclusters seem to be intact when deposited

on the film. To be sure, a XRD pattern of the TiO_2 films was recorded and diffraction peaks of gold were observed on the TiO_2 film with 5 wt% Au nanoparticles (Figure 56). However, these peaks could not be seen on the XRD spectrum of the Au6 nanoclusters (Figure 56) at the same loading. To confirm that these films indeed had enough Au on them to show diffraction peaks (if the particles were large enough), the Au6 nanocluster – TiO_2 film was heated at 450 ºC for 1 hour to sinter the gold nanoclusters together. After sintering, the XRD spectrum of the TiO_2 film with 8.5 wt% of Au nanoclusters showed characteristic Au peaks. It confirms the presence of Au6 were still in the form of nanoclusters in the not sintered in Au nanoparticles on the TiO_2 film (Figure 56).

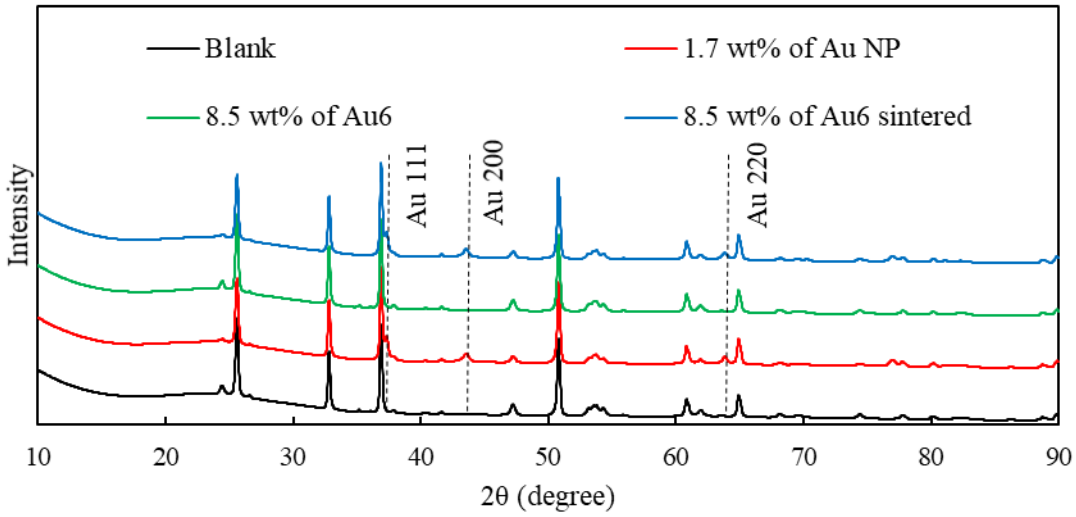

Figure 56: X-Ray diffraction pattern of a standard TiO_2 film, a TiO_2 film with 5 wt% Au loading of Au nanoparticles, and a TiO_2 film with 8.5 wt% Au loading of Au_6 nanoclusters.

To be able to confirm that the addition of Au nanoparticle and Au6 nanoclusters on TiO_2 film increase the light absorption range, Photocurrent at 0.5 V *vs.* Ag|AgCl was recorded with an LED lamp at different wavelengths (Figure 57). Each lamp wavelength was set up at a light power equal to the average power of the sun spectra for the wavelength range between its wavelength and the previous one: 200 nm-365 nm, 365 nm-385 nm, 385 nm-405 nm and 405 nm-420 nm. The photocurrent observed with a standard TiO_2 film had the highest photocurrent (9.8 ± 0.1 µA cm^{-2} mg^{-1}) at 365 nm, at 385 nm the photocurrent was approximately one-third of the one at 365nm (2.4 ± 0.1 µA cm^{-2} mg^{-1}), before reaching almost zero at 405 nm.

In contrast, the two films containing Au shown a lower photocurrent at 365 nm but a higher photocurrent at 405 nm. It confirms that the decrease of the bandgap leads to a broader light absorption range [200], [201], [210], [202]–[209]. The photocurrent at 365 nm and 385 nm

were larger for Au6 nanoclusters (7.9 ± 0.1 µA cm^{-2} mg^{-1} at 365 nm and 1.8 ± 0.1 µA cm^{-2} mg^{-1}) than for Au nanoparticles (6.0 ± 0.1 µA cm^{-2} mg^{-1} at 365 nm and 1.6 ± 0.1 µA cm^{-2} mg^{-1}). However, the photocurrent at 405 nm was slightly higher for Au nanoparticles (0.5 ± 0.01 µA cm^{-2} mg^{-1} against 0.45 ± 0.01 µA cm^{-2} mg^{-1} for nanoclusters). A lower bandgap could explain it in the case of the Au nanoparticle. However, the photocurrent improvement was more significant in the case of the Au6 nanoclusters, a better balance between an efficiency loss in UV and an efficiency gain in the low visible spectrum.

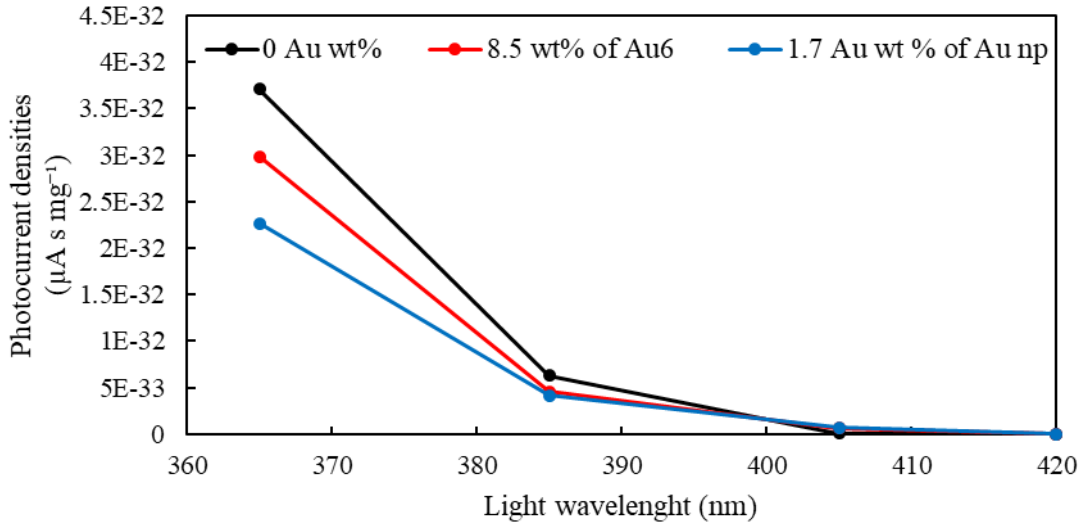

Figure 57: Photocurrent normalized by LED photon flux obtain with standard TiO_2 film alone, with 8.5 wt% Au Au_6 loading, with 1.7 wt% Au of Au nanoparticles

5.4 Conclusion

In conclusion, this study has shown that using nanoparticle and nanoclusters deposited on the surface of a TiO_2 film can improve the photocurrent of the photoanode of a full vanadium solar redox flow battery. Indeed, by adding 1.7 wt% Au nanoparticles, the photocurrent was enhanced by 30 % and by adding 8.5 wt% of Au_6 nanoclusters we obtain an increase of a 50% of the photocurrent mainly due to the extension of the absorption range. Besides, the Au_6 nanoclusters have been shown maintain their cluster structure even at high loading. However, the synthesis of Au nanocluster was more complicated and more expensive than the production of the Au nanoparticle. Therefore, the used of Au nanoparticles or Au_6 nanoclusters depends on which parameters need to be optimised: Au nanoparticles decrease the electron-hole recombination but it was not stable on long term, and Au_6 nanoclusters were more expensive, and longer to synthesise but have a better improvement of the photocurrent on a longer time and can add more gold without being saturated.

6. A study of potential redox couple for a solar redox flow battery with a TiO_2 photoanode.

6.1. Introduction

The previous part of this thesis has shown that V^{4+} cannot be easily photo oxidised, therefore different redox couples for the photoanode including vanadium IV/V, iron II/III, triiodide/iodine, bromine/bromate and cerium IV/V have been investigated. One of the critical aspects of a photoelectrochemical cell is the interface between the semiconductor and the redox couple. When this semiconductor is placed in contact with an electrolyte containing a redox couple, an initial electrical current may flow to establish an equilibrium between the Fermi level of the semiconductor and the redox potential of the redox couple in the electrolyte. This electron transfer leads to the formation of electrolytic double layers in bulk electrolyte. This effect depends on the initial Fermi level of the semiconductor compared to the redox potential: if the Fermi level is equal to the redox potential, a flat layer with no excess charge on each side of the interface will be observed [6]. Compared to the redox potential, a lower Fermi level results in an accumulation of electrons at the surface of the semi-conductor, while a higher Fermi level causes a depletion of electron and a creation of positive charge at the interface [6].. The criteria of choosing semiconductor are, therefore, to match the energy level of semiconductor bandgap with the redox potential of the electrolyte (Figure **8**) [6], [50], [71]–[73].

In the case of a n-type photoelectrode, the potential of the redox couple in direct contact with the photoelectrode should be close to the valence band. The redox couples chosen were selected from their high redox potential and their proximity with the valence band of the TiO_2 (Table **8**). Conversely, the redox couple in the negative (counter electrode) electrolyte have been chosen from their compatibility with the conduction band of the n-type semiconductor and their previous use in traditional redox flow batteries. In most cases, redox couples which can be dissolved in aqueous electrolytes are most common for industrial use due to the low price and the good stability of these electrolytes (water based). The most used and known redox couples dissolved in an aqueous electrolyte are iron/chromium, all-vanadium and vanadium/bromide. Their cell voltage are 1.18 V *vs*. SHE, 1.26 V *vs*. SHE and 1.35 V *vs*. SHE respectively [11].

In addition, the redox potential of two redox couples including ferricyanide/ferrocyanide for their well-known redox potential [302], [303],and triiodide/iodine for their use in the dye-sensitised solar cell have been studied. Finally, a non-aqueous redox couple (vanadium IV/V in acetonitrile) has been investigated which aims to suppress the water-splitting side reaction and avoid other problems of the aqueous electrolyte.

Table 8: Redox potential of commons redox couples

Redox couple	Redox potential *vs.* SHE
$Cr^{3+/2+}$	−0.42 V [6]
Fe/ Fe^{2+}	-0.3 V [11]
$V^{3+/2+}$	−0.26 V [6]
O_2/HO^-	-0.13 V [6]
H^+/H_2	0 V [6]
$V^{3+/4+}$	+0.34 V [225]
$[Fe(CN)]^{3-/4-}$	+0.3704 V [304]
I^-/I_3^-	+0.53 V [6]
$Fe^{2+/3+}$	+0.77 V [6]
$V^{4+/5+}$	+1.0 V [6]
Br^-/Br_2^-	+1.09 V[11]
H_2O/O_2	+1.229 V [6]

6.2. Experimental

6.2.1. TiO_2 deposition process

FTO glasses (FTO type: NSG TEC 10, size: 1.1mm x 20 mm x 15 mm, FTO thickness 750 nm, resistance: 9.39 ± 0.38 Ω FTO work function: 4.4 eV - 4.7 eV, transmission 83.4%, Provider: Ossila) were cleaned by immersion in Milli-Q water and ultrasonication for 30 min ,followed by ultrasonication in propan-2-ol for 30 min. Finally, they were treated in a UV-ozone cleaner (MTI corporation, compact UV-ozone cleaner, with 55 W UV lamp of 254 nm and 185 nm maxima of irradiation with peak UV intensity of 4.6 $mW \cdot cm^{-2}$) for 20 min. The FTO glasses were placed on heating support and covered by a stainless steel mask with an opening of 1 cm^2 over each slide. Titanium suspension was prepared by mixing TiO_2 P25 (Degussa) suspension in propan-2-ol (20 mg mL^{-1}) with titanium isopropoxide solution (TTIP, Aldrich 97%) in propan-2-ol (71 mg mL^{-1}). The weight ratio of TiO_2 and titanium isopropoxide was 85:15 (on an oxide basis). The deposition was performed using an ultrasonic atomiser (Sonozap) at 60

kHz. The titania suspension was fed at 1 mL min^{-1} through a syringe pump (New Era Pump System Inc.) allowing the formation of a thin mist of the titania suspension. This ultrasonic spray was mounted on the x-y carriage and followed a pattern on the top of the mask. The obtained TiO_2 films (loading approximately 0.7 mg cm^{-2}) were sintered at 450°C for 30 min under static air.

6.2.2. Electrolyte fabrication

For the electrolyte preparation, the following chemicals were used. H_2SO_4 (purity 95 % - 98 %, supplier Univar), $VOSO_4$ (purity 99.9 %, Supplier Alpha Aesar), VCl_3 (purity 97 %, supplier Sigma Aldrich), VO_2(acac) (purity 97 %, supplier Sigma Aldrich), V(acac) (purity 98 %, supplier Sigma Aldrich), $KFeCN_6$ (purity > 99 %, supplier vikers laboratories limited), $K_4Fe(CN)_6$ (purity > 99 %, supplier Analar), KNO_2 (purity 99 %, supplier Univar), $FeSO_4$ (purity >99%, supplier BDH), $CrCl_3$ (purity 98 %, Supplier Analar), triiodide electrolyte (supplier Solarnix), NaBr (purity > 99 %,supplier BDH).

The following redox couples and cells were tested in both two electrode and three electrode configurations. For testing, these redox couple combinations were in their 100% discharged state:

The full vanadium cell:

TiO_2 | 0.1 M $VOSO_4$, 0.5 M H_2SO_4 || 117 Nafion || 0.1 M VCl_3, 0.5 M H_2SO_4 | Pt

Photoelectrode:	$VO_2^+ + 2H^+ + e^- \leftrightharpoons VO^{2+} + H_2O$	E = 1 V *vs.* SHE [11]
Negative electrode:	$V^{3+} + e \leftrightharpoons V^{2+}$	E = -0.26 V *vs.* SHE [11]

The full vanadium non-aqueous cell:

TiO_2 | 0.1 M VO_2(acac), acetonitrile || 117 Nafion || 0.1 M V(acac) (III), acetonitrile| Pt

Photoelectrode:	$V(acac)_3 \leftrightharpoons [V(acac)_3]^+ + e^-$	E = 0.4 V *vs.* SHE [305]
Negative electrode:	$V(acac)_3 + e^- \leftrightharpoons [V(acac)_3]^-$	E = -1.81 V *vs.* SHE [305]

The ferrocyanide/ferricyanide cell:

TiO_2 | 0.1 M), $KFeCN_6$ 1.0 M KNO_2|| 117 Nafion || 0.1 M $K_4Fe(CN)_6$, 1.0 M KNO_2| Pt

Photoelectrode:	$[Fe(CN)]^{4-} \leftrightharpoons [Fe(CN)]^{3-} + e^-$	E = 0.37 V *vs.* SHE [306]
Negative electrode:	$[Fe(CN)]^{3-} + e^- \leftrightharpoons [Fe(CN)]^{4}$	E = 0.37 V *vs.* SHE [306]

The ferrous chromium cell:

TiO_2 | 0.1 M $FeSO_4$, 0.5 M H_2SO_4|| 117 Nafion || 0.1 M $CrCl_3$, 0.5 M H_2SO_4| Pt

Photoelectrode:	$Fe^{2+} \leftrightharpoons Fe^{3+} + e^-$	E = 0.77 V *vs.* SHE [11]
Negative electrode:	$Cr^{3+} + e^- \leftrightharpoons Cr^{2+}$	E = -0.41 V *vs.* SHE [11]

The full ferrous cell:

TiO_2 | 0.1 M $FeSO_4$, 0.5 M H_2SO_4|| 117 Nafion || 0.1 M $FeSO_4$, 0.5 M H_2SO_4| Pt

Photoelectrode:	$Fe^{2+} \leftrightharpoons Fe^{3+} + e^-$	E = 0.77V *vs.* SHE [11]
Negative electrode:	$Fe^{2+} + 2e^- \leftrightharpoons Fe$	E = -0.3 V *vs.* SHE [11]

The triiodide-vanadium cell:

TiO_2 | 0.1 M triiodide electrolyte || 117 Nafion || 0.1 M VCl_3, 0.5 M H_2SO_4 | Pt

Photoelectrode:	$I_3^- \leftrightharpoons 3I^- + 3e^-$	E = 0.53 V *vs.* SHE [11]
Negative electrode:	$V^{3+} + e^- \leftrightharpoons V^{2+}$	E = -0.26 V *vs.* SHE [11]

The bromide-vanadium cell:

TiO_2 | 0.1 M NaBr, 0.5 M H_2SO_4 || 117 Nafion || 0.1 M VCl_3, 0.5 M H_2SO_4 | Pt

Photoelectrode:	$2Br^- + Cl^- \leftrightharpoons Br_2Cl^- + 2e^-$	E = 1.09 V *vs.* SHE [11]
Negative electrode:	$2VCl_3 + 2e^- \leftrightharpoons 2VCl_2 + 2Cl$-	E = -0.26 V *vs.* SHE [11]

6.2.3. Cell design

Two glass cells separated by a 117 Nafion membrane were set up to record the photoelectrochemical performance of photoanode. In the first counter electrode cell, a platinum wire was dipped inside the chosen electrolyte. The photoelectrode was clipped onto the second glass cell in the direct contact with the negative electrolyte and an Ag|AgCl counter electrode. A shutter was placed in front of a solar simulator (Xenon lamp) at one sun with a 1.5 AM filter to illuminate the photoelectrode or in front of a 365 nm LED lamp at different power to illuminate the photoelectrode.

6.3. Results

6.3.1. Three electrode measurements

The different redox couples have been chosen for several reasons. Aqueous $VOSO_4$ ($V^{4+/}V^{5+}$) and VCl_3 ($V^{3+/}V^{2+}$) electrolyte were chosen to be able to compare with the previous studies. The use of the same redox couple in acetonitrile has been chosen to remove any chance of water splitting and oxygen evolution. Indeed, as previously show the vanadium redox couple in water showed some water splitting at the photoanode and oxygen evolution at the counter electrode. The use of ferrocyanide/ferricyanide couple was chosen for their large used in the literature due to their god kinetics and defined redox potential [306]–[308] as redox mediator. The $Fe^{2+/3+}$ couple has been chosen for this redox potential of 0.77 V vs NHE and the low price of this couple. In the literature, [11] the redox couple used at the negative electrode was $Cr^{3+/2+}$ given an overall cell voltage of 1.19 V vs NHE. However, this couple is quite expensive and not environment friendly so the redox couple $Fe^{2+/}Fe$ was used with a Pt counter electrode to test a half-solid solar redox flow battery. Another common redox flow battery in the literature was constituted of Br_2^-/Br^- at the anode and $V^{3+/}V^{2+}$ at the cathode and was tested for solar redox flow battery. Finally, to related to the dye-sensitised solar cell technology and some solar redox flow battery publication [6], [33], [38]–[43], [93], [223], the triiodide electrolyte were tested at the photoanode, and the usual $V^{3+/}V^{2+}$ couple were used at the counter electrode.

Firstly, the different anodic redox couples have been tested in a three-electrode measurement under chopped light. The use of $VOSO_4$ in H_2SO_4 as electrolyte (Figure 58 a) showed a reductive current from 0 V *vs.* Ag|AgCl to 0.15V *vs.* Ag|AgCl in the presence of anodic and

cathodic peak from 0 to 0.3 V *vs.* Ag|AgCl with a maximum of recombination from 0.15 V *vs.* Ag|AgCl to 0.2 V *vs.* Ag|AgCl. Finally, the current stabilised after 0.4 V *vs.* Ag|AgCl and the photocurrent remained constant until 0.7 V *vs.* Ag|AgCl. As shown previously, this reducing current is attributed to the reduction of V^{4+} to $V^{3+,}$ which is thermodynamically possible below approx. 0.143 V vs. Ag|AgCl. [32]. The anodic and cathodic peak was linked to the electron-hole recombination at the surface of the film.

However, a change in the polarisation curve was observed when the electrolyte was changed to a VO_2(acac) in acetonitrile electrolyte (Figure 58 b). The reductive currents are much higher (-190 µA cm^{-2} mg^{-1} at 0 V *vs.* Ag|AgCl against -30 µA cm^{-2} mg^{-1} at 0 V *vs.* Ag|AgCl) and still occurs until 0.35 V vs AgAg|Cl. The electron-hole recombination occurs only until 0.25 V *vs.* Ag|AgCl. The overall photocurrent using a VO_2(acac) in acetonitrile electrolyte is lower than that using $VOSO_4$ in H_2SO_4 electrolyte (5 µA cm^{-2} mg^{-1} at 0.5 V *vs.* Ag|AgCl against 10 µA cm^{-2} mg^{-1} at 0.5 V *vs.* Ag|AgCl). With the same vanadium IV ion presented in the electrolyte, the change in the photocurrent could be due to the absence of water splitting side reaction. However, as shown in the previous study on $V^{4+/}V^{5+}$ in H_2SO_4 the water-splitting reaction at this electrolyte concentration could not give 50% of the photocurrent. So it could be due to the difference in electrolyte solvent: acetonitrile *cf.* water (side reaction or reaction site blocking by the acetonitrile) or the difference in electrolyte acidity-basicity (which could explain the reductive current switch occurring at a higher voltage [309]) or both phenomenon in parallel. It is also possible that the reaction kinetics of the V^{4+} oxidation are faster in non-aqueous electrolytes as the complex rearrangement of the hydration shell or bond breaking (e.g. VO^{2+} + H_2O → VO_2^{+}) is not required in the non-aqueous version of the V^{4+} oxidation [305], [310], [311].

The change of the redox couple to ferrocyanide/ferricyanide resulted in completely different linear sweep voltammetry (Figure 58 c). First, a massive electrochemical oxidation current (up to 6 mA) without photoinduced oxidation was observed around 0.2 V *vs.* Ag|AgCl. This is due to the oxidation potential of the couple of 0.37 V *vs.* RHE, which is, therefore, 0.17 V *vs.* Ag|AgCl. The second interesting feature is the absence of reductive current below 0.2 V *vs.* Ag|AgCl in the first linear sweep voltammetry which indicates the absence of $[Fe(CN)6]^{4-}$ complexes in the initial solution. However, after the first test, the complexes were formed prior to reduction at the beginning of the second linear sweep voltammetry test. The two different films showed a low electrochemical oxidation reproducibility of the polarisation, but a high reproducibility of the photocurrent. When the light is on, instead of a rapid increase of the current, a slow increase was observed similar to that found when the light is off. It seems to be

due to the difficulty of the ion complexes diffusion in the electrolyte [309]. This redox couple is not suitable for the solar redox flow battery.

The same phenomenon as that found in ferrocyanide electrolyte was also observed using Fe^{2+}/Fe^{3+} in H_2SO_4 (Figure 58 d): electrochemical oxidation at 0.4 V *vs.* Ag|AgCl (theoretical at 0.57 V *vs.* Ag|AgCl). However, electron-hole recombination can be observed from 0 V *vs.* Ag|AgCl to 0.25 V *vs.* Ag|AgCl and when the light is turned on the photocurrent occurs immediately. The redox couple seems to be a very good candidate for a solar redox flow battery (photocurrent of 119 ± 8 µA cm^{-2} mg^{-1} at 0.5 V *vs.* Ag|AgCl against 10 ± 1 µA cm^{-2} mg^{-1} for $V^{4+/}V^{5+}$ in H_2SO_4). However, two issues could be observed, the high photocurrent of 119 ± 8 µA cm^{-2} mg^{-1} was achieved after 0.25 V *vs.* Ag|AgCl, but not below, and the low oxidising potential could lead to a low cell voltage in the function of the redox couple choose at the counter electrode

The triiodide (Figure 58 e) electrolyte showed a steady photocurrent of 59.5 ± 0.5 µA cm^{-2} mg^{-1}until approximately 0.3 V *vs.* Ag|AgCl where an electrochemical reaction starts to occur which corresponds to the value of the oxidation of I_3^- in Ag|AgCl. This electrochemical oxidation increase after 0.5 V *vs.* Ag|AgCl only. Of note, the non-aqueous electrolyte could lead to a misinterpretation of the potential. The presence of high steady photocurrent and the absence of reductive current make a proper electrolyte for solar redox flow battery as shown in the literature [33].

Finally, the bromide electrolyte in HCl (Figure 58 f) showed electron-hole recombination anodic and cathodic peak and a small reductive current from 0V to 0.4V *vs.* Ag|AgCl. The photocurrent increases with the increase of potential until reaching a maximum photocurrent of 43 ± 2 µA cm^{-2} mg^{-1}. The higher photocurrent compare to the $V^{4+/}V^{5+}$ in H_2SO_4 make it an interesting electrolyte, but the use of bromide could be an environmental and safety issue (toxic gas produced).Among the redox couples, the triiodide electrolyte and $Fe^{2+/}Fe^{3+}$ in H_2SO_4 were the most promising couple allowing the reaction to take place around 0.5V *vs.* Ag|AgCl, if the cathodic electrolyte permits it.

a)

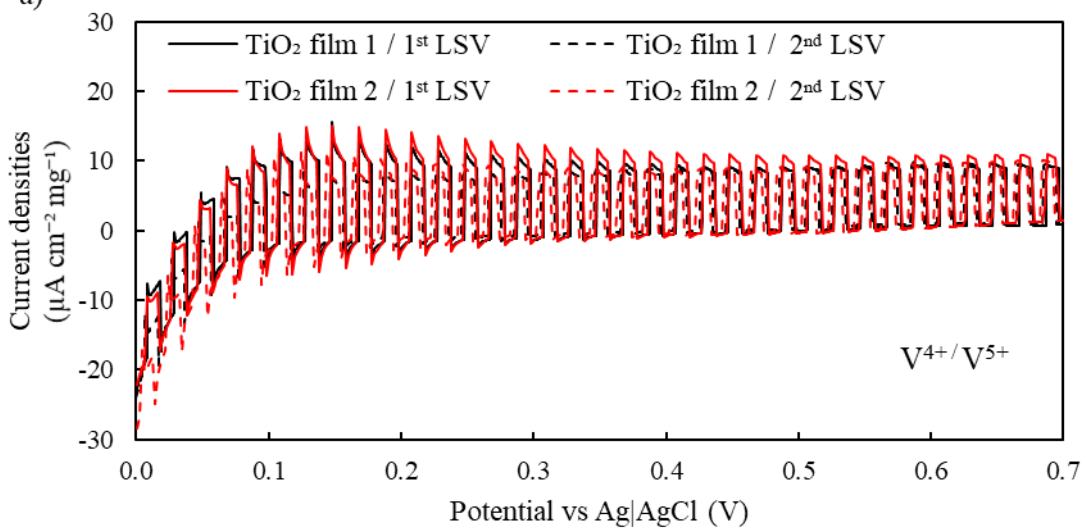
TiO₂ film 1 / 1st LSV
TiO₂ film 1 / 2nd LSV
TiO₂ film 2 / 1st LSV
TiO₂ film 2 / 2nd LSV
Current densities (µA cm⁻² mg⁻¹)
30
20
10
0
-10
-20
-30
0.0
0.1
0.2
0.3
0.4
0.5
0.6
0.7
Potential vs Ag|AgCl (V)
V4+ / V5+

b)

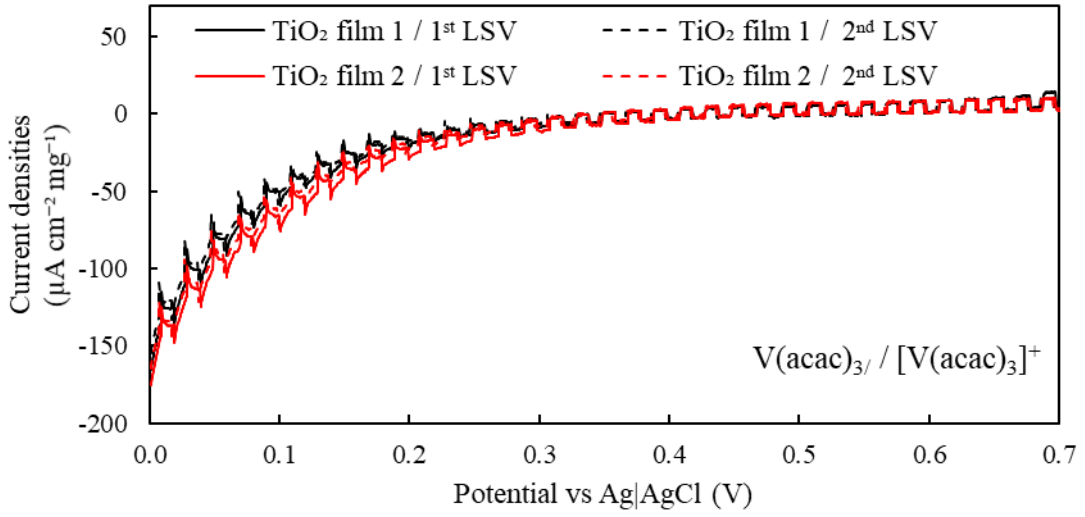
TiO₂ film 1 / 1st LSV
TiO₂ film 1 / 2nd LSV
TiO₂ film 2 / 1st LSV
TiO₂ film 2 / 2nd LSV
Current densities (µA cm⁻² mg⁻¹)
50
0
-50
-100
-150
-200
0.0
0.1
0.2
0.3
0.4
0.5
0.6
0.7
Potential vs Ag|AgCl (V)
V(acac)3/ / [V(acac)3]+

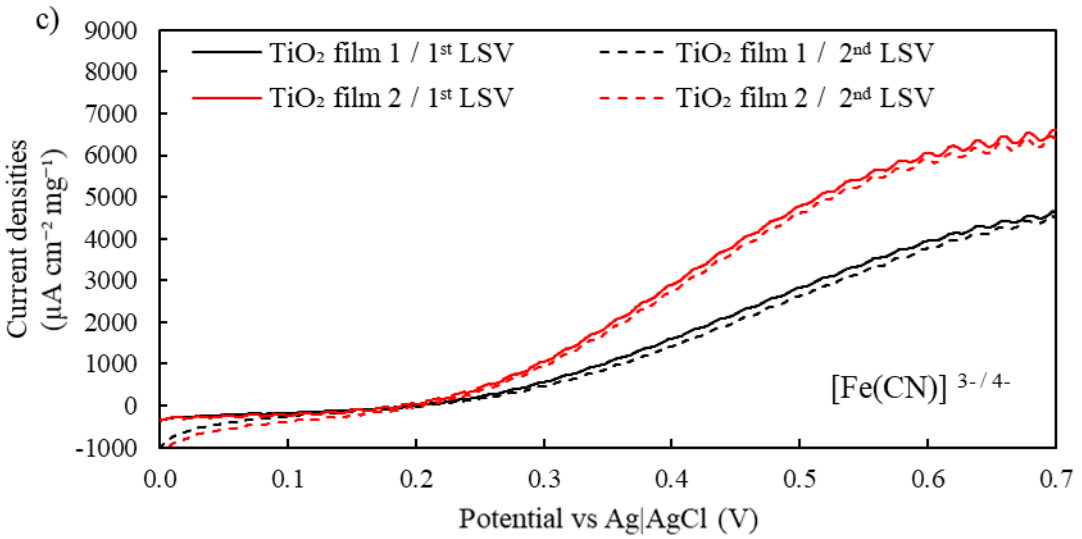
c)
TiO₂ film 1 / 1st LSV
TiO₂ film 1 / 2nd LSV
TiO₂ film 2 / 1st LSV
TiO₂ film 2 / 2nd LSV
[Fe(CN)] 3-/4-
Current densities (µA cm⁻² mg⁻¹)
Potential vs Ag|AgCl (V)

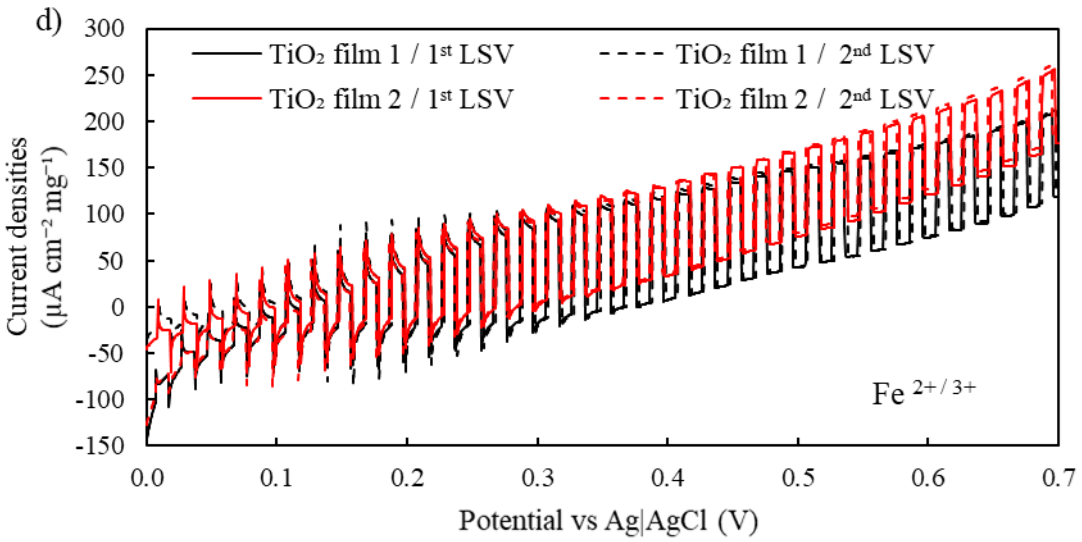
d)
TiO₂ film 1 / 1st LSV
TiO₂ film 1 / 2nd LSV
TiO₂ film 2 / 1st LSV
TiO₂ film 2 / 2nd LSV
Fe 2+/3+
Current densities (µA cm⁻² mg⁻¹)
Potential vs Ag|AgCl (V)

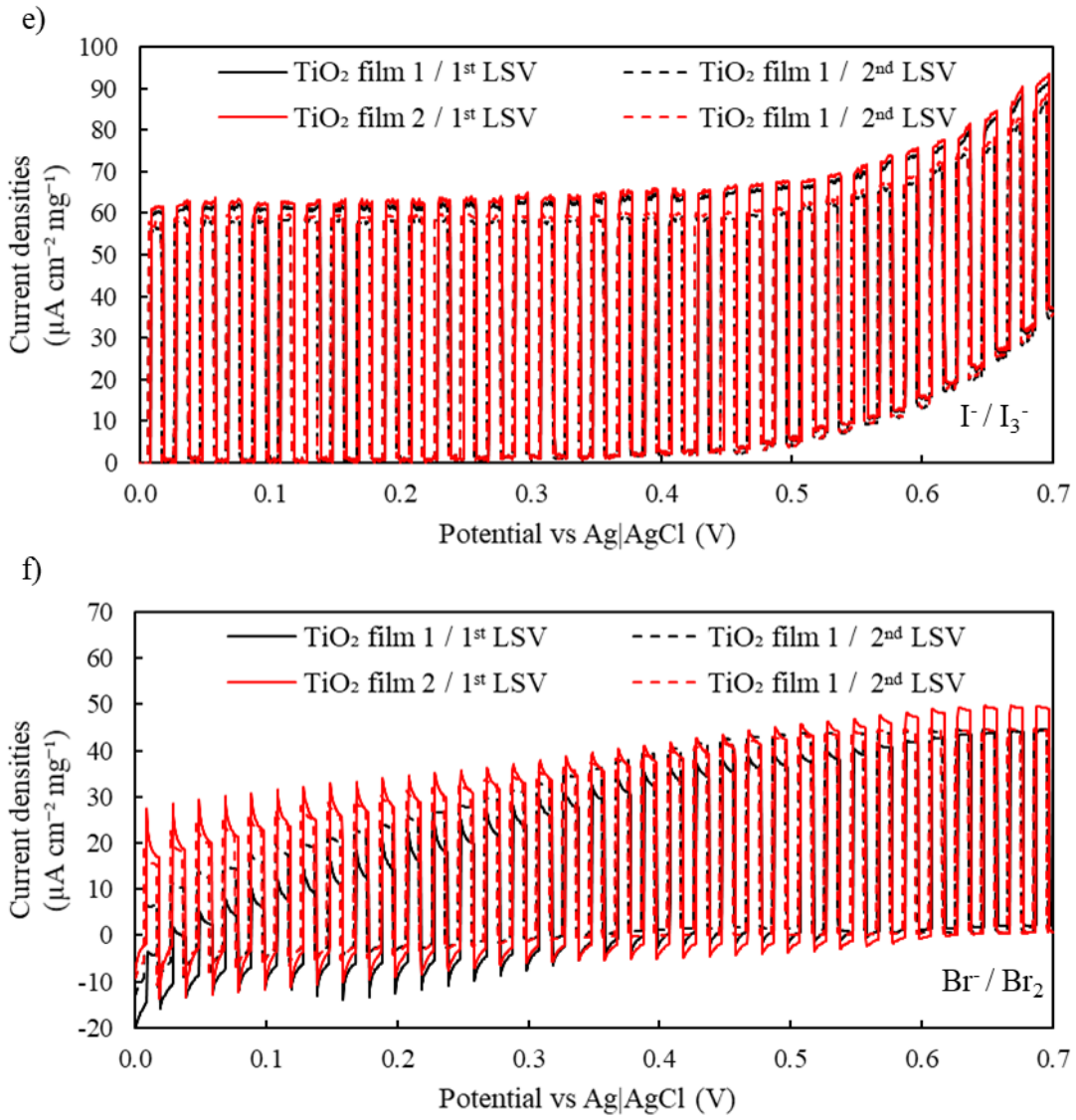

Figure 58: Linear sweep voltammetry between 0 V *vs.* Ag|AgCl and 0.7 V vs. Ag|AgCl with a scan rate of 0.5 mV s^{-1} under chopped light (The shutter was closed for 20 seconds and opened for 20 seconds) for a a) full vanadium cell, b) full vanadium non-aqueous cell, c) ferrocyanide/ferricyanide cell, d) ferrous chromium cell e) triiodide-vanadium cell and f) bromide-vanadium cell.

6.3.2. Two electrode measurements

To test the full cell behaviour, the cell combinations described above were tested in two-electrode mode, with a TiO_2 photoanode and a Pt negative electrode. In this set-up the photo-anode was connected to the working electrode cable and the negative electrode connected to the counter electrode cable of the potentiostats. The reference electrode cable from the potentiostats was then connected to the negative electrode, and the cell voltage (photoanode – Pt negative electrode) potential was controlled at 0 V *vs.* Ag|AgCl under chopped light. This is a zero-bias cell configuration.

Full vanadium cell has been tested [11]. The chronoamperometry (Figure 58 a) presents a photocurrent of 10 µA cm^{-2} mg^{-1} which is similar than the value on the linear sweep voltammetry. The presence of the anodic and cathodic peak was found to be related to the electron-hole recombination when the light was switched. The potential (Figure 60 a) of the photoanode, when the light was on, decreased from 0.2 V *vs.* Ag|AgCl to 0.13 V *vs.* Ag|AgCl in 20 s while that, when the light was off, increased back to 0.2 V *vs.* Ag|AgCl. The absence of instantaneous increase and decrease of the potential indicates trap sites [63]–[66], where charge carriers were trapped in a system and no longer participate in the charge transport. As shown in the previous study, the reaction in the cathode was driven by oxygen reduction, not by V^{3+} reduction.

When using the full vanadium non-aqueous cell, the use of acetonitrile as a solvent provides the photoinduced water splitting. The chronoamperometry showed a photooxidation of the V^{4+} to V^{5+} (2 µA cm^{-2} mg^{-1}, Figure 58 b) with the same shape as that of the previous experiment. However, the potential curves were difficult to interpret due to a large instability (Figure 60 b). According to the different pH and solvent used in these two systems, the clear conclusion of undergoing reactions on both electrodes could not be easily drawn.

In the case of $Fe^{2+/}Fe^{3+}$, two cathodic electrolytes have been tested. First, ferrous chromium cell was tested[11].The photocurrent (Figure 58 c) from chromic chloride was two times higher as compared to vanadium. However, a massive part of the photocurrent seems to be lost due to the electron-hole recombination. However, the fast decrease and increase of the potential when the light was switched suggested a low number of trap sites. The potential of the photoelectrode (Figure 60 c) both in the dark (0.37 V *vs.* Ag|AgCl) and in the light (0.26 V *vs.* Ag|AgCl) was higher than those of the vanadium. However, the difference was probably associated with a better counter electrode oxygen evolution.

Apart from chromic chloride, 0.1 M ferrous sulphate was employed to test the feasibility of a full iron half solid solar redox flow battery [11]. A test of a similar cell but with a pt negative (counter electrode) have been realised. The iron solid formed were deposit on the pt electrode. The photocurrent using ferrous sulphate electrolyte (Figure 58 d) was higher than that using vanadium but lower than that using chromium electrolyte (15 µA cm^{-2} mg^{-1}) and did not show any electron-hole recombination. The potential when the light was on indicated a low number of trap sites. The potential of the photoelectrode (Figure 60 d) was 0.38 V *vs.* Ag|AgCl in the dark and 0.37 V *vs.* Ag|AgCl in the light. Therefore, the potential difference was only 0.01 V *vs.* Ag|AgCl and still induced a higher photocurrent than vanadium.

In the case of triiodide-vanadium cell, the test has been performed against a V^{3+} in H_2SO_4 electrolyte. The photocurrent (Figure 58 e) was much higher than the one from full vanadium cell (50 µA cm^{-2} mg^{-1}) without any electron-hole recombination. The potential when the light was on suggested a large number of trap sites. However, the potential of the photoelectrode (Figure 60 e) was -0.01 V *vs.* Ag|AgCl in the dark and -0.12 V *vs.* Ag|AgCl in the light. However, because triiodide electrolyte used was not an aqueous electrolyte, the potential could be misinterpreted.

Finally, bromide-vanadium cell was tested [11]. The chronoamperometry (Figure 58 f) shows photocurrent, which is equal to the full iron, but with lot of electron-hole recombination anodic and cathodic peaks. The potential when the light was on suggests a large number of trap sites. However, the potential of the photoelectrode (Figure 60 f) was 0.15 V *vs.* Ag|AgCl in the dark and 0 V *vs.* Ag|AgCl in the light. Among redox couples, vanadium/bromide, vanadium/triiodide and iron/chromium and full iron cell appear as a promising candidate for replacing the full vanadium solar redox flow battery.

Unfortunately, in the case of ferrous based cell, the large photocurrent seen in the three-electrode measurement was not translated into a high photocurrent in the two electrodes measurement. Therefore, the two electrodes measurement could be conducted with an external applied potential (bias) to shift the photoanode potential and try to increase the photocurrent. First, this test has been performed on a full vanadium cell (Figure 61 a). the addition of a bias potential in the cell affected the diminution of the electron-hole recombination leading to an increase of the photocurrent from 10 µA cm^{-2} mg^{-1} to 20 µA cm^{-2} mg^{-1}. However, in the case of the ferrous chromium cell (Figure 61 b):, the introduction of a bias showed a significant effect on the oxidation of Fe^{2+} in Fe^{3+}. The oxidation increased even in the dark and besides the photocurrent increased significantly by the diminution of the electron-hole recombination. In conclusion, in the case of a full vanadium cell, the introduction of bias did not seem to improve the photocurrent drastically. However, in the case of ferrous chromium cell, the addition of a 0.5 V *vs.* Pt bias increased the photocurrent to 50 µA cm^{-2} mg^{-1}.

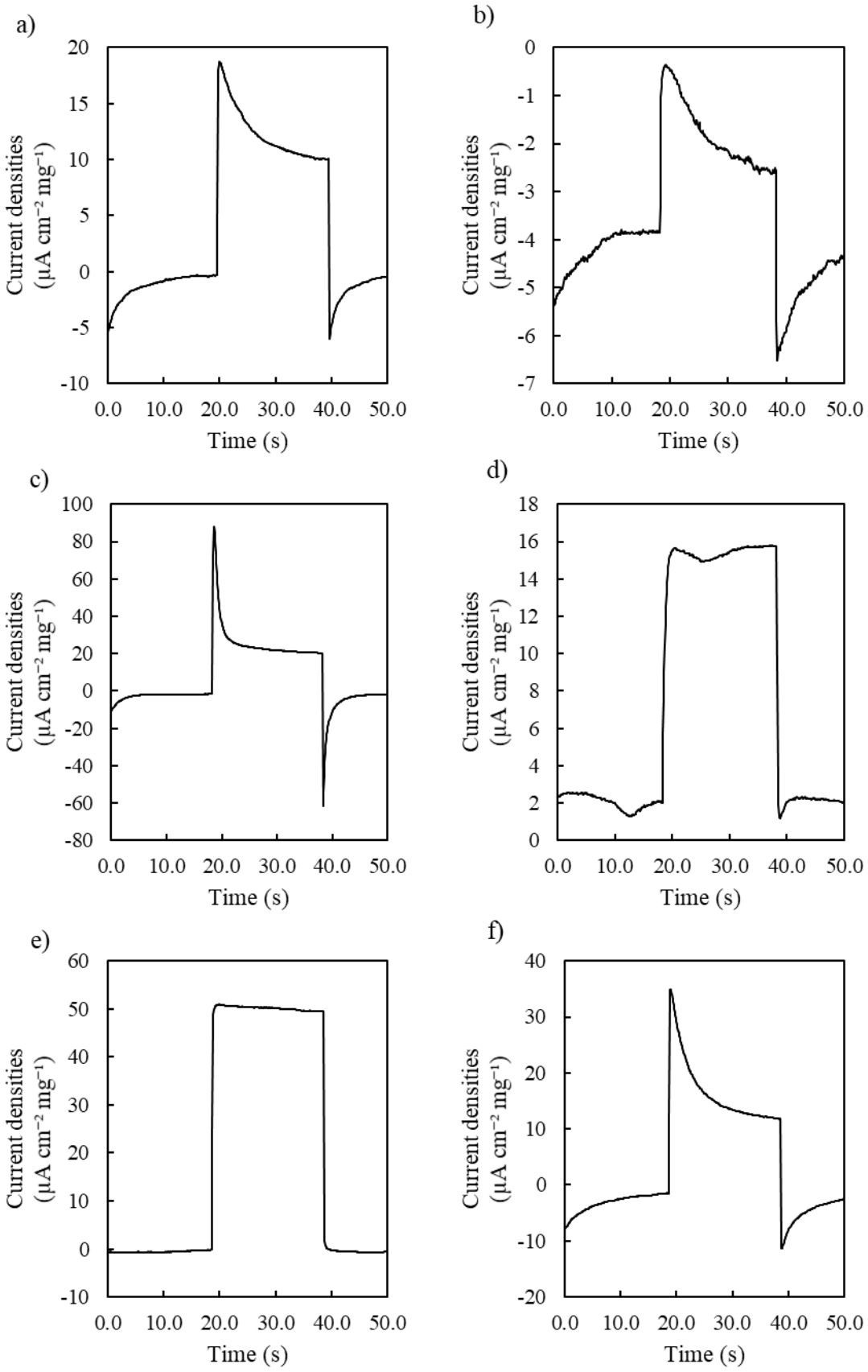

Figure 59: Current density chronoamperometry under zero bias conditions under chopped light a) full vanadium cell, b) full vanadium non-aqueous cell, c) ferrous chromium cell, d) full ferrous cell ferrous chromium cell e) triiodide-vanadium cell and f) bromide-vanadium cell.

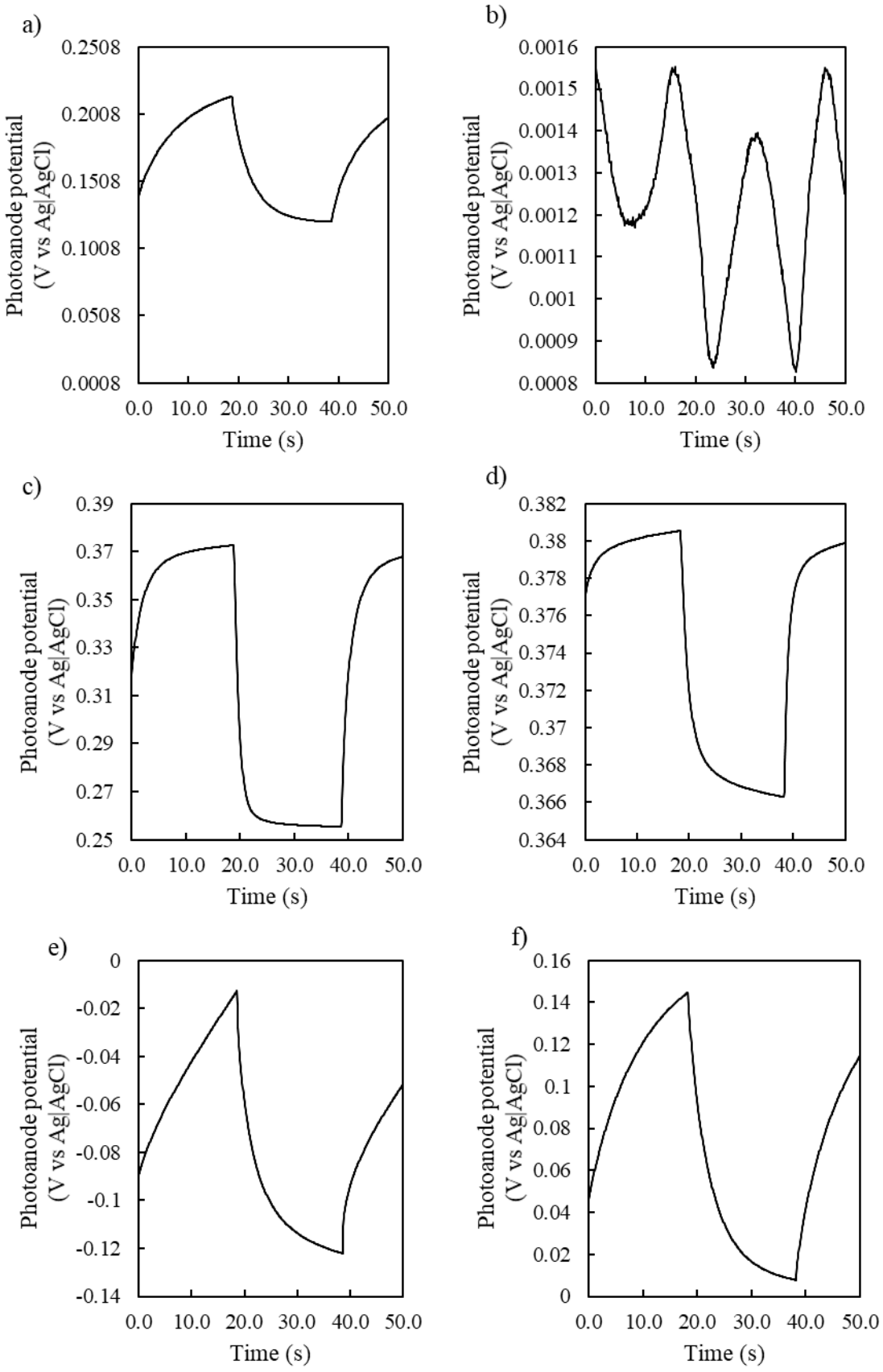

Figure 60: Potential of the photoanode during the chronoamperometry under zero bias conditions under chopped light a) full vanadium cell, b) full vanadium non-aqueous cell, c) ferrous chromium cell, d) full ferrous cell ferrous chromium cell e) triiodide-vanadium cell and f) bromide-vanadium cell.

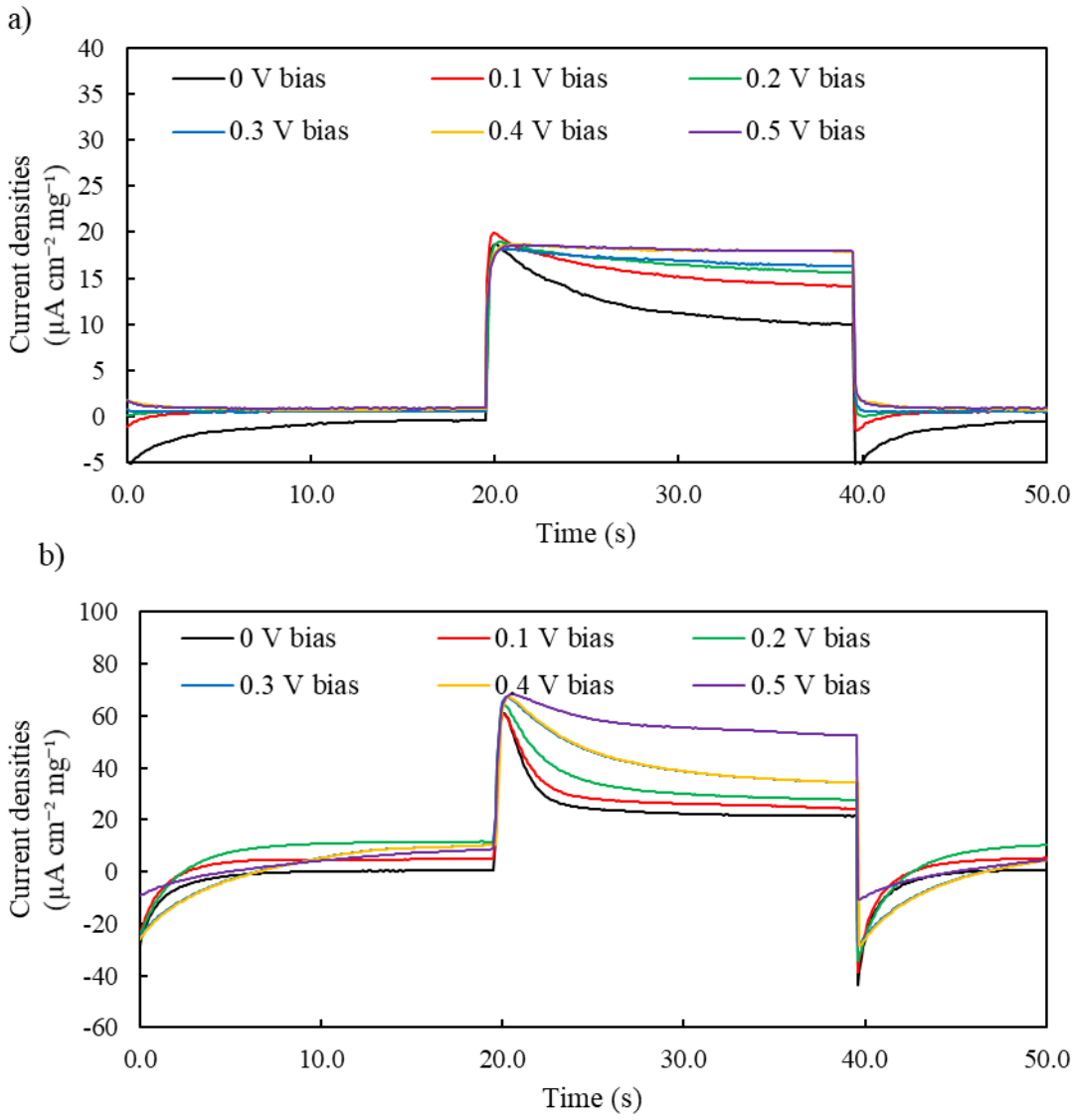

Figure 61: Chronoamperometry with different cell voltage (bias) under chopped light. a) full vanadium cell, b) ferrous chromium cell.

6.4. Conclusion

In conclusion, one of the promising redox couples was bromide, which gave a higher photocurrent of 43 ± 2 µA cm^{-2} mg^{-1} compared to that of $VOSO_4$. However, the bromide is a toxic material, which is challenging to be reuse or recycle. Another promising redox couple was a standard dye-sensitised redox couple triiodide/iodide which gave a photocurrent of 59.5 ± 0.5 µA cm^{-2} mg^{-1} and that of 50 µA cm^{-2} mg^{-1} against V^{3+} cathodic electrolyte on a cell without bias. It exhibited five times higher photocurrent compared to that obtained from V^{4+} anodic electrolyte. However, the reaction is kinetically complex: I_3^- gave a mix of I_2 and I^- where the I_2 could be reduced to $I_2^-$and further reduced to form I_3^- and I^-. While the I_2 recombination process was slow because very few I_2 got absorbed. I_2 is highly volatile and corrosive. Apart from bromide and triiodide/iodide redox couples, iron III/II also appear as a promising candidate as it is surprisingly the less expensive and the most environmentally friendly redox couple. The iron III/II was shown to give a photocurrent of 119 ± 8 µA cm^{-2} mg^{-1} at 0.5 V *vs.* Ag|AgCl. The use of iron (II) as cathodic electrolyte allowed the creation of a full iron battery. However, the photocurrent obtained was only 15 µA cm^{-2} mg^{-1} while the use of chromium as cathodic could improve the photocurrent to 20 µA cm^{-2} mg^{-1}. Finally, by applying the bias potential of 0.5 V *vs.* Pt, the photocurrent reached 50 µA cm^{-2} mg^{-1}.

7. Conclusion and Future Work

7.1. Overall summary

In this work, the first objective was to explain the different reactions at the photo-electrodes. Therefore, a series of three-electrode measurements and UV-Vis spectroscopy was performed. It was concluded that during tow electrode, zero bias conditions, the presence of oxygen in the negative electrolyte chamber (the counter electrode chamber in three-electrode measurements) allowed the oxygen reduction reaction to occur rather than the reduction of vanadium species. As the potential for the oxygen reduction reaction on Pt was more positive that the V^{3+} reduction reactions (in the negative chamber), under zero-bias conditions to causes the potential of the photoanode to be more positive and thus higher photo currents could occur.

In the photoelectrode, when the light was off the potential is at 0.35 V *vs*. Ag|AgCl (when $VOSO_4$ is used in the non-deaerated counter electrode chamber without) or 0.3 V *vs*. Ag|AgCl (when VCl_3 is used in the non-deaerated counter electrode chamber. When the light was on, two phenomena took place; the first was the formation of a double layer due to the change between the open circuit potential and the light-induced potential. This double layer vanished in a few minutes. The second phenomenon was an anodic peak due to the electron-hole recombination by the reduction of the photogenerated V^{5+} species at the surface of the electrode. However, after a few seconds, the photo-oxidation reached an equilibrium while the photocurrent remained steady. Water splitting was observed leading to a release of gas into the system. Finally, when the light was turned back to off, a cathodic current occurred. It was due to the recombination of the holes at the surface of the V^{5+} with the electrons still in the surface of the semiconductor, resulting in an increase of V^{5+} reduction.

After the reactions were identified, the second objective was to improve the obtained photocurrent. The effect of the different deposition processes to form P-25 TiO_2 based layers, including screen printing, doctor blading, airflow spray coating, and ultrasonic spray coating on the photocurrent were investigated. The conclusion was that the ultrasonic spray coating was the most reproducible technique. Changing the solvent and evaporation temperature have an effect on the structure of the film but did not result in a major improvement of the photocurrent (photocurrents around 10 $\mu A\ cm^{-2}\ mg^{-1}$). Therefore, a change in the structure of the TiO_2 layer by adding titanium isopropoxide was investigated. It was proposed that this

titanium isopropoxide addition would allow the formation of a better network between the particles. The composition of 85 wt% of P25 powder and 15 wt% of TiO_2 from the titanium isopropoxide hydrolysis was the best composition. This result supported the hypothesis that a better connection between the FTO and TiO_2 particles was the key to improve the photocurrent. To confirm this, thin and compact underlayers were investigated. The best one was obtained by growing an initial layer between the FTO and the main TiO_2 layer *via* a hydrothermal method, which resulted in a highly crystalline underlayer.

Another way to increase the photocurrent was to deposit some gold nanoclusters or nanoparticles on the top of the TiO_2 film. The deposition of 1.7 wt% 25 nm-gold nanoparticles led to 30 % increase in the photocurrent compared to the standard film. However, the improvement was temporary and disappeared after a few cycles. Besides, the deposition of 8.5 wt% of Au_6 nanoclusters resulted in up to 50% higher the photocurrent compared to that of bare TiO_2 with much higher stability.

Finally, a way to improve the photocurrent of the photoelectrode was to use different redox couples. One of the most promising redox couples was bromide which gave a higher photocurrent of 43 ± 2 µA cm^{-2} mg^{-1}, similar to that of $VOSO_4$. However, the bromide is a toxic material which is challenging to be reused and recycled. Another one was a standard dye-sensitised redox couple, triiodide/iodide, which gave a photocurrent of 59.5 ± 0.5 µA cm^{-2} mg^{-1} and showed a photocurrent of 50 µA cm^{-2} mg^{-1} against vanadium (III) cathodic electrolyte on a cell without the bias. It exhibited five times higher photocurrent compared to that obtained from vanadium (IV) anodic electrolyte. However, the reaction is complex: I_3^- give a mix of I_2 and I^- where I_2 could be reduced to I_2^- and further reduced to form I_3^- and I^-. While the I_2 recombination process was slow because very few I_2 got absorbed. However, the production of I_2 is an issue due to its highly volatile and corrosive behaviour. Besides, iron III/II appear as another promising redox couple as it is surprisingly less expensive and more environmentally friendly. The iron (III)/ iron (II) give a photocurrent of 119 ± 8 µA cm^{-2} mg^{-1} at 0.5 V *vs.* Ag|AgCl. The use of iron (II) as cathodic electrolyte allowed the creation of a full iron battery, however, the photocurrent obtained was only 15 µA cm^{-2} mg^{-1}. A higher photocurrent of 20 µA cm^{-2} mg^{-1} could be achieved using chromium as cathodic gave. Finally, by creating a bias of 0.5 V *vs.* Pt, the photocurrent reached 50 µA cm^{-2} mg^{-1}.

Therefore, by combining the best photocurrent of each study, a photocurrent of 82 ± 0.5 µA cm^{-2} (410 ± 0.5 µA cm^{-2} mg^{-1}) could be achieved for $VOSO_4$ electrolyte at 0.5 V *vs.* Ag|AgCl

with the addition of 8.5 wt% of Au_6 nanoclusters to the hydrothermal growth film with an additional 85% P-25 15% TTIP film (Figure 62). The linear sweep voltammetry showed, in both cases, the increase of the photocurrent when the potential increase. With the addition of Au_6 nanoclusters, the apparition of electron-hole recombination is higher until 0.3 V *vs.* Ag|AgCl. The triiodide electrolyte gave a photocurrent of 99.3 ± 0.2 µA cm^{-2} (496 ± 0.2 µA cm^{-2} mg^{-1}) ^{at} 0.5 V *vs.* Ag|AgCl. However, there is no sign of electron-hole recombination. The Fe^{2+} electrolyte allowed a photocurrent of 107 ± 0.4 µA cm^{-2} (535± 0.4 µA cm^{-2} mg^{-1}) at 0.5 V *vs.* Ag|AgCl (Figure 63) with the same electron-hole recombination peak as that using $VOSO_4$ electrolyte.

In term of power, even with the improvement of the photocurrent of 82 ± 0.5 µA cm^{-2}, the Solar redox flow battery develop a power of 82 µW cm^{-2} (usual dye sensitized solar cell 120 000 µW cm^{-2}). Which leads to an cell efficiency of 0.0003% against 12-24 % [312] for dye sensitized solar cell. In term of price, a dye-sensitized solar cell will cost around 18 000 USD m^{-2} plus a Li-ion battery at 130-200 USD per battery. For the full vanadium solar redox flow battery the photoelectrode will cost about 40 USD m^{-2} without gold cluster, 73 USD L^{-1} for the electrolyte 16 000 -26 000 USD per redox flow battery (could require two one photo charging and another for discharge). Unfortunately, the two technologies are difficult to compare due to the uncertainty and the usage difference, but the advantage of the solar redox flow battery is the fix cost of the redox flow battery (except the electrolyte) and in comparison, the small price of the photo electrode by m^{-2}.

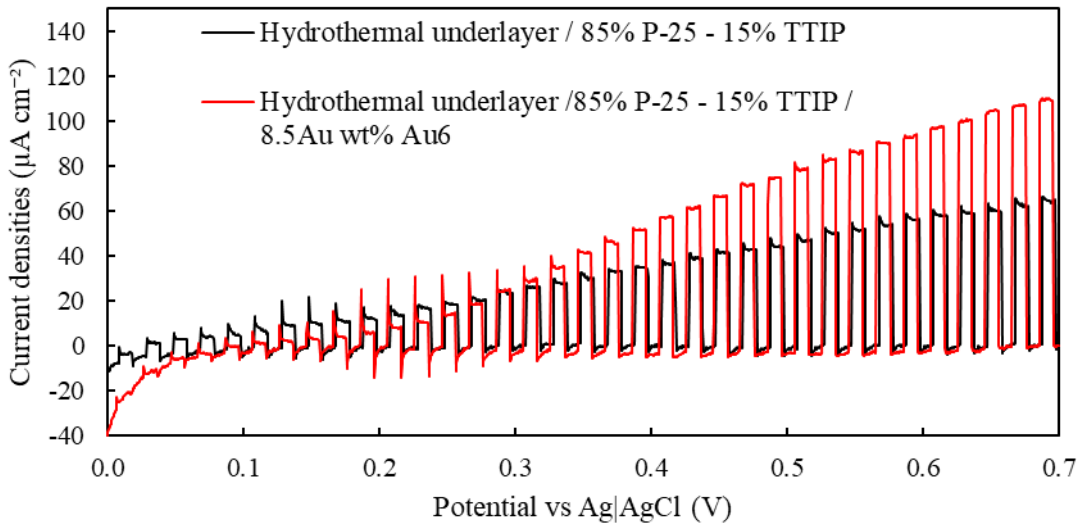

Figure 62: Linear sweep voltammetry of the hydrothermal with 85-15 TiO_2 film with and without Au_6 nanoclusters using $VOSO_4$ electrolyte.

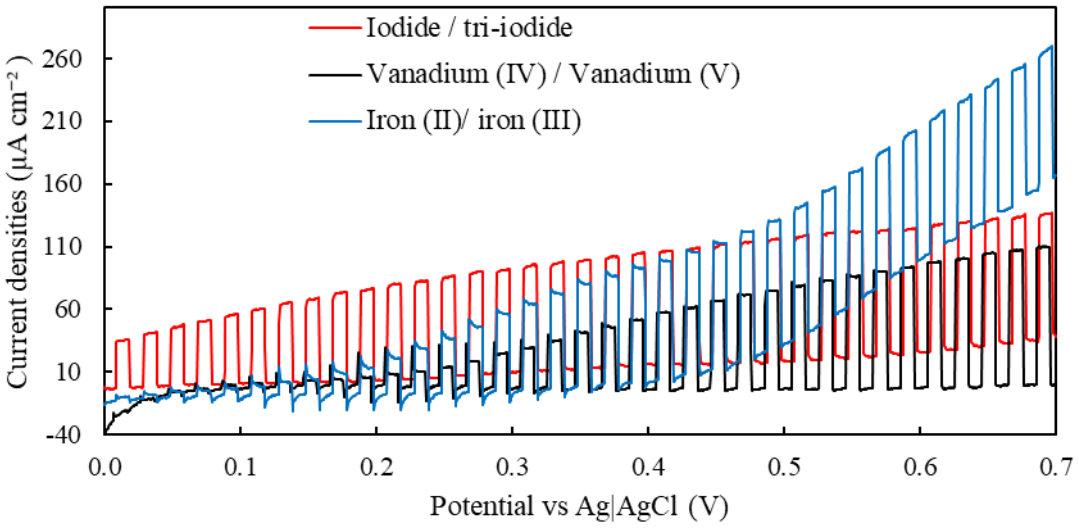

Figure 63: Linear sweep voltammetry of the hydrothermal with 85-15 TiO_2 film with Au_6 nanoclusters using $VOSO_4$, I_3^-, and Fe^{2+} electrolyte.

7.2. Future works.

Firstly, the reactions at the photoelectrode have been well studied, however, further study could be conducted on the counter electrode. A better counter electrode is required to be able to obtain a good solar redox flow battery. As shown the used 85% P-25 15% TTIP film deposited by ultrasonic spraying was a proper deposition process specially combined with the deposition of underlayer. However, the deposition of the underlayer has not been fully investigated, in particular, the hydrothermal growth of the TiO_2 films could be largely improved and used as a way to grow a complete film. The reproducibility of such process is quite challenging. The effect of various parameters such as temperature, moisture etc. on TiO_2 growth would allow a better understanding and hence improve the performance. Finally, another deposition method could be investigated to obtain proper underlayer.

The test of Au nanoparticles and nanoclusters deposited on TiO_2 film has been focused on nanoclusters and the effect of the different Au nanoparticle deposition methods, whereas the Au nanoparticles size effect has not been explored. Besides gold nanoclusters, the effect of the deposition of other metal nanoclusters, for example Pt, Ru and Ag nanoclusters onto TiO_2 film, is also an interesting direction to investigate. The formation of porous TiO_2 nanosphere could lead to the direct incorporation of the nanoclusters within the spheres. The porous sphere improving the stability of the clusters, then protected the clusters. The obtained metal cluster doped TiO_2 film could then have a longer lifetime.

The study realised on different redox couples leads to an opening of the project. indeed, by using triiodide, for example, it could allow the use of dye particles for absorbing a larger part of the solar spectrum. However, the use of dye will involve some research on the way to keep them on the semiconductor surface under the electrolyte flow. The use of Fe^{2+} and the improvement of the photocurrent by the introduction of bias, lead to the study of a bias dual photovoltaic and photoelectrochemical cell. the solar redox flow battery study should go to a focus on solar driven redox flow battery? Or, is an unbiased commercial solar redox flow battery possible?

REFERENCES

[1] M. Šúri, T. A. Huld, E. D. Dunlop, and H. A. Ossenbrink, "Potential of solar electricity generation in the European Union member states and candidate countries," *Sol. Energy*, vol. 81, no. 10, pp. 1295–1305, 2007, doi: 10.1016/j.solener.2006.12.007.

[2] P. M. Cox, R. a Betts, C. D. Jones, S. a Spall, and I. J. Totterdell, "Acceleration of global warming due to carbon-cycle feedbacks in a coupled climate model (vol 408, pg 184, 2000)," *Nature*, vol. 408, no. 6813, p. 750, 2000, doi: 10.1038/35041539.

[3] N. A. Owen, O. R. Inderwildi, and D. A. King, "The status of conventional world oil reserves-Hype or cause for concern?," *Energy Policy*, vol. 38, no. 8, pp. 4743–4749, 2010, doi: 10.1016/j.enpol.2010.02.026.

[4] N. L. Panwar, S. C. Kaushik, and S. Kothari, "Role of renewable energy sources in environmental protection: A review," *Renew. Sustain. Energy Rev.*, vol. 15, no. 3, pp. 1513–1524, 2011, doi: 10.1016/j.rser.2010.11.037.

[5] B. Liu, X. Zhao, C. Terashima, A. Fujishima, and K. Nakata, "Thermodynamic and kinetic analysis of heterogeneous photocatalysis for semiconductor systems," *Phys. Chem. Chem. Phys.*, vol. 16, no. 19, p. 8751, 2014, doi: 10.1039/c3cp55317e.

[6] M. Grätzel, "Photoelectrochemical Cells," *Nature*, vol. 414, no. November, pp. 457–481, 2001, doi: 10.1007/978-1-4899-0418-8_11.

[7] J. P. Painuly, "Barriers to renewable energy penetration: A framework for analysis," *Renew. Energy*, vol. 24, no. 1, pp. 73–89, 2001, doi: 10.1016/S0960-1481(00)00186-5.

[8] I. Dincer, "Renewable energy and sustainable development: a crucial review," *Renew. Sustain. Energy Rev.*, vol. 4, no. 2, pp. 157–175, 2000, doi: 10.1016/S1364-0321(99)00011-8.

[9] J. D. Hamilton, "CAUSES AND CONSEQUENCES OF THE OIL SHOCK OF 2007-08," *NBER Work. Pap.*, 2009.

[10] Ministry of Business Innovation & Employment (MBIE), "Energy in New Zealand 2017," p. 47, 2017, [Online]. Available: http://www.med.govt.nz/sectors-industries/energy/energy-modelling/publications/energy-in-new-zealand-2013/Energy-in-New-Zealand-2013.pdf.

[11] A. Z. Weber, M. M. Mench, J. P. Meyers, P. N. Ross, J. T. Gostick, and Q. Liu, "Redox flow batteries: A review," *J. Appl. Electrochem.*, vol. 41, no. 10, pp. 1137–1164, 2011, doi: 10.1007/s10800-011-0348-2.

[12] S. (Arcadia, C. U. Narayan, S. G. K. (Hacienda H. C. U. Prakash, B. (Los A. C. U.

Yang, L. (Los A. C. U. Hoober-burkhardt, and S. (Los A. C. U. Krishnamoorthy, "INEXPENSIVE METAL-FREE ORGANIC REDOX FLOW BATTERY (ORBAT) FOR GRID-SCALE STORAGE - UNIVERSITY OF SOUTHERN CALIFORNIA," Apr. 06, 2020.

[13] B. Yang, L. Hoober-Burkhardt, F. Wang, G. K. Surya Prakash, and S. R. Narayanan, "An Inexpensive Aqueous Flow Battery for Large-Scale Electrical Energy Storage Based on Water-Soluble Organic Redox Couples," *J. Electrochem. Soc.*, vol. 161, no. 9, pp. A1371–A1380, 2014, doi: 10.1149/2.1001409jes.

[14] C. Chu, W. Lee, and Y. Kwon, "The effect of additives on the performance of aqueous organic redox flow battery using quinoxaline and ferrocyanide redox couple," *Korean Chem. Eng. Res.*, vol. 57, no. 6, pp. 847–852, 2019, doi: 10.9713/kcer.2019.57.6.847.

[15] J. Winsberg *et al.*, "Poly(boron-dipyrromethene)-A Redox-Active Polymer Class for Polymer Redox-Flow Batteries," *Chem. Mater.*, vol. 28, no. 10, pp. 3401–3405, 2016, doi: 10.1021/acs.chemmater.6b00640.

[16] T. Janoschka *et al.*, "An aqueous, polymer-based redox-flow battery using non-corrosive, safe, and low-cost materials," *Nature*, vol. 527, no. 7576, pp. 78–81, 2015, doi: 10.1038/nature15746.

[17] M. Skyllas-Kozocos and F. Grossmith, "Efficient Vanadium Redox Flow Cell," *J. Electrochem. Soc.*, vol. 134, no. 12, pp. 2950–2953, 1987, doi: 10.1149/1.2100321.

[18] C. Ding, H. Zhang, X. Li, T. Liu, and F. Xing, "Vanadium flow battery for energy storage: Prospects and challenges," *J. Phys. Chem. Lett.*, vol. 4, no. 8, pp. 1281–1294, 2013, doi: 10.1021/jz4001032.

[19] M. Rychcik and M. Skyllas-Kazacos, "Evaluation of electrode materials for vanadium redox cell," *J. Power Sources*, vol. 19, no. 1, pp. 45–54, 1987, doi: 10.1016/0378-7753(87)80006-X.

[20] M. Skyllas-Kazacos, "Efficient Vanadium Redox Flow Cell," *J. Electrochem. Soc.*, vol. 134, no. 12, p. 2950, 1987, doi: 10.1149/1.2100321.

[21] E. Sum and M. Skyllas-Kazacos, "A study of the V(II)/V(III) redox couple for redox flow cell applications," *J. Power Sources*, vol. 15, no. 2–3, pp. 179–190, 1985, doi: 10.1016/0378-7753(85)80071-9.

[22] M. Rychcik and M. Skyllas-Kazacos, "Characteristics of a new all-vanadium redox flow battery," *J. Power Sources*, vol. 22, no. 1, pp. 59–67, Jan. 1988, doi: 10.1016/0378-7753(88)80005-3.

[23] M. Kazacos, M. Cheng, and M. Skyllas-Kazacos, "Vanadium redox cell electrolyte optimization studies," *J. Appl. Electrochem.*, vol. 20, no. 3, pp. 463–467, 1990, doi:

10.1007/BF01076057.

[24] M. Skyllas-Kazacos, “Thermal Stability of Concentrated V(V) Electrolytes in the Vanadium Redox Cell,” *J. Electrochem. Soc.*, vol. 143, no. 4, p. L86, 1996, doi: 10.1149/1.1836609.

[25] F. Rahman and M. Skyllas-Kazacos, “Solubility of vanadyl sulfate in concentrated sulfuric acid solutions,” *J. Power Sources*, vol. 72, no. 2, pp. 105–110, 1998, doi: 10.1016/S0378-7753(97)02692-X.

[26] L. Li *et al.*, “A stable vanadium redox-flow battery with high energy density for large-scale energy storage,” *Adv. Energy Mater.*, vol. 1, no. 3, pp. 394–400, 2011, doi: 10.1002/aenm.201100008.

[27] M. Skyllas-Kazacos, M. H. Chakrabarti, S. A. Hajimolana, F. S. Mjalli, and M. Saleem, “Progress in Flow Battery Research and Development,” *J. Electrochem. Soc.*, vol. 158, no. 8, p. R55, 2011, doi: 10.1149/1.3599565.

[28] P. Leung, X. Li, C. Ponce de León, L. Berlouis, C. T. J. Low, and F. C. Walsh, “Progress in redox flow batteries, remaining challenges and their applications in energy storage,” *RSC Adv.*, vol. 2, no. 27, p. 10125, 2012, doi: 10.1039/c2ra21342g.

[29] J. M. Dickson, “(12) Patent Application Publication (10) Pub . No .: US 2003 / 0168404 A1 Pervaporation with Water / Ethanol Mixtures : Effect of Temperature Temperature (C) Separation FG . A Temperature (C) Flux,” 2003.

[30] K. W. Knehr and E. C. Kumbur, “Open circuit voltage of vanadium redox flow batteries: Discrepancy between models and experiments,” *Electrochem. commun.*, vol. 13, no. 4, pp. 342–345, 2011, doi: 10.1016/j.elecom.2011.01.020.

[31] C. H. Li, X. J. Zhu, G. Y. Cao, S. Sui, and M. R. Hu, “Dynamic modeling and sizing optimization of stand-alone photovoltaic power systems using hybrid energy storage technology,” *Renew. Energy*, vol. 34, no. 3, pp. 815–826, 2009, doi: 10.1016/j.renene.2008.04.018.

[32] reportsnreports, “Redox Flow Battery Market Value to Hit 370 Million US$ by 2025, at a CAGR of 14.3%, Business Trends, Global Projections 2019.” https://www.prnewswire.com/news-releases/redox-flow-battery-market-value-to-hit-370-million-us-by-2025--at-a-cagr-of-14-3-business-trends-global-projections-2019--300903369.html (accessed May 04, 2020).

[33] J. R. McKone, F. J. DiSalvo, and H. D. Abruña, “Solar energy conversion, storage, and release using an integrated solar-driven redox flow battery,” *J. Mater. Chem. A*, vol. 5, no. 11, pp. 5362–5372, 2017, doi: 10.1039/C7TA00555E.

[34] G. Hodes, D. Cahen, and J. Manassen, “Tungsten trioxide as a photoanode for a

photoelectrochemical cell (PEC)," *Nature*, vol. 260, no. 5549, pp. 312–313, 1976, doi: 10.1038/260312a0.

[35] S. Licht and D. Peramunage, "Efficient photoelectrochemical solar cells from electrolyte modification," *Nature*, vol. 345, pp. 330–333, 1990, doi: 10.1038/345330a0.

[36] S. Licht *et al.*, "High efficiency n-Cd(Se,Te)/S photoelectrochemical cell resulting from solution chemistry control," *Appl. Phys. Lett.*, vol. 46, no. 6, pp. 608–610, 1985, doi: 10.1063/1.95556.

[37] M. Grätzel, "Dye-sensitized solar cells," *J. Photochem. Photobiol. C Photochem. Rev.*, vol. 4, no. 2, pp. 145–153, 2003, doi: 10.1016/S1389-5567(03)00026-1.

[38] S.-Q. Fan, C.-J. Li, C.-X. Li, G.-J. Liu, G.-J. Yang, and L.-Z. Zhang, "Preliminary Study of Performance of Dye-Sensitized Solar Cell of Nano-TiO2 Coating Deposited by Vacuum Cold Spraying," *Mater. Trans.*, vol. 47, no. 7, pp. 1703–1709, 2006, doi: 10.2320/matertrans.47.1703.

[39] B. O'Regan and M. Grätzel, "A low-cost, high-efficiency solar cell based on dye-sensitized colloidal TiO2 films," *Nature*, vol. 353, no. 6346, pp. 737–740, 1991, doi: 10.1038/353737a0.

[40] M. A. Mahmoudzadeh, A. R. Usgaocar, J. Giorgio, D. L. Officer, G. G. Wallace, and J. D. W. Madden, "A high energy density solar rechargeable redox battery," *J. Mater. Chem. A*, vol. 4, no. 9, pp. 3446–3452, 2016, doi: 10.1039/C5TA08618C.

[41] N. F. Yan, G. R. Li, and X. P. Gao, "Solar rechargeable redox flow battery based on Li2WO4/LiI couples in dual-phase electrolytes," *J. Mater. Chem. A*, vol. 1, no. 24, p. 7012, 2013, doi: 10.1039/c3ta11360d.

[42] H. Nagai and H. Segawa, "Energy-storable dye-sensitized solar cell with a polypyrrole electrode," *Chem. Commun.*, no. 8, pp. 974–975, 2004, doi: 10.1039/B400439F.

[43] P. Liu, Y. L. Cao, G. R. Li, X. P. Gao, X. P. Ai, and H. X. Yang, "A solar rechargeable flow battery based on photoregeneration of two soluble redox couples," *ChemSusChem*, vol. 6, no. 5, pp. 802–806, 2013, doi: 10.1002/cssc.201200962.

[44] B. Keita and L. Nadjo, "Electrochemistry and photoelectrochemistry of sodium 9,10-anthraquinone-2,6-disulfonate in aqueous media. Application to rechargeable solar cells and to the synthesis of hydrogen peroxide," *J. Electroanal. Chem.*, vol. 163, no. 1–2, pp. 171–188, Mar. 1984, doi: 10.1016/S0022-0728(84)80050-9.

[45] M. Sharon, S. Kumar, N. P. Sathe, and S. R. Jawalekar, "Saur Viddyut Kosh IV: Study of a rechargeable solar battery with n-Pb3O4electrodes," *Sol. Cells*, vol. 12, no. 4, pp. 353–361, 1984, doi: 10.1016/0379-6787(84)90030-9.

[46] G. Betz, S. Fiechter, and H. Tributsch, “Photon energy conversion and storage with a light-driven insertion reaction,” *J. Appl. Phys.*, vol. 62, no. 11, pp. 4597–4605, 1987, doi: 10.1063/1.339056.

[47] M. Yu, W. D. McCulloch, D. R. Beauchamp, Z. Huang, X. Ren, and Y. Wu, “Aqueous Lithium-Iodine Solar Flow Battery for the Simultaneous Conversion and Storage of Solar Energy,” *J. Am. Chem. Soc.*, vol. 137, no. 26, pp. 8332–8335, 2015, doi: 10.1021/jacs.5b03626.

[48] W. Guo, X. Xue, S. Wang, C. Lin, and Z. L. Wang, “An integrated power pack of dye-sensitized solar cell and Li battery based on double-sided TiO2 nanotube arrays,” *Nano Lett.*, vol. 12, pp. 2520–2523, 2012, doi: 10.1021/nl3007159.

[49] Z. Wei, D. Liu, C. Hsu, and F. Liu, “All-vanadium redox photoelectrochemical cell: An approach to store solar energy,” *Electrochem. commun.*, vol. 45, pp. 79–82, 2014, doi: 10.1016/j.elecom.2014.05.018.

[50] D. Liu, Z. Wei, C. J. Hsu, Y. Shen, and F. Liu, “Efficient solar energy storage using A TiO2/WO3 tandem photoelectrode in an all-vanadium photoelectrochemical cell,” *Electrochim. Acta*, vol. 136, pp. 435–441, 2014, doi: 10.1016/j.electacta.2014.05.129.

[51] J. Azevedo *et al.*, “Unbiased solar energy storage: Photoelectrochemical redox flow battery,” *Nano Energy*, vol. 22, pp. 396–405, 2016, doi: 10.1016/j.nanoen.2016.02.029.

[52] X. Jiao *et al.*, “A microfluidic all-vanadium photoelectrochemical cell for solar energy storage,” *Electrochim. Acta*, vol. 258, pp. 842–849, 2017, doi: 10.1016/j.electacta.2017.11.134.

[53] Z. Wei, Y. Shen, D. Liu, and F. Liu, “An All-vanadium Continuous-flow Photoelectrochemical Cell for Extending State-of-charge in Solar Energy Storage,” *Sci. Rep.*, vol. 7, no. 1, pp. 1–9, 2017, doi: 10.1038/s41598-017-00585-y.

[54] D. Liu *et al.*, “Reversible Electron Storage in an All-Vanadium Photoelectrochemical Storage Cell: Synergy between Vanadium Redox and Hybrid Photocatalyst,” *ACS Catal.*, vol. 5, no. 4, pp. 2632–2639, 2015, doi: 10.1021/cs502024k.

[55] Q. Zhang and G. Cao, “Nanostructured photoelectrodes for dye-sensitized solar cells,” *Nano Today*, vol. 6, no. 1, pp. 91–109, 2011, doi: 10.1016/j.nantod.2010.12.007.

[56] Y. Diamant, S. Chappel, S. G. Chen, O. Melamed, and A. Zaban, “Core–shell nanoporous electrode for dye sensitized solar cells: the effect of shell characteristics on the electronic properties of the electrode,” *Coord. Chem. Rev.*, vol. 248, pp. 1271–1276, 2004, doi: 10.1016/j.ccr.2004.03.003.

[57] H. Choi, W. T. Chen, and P. V. Kamat, “Know thy nano neighbor. Plasmonic versus

electron charging effects of metal nanoparticles in dye-sensitized solar cells," *ACS Nano*, vol. 6, no. 5, pp. 4418–4427, 2012, doi: 10.1021/nn301137r.

[58] K. Uzaki, T. Nishimura, J. Usagawa, S. Hayase, M. Kono, and Y. Yamaguchi, "Dye-Sensitized Solar Cells Consisting of 3D-Electrodes—A Review: Aiming at High Efficiency From the View Point of Light Harvesting and Charge Collection," *J. Sol. Energy Eng.*, vol. 132, no. 2, p. 021204, May 2010, doi: 10.1115/1.4001182.

[59] A. M. Smith and S. Nie, "Semiconductor nanocrystals: Structure, properties, and band gap engineering," *Acc. Chem. Res.*, vol. 43, no. 2, pp. 190–200, 2010, doi: 10.1021/ar9001069.

[60] A. Kahn, "Fermi level, work function and vacuum level," *Mater. Horizons*, vol. 3, no. 1, pp. 7–10, 2016, doi: 10.1039/c5mh00160a.

[61] N. SATO, "Electrocthemistry of Semiconductors," *Tetsu-to-Hagane*, vol. 76, no. 9, pp. 1423–1436, 1990, doi: 10.2355/tetsutohagane1955.76.9_1423.

[62] J. T. Fulton, "Electrochemistry of the Neuron," *Process. Biol. Vis.*, vol. 1, no. 949, pp. 10–14, 2004.

[63] B. Mukherjee, W. Wilson, and V. Subramanian, "TiO2 nanotube (T-NT) surface treatment revisited: Implications of ZnO, TiCl4, and H2O2 treatment on the photoelectrochemical properties of T-NT and T-NT-CdSe," *Nanoscale*, vol. 5, no. 1, pp. 269–274, 2013, doi: 10.1039/c2nr31660a.

[64] G. Yun *et al.*, "Beneficial surface passivation of hydrothermally grown TiO 2 nanowires for solar water oxidation," *Appl. Surf. Sci.*, vol. 366, pp. 561–566, 2016, doi: 10.1016/j.apsusc.2016.01.111.

[65] Y. C. Pu *et al.*, "Au nanostructure-decorated TiO2 nanowires exhibiting photoactivity across entire UV-visible region for photoelectrochemical water splitting," *Nano Lett.*, vol. 13, no. 8, pp. 3817–3823, 2013, doi: 10.1021/nl4018385.

[66] G. Horowitz, "Capacitance-voltage measurements and flat-band potential determination on Zr-doped α-Fe2O3 single-crystal electrodes," *J. Electroanal. Chem.*, vol. 159, no. 2, pp. 421–436, 1983, doi: 10.1016/S0022-0728(83)80638-X.

[67] K. Ozawa *et al.*, "Electron-hole recombination time at TiO 2 single-crystal surfaces: Influence of surface band bending," *J. Phys. Chem. Lett.*, vol. 5, no. 11, pp. 1953–1957, 2014, doi: 10.1021/jz500770c.

[68] D. D. F. Aplicada, E. T. S. I. Telecomunicacion, and U. Polit, "Photoelectrolysis at n-Ti02 Electrodes," vol. 137, no. 6, pp. 1810–1815, 1990.

[69] X. Chen and S. S. Mao, "Synthesis of titanium dioxide (TiO <inf>2</inf>) nanomaterials," *J. Nanosci. Nanotechnol.*, vol. 6, no. 4, pp. 906–925, 2006, doi:

10.1166/jnn.2006.160.

[70] A. Paracchino, V. Laporte, K. Sivula, M. Grätzel, and E. Thimsen, “Highly active oxide photocathode for photoelectrochemical water reduction,” *Nat. Mater.*, vol. 10, no. 6, pp. 456–461, 2011, doi: 10.1038/nmat3017.

[71] O. Ola and M. M. Maroto-Valer, “Review of material design and reactor engineering on TiO2 photocatalysis for CO2 reduction,” *J. Photochem. Photobiol. C Photochem. Rev.*, vol. 24, pp. 16–42, 2015, doi: 10.1016/j.jphotochemrev.2015.06.001.

[72] S. Wang *et al.*, “Recent Progress on Visible Light Responsive Heterojunctions for Photocatalytic Applications,” *J. Mater. Sci. Technol.*, vol. 33, no. 1, pp. 1–22, Jan. 2017, doi: 10.1016/j.jmst.2016.11.017.

[73] S. Nahar, M. Zain, A. Kadhum, H. Hasan, and M. Hasan, “Advances in Photocatalytic CO2 Reduction with Water: A Review,” *Materials (Basel).*, vol. 10, no. 6, p. 629, 2017, doi: 10.3390/ma10060629.

[74] W. Chen, “Development of Efficient Low-Cost Semiconductor Photocatalysts for Solar H 2 Production,” 2017.

[75] H. M. Chen, C. K. Chen, R.-S. Liu, L. Zhang, J. Zhang, and D. P. Wilkinson, “Nano-architecture and material designs for water splitting photoelectrodes,” *Chem. Soc. Rev.*, vol. 41, no. 17, p. 5654, 2012, doi: 10.1039/c2cs35019j.

[76] A. Wolcott, W. A. Smith, T. R. Kuykendall, Y. Zhao, and J. Z. Zhang, “Photoelectrochemical Water Splitting Using Dense and Aligned TiO $_2$ Nanorod Arrays,” *Small*, vol. 5, no. 1, pp. 104–111, 2009, doi: 10.1002/smll.200800902.

[77] I. S. Cho *et al.*, “Branched TiO2 nanorods for photoelectrochemical hydrogen production,” *Nano Lett.*, vol. 11, no. 11, pp. 4978–4984, 2011, doi: 10.1021/nl2029392.

[78] M. Liu, N. de Leon Snapp, and H. Park, “Water photolysis with a cross-linked titanium dioxide nanowire anode,” *Chem. Sci.*, vol. 2, no. 1, pp. 80–87, 2011, doi: 10.1039/C0SC00321B.

[79] A. Wolcott, W. A. Smith, T. R. Kuykendall, Y. Zhao, and J. Z. Zhang, “Photoelectrochemical study of nanostructured Zno thin films for hydrogen generation from water splitting,” *Adv. Funct. Mater.*, vol. 19, no. 12, pp. 1849–1856, 2009, doi: 10.1002/adfm.200801363.

[80] B. D. Alexander, P. J. Kulesza, I. Rutkowska, R. Solarska, and J. Augustynski, “Metal oxide photoanodes for solar hydrogen production,” *J. Mater. Chem.*, vol. 18, no. 20, p. 2298, 2008, doi: 10.1039/b718644d.

[81] V. Cristino, S. Caramori, R. Argazzi, L. Meda, G. L. Marra, and C. A. Bignozzi,

"Efficient photoelectrochemical water splitting by anodically grown WO 3 electrodes," *Langmuir*, vol. 27, no. 11, pp. 7276–7284, 2011, doi: 10.1021/la200595x.

[82] V. Chakrapani, J. Thangala, and M. K. Sunkara, "WO3 and W2N nanowire arrays for photoelectrochemical hydrogen production," *Int. J. Hydrogen Energy*, vol. 34, no. 22, pp. 9050–9059, 2009, doi: 10.1016/j.ijhydene.2009.09.031.

[83] S. P. Berglund, D. W. Flaherty, N. T. Hahn, A. J. Bard, and C. B. Mullins, "Photoelectrochemical oxidation of water using nanostructured BiVO 4 films," *J. Phys. Chem. C*, vol. 115, no. 9, pp. 3794–3802, 2011, doi: 10.1021/jp1109459.

[84] R. Morrish, M. Rahman, J. M. D. MacElroy, and C. A. Wolden, "Activation of hematite nanorod arrays for photoelectrochemical water splitting," *ChemSusChem*, vol. 4, no. 4, pp. 474–479, 2011, doi: 10.1002/cssc.201100066.

[85] K. Keis *et al.*, "A 5% efficient photoelectrochemical solar cell based on nanostructured ZnO electrodes," *Sol. Energy Mater. Sol. Cells*, vol. 73, no. 1, pp. 51–58, 2002, doi: 10.1016/S0927-0248(01)00110-6.

[86] K. Tennakone, G. R. R. a. Kumara, I. R. M. Kottegoda, and V. P. S. Perera, "An efficient dye-sensitized photoelectrochemical solar cell made from oxides of tin and zinc," *Chem. Commun.*, no. 1, pp. 15–16, 1999, doi: 10.1039/a806801a.

[87] B. V. Bergeron, A. Marton, G. Oskam, and G. J. Meyer, "Dye-sensitized SnO 2 electrodes with iodide and pseudohalide redox mediators," *J. Phys. Chem. B*, vol. 109, no. 2, pp. 937–943, 2005, doi: 10.1021/jp0461347.

[88] S. Chappel and a. Zaban, "Nanoporous SnO2 electrodes for dye-sensitized solar cells: improved cell performance by the synthesis of 18nm SnO2 colloids," *Sol. Energy Mater. Sol. Cells*, vol. 71, pp. 141–152, 2002, doi: 10.1016/S0927-0248(01)00050-2.

[89] K. Sayama, H. Sugihara, and H. Arakawa, "Photoelectrochemical Properties of a Porous Nb $_2$ O $_5$ Electrode Sensitized by a Ruthenium Dye," *Chem. Mater.*, vol. 10, no. 12, pp. 3825–3832, 1998, doi: 10.1021/cm980111l.

[90] P. Guo and M. A. Aegerter, "Ru(II) sensitized Nb_{2}O_{5} solar cell made by the sol-gel process," *Thin Solid Films*, vol. 351, no. 1–2, pp. 290–294, 1999, doi: 10.1016/S0040-6090(99)00215-1.

[91] S. Burnside, J.-E. Moser, K. Brooks, M. Grätzel, and D. Cahen, "Nanocrystalline Mesoporous Strontium Titanate as Photoelectrode Material for Photosensitized Solar Devices: Increasing Photovoltage through Flatband Potential Engineering," *J. Phys. Chem. B*, vol. 103, no. 43, pp. 9328–9332, 1999, doi: 10.1021/jp9913867.

[92] B. Tan, E. Toman, Y. Li, and Y. Wu, "Zinc stannate (Zn2SnO4) dye-sensitized solar cells," *J. Am. Chem. Soc.*, vol. 129, no. 14, pp. 4162–4163, 2007, doi:

10.1021/ja070804f.

[93] N. F. Yan, G. R. Li, G. L. Pan, and X. P. Gao, “TiN Nanotube Arrays as Electrocatalytic Electrode for Solar Storable Rechargeable Battery,” *J. Electrochem. Soc.*, vol. 159, no. 11, pp. A1770–A1774, 2012, doi: 10.1149/2.019211jes.

[94] Z. Kebede and S.-E. Lindquist, “The obstructed diffusion of the I3- ion in mesoscopic TiO2 membranes,” *Sol. Energy Mater. Sol. Cells*, vol. 51, no. 3–4, pp. 291–303, 1998, doi: 10.1016/S0927-0248(97)00229-8.

[95] F. Cao, G. Oskam, G. J. Meyer, and P. C. Searson, “Electron Transport in Porous Nanocrystalline TiO 2 Photoelectrochemical Cells,” *J. Phys. Chem.*, vol. 100, no. 42, pp. 17021–17027, 1996, doi: 10.1021/jp9616573.

[96] D. Dambournet, I. Belharouak, and K. Amine, “Tailored Preparation Methods of TiO $_2$ Anatase, Rutile, Brookite: Mechanism of Formation and Electrochemical Properties †,” *Chem. Mater.*, vol. 22, no. 3, pp. 1173–1179, 2010, doi: 10.1021/cm902613h.

[97] A. L. Linsebigler, G. Lu, and J. T. Yates, “Photocatalysis on TiO2Surfaces: Principles, Mechanisms, and Selected Results,” *Chem. Rev.*, vol. 95, no. 3, pp. 735–758, 1995, doi: 10.1021/cr00035a013.

[98] N.-G. Park, J. van de Lagemaat, and A. J. Frank, “Comparison of Dye-Sensitized Rutile- and Anatase-Based TiO 2 Solar Cells,” *J. Phys. Chem. B*, vol. 104, no. 38, pp. 8989–8994, 2000, doi: 10.1021/jp994365l.

[99] T. Ohno, K. Sarukawa, K. Tokieda, and M. Matsumura, “Morphology of a TiO2photocatalyst (Degussa, P-25) consisting of anatase and rutile crystalline phases,” *J. Catal.*, vol. 203, no. 1, pp. 82–86, 2001, doi: 10.1006/jcat.2001.3316.

[100] K. Al-Attafi *et al.*, “The effect of amorphous TiO 2 in P25 on dye-sensitized solar cell performance,” *Chem. Commun. Chem. Commun*, vol. 54, no. 54, pp. 381–384, 2018, doi: 10.1039/c7cc07559f.

[101] A. Hagfeldt and M. Grätzel, “Molecular photovoltaics,” *Acc. Chem. Res.*, vol. 33, no. 5, pp. 269–277, 2000, doi: 10.1021/ar980112j.

[102] J. M. Kroon *et al.*, “Nanocrystalline dye-sensitized solar cells having maximum performance,” *Prog. Photovoltaics Res. Appl.*, vol. 15, no. 1, pp. 1–18, Jan. 2007, doi: 10.1002/pip.707.

[103] P. M. Sommeling *et al.*, “Influence of a TiCl4 post-treatment on nanocrystalline TiO 2 films in dye-sensitized solar cells,” *J. Phys. Chem. B*, vol. 110, no. 39, pp. 19191–19197, 2006, doi: 10.1021/jp061346k.

[104] B. O’Regan and M. Gratzel, “A Low-Cost, High-Efficiency Solar-Cell Based on Dye-Sensitized Colloidal TiO2 Films,” *Nature*, vol. 353, no. 6346, pp. 737–740, Oct. 1991,

doi: 10.1038/353737a0.

[105] D. Liu *et al.*, “Reversible Electron Storage in an All-Vanadium Photoelectrochemical Storage Cell: Synergy between Vanadium Redox and Hybrid Photocatalyst,” *ACS Catal.*, vol. 5, no. 4, pp. 2632–2639, 2015, doi: 10.1021/cs502024k.

[106] S. G. Chen, S. Chappel, Y. Diamant, and A. Zaban, “Preparation of Nb2O5 coated TiO2 nanoporous electrodes and their application in dye-sensitized solar cells,” *Chem. Mater.*, vol. 13, no. 12, pp. 4629–4634, 2001, doi: 10.1021/cm010343b.

[107] D. Cahen, G. Hodes, M. Grätzel, J. F. Guillemoles, and I. Riess, “Nature of Photovoltaic Action in Dye-Sensitized Solar Cells,” *J. Phys. Chem. B*, vol. 104, no. 9, pp. 2053–2059, 2000, doi: 10.1021/jp993187t.

[108] Y. Diamant, S. G. Chen, O. Melamed, and A. Zaban, “Core-shell nanoporous electrode for dye sensitized solar cells: The effect of the SrTiO3 shell on the electronic properties of the TiO2 core,” *J. Phys. Chem. B*, vol. 107, no. 9, pp. 1977–1981, 2003, doi: 10.1021/jp027827v.

[109] J. van de Lagemaat, N.-G. Park, and A. J. Frank, “Influence of Electrical Potential Distribution, Charge Transport, and Recombination on the Photopotential and Photocurrent Conversion Efficiency of Dye-Sensitized Nanocrystalline TiO 2 Solar Cells: A Study by Electrical Impedance and Optical Modulation Te,” *J. Phys. Chem. B*, vol. 104, no. 9, pp. 2044–2052, 2000, doi: 10.1021/jp993172v.

[110] L. M. Peter, “Dye-sensitized nanocrystalline solar cells,” *Phys. Chem. Chem. Phys.*, vol. 9, no. 21, p. 2630, 2007, doi: 10.1039/b617073k.

[111] Z.-Q. Li, W.-C. Chen, F.-L. Guo, L.-E. Mo, L.-H. Hu, and S.-Y. Dai, “Mesoporous TiO2 Yolk-Shell Microspheres for Dye-sensitized Solar Cells with a High Efficiency Exceeding 11%,” *Sci. Rep.*, vol. 5, no. 1, p. 14178, 2015, doi: 10.1038/srep14178.

[112] E. Palomares, J. N. Clifford, S. A. Haque, T. Lutz, and J. R. Durrant, “Control of charge recombination dynamics in dye sensitized solar cells by the use of conformally deposited metal oxide blocking layers,” *J. Am. Chem. Soc.*, vol. 125, no. 2, pp. 475–482, 2003, doi: 10.1021/ja027945w.

[113] Z. Liu, W. Hou, P. Pavaskar, M. Aykol, and S. B. Cronin, “Plasmon resonant enhancement of photocatalytic water splitting under visible illumination,” *Nano Lett.*, vol. 11, no. 3, pp. 1111–1116, 2011, doi: 10.1021/nl104005n.

[114] X. Feng, K. Shankar, O. K. Varghese, M. Paulose, T. J. Latempa, and C. A. Grimes, “Vertically aligned single crystal TiO2nanowire arrays grown directly on transparent conducting oxide coated glass: Synthesis details and applications,” *Nano Lett.*, vol. 8, no. 11, pp. 3781–3786, 2008, doi: 10.1021/nl802096a.

[115] W. Liu, B. Zou, J. Zhao, and H. Cui, “Optimizing sol-gel infiltration for the fabrication of high-quality titania inverse opal and its photocatalytic activity,” *Thin Solid Films*, vol. 518, no. 17, pp. 4923–4927, 2010, doi: 10.1016/j.tsf.2010.02.043.

[116] G. K. Mor, K. Shankar, M. Paulose, O. K. Varghese, and C. A. Grimes, “Use of highly-ordered TiO 2 nanotube arrays in dye-sensitized solar cells,” *Nano Lett.*, vol. 6, no. 2, pp. 215–218, 2006, doi: 10.1021/nl052099j.

[117] H. Kokubo, B. Ding, T. Naka, H. Tsuchihira, and S. Shiratori, “Multi-core cable-like TiO2 nanofibrous membranes for dye-sensitized solar cells,” *Nanotechnology*, vol. 18, no. 16, pp. 165604–6, 2007, doi: 10.1088/0957-4484/18/16/165604.

[118] K. Fujihara, A. Kumar, R. Jose, S. Ramakrishna, and S. Uchida, “Spray deposition of electrospun TiO 2 nanorods for dye-sensitized solar cell,” *Nanotechnology*, vol. 18, no. 36, p. 365709, 2007, doi: 10.1088/0957-4484/18/36/365709.

[119] M. Y. Song, D. K. Kim, K. J. Ihn, S. M. Jo, and D. Y. Kim, “Electrospun TiO2 electrodes for dye-sensitized solar cells,” *Nanotechnology*, vol. 15, no. 12, pp. 1861–1865, 2004, doi: 10.1088/0957-4484/15/12/030.

[120] J. Wang, L. Zhao, V. S.-Y. Lin, and Z. Lin, “Formation of various TiO2 nanostructures from electrochemically anodized titanium,” *J. Mater. Chem.*, vol. 19, no. 22, p. 3682, 2009, doi: 10.1039/b904247d.

[121] W. Guo *et al.*, “Rectangular Bunched Rutile TiO_2 Nanorod Arrays Grown on Carbon Fiber for Dye-Sensitized Solar Cells,” *J. Am. Chem. Soc.*, vol. 134, no. 9, pp. 4437–4441, 2012, doi: 10.1021/ja2120585.

[122] Q. Huang, G. Zhou, L. Fang, L. Hu, and Z.-S. Wang, “TiO2 nanorod arrays grown from a mixed acid medium for efficient dye-sensitized solar cells,” *Energy Environ. Sci.*, vol. 4, no. 6, p. 2145, 2011, doi: 10.1039/c1ee01166a.

[123] T. Morimoto *et al.*, “TiO 2 -Anatase Nanowire Dispersed Composite Electrode for Dye-Sensitized Solar Cells Parametric Optimization of Experimental Conditions for Dye-Sensitized Solar Cells based on Far-red Sensitive Squaraine Dye TiO 2 -Anatase Nanowire Dispersed Composite Ele,” *J. Phys. Conf. Ser. J. Phys. Conf. Ser*, vol. 61, Accessed: Feb. 13, 2018. [Online]. Available: http://iopscience.iop.org/article/10.1088/1742-6596/61/1/220/pdf.

[124] C.-H. Ku and J.-J. Wu, “Chemical bath deposition of ZnO nanowire–nanoparticle composite electrodes for use in dye-sensitized solar cells,” *Nanotechnology*, vol. 18, no. 50, p. 505706, 2007, doi: 10.1088/0957-4484/18/50/505706.

[125] Y. J. Kim *et al.*, “Formation of highly efficient dye-sensitized solar cells by hierarchical pore generation with nanoporous TiO2spheres,” *Adv. Mater.*, vol. 21, no.

36, pp. 3668–3673, Sep. 2009, doi: 10.1002/adma.200900294.

[126] H. J. Koo, Y. J. Kim, Y. H. Lee, W. I. Lee, K. Kim, and N. G. Park, “Nano-embossed hollow spherical TiO2as bifunctional material for high-efficiency dye-sensitized solar cells,” *Adv. Mater.*, vol. 20, no. 1, pp. 195–199, Jan. 2008, doi: 10.1002/adma.200700840.

[127] F. Sauvage *et al.*, “Hierarchical TiO2 photoanode for dye-sensitized solar cells,” *Nano Lett.*, vol. 10, no. 7, pp. 2562–2567, 2010, doi: 10.1021/nl101198b.

[128] P. At, U. The, T. Ls, K. We, and F. Ls, “Preparation of Photonic Crystals Made of Air Spheres in Titania,” vol. 281, no. August, pp. 802–805, 1998.

[129] Y. Cao *et al.*, “Fabrication of anatase titania inverse opal films using polystyrene templates,” *Superlattices Microstruct.*, vol. 40, no. 3, pp. 155–160, 2006, doi: 10.1016/j.spmi.2006.07.005.

[130] G. I. N. Waterhouse and M. R. Waterland, “Opal and inverse opal photonic crystals: Fabrication and characterization,” *Polyhedron*, vol. 26, no. 2, pp. 356–368, 2007, doi: 10.1016/j.poly.2006.06.024.

[131] Y. G. Seo, K. Woo, J. Kim, H. Lee, and W. Lee, “Rapid fabrication of an inverse opal TiO2 photoelectrode for DSSC using a binary mixture of TiO2 nanoparticles and polymer microspheres,” *Adv. Funct. Mater.*, vol. 21, no. 16, pp. 3094–3103, 2011, doi: 10.1002/adfm.201002489.

[132] T. K. Rahul and N. Sandhyarani, “Nitrogen-fluorine co-doped titania inverse opals for enhanced solar light driven photocatalysis,” *Nanoscale*, vol. 7, no. 43, pp. 18259–18270, 2015, doi: 10.1039/C5NR04663G.

[133] T. K. Rahul and N. Sandhyarani, “In Situ Gold-Loaded Fluorinated Titania Inverse Opal Photocatalysts for Enhanced Solar-Light-Driven Hydrogen Production,” *ChemNanoMat*, vol. 3, no. 7, pp. 503–510, 2017, doi: 10.1002/cnma.201700062.

[134] E. S. Kwak, W. Lee, N. C. Park, J. Kim, and H. Lee, “Compact inverse-opal electrode using non-aggregated TiO2 nanoparticles for dye-sensitized solar cells,” *Adv. Funct. Mater.*, vol. 19, no. 7, pp. 1093–1099, 2009, doi: 10.1002/adfm.200801540.

[135] B. Liu and E. S. Aydil, “Growth of oriented single-crystalline rutile TiO 2 nanorods on transparent conducting substrates for dye-sensitized solar cells,” *J. Am. Chem. Soc.*, vol. 131, no. 11, pp. 3985–3990, 2009, doi: 10.1021/ja8078972.

[136] J. Zhao, X. Wang, R. Chen, and L. Li, “Fabrication of titanium oxide nanotube arrays by anodic oxidation,” *Solid State Commun.*, vol. 134, no. 10, pp. 705–710, 2005, doi: 10.1016/j.ssc.2005.02.028.

[137] W. Lee, M. Alhoshan, and W. H. Smyrl, “Titanium Dioxide Nanotube Arrays

Fabricated by Anodizing Electrochemical Properties," *J. Electrochem. Soc.*, vol. 153, no. 11, pp. B499–B505, 2006, doi: 10.1149/1.2347098.

[138] E. Y. Kim, J. H. Park, and G. Y. Han, "Design of TiO2nanotube array-based water-splitting reactor for hydrogen generation," *J. Power Sources*, vol. 184, no. 1, pp. 284–287, 2008, doi: 10.1016/j.jpowsour.2008.05.059.

[139] J. H. Park, T.-W. Lee, and M. G. Kang, "Growth, detachment and transfer of highly-ordered TiO2 nanotube arrays: use in dye-sensitized solar cells," *Chem. Commun.*, no. 25, p. 2867, 2008, doi: 10.1039/b800660a.

[140] Y. S. Sohn, Y. R. Smith, M. Misra, and V. (Ravi) Subramanian, "Electrochemically assisted photocatalytic degradation of methyl orange using anodized titanium dioxide nanotubes," *Appl. Catal. B Environ.*, vol. 84, no. 3–4, pp. 372–378, 2008, doi: 10.1016/j.apcatb.2008.04.021.

[141] X. Wang *et al.*, "A metal-free polymeric photocatalyst for hydrogen production from water under visible light," *Nat. Mater.*, vol. 8, no. 1, pp. 76–80, Jan. 2009, doi: 10.1038/nmat2317.

[142] K. Shin, S. il Seok, S. H. Im, and J. H. Park, "CdS or CdSe decorated TiO2 nanotube arrays from spray pyrolysis deposition: use in photoelectrochemical cells," *Chem. Commun.*, vol. 46, no. 14, p. 2385, 2010, doi: 10.1039/b923022j.

[143] P. Zhong, X. Chen, H. Xi, Y. Lei, and X. Ma, "Freeze Drying as a Novel Approach to Improve Charge Transport in Titanium Dioxide Nanorod Arrays," *ChemElectroChem*, vol. 4, no. 11, pp. 2783–2787, 2017, doi: 10.1002/celc.201700572.

[144] Y. Yu and M. Lira-Cantu, "Solid state dye sensitized solar cells applying conducting organic polymers as hole conductors," *Phys. Procedia*, vol. 8, pp. 22–27, 2010, doi: 10.1016/j.phpro.2010.10.006.

[145] R. Grünwald and H. Tributsch, "Mechanisms of Instability in Ru-Based Dye Sensitization Solar Cells," *J. Phys. Chem. B*, vol. 101, no. 96, pp. 2564–2575, 1997, doi: 10.1021/jp9624919.

[146] G. Oskam, B. V Bergeron, G. J. Meyer, and P. C. Searson, "Pseudohalogens for dye-sensitized TiO_{2} photoelectrochemical cells," *J. Phys. Chem. B*, vol. 105, no. 29, pp. 6867–6873, 2001, doi: 10.1021/jp004411d.

[147] B. A. Gregg, F. Pichot, S. Ferrere, and C. L. Fields, "Interfacial Recombination Processes in Dye-Sensitized Solar Cells and Methods To Passivate the Interfaces," *J. Phys. Chem. B*, vol. 105, no. 7, pp. 1422–1429, 2001, doi: 10.1021/jp003000u.

[148] Y. Hao *et al.*, "A small electron donor in cobalt complex electrolyte significantly improves efficiency in dye-sensitized solar cells," *Nat. Commun.*, vol. 7, pp. 1–8,

2016, doi: 10.1038/ncomms13934.

[149] S. M. Feldt, E. A. Gibson, E. Gabrielsson, L. Sun, G. Boschloo, and A. Hagfeldt, "Design of organic dyes and cobalt polypyridine redox mediators for high-efficiency dye-sensitized solar cells," *J. Am. Chem. Soc.*, vol. 132, no. 46, pp. 16714–16724, 2010, doi: 10.1021/ja1088869.

[150] J.-H. Yum *et al.*, "A cobalt complex redox shuttle for dye-sensitized solar cells with high open-circuit potentials," *Nat. Commun.*, vol. 3, p. 631, 2012, doi: 10.1038/ncomms1655.

[151] A. M. C. Senevirathne, V. A. Seneviratne, O. A. Ileperuma, H. M. N. Bandara, and R. M. G. Rajapakse, "Novel Quasi-Solid-State Electrolyte Based on γ-Butyrolactone and Tetrapropylammonium Iodide for Dye-Sensitized Solar Cells Using Fumed Silica as the Gelling Agent," *Procedia Eng.*, vol. 139, pp. 87–92, 2016, doi: 10.1016/j.proeng.2015.08.1117.

[152] S. V. N. and A. S. N. T. G. Deepak, G. S. Anjusree, K. R. Narendra Pai, Devika Subash, "Fabrication of a dye-sensitized solar cell module using spray pyrolysis deposition of a TiO2 colloid," *RSC Adv.*, vol. 4, pp. 23299–23303, 2014.

[153] P. Wang, S. M. Zakeeruddin, J.-E. Moser, and M. Grätzel, "A New Ionic Liquid Electrolyte Enhances the Conversion Efficiency of Dye-Sensitized Solar Cells," *J. Phys. Chem. B*, vol. 107, no. 48, pp. 13280–13285, 2003, doi: 10.1021/jp0355399.

[154] Y. Liu, H. Tsunoyama, T. Akita, and T. Tsukuda, "Preparation of ∼1 nm Gold Clusters Confined within Mesoporous Silica and Microwave-Assisted Catalytic Application for Alcohol Oxidation," *J. Phys. Chem. C*, vol. 113, no. 31, pp. 13457–13461, 2009, doi: 10.1021/jp904700p.

[155] B. Guo, Z. Liu, L. Hong, and H. Jiang, "Sol gel derived photocatalytic porous TiO2 thin films," *Surf. Coatings Technol.*, vol. 198, no. 1-3 SPEC. ISS., pp. 24–29, 2005, doi: 10.1016/j.surfcoat.2004.10.055.

[156] M. H. Mamat *et al.*, "Effect of annealing temperature on the surface morphology and electrical properties of aluminum doped zinc oxide thin films prepared by sol-gel spin-coating method," *AIP Conf. Proc.*, vol. 1017, no. May, pp. 139–143, 2008, doi: 10.1063/1.2940614.

[157] G. Xi, Junting; Dahoudi, Naji AL; Zhang, Qifeng; Sun, Yueming; Cao, "Effect of Annealing Temperature on the Performances and Electrochemical Properties of TiO2 Dye-Sensitized Solar Cell," *Sci. Adv. Mater.*, vol. 4, no. 7, pp. 727–733, 2012.

[158] B. M. John, S. W. Mugo, and J. M. Ngaruiya, "Effect of Annealing Rates on Surface Roughness of TiO 2 Thin films," no. December, 2018, doi: 10.12691/jmpc-6-2-3.

[159] U. Bach *et al.*, “Solid-state dye-sensitized mesoporous TiO2 solar cells with high photon-to-electron conversion efficiencies,” *Nature*, vol. 395, no. 6702, pp. 583–585, 1998, doi: 10.1038/26936.

[160] M. Okuya, K. Nakade, and S. Kaneko, “Porous TiO 2 thin films synthesized by a spray pyrolysis deposition (SPD) technique and their application to dye-sensitized solar cells,” *Sol. Energy Mater. Sol. Cells*, vol. 70, pp. 425–435, 2002, doi: 10.1016/S0927-0248(01)00033-2.

[161] M. O. Abou-Helal and W. T. Seeber, “Preparation of TiO2 thin films by spray pyrolysis to be used as a photocatalyst,” *Appl. Surf. Sci.*, vol. 195, no. 1–4, pp. 53–62, 2002, doi: 10.1016/S0169-4332(02)00533-0.

[162] D. Li, H. Haneda, S. Hishita, N. Ohashi, and N. K. Labhsetwar, “Fluorine-doped TiO 2 powders prepared by spray pyrolysis and their improved photocatalytic activity for decomposition of gas-phase acetaldehyde,” *J. Fluor. Chem.*, vol. 126, no. 1, pp. 69–77, 2005, doi: 10.1016/j.jfluchem.2004.10.044.

[163] D. Li, H. Haneda, S. Hishita, and N. Ohashi, “Visible-light-driven N-F-codoped TiO2 photocatalysts. 1. Synthesis by spray pyrolysis and surface characterization,” *Chem. Mater.*, vol. 17, no. 10, pp. 2588–2595, 2005, doi: 10.1021/cm049100k.

[164] S.-Q. Fan, C.-J. Li, G.-J. Yang, L.-Z. Zhang, J.-C. Gao, and Y.-X. Xi, “Fabrication of Nano-TiO2 Coating for Dye-Sensitized Solar Cell by Vacuum Cold Spraying at Room Temperature,” *J. Therm. Spray Technol.*, vol. 16, no. 5–6, pp. 893–897, 2007, doi: 10.1007/s11666-007-9090-z.

[165] S. Q. Fan, G. J. Yang, C. J. Li, G. J. Liu, C. X. Li, and L. Z. Zhang, “Characterization of microstructure of nano-TiO2 coating deposited by vacuum cold spraying,” *Proc. Int. Therm. Spray Conf.*, vol. 15, no. December, pp. 513–517, 2006, doi: 10.1361/105996306X146901.

[166] C. D. Lokhande, B. O. Park, H. S. Park, K. D. Jung, and O. S. Joo, “Electrodeposition of TiO2and RuO2thin films for morphology-dependent applications,” *Ultramicroscopy*, vol. 105, no. 1–4, pp. 267–274, 2005, doi: 10.1016/j.ultramic.2005.06.048.

[167] K. Wessels, M. Maekawa, J. Rathousky, and T. Oekermann, “One-step electrodeposition of TiO2/dye hybrid films,” *Thin Solid Films*, vol. 515, no. 16 SPEC. ISS., pp. 6497–6500, 2007, doi: 10.1016/j.tsf.2006.11.081.

[168] B. Endrődi, E. Kecsenovity, K. Rajeshwar, and C. Janáky, “One-step Electrodeposition of Nanocrystalline TiO2 Films with Enhanced Photoelectrochemical Performance and Charge Storage,” *ACS Appl. Energy Mater.*, p. acsaem.7b00289, 2018, doi:

10.1021/acsaem.7b00289.

[169] S. Z. Chu, S. Inoue, K. Wada, and S. Hishita, “Fabrication of TiO[sub 2]-Ru(O[sub 2])/Al[sub 2]O[sub 3] Composite Nanostructures on Glass by Al Anodization and Electrodeposition,” *J. Electrochem. Soc.*, vol. 151, no. 1, p. C38, 2004, doi: 10.1149/1.1627346.

[170] T. V. Nguyen, H. C. Lee, M. Alam Khan, and O. B. Yang, “Electrodeposition of TiO2/SiO2nanocomposite for dye-sensitized solar cell,” *Sol. Energy*, vol. 81, no. 4, pp. 529–534, 2007, doi: 10.1016/j.solener.2006.07.008.

[171] M. Wu *et al.*, “High photocatalytic activity enhancement of titania inverse opal films by slow photon effect induced strong light absorption,” *J. Mater. Chem. A*, vol. 1, no. 48, p. 15491, 2013, doi: 10.1039/c3ta13574h.

[172] J. Xu, B. Yang, M. Wu, Z. Fu, Y. Lv, and Y. Zhao, “Novel N - F-Codoped TiO 2 Inverse Opal with a Hierarchical Meso/Macroporous Structure: Synthesis, Characterization, and Photocatalysis,” pp. 15251–15259, 2010.

[173] E. S. Kwak, W. Lee, N. C. Park, J. Kim, and H. Lee, “Compact inverse-opal electrode using non-aggregated TiO 2 nanoparticles for dye-sensitized solar cells,” *Adv. Funct. Mater.*, vol. 19, no. 7, pp. 1093–1099, 2009, doi: 10.1002/adfm.200801540.

[174] G. Lui, “Design of Novel Titanium Dioxide-Based Multifunctional Electrochemical Cells,” University of Waterloo, 2018.

[175] G. Raza, “Titanium Dioxide Nanomaterials, Synthesis, Stability and Mobility in Natural and Synthetic Porous Media,” The University of Birmingham, 2017.

[176] S. Bagheri, Z. A. Mohd Hir, A. Termeh Yousefi, and S. Bee Abdul Hamid, “Progress on mesoporous titanium dioxide: Synthesis, modification and applications,” *Microporous Mesoporous Mater.*, vol. 218, pp. 206–222, 2015, doi: 10.1016/j.micromeso.2015.05.028.

[177] S. Rouxel, D., Fleutot, S., Cherni, N., Darne, C., Gate, L., & Binet, “Synthesis of Nanoparticles of Titanium Dioxide TiO2 for Toxicological Studies: A Short Review,” *Glob. J. Nanomedicine*, vol. 3, no. 1, p. 2, 2017.

[178] A. B. Djurišić, Y. H. Leung, and A. M. Ching Ng, “Strategies for improving the efficiency of semiconductor metal oxide photocatalysis,” *Mater. Horizons*, vol. 1, no. 4, pp. 400–410, 2014, doi: 10.1039/c4mh00031e.

[179] S. Hoang, T. Q. Ngo, S. P. Berglund, R. R. Fullon, J. G. Ekerdt, and C. B. Mullins, “Improvement of solar energy conversion with Nb-incorporated TiO2 hierarchical microspheres,” *ChemPhysChem*, vol. 14, no. 10, pp. 2270–2276, Jul. 2013, doi: 10.1002/cphc.201201092.

[180] E. Burstein, “Anomalous optical absorption limit in InSb [4],” *Phys. Rev.*, vol. 93, no. 3, pp. 632–633, 1954, doi: 10.1103/PhysRev.93.632.

[181] Y. Liu, Z. Wang, W. Wang, and W. Huang, “Engineering highly active TiO2 photocatalysts via the surface-phase junction strategy employing a titanate nanotube precursor,” *J. Catal.*, vol. 310, pp. 16–23, 2014, doi: 10.1016/j.jcat.2013.03.024.

[182] S. Harrison and M. Hayne, “Photoelectrolysis Using Type-II Semiconductor Heterojunctions,” *Sci. Rep.*, vol. 7, no. 1, pp. 1–11, 2017, doi: 10.1038/s41598-017-11971-x.

[183] *An Essential Guide to Electronic Material Surfaces and Interfaces*, vol. Semiconduc. .

[184] T. H. Lee and K. M. Ervin, “Reactions of copper group cluster anions with oxygen and carbon monoxide,” *J. Phys. Chem.*, vol. 98, no. 40, pp. 10023–10031, 1994, doi: 10.1021/j100091a014.

[185] D. M. Cox, R. Brickman, K. Creegan, and A. Kaldor, “Gold clusters: reactions and deuterium uptake,” *Zeitschrift für Phys. D Atoms, Mol. Clust.*, vol. 19, no. 4, pp. 353–355, 1991, doi: 10.1007/BF01448327.

[186] K. Awazu *et al.*, “A plasmonic photocatalyst consisting of silver nanoparticles embedded in titanium dioxide,” *J. Am. Chem. Soc.*, vol. 130, no. 5, pp. 1676–1680, 2008, doi: 10.1021/ja076503n.

[187] J. Zhang *et al.*, “Engineering the Absorption and Field Enhancement Properties of Au-TiO2 Nanohybrids via Whispering Gallery Mode Resonances for Photocatalytic Water Splitting,” *ACS Nano*, vol. 10, no. 4, pp. 4496–4503, 2016, doi: 10.1021/acsnano.6b00263.

[188] P. V. Kamat, “Manipulation of charge transfer across semiconductor interface. A criterion that cannot be ignored in photocatalyst design,” *J. Phys. Chem. Lett.*, vol. 3, no. 5, pp. 663–672, 2012, doi: 10.1021/jz201629p.

[189] P. V. Kamat, “Photophysical, photochemical and photocatalytic aspects of metal nanoparticles,” *J. Phys. Chem. B*, vol. 106, no. 32, pp. 7729–7744, 2002, doi: 10.1021/jp0209289.

[190] A. Kudo and Y. Miseki, “Heterogeneous photocatalyst materials for water splitting,” *Chem. Soc. Rev.*, vol. 38, no. 1, pp. 253–278, 2009, doi: 10.1039/b800489g.

[191] A. Takai and P. V. Kamat, “Capture, store, and discharge. Shuttling photogenerated electrons across TiO2-silver interface,” *ACS Nano*, vol. 5, no. 9, pp. 7369–7376, 2011, doi: 10.1021/nn202294b.

[192] V. Subramanian, E. E. Wolf, and P. V. Kamat, “Green emission to probe photoinduced charging events in ZnO-Au nanoparticles. Charge distribution and Fermi-level

equilibration," *J. Phys. Chem. B*, vol. 107, no. 30, pp. 7479–7485, 2003, doi: 10.1021/jp0275037.

[193] V. Subramanian, E. E. Wolf, and P. V. Kamat, "Catalysis with TiO2/Gold Nanocomposites. Effect of Metal Particle Size on the Fermi Level Equilibration," *J. Am. Chem. Soc.*, vol. 126, no. 15, pp. 4943–4950, 2004, doi: 10.1021/ja0315199.

[194] S. Chen *et al.*, "Gold nanoelectrodes of varied size: Transition to molecule-like charging," *Science (80-.).*, vol. 280, no. 5372, pp. 2098–2101, 1998, doi: 10.1126/science.280.5372.2098.

[195] J. J. Pietron, J. F. Hicks, and R. W. Murray, "Using electrons stored on quantized capacitors in electron transfer reactions," *J. Am. Chem. Soc.*, vol. 121, no. 23, pp. 5565–5570, 1999, doi: 10.1021/ja990320m.

[196] A. C. Templeton, W. P. Wuelfing, and R. W. Murray, "Monolayer-protected cluster molecules," *Acc. Chem. Res.*, vol. 33, no. 1, pp. 27–36, 2000, doi: 10.1021/ar9602664.

[197] P. K. Sudeep, K. Takechi, and P. V. Kamat, "Harvesting photons in the infrared. Electron injection from excited tricarbocyanine dye (IR-125) into TiO2 and Ag@TiO2 core-shell nanoparticles," *J. Phys. Chem. C*, vol. 111, no. 1, pp. 488–494, 2007, doi: 10.1021/jp0665022.

[198] S. Mubeen, G. Hernandez-Sosa, D. Moses, J. Lee, and M. Moskovits, "Plasmonic photosensitization of a wide band gap semiconductor: Converting plasmons to charge carriers," *Nano Lett.*, vol. 11, no. 12, pp. 5548–5552, 2011, doi: 10.1021/nl203457v.

[199] Y. Tian and T. Tatsuma, "Mechanisms and applications of plasmon-induced charge separation at TiO2 films loaded with gold nanoparticles," *J. Am. Chem. Soc.*, vol. 127, no. 20, pp. 7632–7637, 2005, doi: 10.1021/ja042192u.

[200] Z. Zhang, L. Zhang, M. N. Hedhili, H. Zhang, and P. Wang, "Plasmonic gold nanocrystals coupled with photonic crystal seamlessly on TiO 2 nanotube photoelectrodes for efficient visible light photoelectrochemical water splitting," *Nano Lett.*, vol. 13, no. 1, pp. 14–20, 2013, doi: 10.1021/nl3029202.

[201] X. Shi, K. Ueno, N. Takabayashi, and H. Misawa, "Plasmon-enhanced photocurrent generation and water oxidation with a gold nanoisland-loaded titanium dioxide photoelectrode," *J. Phys. Chem. C*, vol. 117, no. 6, pp. 2494–2499, 2013, doi: 10.1021/jp3064036.

[202] A. Dawson and P. V. Kamat, " Semiconductor−Metal Nanocomposites. Photoinduced Fusion and Photocatalysis of Gold-Capped TiO 2 (TiO 2 /Gold) Nanoparticles ," *J. Phys. Chem. B*, vol. 105, no. 5, pp. 960–966, 2002, doi: 10.1021/jp0033263.

[203] M. Haro, R. Abargues, I. Herraiz-Cardona, J. Martínez-Pastor, and S. Giménez,

"Plasmonic versus catalytic effect of gold nanoparticles on mesoporous TiO2electrodes for water splitting," *Electrochim. Acta*, vol. 144, pp. 64–70, 2014, doi: 10.1016/j.electacta.2014.07.146.

[204] J. W. Yoon, T. Sasaki, and N. Koshizaki, "Dispersion of nanosized noble metals in TiO2 matrix and their photoelectrode properties," *Thin Solid Films*, vol. 483, no. 1–2, pp. 276–282, 2005, doi: 10.1016/j.tsf.2005.01.006.

[205] A. Primo, A. Corma, and H. García, "Titania supported gold nanoparticles as photocatalyst," *Phys. Chem. Chem. Phys.*, vol. 13, no. 3, pp. 886–910, 2011, doi: 10.1039/c0cp00917b.

[206] Y. C. Yen, J. A. Chen, S. Ou, Y. S. Chen, and K. J. Lin, "Plasmon-Enhanced Photocurrent using Gold Nanoparticles on a Three-Dimensional TiO2 Nanowire-Web Electrode," *Sci. Rep.*, vol. 7, no. February, pp. 1–8, 2017, doi: 10.1038/srep42524.

[207] C. Seghetti, "Gold/TiO2 nanocomposites as photoactive materials for environmental remediation," 2016.

[208] G. Kawamura, T. Arai, H. Muto, and A. Matsuda, "Charge behavior in a plasmonic photocatalyst composed of Au and TiO 2," *Catal. Sci. Technol.*, vol. 8, no. 7, pp. 1813–1818, 2018, doi: 10.1039/c8cy00120k.

[209] A. Tanaka, K. Hashimoto, and H. Kominami, "A very simple method for the preparation of Au/TiO2 plasmonic photocatalysts working under irradiation of visible light in the range of 600-700 nm," *Chem. Commun.*, vol. 53, no. 35, pp. 4759–4762, 2017, doi: 10.1039/c7cc01444a.

[210] R. Siavash Moakhar *et al.*, "AuPd bimetallic nanoparticle decorated TiO2 rutile nanorod arrays for enhanced photoelectrochemical water splitting," *J. Appl. Electrochem.*, vol. 48, no. 9, pp. 995–1007, 2018, doi: 10.1007/s10800-018-1231-1.

[211] G. Schmid and D. Fenske, "Metal clusters and nanoparticles," *Philos. Trans. R. Soc. A Math. Phys. Eng. Sci.*, vol. 368, no. 1915, pp. 1207–1210, 2010, doi: 10.1098/rsta.2009.0281.

[212] R. Meyer, C. Lemire, S. K. Shaikhutdinov, and H. J. Freund, "Surface chemistry of catalysis by gold," *Gold Bull.*, vol. 37, no. 1–2, pp. 72–124, 2004, doi: 10.1007/BF03215519.

[213] M. Valden, X. Lai, and D. W. Goodman, "Onset of catalytic activity of gold clusters on titania with the appearance of nonmetallic properties," *Science (80-.).*, vol. 281, no. 5383, pp. 1647–1650, 1998, doi: 10.1126/science.281.5383.1647.

[214] K. Okazaki, S. Ichikawa, Y. Maeda, M. Haruta, and M. Kohyama, "Electronic structures of Au supported on TiO2," *Appl. Catal. A Gen.*, vol. 291, no. 1–2, pp. 45–

54, 2005, doi: 10.1016/j.apcata.2005.02.047.

[215] P. Maity, S. Xie, M. Yamauchi, and T. Tsukuda, “Stabilized gold clusters: From isolation toward controlled synthesis,” *Nanoscale*, vol. 4, no. 14, pp. 4027–4037, 2012, doi: 10.1039/c2nr30900a.

[216] D. P. Anderson *et al.*, “Chemically-synthesised, atomically-precise gold clusters deposited and activated on titania,” *Phys. Chem. Chem. Phys*, no. 15, pp. 3917–3929, 2013, doi: 10.1039/c3cp44005b.

[217] Jason Frankie Alvino, “The Characterisation, Photocatalytic Performance, and Theoretical Investigation of Small Gold Clusters Supported on Titanium Dioxide Nanoparticles,” The university of adelaid, 2015.

[218] D. P. Anderson *et al.*, “Chemically synthesised atomically precise gold clusters deposited and activated on titania. Part II,” 2013.

[219] A. Zaban, M. Greenshtein, and J. Bisquert, “Determination of the electron lifetime in nanocrystalline dye solar cells by open-circuit voltage decay measurements,” *ChemPhysChem*, vol. 4, no. 8, pp. 859–864, 2003, doi: 10.1002/cphc.200200615.

[220] G. Hodes, “Photoelectrochemical cell measurements: Getting the basics right,” *J. Phys. Chem. Lett.*, vol. 3, no. 9, pp. 1208–1213, 2012, doi: 10.1021/jz300220b.

[221] D. C. J. De Joseph I. Goldstein, Dale E. Newbury, Joseph R. Michael, Nicholas W.M. Ritchie, John Henry J. Scott, *Scanning Electron Microscopy and X-Ray Microanalysis*. Springers, 2017.

[222] O. H. Seeck and B. Murphy, Eds., *X-Ray Diffraction*. Jenny Stanford Publishing, 2015.

[223] G. Kim, M. Oh, and Y. Park, “Solar-rechargeable battery based on photoelectrochemical water oxidation: Solar water battery,” *Sci. Rep.*, vol. 6, no. September, pp. 1–9, 2016, doi: 10.1038/srep33400.

[224] M. Nagao, K. Kobayashi, Y. Yamamoto, T. Yamaguchi, A. Oogushi, and T. Hibino, “Rechargeable Metal-Air Proton-Exchange Membrane Batteries for Renewable Energy Storage,” *ChemElectroChem*, vol. 3, no. 2, pp. 247–255, 2016, doi: 10.1002/celc.201500473.

[225] Marcel Pourbaix, *Atlas of Electrochemical Equilibria in Aqueous Solutions*. Houston, Texas; Cebelcor, Brussels: NACE International, 1966.

[226] J. A. Bard and R. L. Faulkner, *Electrochemical Methods: Fundamentals and Applications*, Second edition., no. 4. 2000.

[227] K. Gelderman, L. Lee, and S. W. Donne, “Flat-band potential of a semiconductor: Using the Mott-Schottky equation,” *J. Chem. Educ.*, vol. 84, no. 4, pp. 685–688, 2007, doi: 10.1021/ed084p685.

[228] Y. X. Zu, X. Wu, and Y. Q. Lv, “Study on the DS/CDMA-CSMA multi-user communication systems,” *Commun. Comput. Inf. Sci.*, vol. 26 CCIS, pp. 98–104, 2009, doi: 10.1007/978-3-642-00205-2_12.

[229] Z. G. Ye, H. M. Meng, and D. B. Sun, “New degradation mechanism of Ti/IrO2 + MnO2 anode for oxygen evolution in 0.5 M H2SO4 solution,” *Electrochim. Acta*, vol. 53, no. 18, pp. 5639–5643, 2008, doi: 10.1016/j.electacta.2008.03.025.

[230] R. P. Brooker, C. J. Bell, L. J. Bonville, H. R. Kunz, and J. M. Fenton, “Determining Vanadium Concentrations Using the UV-Vis Response Method,” *J. Electrochem. Soc.*, vol. 162, no. 4, pp. A608–A613, 2015, doi: 10.1149/2.0371504jes.

[231] J. Barber, J. Mills, and A. Love, “Electrical diffuse layers and their influence on photosynthetic processes,” *FEBS Letters*, vol. 74, no. 2. pp. 174–181, 1977, doi: 10.1016/0014-5793(77)80841-7.

[232] N. Ghrairi and M. Bouaicha, “Structural, morphological, and optical properties of TiO2 thin films synthesized by the electro phoretic deposition technique,” *Nanoscale Res. Lett.*, vol. 7, no. 1, pp. 1–17, 2012, doi: 10.1186/1556-276X-7-1.

[233] D. C. Grahame, “The electrical double layer and the theory of electrocapillarity,” *Chem. Rev.*, vol. 41, no. 3, pp. 441–501, 1947, doi: 10.1021/cr60130a002.

[234] W. J. Albery, “Modulated Light Studies of the Electrochemistry of Semiconductors,” *J. Electrochem. Soc.*, vol. 134, no. 10, p. 2486, 1987, doi: 10.1149/1.2100227.

[235] N. J. Cherepy, G. P. Smestad, M. Grätzel, and J. Z. Zhang, “Ultrafast electron injection: Implications for a photoelectrochemical cell utilizing an anthocyanin dye-sensitized TiO2 nanocrystalline electrode,” *J. Phys. Chem. B*, vol. 101, no. 45, pp. 9342–9351, 1997, doi: 10.1021/jp972197w.

[236] K. P. Regan, C. Koenigsmann, S. W. Sheehan, S. J. Konezny, and C. A. Schmuttenmaer, “Size-dependent ultrafast charge carrier dynamics of WO3 for photoelectrochemical cells,” *J. Phys. Chem. C*, vol. 120, no. 27, pp. 14926–14933, 2016, doi: 10.1021/acs.jpcc.6b04390.

[237] Q. Zhang *et al.*, “Highly efficient CdS/CdSe-sensitized solar cells controlled by the structural properties of compact porous TiO2 photoelectrodes,” *Phys. Chem. Chem. Phys.*, vol. 13, no. 10, p. 4659, 2011, doi: 10.1039/c0cp02099k.

[238] J. Halme, J. Saarinen, and P. Lund, “Spray deposition and compression of TiO2 nanoparticle films for dye-sensitized solar cells on plastic substrates,” *Sol. Energy Mater. Sol. Cells*, vol. 90, no. 7–8, pp. 887–899, 2006, doi: 10.1016/j.solmat.2005.05.013.

[239] H. Choi *et al.*, “The effect of TiCl 4 -treated TiO 2 compact layer on the performance

of dye-sensitized solar cell," *Curr. Appl. Phys.*, vol. 12, no. 3, pp. 737–741, 2012, doi: 10.1016/j.cap.2011.10.011.

[240] S. J. Kim, S. D. Park, Y. H. Jeong, and S. Park, "Homogeneous precipitation of TiO2 ultrafine powders from aqueous TiOCl2 solution," *J. Am. Ceram. Soc.*, vol. 82, no. 4, pp. 927–932, 1999, doi: 10.1111/j.1151-2916.1999.tb01855.x.

[241] G. J. A. A. Soler-Illia, P. C. Angelomé, M. C. Fuertes, D. Grosso, and C. Boissiere, "Critical aspects in the production of periodically ordered mesoporous titania thin films," *Nanoscale*, vol. 4, no. 8, pp. 2549–2566, 2012, doi: 10.1039/c2nr11817c.

[242] C. J. Brinker, Y. Lu, A. Sellinger, and H. Fan, "ChemInform Abstract: Evaporation-Induced Self-Assembly: Nanostructures Made Easy," *ChemInform*, vol. 30, no. 28, p. no-no, 2010, doi: 10.1002/chin.199928288.

[243] S. Y. Choi, M. Mamak, N. Coombs, N. Chopra, and G. A. Ozin, "Thermally stable two-dimensional hexagonal mesoporous nanocrystalline anatase, meso-nc-TiO2: Bulk and crack-free thin film morphologies," *Adv. Funct. Mater.*, vol. 14, no. 4, pp. 335–344, 2004, doi: 10.1002/adfm.200305039.

[244] M. Yu *et al.*, "Solar-powered electrochemical energy storage: an alternative to solar fuels," *J. Mater. Chem. A*, vol. 4, no. 8, pp. 2766–2782, 2016, doi: 10.1039/C5TA06950E.

[245] M. Ge *et al.*, "A review of one-dimensional TiO_2 nanostructured materials for environmental and energy applications," *J. Mater. Chem. A*, vol. 4, no. 18, pp. 6772–6801, 2016, doi: 10.1039/C5TA09323F.

[246] C. Euvananont, C. Junin, K. Inpor, P. Limthongkul, and C. Thanachayanont, "TiO2 optical coating layers for self-cleaning applications," *Ceram. Int.*, 2008, doi: 10.1016/j.ceramint.2007.09.043.

[247] A. Moretti *et al.*, "Investigation of different binding agents for nanocrystalline anatase TiO 2 anodes and its application in a novel, green lithium-ion battery," *J. Power Sources*, vol. 221, pp. 419–426, 2013, doi: 10.1016/j.jpowsour.2012.07.142.

[248] J. Chong *et al.*, "A comparative study of polyacrylic acid and poly(vinylidene difluoride) binders for spherical natural graphite/LiFePO4 electrodes and cells," *J. Power Sources*, vol. 196, no. 18, pp. 7707–7714, 2011, doi: 10.1016/j.jpowsour.2011.04.043.

[249] D. Vak *et al.*, "Fabrication of organic bulk heterojunction solar cells by a spray deposition method for low-cost power generation," *Appl. Phys. Lett.*, vol. 91, no. 8, pp. 1–4, 2007, doi: 10.1063/1.2772766.

[250] I. M. Smallwood, *Handbook of Organic Solvent Properties*. 2012.

[251] Jacob N. Israelachvili, *Intermolecular and Surface Forces*, Thied edit. San Diego, 2011.

[252] R. H. Chen, T. X. Phuoc, and D. Martello, "Surface tension of evaporating nanofluid droplets," *Int. J. Heat Mass Transf.*, vol. 54, no. 11–12, pp. 2459–2466, 2011, doi: 10.1016/j.ijheatmasstransfer.2011.02.016.

[253] D. Zheng, J. Huang, Y. Zheng, and J. Yu, "High performance airbrush spray coated organic solar cells via tuning the surface tension and saturated vapor pressure of different ternary solvent systems," *Org. Electron.*, vol. 25, pp. 275–282, 2015, doi: 10.1016/j.orgel.2015.07.001.

[254] G. Strotos, M. Gavaises, A. Theodorakakos, and G. Bergeles, "Numerical investigation on the evaporation of droplets depositing on heated surfaces at low Weber numbers," *Int. J. Heat Mass Transf.*, vol. 51, no. 7–8, pp. 1516–1529, 2008, doi: 10.1016/j.ijheatmasstransfer.2007.07.045.

[255] M. E. R. Moffat, J.R., Sefiane, K., Shanahan, "Nanofluid Droplet Evaporation Kinetics and Wetting Dynamics on Flat Substrates," *J. Nano Res. 7*, pp. 75–80, 2009.

[256] W. P. Lee and A. F. Routh, "Why do drying films crack?," *Langmuir*, vol. 20, no. 23, pp. 9885–9888, 2004, doi: 10.1021/la049020v.

[257] J. A. Byrne, B. R. Eggins, N. M. D. Brown, B. McKinney, and M. Rouse, "Immobilisation of TiO2 powder for the treatment of polluted water," *Appl. Catal. B Environ.*, vol. 17, no. 1–2, pp. 25–36, 1998, doi: 10.1016/S0926-3373(97)00101-X.

[258] N. I. of S. and Technology and technology, "WebBook de Chimie NIST, SRD 69." .

[259] G. Syrrokostas, M. Giannouli, and P. Yianoulis, "Effects of paste storage on the properties of nanostructured thin films for the development of dye-sensitized solar cells," *Renew. Energy*, vol. 34, no. 7, pp. 1759–1764, 2009, doi: 10.1016/j.renene.2008.12.029.

[260] A. Abdellah *et al.*, "Successive spray deposition of P3HT/PCBM organic photoactive layers: Material composition and device characteristics," *Adv. Funct. Mater.*, vol. 22, no. 19, pp. 4078–4086, 2012, doi: 10.1002/adfm.201200548.

[261] H. Y. Park, K. Kim, D. Y. Kim, S. K. Choi, S. M. Jo, and S. Y. Jang, "Facile external treatment for efficient nanoscale morphology control of polymer solar cells using a gas-assisted spray method," *J. Mater. Chem.*, vol. 21, no. 12, pp. 4457–4464, 2011, doi: 10.1039/c0jm03899g.

[262] A. P. Xagas, E. Androulaki, A. Hiskia, and P. Falaras, "Preparation, fractal surface morphology and photocatalytic properties of TiO2 films," *Thin Solid Films*, vol. 357, no. 2, pp. 173–178, 1999, doi: 10.1016/S0040-6090(99)00561-1.

[263] P. Kebarle, “A brief overview of the present status of the mechanisms involved in electrospray mass spectrometry,” *J. Mass Spectrom.*, vol. 35, no. 7, pp. 804–817, 2000, doi: 10.1002/1096-9888(200007)35:7<804::AID-JMS22>3.0.CO;2-Q.

[264] S. Ben Ameur *et al.*, “Physical investigations on undoped and Fluorine doped SnO2 nanofilms on flexible substrate along with wettability and photocatalytic activity tests,” *Mater. Sci. Semicond. Process.*, vol. 61, no. December 2016, pp. 17–26, 2017, doi: 10.1016/j.mssp.2016.12.019.

[265] N. L. Tarwal and P. S. Patil, “Superhydrophobic and transparent ZnO thin films synthesized by spray pyrolysis technique,” *Appl. Surf. Sci.*, vol. 256, no. 24, pp. 7451–7456, 2010, doi: 10.1016/j.apsusc.2010.05.089.

[266] B. Bhushan and Y. C. Jung, “Micro- and nanoscale characterization of hydrophobic and hydrophilic leaf surfaces,” *Nanotechnology*, vol. 17, no. 11, pp. 2758–2772, 2006, doi: 10.1088/0957-4484/17/11/008.

[267] M. R. Golobostanfard and H. Abdizadeh, “Effect of mixed solvent on structural, morphological, and optoelectrical properties of spin-coated TiO 2 thin films,” *Ceram. Int.*, vol. 38, no. 7, pp. 5843–5851, 2012, doi: 10.1016/j.ceramint.2012.04.034.

[268] L. Lopez, W. A. Daoud, D. Dutta, B. C. Panther, and T. W. Turney, “Effect of substrate on surface morphology and photocatalysis of large-scale TiO 2 films,” *Appl. Surf. Sci.*, vol. 265, pp. 162–168, 2013, doi: 10.1016/j.apsusc.2012.10.156.

[269] C. Barry Carter and M. Grant Norton, *Ceramic materials: Science and engineering*. 2007.

[270] C. M. Firdaus, M. S. B. Shah Rizam, M. Rusop, and S. Rahmatul Hidayah, “Characterization of ZnO and ZnO: TiO2 thin films prepared by sol-gel spray-spin coating technique,” *Procedia Eng.*, vol. 41, no. Iris, pp. 1367–1373, 2012, doi: 10.1016/j.proeng.2012.07.323.

[271] S. Mahshid, M. Askari, and M. S. Ghamsari, “Synthesis of TiO2 nanoparticles by hydrolysis and peptization of titanium isopropoxide solution,” *J. Mater. Process. Technol.*, vol. 189, no. 1–3, pp. 296–300, 2007, doi: 10.1016/j.jmatprotec.2007.01.040.

[272] M. A. Khan, M. Shaheer Akhtar, and O. B. Yang, “Synthesis, characterization and application of sol-gel derived mesoporous TiO2 nanoparticles for dye-sensitized solar cells,” *Sol. Energy*, vol. 84, no. 12, pp. 2195–2201, 2010, doi: 10.1016/j.solener.2010.08.008.

[273] P. Pookmanee and S. Phanichphant, “Titanium dioxide powder prepared by a sol-gel method,” *J. Ceram. Process. Res.*, vol. 10, no. 2, pp. 167–170, 2009.

[274] V. Gourinchas Courtecuisse, J. F. Bocquet, K. Chhor, and C. Pommier, “Modeling of a

continuous reactor for TiO2 powder synthesis in a supercritical fluid - Experimental validation," *J. Supercrit. Fluids*, vol. 9, no. 4, pp. 222–226, 1996, doi: 10.1016/s0896-8446(96)90052-2.

[275] P. Malliga, J. Pandiarajan, N. Prithivikumaran, and K. Neyvasagam, "Influence of Film Thickness on Structural and Optical Properties of Sol – Gel Spin Coated TiO2 Thin Film," *IOSR J. Appl. Phys.*, vol. 6, no. 1, pp. 22–28, 2014, doi: 10.9790/4861-06112228.

[276] B. Henkel, A. Vahl, O. C. Aktas, T. Strunskus, and F. Faupel, "Self-organized nanocrack networks: A pathway to enlarge catalytic surface area in sputtered ceramic thin films, showcased for photocatalytic TiO2," *Nanotechnology*, vol. 29, no. 3, 2018, doi: 10.1088/1361-6528/aa9d35.

[277] D. R. Hummer, P. J. Heaney, and J. E. Post, "Thermal expansion of anatase and rutile between 300 and 575 K using synchrotron powder X-ray diffraction," *Powder Diffr.*, vol. 22, no. 4, pp. 352–357, 2007, doi: 10.1154/1.2790965.

[278] L. Vesce, R. Riccitelli, G. Soscia, T. M. Brown, A. Di Carlo, and A. Reale, "Optimization of nanostructured titania photoanodes for dye-sensitized solar cells: Study and experimentation of TiCl4treatment," *J. Non. Cryst. Solids*, vol. 356, no. 37–40, pp. 1958–1961, 2010, doi: 10.1016/j.jnoncrysol.2010.05.070.

[279] S. Y. Choi *et al.*, "3D hexagonal (R-3m) mesostructured nanocrystalline titania thin films: Synthesis and characterization," *Adv. Funct. Mater.*, vol. 16, no. 13, pp. 1731–1738, 2006, doi: 10.1002/adfm.200500507.

[280] B. W. Eggiman, M. P. Tate, and H. W. Hillhouse, "Rhombohedral structure of highly ordered and oriented self-assembled nanoporous silica thin films," *Chem. Mater.*, vol. 18, no. 3, pp. 723–730, 2006, doi: 10.1021/cm0520766.

[281] P. Y. Steinberg, M. M. Zalduendo, G. Giménez, G. J. A. A. Soler-Illia, and P. C. Angelomé, "TiO2 mesoporous thin film architecture as a tool to control Au nanoparticles growth and sensing capabilities," *Phys. Chem. Chem. Phys.*, vol. 21, no. 20, pp. 10347–10356, 2019, doi: 10.1039/c9cp01896d.

[282] M. C. Fuertes, M. Marchena, M. C. Marchi, A. Wolosiuk, and G. J. A. A. Soler-Illia, "Controlled deposition of silver nanoparticles in mesoporous single- Or multilayer thin films: From tuned pore filling to selective spatial location of nanometric objects," *Small*, vol. 5, no. 2, pp. 272–280, 2009, doi: 10.1002/smll.200800894.

[283] A. Gibaud, S. Dourdain, and G. Vignaud, "Analysis of mesoporous thin films by X-ray reflectivity, optical reflectivity and grazing incidence small angle X-ray scattering," *Appl. Surf. Sci.*, vol. 253, no. 1 SPEC. ISS., pp. 3–11, 2006, doi:

10.1016/j.apsusc.2006.05.121.

[284] A. Van der Lee, “Grazing incidence specular reflectivity: Theory, experiment, and applications,” *Solid State Sci.*, vol. 2, no. 2, pp. 257–278, 2000, doi: 10.1016/S1293-2558(00)00119-9.

[285] B. Liu and E. S. Aydil, “Growth of oriented single-crystalline rutile TiO 2 nanorods on transparent conducting substrates for dye-sensitized solar cells,” *J. Am. Chem. Soc.*, vol. 131, no. 11, pp. 3985–3990, 2009, doi: 10.1021/ja8078972.

[286] A. A. Shinkle, A. E. S. Sleightholme, L. T. Thompson, and C. W. Monroe, “Electrode kinetics in non-aqueous vanadium acetylacetonate redox flow batteries,” *J. Appl. Electrochem.*, vol. 41, no. 10, pp. 1191–1199, 2011, doi: 10.1007/s10800-011-0314-z.

[287] G. Chen and H. Liu, “Understanding the Reduction Kinetics of Aqueous Vanadium(V) and Transformation Products Using Rotating Ring-Disk Electrodes,” *Environ. Sci. Technol.*, vol. 51, no. 20, pp. 11643–11651, 2017, doi: 10.1021/acs.est.7b02021.

[288] E. C. Tyo and S. Vajda, “Catalysis by clusters with precise numbers of atoms,” *Nat. Nanotechnol.*, vol. 10, no. 7, pp. 577–588, 2015, doi: 10.1038/NNANO.2015.140.

[289] R. Jin, C. Zeng, M. Zhou, and Y. Chen, “Atomically Precise Colloidal Metal Nanoclusters and Nanoparticles: Fundamentals and Opportunities,” *Chem. Rev.*, vol. 116, no. 18, pp. 10346–10413, 2016, doi: 10.1021/acs.chemrev.5b00703.

[290] J. Turkevich, P. C. Stevenson, and J. Hillier, “A study of the nucleation and growth processes in the synthesis of colloidal gold,” *Discuss. Faraday Soc.*, vol. 11, no. c, pp. 55–75, 1951, doi: 10.1039/DF9511100055.

[291] V. Poonthiyil, V. B. Golovko, and A. J. Fairbanks, “Control of gold nanostructure morphology by variation of temperature and reagent ratios in the Turkevich reaction,” *Aust. J. Chem.*, vol. 68, no. 6, pp. 858–862, 2015, doi: 10.1071/CH14446.

[292] J. Y. Ruzicka *et al.*, “Toward Control of Gold Cluster Aggregation on TiO2 via Surface Treatments,” *J. Phys. Chem. C*, vol. 119, no. 43, pp. 24465–24474, 2015, doi: 10.1021/acs.jpcc.5b07732.

[293] D. Buso, J. Pacifico, A. Martucci, and P. Mulvaney, “Gold-nanoparticle-doped TiO2 semiconductor thin films: Optical characterization,” *Adv. Funct. Mater.*, vol. 17, no. 3, pp. 347–354, 2007, doi: 10.1002/adfm.200600349.

[294] A. Ayati, A. Ahmadpour, F. F. Bamoharram, B. Tanhaei, M. Mänttäri, and M. Sillanpää, “A review on catalytic applications of Au/TiO2 nanoparticles in the removal of water pollutant,” *Chemosphere*, vol. 107, pp. 163–174, 2014, doi: 10.1016/j.chemosphere.2014.01.040.

[295] E. Pedrueza *et al.*, “Novel method of preparation of gold-nanoparticle-doped TiO2 and

SiO2 plasmonic thin films: Optical characterization and comparison with Maxwell-Garnett modeling," *Adv. Funct. Mater.*, vol. 21, no. 18, pp. 3502–3507, 2011, doi: 10.1002/adfm.201101020.

[296] N. Chandrasekharan and P. Y. Kainat, "Improving the photoelectrochemical performance of nanostructured TiO2 films by adsorption of gold nanoparticles," *J. Phys. Chem. B*, vol. 104, no. 46, pp. 10851–10857, 2000, doi: 10.1021/jp0010029.

[297] F. Frederix *et al.*, "Biosensing Based on Light Absorption of Nanoscaled Gold and Silver Particles," *Anal. Chem.*, vol. 75, no. 24, pp. 6894–6900, 2003, doi: 10.1021/ac0346609.

[298] P. Wongwisate, S. Chavadej, E. Gulari, T. Sreethawong, and P. Rangsunvigit, "Effects of monometallic and bimetallic Au-Ag supported on sol-gel TiO2 on photocatalytic degradation of 4-chlorophenol and its intermediates," *Desalination*, vol. 272, no. 1–3, pp. 154–163, 2011, doi: 10.1016/j.desal.2011.01.016.

[299] B. Tian, C. Li, F. Gu, and H. Jiang, "Synergetic effects of nitrogen doping and Au loading on enhancing the visible-light photocatalytic activity of nano-TiO2," *Catal. Commun.*, vol. 10, no. 6, pp. 925–929, 2009, doi: 10.1016/j.catcom.2008.12.029.

[300] N. Ta *et al.*, "Stabilized gold nanoparticles on ceria nanorods by strong interfacial anchoring," *J. Am. Chem. Soc.*, vol. 134, no. 51, pp. 20585–20588, Dec. 2012, doi: 10.1021/ja310341j.

[301] D. Matthey *et al.*, "Enhanced bonding of gold nanoparticles on oxidized TiO2(110)," *Science (80-.).*, vol. 315, no. 5819, pp. 1692–1696, 2007, doi: 10.1126/science.1135752.

[302] C. M. Pharr and P. R. Griffiths, "Infrared Spectroelectrochemical Analysis of Adsorbed Hexacyanoferrate Species Formed during Potential Cycling in the Ferrocyanide/Ferricyanide Redox Couple," *Anal. Chem.*, vol. 69, no. 22, pp. 4673–4679, 1997, doi: 10.1021/ac961120l.

[303] P. H. Daum and C. G. Enke, "Electrochemical Kinetics of the Ferri—Ferrocyanide Couple on Platinum," *Anal. Chem.*, vol. 41, no. 4, pp. 653–656, 1969, doi: 10.1021/ac60273a007.

[304] P. A. Rock, "The standard oxidation potential of the ferrocyanide-ferricyanide electrode at 25° and the entropy of ferrocyanide ion," *J. Phys. Chem.*, vol. 70, no. 2, pp. 576–580, 1966, doi: 10.1021/j100874a042.

[305] A. A. Shinkle, A. E. S. Sleightholme, L. T. Thompson, and C. W. Monroe, "Electrode kinetics in non-aqueous vanadium acetylacetonate redox flow batteries," *J. Appl. Electrochem.*, vol. 41, no. 10, pp. 1191–1199, 2011, doi: 10.1007/s10800-011-0314-z.

[306] R. P. Mitra, D. V. S. Jain, A. K. Bannerjee, and K. V. Raghavachari, “Role of free radicals in the photo-oxidation of Fe+2 in acidic solutions of ferrocyanide [11],” *Nature*, vol. 200, no. 4902. pp. 163–164, 1963, doi: 10.1038/200163a0.

[307] S. Izawa and D. R. Ort, “Photooxidation of ferrocyanide and iodide ions and associated phosphorylation in NH2OH-treated chloroplasts,” *BBA - Bioenerg.*, vol. 357, no. 1, pp. 127–143, Jul. 1974, doi: 10.1016/0005-2728(74)90118-2.

[308] R. K. Clayton and S. C. Straley, “Photochemical Electron Transport in Photosynthetic Reaction Centers: IV. Observations Related to the Reduced Photoproducts,” *Biophys. J.*, vol. 12, no. 10, pp. 1221–1234, 1972, doi: 10.1016/S0006-3495(72)86158-7.

[309] S. J. Konopka and B. McDuffie, “Diffusion Coefficients of Ferri- and Ferrocyanide Ions in Aqueous Media, Using Twin-Electrode Thin-Layer Electrochemistry,” *Anal. Chem.*, vol. 42, no. 14, pp. 1741–1746, 1970, doi: 10.1021/ac50160a042.

[310] A. A. Shinkle, A. E. S. Sleightholme, L. D. Griffith, L. T. Thompson, and C. W. Monroe, “Degradation mechanisms in the non-aqueous vanadium acetylacetonate redox flow battery,” in *Journal of Power Sources*, May 2012, vol. 206, pp. 490–496, doi: 10.1016/j.jpowsour.2010.12.096.

[311] Q. Liu, A. E. S. Sleightholme, A. A. Shinkle, Y. Li, and L. T. Thompson, “Non-aqueous vanadium acetylacetonate electrolyte for redox flow batteries,” *Electrochem. commun.*, vol. 11, no. 12, pp. 2312–2315, Dec. 2009, doi: 10.1016/j.elecom.2009.10.006.

[312] NREL, “Photovoltaic Research: Best Research Cell Efficiency Chart,” *Natl. Renew. Energy Lab.*, Accessed: Oct. 14, 2020. [Online]. Available: https://www.nrel.gov/pv/cell-efficiency.html.

[313] D. P. Anderson *et al.*, “Chemically-synthesised, atomically-precise gold clusters deposited and activated on titania,” *Phys. Chem. Chem. Phys.*, vol. 15, no. 11, pp. 3917–3929, 2013, doi: 10.1039/c3cp44005b.

[314] Y. Shichibu and K. Konishi, “HCL-induced nuclearity convergence in diphosphine-protected ultrasmall gold clusters: A novel synthetic route to ‘Magic-Number’ Au13 clusters,” *Small*, vol. 6, no. 11, pp. 1216–1220, 2010, doi: 10.1002/smll.200902398.

[315] X. K. Wan, S. F. Yuan, Z. W. Lin, and Q. M. Wang, “A chiral gold nanocluster Au20 protected by tetradentate phosphine ligands,” *Angew. Chemie - Int. Ed.*, vol. 53, no. 11, pp. 2923–2926, 2014, doi: 10.1002/anie.201308599.

[316] W. W. Weare, S. M. Reed, M. G. Warner, and J. E. Hutchison, “Improved synthesis of small (dCORE ≈ 1.5 nm) phosphine-stabilized gold nanoparticies [14],” *J. Am. Chem. Soc.*, vol. 122, no. 51, pp. 12890–12891, 2000, doi: 10.1021/ja002673n.

[2] P. M. Cox, R. a Betts, C. D. Jones, S. a Spall, and I. J. Totterdell, “Acceleration of global warming due to carbon-cycle feedbacks in a coupled climate model (vol 408, pg 184, 2000),” *Nature*, vol. 408, no. 6813, p. 750, 2000, doi: 10.1038/35041539.

[3] N. A. Owen, O. R. Inderwildi, and D. A. King, “The status of conventional world oil reserves-Hype or cause for concern?,” *Energy Policy*, vol. 38, no. 8, pp. 4743–4749, 2010, doi: 10.1016/j.enpol.2010.02.026.

[4] N. L. Panwar, S. C. Kaushik, and S. Kothari, “Role of renewable energy sources in environmental protection: A review,” *Renew. Sustain. Energy Rev.*, vol. 15, no. 3, pp. 1513–1524, 2011, doi: 10.1016/j.rser.2010.11.037.

[5] B. Liu, X. Zhao, C. Terashima, A. Fujishima, and K. Nakata, “Thermodynamic and kinetic analysis of heterogeneous photocatalysis for semiconductor systems,” *Phys. Chem. Chem. Phys.*, vol. 16, no. 19, p. 8751, 2014, doi: 10.1039/c3cp55317e.

[6] M. Grätzel, “Photoelectrochemical Cells,” *Nature*, vol. 414, no. November, pp. 457–481, 2001, doi: 10.1007/978-1-4899-0418-8_11.

[7] J. P. Painuly, “Barriers to renewable energy penetration: A framework for analysis,” *Renew. Energy*, vol. 24, no. 1, pp. 73–89, 2001, doi: 10.1016/S0960-1481(00)00186-5.

[8] I. Dincer, “Renewable energy and sustainable development: a crucial review,” *Renew. Sustain. Energy Rev.*, vol. 4, no. 2, pp. 157–175, 2000, doi: 10.1016/S1364-0321(99)00011-8.

[9] J. D. Hamilton, “CAUSES AND CONSEQUENCES OF THE OIL SHOCK OF 2007-08,” *NBER Work. Pap.*, 2009.

[10] Ministry of Business Innovation & Employment (MBIE), “Energy in New Zealand 2017,” p. 47, 2017, [Online]. Available: http://www.med.govt.nz/sectors-industries/energy/energy-modelling/publications/energy-in-new-zealand-2013/Energy-in-New-Zealand-2013.pdf.

[11] A. Z. Weber, M. M. Mench, J. P. Meyers, P. N. Ross, J. T. Gostick, and Q. Liu, “Redox flow batteries: A review,” *J. Appl. Electrochem.*, vol. 41, no. 10, pp. 1137–1164, 2011, doi: 10.1007/s10800-011-0348-2.

[12] M. Skyllas-Kozocos and F. Grossmith, “Efficient Vanadium Redox Flow Cell,” *J. Electrochem. Soc.*, vol. 134, no. 12, pp. 2950–2953, 1987, doi: 10.1149/1.2100321.

[13] C. Ding, H. Zhang, X. Li, T. Liu, and F. Xing, “Vanadium flow battery for energy storage: Prospects and challenges,” *J. Phys. Chem. Lett.*, vol. 4, no. 8, pp. 1281–1294, 2013, doi: 10.1021/jz4001032.

[14] M. Rychcik and M. Skyllas-Kazacos, “Evaluation of electrode materials for vanadium

redox cell," *J. Power Sources*, vol. 19, no. 1, pp. 45–54, 1987, doi: 10.1016/0378-7753(87)80006-X.

[15] M. Skyllas-Kazacos, "Efficient Vanadium Redox Flow Cell," *J. Electrochem. Soc.*, vol. 134, no. 12, p. 2950, 1987, doi: 10.1149/1.2100321.

[16] E. Sum and M. Skyllas-Kazacos, "A study of the V(II)/V(III) redox couple for redox flow cell applications," *J. Power Sources*, vol. 15, no. 2–3, pp. 179–190, 1985, doi: 10.1016/0378-7753(85)80071-9.

[17] M. Rychcik and M. Skyllas-Kazacos, "Characteristics of a new all-vanadium redox flow battery," *J. Power Sources*, vol. 22, no. 1, pp. 59–67, Jan. 1988, doi: 10.1016/0378-7753(88)80005-3.

[18] M. Kazacos, M. Cheng, and M. Skyllas-Kazacos, "Vanadium redox cell electrolyte optimization studies," *J. Appl. Electrochem.*, vol. 20, no. 3, pp. 463–467, 1990, doi: 10.1007/BF01076057.

[19] M. Skyllas-Kazacos, "Thermal Stability of Concentrated V(V) Electrolytes in the Vanadium Redox Cell," *J. Electrochem. Soc.*, vol. 143, no. 4, p. L86, 1996, doi: 10.1149/1.1836609.

[20] F. Rahman and M. Skyllas-Kazacos, "Solubility of vanadyl sulfate in concentrated sulfuric acid solutions," *J. Power Sources*, vol. 72, no. 2, pp. 105–110, 1998, doi: 10.1016/S0378-7753(97)02692-X.

[21] L. Li *et al.*, "A stable vanadium redox-flow battery with high energy density for large-scale energy storage," *Adv. Energy Mater.*, vol. 1, no. 3, pp. 394–400, 2011, doi: 10.1002/aenm.201100008.

[22] M. Skyllas-Kazacos, M. H. Chakrabarti, S. A. Hajimolana, F. S. Mjalli, and M. Saleem, "Progress in Flow Battery Research and Development," *J. Electrochem. Soc.*, vol. 158, no. 8, p. R55, 2011, doi: 10.1149/1.3599565.

[23] P. Leung, X. Li, C. Ponce de León, L. Berlouis, C. T. J. Low, and F. C. Walsh, "Progress in redox flow batteries, remaining challenges and their applications in energy storage," *RSC Adv.*, vol. 2, no. 27, p. 10125, 2012, doi: 10.1039/c2ra21342g.

[24] J. M. Dickson, "(12) Patent Application Publication (10) Pub . No .: US 2003 / 0168404 A1 Pervaporation with Water / Ethanol Mixtures : Effect of Temperature Temperature (C) Separation FG . A Temperature (C) Flux," 2003.

[25] K. W. Knehr and E. C. Kumbur, "Open circuit voltage of vanadium redox flow batteries: Discrepancy between models and experiments," *Electrochem. commun.*, vol. 13, no. 4, pp. 342–345, 2011, doi: 10.1016/j.elecom.2011.01.020.

[26] C. H. Li, X. J. Zhu, G. Y. Cao, S. Sui, and M. R. Hu, "Dynamic modeling and sizing

optimization of stand-alone photovoltaic power systems using hybrid energy storage technology," *Renew. Energy*, vol. 34, no. 3, pp. 815–826, 2009, doi: 10.1016/j.renene.2008.04.018.

[27] reportsnreports, "Redox Flow Battery Market Value to Hit 370 Million US$ by 2025, at a CAGR of 14.3%, Business Trends, Global Projections 2019." https://www.prnewswire.com/news-releases/redox-flow-battery-market-value-to-hit-370-million-us-by-2025--at-a-cagr-of-14-3-business-trends-global-projections-2019--300903369.html (accessed May 04, 2020).

[28] G. Hodes, D. Cahen, and J. Manassen, "Tungsten trioxide as a photoanode for a photoelectrochemical cell (PEC)," *Nature*, vol. 260, no. 5549, pp. 312–313, 1976, doi: 10.1038/260312a0.

[29] S. Licht and D. Peramunage, "Efficient photoelectrochemical solar cells from electrolyte modification," *Nature*, vol. 345, pp. 330–333, 1990, doi: 10.1038/345330a0.

[30] S. Licht *et al.*, "High efficiency n-Cd(Se,Te)/S photoelectrochemical cell resulting from solution chemistry control," *Appl. Phys. Lett.*, vol. 46, no. 6, pp. 608–610, 1985, doi: 10.1063/1.95556.

[31] J. R. McKone, F. J. DiSalvo, and H. D. Abruña, "Solar energy conversion, storage, and release using an integrated solar-driven redox flow battery," *J. Mater. Chem. A*, vol. 5, no. 11, pp. 5362–5372, 2017, doi: 10.1039/C7TA00555E.

[32] M. Grätzel, "Dye-sensitized solar cells," *J. Photochem. Photobiol. C Photochem. Rev.*, vol. 4, no. 2, pp. 145–153, 2003, doi: 10.1016/S1389-5567(03)00026-1.

[33] S.-Q. Fan, C.-J. Li, C.-X. Li, G.-J. Liu, G.-J. Yang, and L.-Z. Zhang, "Preliminary Study of Performance of Dye-Sensitized Solar Cell of Nano-TiO2 Coating Deposited by Vacuum Cold Spraying," *Mater. Trans.*, vol. 47, no. 7, pp. 1703–1709, 2006, doi: 10.2320/matertrans.47.1703.

[34] B. O'Regan and M. Grätzel, "A low-cost, high-efficiency solar cell based on dye-sensitized colloidal TiO2 films," *Nature*, vol. 353, no. 6346, pp. 737–740, 1991, doi: 10.1038/353737a0.

[35] M. A. Mahmoudzadeh, A. R. Usgaocar, J. Giorgio, D. L. Officer, G. G. Wallace, and J. D. W. Madden, "A high energy density solar rechargeable redox battery," *J. Mater. Chem. A*, vol. 4, no. 9, pp. 3446–3452, 2016, doi: 10.1039/C5TA08618C.

[36] N. F. Yan, G. R. Li, and X. P. Gao, "Solar rechargeable redox flow battery based on Li2WO4/LiI couples in dual-phase electrolytes," *J. Mater. Chem. A*, vol. 1, no. 24, p. 7012, 2013, doi: 10.1039/c3ta11360d.

[37] H. Nagai and H. Segawa, “Energy-storable dye-sensitized solar cell with a polypyrrole electrode,” *Chem. Commun.*, no. 8, pp. 974–975, 2004, doi: 10.1039/B400439F.

[38] P. Liu, Y. L. Cao, G. R. Li, X. P. Gao, X. P. Ai, and H. X. Yang, “A solar rechargeable flow battery based on photoregeneration of two soluble redox couples,” *ChemSusChem*, vol. 6, no. 5, pp. 802–806, 2013, doi: 10.1002/cssc.201200962.

[39] B. Keita and L. Nadjo, “Electrochemistry and photoelectrochemistry of sodium 9,10-anthraquinone-2,6-disulfonate in aqueous media. Application to rechargeable solar cells and to the synthesis of hydrogen peroxide,” *J. Electroanal. Chem.*, vol. 163, no. 1–2, pp. 171–188, Mar. 1984, doi: 10.1016/S0022-0728(84)80050-9.

[40] M. Sharon, S. Kumar, N. P. Sathe, and S. R. Jawalekar, “Saur Viddyut Kosh IV: Study of a rechargeable solar battery with n-Pb3O4electrodes,” *Sol. Cells*, vol. 12, no. 4, pp. 353–361, 1984, doi: 10.1016/0379-6787(84)90030-9.

[41] G. Betz, S. Fiechter, and H. Tributsch, “Photon energy conversion and storage with a light-driven insertion reaction,” *J. Appl. Phys.*, vol. 62, no. 11, pp. 4597–4605, 1987, doi: 10.1063/1.339056.

[42] M. Yu, W. D. McCulloch, D. R. Beauchamp, Z. Huang, X. Ren, and Y. Wu, “Aqueous Lithium-Iodine Solar Flow Battery for the Simultaneous Conversion and Storage of Solar Energy,” *J. Am. Chem. Soc.*, vol. 137, no. 26, pp. 8332–8335, 2015, doi: 10.1021/jacs.5b03626.

[43] W. Guo, X. Xue, S. Wang, C. Lin, and Z. L. Wang, “An integrated power pack of dye-sensitized solar cell and Li battery based on double-sided TiO2 nanotube arrays,” *Nano Lett.*, vol. 12, pp. 2520–2523, 2012, doi: 10.1021/nl3007159.

[44] Z. Wei, D. Liu, C. Hsu, and F. Liu, “All-vanadium redox photoelectrochemical cell: An approach to store solar energy,” *Electrochem. commun.*, vol. 45, pp. 79–82, 2014, doi: 10.1016/j.elecom.2014.05.018.

[45] D. Liu, Z. Wei, C. J. Hsu, Y. Shen, and F. Liu, “Efficient solar energy storage using A TiO2/WO3 tandem photoelectrode in an all-vanadium photoelectrochemical cell,” *Electrochim. Acta*, vol. 136, pp. 435–441, 2014, doi: 10.1016/j.electacta.2014.05.129.

[46] J. Azevedo *et al.*, “Unbiased solar energy storage: Photoelectrochemical redox flow battery,” *Nano Energy*, vol. 22, pp. 396–405, 2016, doi: 10.1016/j.nanoen.2016.02.029.

[47] X. Jiao *et al.*, “A microfluidic all-vanadium photoelectrochemical cell for solar energy storage,” *Electrochim. Acta*, vol. 258, pp. 842–849, 2017, doi: 10.1016/j.electacta.2017.11.134.

[48] Z. Wei, Y. Shen, D. Liu, and F. Liu, “An All-vanadium Continuous-flow

Photoelectrochemical Cell for Extending State-of-charge in Solar Energy Storage," *Sci. Rep.*, vol. 7, no. 1, pp. 1–9, 2017, doi: 10.1038/s41598-017-00585-y.

[49] D. Liu *et al.*, "Reversible Electron Storage in an All-Vanadium Photoelectrochemical Storage Cell: Synergy between Vanadium Redox and Hybrid Photocatalyst," *ACS Catal.*, vol. 5, no. 4, pp. 2632–2639, 2015, doi: 10.1021/cs502024k.

[50] Q. Zhang and G. Cao, "Nanostructured photoelectrodes for dye-sensitized solar cells," *Nano Today*, vol. 6, no. 1, pp. 91–109, 2011, doi: 10.1016/j.nantod.2010.12.007.

[51] Y. Diamant, S. Chappel, S. G. Chen, O. Melamed, and A. Zaban, "Core–shell nanoporous electrode for dye sensitized solar cells: the effect of shell characteristics on the electronic properties of the electrode," *Coord. Chem. Rev.*, vol. 248, pp. 1271–1276, 2004, doi: 10.1016/j.ccr.2004.03.003.

[52] H. Choi, W. T. Chen, and P. V. Kamat, "Know thy nano neighbor. Plasmonic versus electron charging effects of metal nanoparticles in dye-sensitized solar cells," *ACS Nano*, vol. 6, no. 5, pp. 4418–4427, 2012, doi: 10.1021/nn301137r.

[53] K. Uzaki, T. Nishimura, J. Usagawa, S. Hayase, M. Kono, and Y. Yamaguchi, "Dye-Sensitized Solar Cells Consisting of 3D-Electrodes—A Review: Aiming at High Efficiency From the View Point of Light Harvesting and Charge Collection," *J. Sol. Energy Eng.*, vol. 132, no. 2, p. 021204, May 2010, doi: 10.1115/1.4001182.

[54] A. M. Smith and S. Nie, "Semiconductor nanocrystals: Structure, properties, and band gap engineering," *Acc. Chem. Res.*, vol. 43, no. 2, pp. 190–200, 2010, doi: 10.1021/ar9001069.

[55] A. Kahn, "Fermi level, work function and vacuum level," *Mater. Horizons*, vol. 3, no. 1, pp. 7–10, 2016, doi: 10.1039/c5mh00160a.

[56] N. SATO, "Electrocthemistry of Semiconductors," *Tetsu-to-Hagane*, vol. 76, no. 9, pp. 1423–1436, 1990, doi: 10.2355/tetsutohagane1955.76.9_1423.

[57] J. T. Fulton, "Electrochemistry of the Neuron," *Process. Biol. Vis.*, vol. 1, no. 949, pp. 10–14, 2004.

[58] B. Mukherjee, W. Wilson, and V. Subramanian, "TiO2 nanotube (T-NT) surface treatment revisited: Implications of ZnO, TiCl4, and H2O2 treatment on the photoelectrochemical properties of T-NT and T-NT-CdSe," *Nanoscale*, vol. 5, no. 1, pp. 269–274, 2013, doi: 10.1039/c2nr31660a.

[59] G. Yun *et al.*, "Beneficial surface passivation of hydrothermally grown TiO 2 nanowires for solar water oxidation," *Appl. Surf. Sci.*, vol. 366, pp. 561–566, 2016, doi: 10.1016/j.apsusc.2016.01.111.

[60] Y. C. Pu *et al.*, "Au nanostructure-decorated TiO2 nanowires exhibiting photoactivity

across entire UV-visible region for photoelectrochemical water splitting," *Nano Lett.*, vol. 13, no. 8, pp. 3817–3823, 2013, doi: 10.1021/nl4018385.

[61] G. Horowitz, "Capacitance-voltage measurements and flat-band potential determination on Zr-doped α-Fe2O3 single-crystal electrodes," *J. Electroanal. Chem.*, vol. 159, no. 2, pp. 421–436, 1983, doi: 10.1016/S0022-0728(83)80638-X.

[62] K. Ozawa *et al.*, "Electron-hole recombination time at TiO 2 single-crystal surfaces: Influence of surface band bending," *J. Phys. Chem. Lett.*, vol. 5, no. 11, pp. 1953–1957, 2014, doi: 10.1021/jz500770c.

[63] D. D. F. Aplicada, E. T. S. I. Telecomunicacion, and U. Polit, "Photoelectrolysis at n-Ti02 Electrodes," vol. 137, no. 6, pp. 1810–1815, 1990.

[64] X. Chen and S. S. Mao, "Synthesis of titanium dioxide (TiO <inf>2</inf>) nanomaterials," *J. Nanosci. Nanotechnol.*, vol. 6, no. 4, pp. 906–925, 2006, doi: 10.1166/jnn.2006.160.

[65] A. Paracchino, V. Laporte, K. Sivula, M. Grätzel, and E. Thimsen, "Highly active oxide photocathode for photoelectrochemical water reduction," *Nat. Mater.*, vol. 10, no. 6, pp. 456–461, 2011, doi: 10.1038/nmat3017.

[66] O. Ola and M. M. Maroto-Valer, "Review of material design and reactor engineering on TiO2 photocatalysis for CO2 reduction," *J. Photochem. Photobiol. C Photochem. Rev.*, vol. 24, pp. 16–42, 2015, doi: 10.1016/j.jphotochemrev.2015.06.001.

[67] S. Wang *et al.*, "Recent Progress on Visible Light Responsive Heterojunctions for Photocatalytic Applications," *J. Mater. Sci. Technol.*, vol. 33, no. 1, pp. 1–22, Jan. 2017, doi: 10.1016/j.jmst.2016.11.017.

[68] S. Nahar, M. Zain, A. Kadhum, H. Hasan, and M. Hasan, "Advances in Photocatalytic CO2 Reduction with Water: A Review," *Materials (Basel).*, vol. 10, no. 6, p. 629, 2017, doi: 10.3390/ma10060629.

[69] W. Chen, "Development of Efficient Low-Cost Semiconductor Photocatalysts for Solar H 2 Production," 2017.

[70] H. M. Chen, C. K. Chen, R.-S. Liu, L. Zhang, J. Zhang, and D. P. Wilkinson, "Nano-architecture and material designs for water splitting photoelectrodes," *Chem. Soc. Rev.*, vol. 41, no. 17, p. 5654, 2012, doi: 10.1039/c2cs35019j.

[71] A. Wolcott, W. A. Smith, T. R. Kuykendall, Y. Zhao, and J. Z. Zhang, "Photoelectrochemical Water Splitting Using Dense and Aligned TiO $_2$ Nanorod Arrays," *Small*, vol. 5, no. 1, pp. 104–111, 2009, doi: 10.1002/smll.200800902.

[72] I. S. Cho *et al.*, "Branched TiO2 nanorods for photoelectrochemical hydrogen production," *Nano Lett.*, vol. 11, no. 11, pp. 4978–4984, 2011, doi:

10.1021/nl2029392.

[73] M. Liu, N. de Leon Snapp, and H. Park, “Water photolysis with a cross-linked titanium dioxide nanowire anode,” *Chem. Sci.*, vol. 2, no. 1, pp. 80–87, 2011, doi: 10.1039/C0SC00321B.

[74] A. Wolcott, W. A. Smith, T. R. Kuykendall, Y. Zhao, and J. Z. Zhang, “Photoelectrochemical study of nanostructured Zno thin films for hydrogen generation from water splitting,” *Adv. Funct. Mater.*, vol. 19, no. 12, pp. 1849–1856, 2009, doi: 10.1002/adfm.200801363.

[75] B. D. Alexander, P. J. Kulesza, I. Rutkowska, R. Solarska, and J. Augustynski, “Metal oxide photoanodes for solar hydrogen production,” *J. Mater. Chem.*, vol. 18, no. 20, p. 2298, 2008, doi: 10.1039/b718644d.

[76] V. Cristino, S. Caramori, R. Argazzi, L. Meda, G. L. Marra, and C. A. Bignozzi, “Efficient photoelectrochemical water splitting by anodically grown WO 3 electrodes,” *Langmuir*, vol. 27, no. 11, pp. 7276–7284, 2011, doi: 10.1021/la200595x.

[77] V. Chakrapani, J. Thangala, and M. K. Sunkara, “WO3 and W2N nanowire arrays for photoelectrochemical hydrogen production,” *Int. J. Hydrogen Energy*, vol. 34, no. 22, pp. 9050–9059, 2009, doi: 10.1016/j.ijhydene.2009.09.031.

[78] S. P. Berglund, D. W. Flaherty, N. T. Hahn, A. J. Bard, and C. B. Mullins, “Photoelectrochemical oxidation of water using nanostructured BiVO 4 films,” *J. Phys. Chem. C*, vol. 115, no. 9, pp. 3794–3802, 2011, doi: 10.1021/jp1109459.

[79] R. Morrish, M. Rahman, J. M. D. MacElroy, and C. A. Wolden, “Activation of hematite nanorod arrays for photoelectrochemical water splitting,” *ChemSusChem*, vol. 4, no. 4, pp. 474–479, 2011, doi: 10.1002/cssc.201100066.

[80] K. Keis *et al.*, “A 5% efficient photoelectrochemical solar cell based on nanostructured ZnO electrodes,” *Sol. Energy Mater. Sol. Cells*, vol. 73, no. 1, pp. 51–58, 2002, doi: 10.1016/S0927-0248(01)00110-6.

[81] K. Tennakone, G. R. R. a. Kumara, I. R. M. Kottegoda, and V. P. S. Perera, “An efficient dye-sensitized photoelectrochemical solar cell made from oxides of tin and zinc,” *Chem. Commun.*, no. 1, pp. 15–16, 1999, doi: 10.1039/a806801a.

[82] B. V. Bergeron, A. Marton, G. Oskam, and G. J. Meyer, “Dye-sensitized SnO 2 electrodes with iodide and pseudohalide redox mediators,” *J. Phys. Chem. B*, vol. 109, no. 2, pp. 937–943, 2005, doi: 10.1021/jp0461347.

[83] S. Chappel and a. Zaban, “Nanoporous SnO2 electrodes for dye-sensitized solar cells: improved cell performance by the synthesis of 18nm SnO2 colloids,” *Sol. Energy Mater. Sol. Cells*, vol. 71, pp. 141–152, 2002, doi: 10.1016/S0927-0248(01)00050-2.

[84] K. Sayama, H. Sugihara, and H. Arakawa, “Photoelectrochemical Properties of a Porous Nb $_2$ O $_5$ Electrode Sensitized by a Ruthenium Dye,” *Chem. Mater.*, vol. 10, no. 12, pp. 3825–3832, 1998, doi: 10.1021/cm980111l.

[85] P. Guo and M. A. Aegerter, “Ru(II) sensitized Nb_{2}O_{5} solar cell made by the sol-gel process,” *Thin Solid Films*, vol. 351, no. 1–2, pp. 290–294, 1999, doi: 10.1016/S0040-6090(99)00215-1.

[86] S. Burnside, J.-E. Moser, K. Brooks, M. Grätzel, and D. Cahen, “Nanocrystalline Mesoporous Strontium Titanate as Photoelectrode Material for Photosensitized Solar Devices: Increasing Photovoltage through Flatband Potential Engineering,” *J. Phys. Chem. B*, vol. 103, no. 43, pp. 9328–9332, 1999, doi: 10.1021/jp9913867.

[87] B. Tan, E. Toman, Y. Li, and Y. Wu, “Zinc stannate (Zn2SnO4) dye-sensitized solar cells,” *J. Am. Chem. Soc.*, vol. 129, no. 14, pp. 4162–4163, 2007, doi: 10.1021/ja070804f.

[88] N. F. Yan, G. R. Li, G. L. Pan, and X. P. Gao, “TiN Nanotube Arrays as Electrocatalytic Electrode for Solar Storable Rechargeable Battery,” *J. Electrochem. Soc.*, vol. 159, no. 11, pp. A1770–A1774, 2012, doi: 10.1149/2.019211jes.

[89] Z. Kebede and S.-E. Lindquist, “The obstructed diffusion of the I3- ion in mesoscopic TiO2 membranes,” *Sol. Energy Mater. Sol. Cells*, vol. 51, no. 3–4, pp. 291–303, 1998, doi: 10.1016/S0927-0248(97)00229-8.

[90] F. Cao, G. Oskam, G. J. Meyer, and P. C. Searson, “Electron Transport in Porous Nanocrystalline TiO 2 Photoelectrochemical Cells,” *J. Phys. Chem.*, vol. 100, no. 42, pp. 17021–17027, 1996, doi: 10.1021/jp9616573.

[91] D. Dambournet, I. Belharouak, and K. Amine, “Tailored Preparation Methods of TiO $_2$ Anatase, Rutile, Brookite: Mechanism of Formation and Electrochemical Properties †,” *Chem. Mater.*, vol. 22, no. 3, pp. 1173–1179, 2010, doi: 10.1021/cm902613h.

[92] A. L. Linsebigler, G. Lu, and J. T. Yates, “Photocatalysis on TiO2Surfaces: Principles, Mechanisms, and Selected Results,” *Chem. Rev.*, vol. 95, no. 3, pp. 735–758, 1995, doi: 10.1021/cr00035a013.

[93] N.-G. Park, J. van de Lagemaat, and A. J. Frank, “Comparison of Dye-Sensitized Rutile- and Anatase-Based TiO 2 Solar Cells,” *J. Phys. Chem. B*, vol. 104, no. 38, pp. 8989–8994, 2000, doi: 10.1021/jp994365l.

[94] T. Ohno, K. Sarukawa, K. Tokieda, and M. Matsumura, “Morphology of a TiO2photocatalyst (Degussa, P-25) consisting of anatase and rutile crystalline phases,” *J. Catal.*, vol. 203, no. 1, pp. 82–86, 2001, doi: 10.1006/jcat.2001.3316.

[95] K. Al-Attafi *et al.*, “The effect of amorphous TiO 2 in P25 on dye-sensitized solar cell

performance," *Chem. Commun. Chem. Commun*, vol. 54, no. 54, pp. 381–384, 2018, doi: 10.1039/c7cc07559f.

[96] A. Hagfeldt and M. Grätzel, "Molecular photovoltaics," *Acc. Chem. Res.*, vol. 33, no. 5, pp. 269–277, 2000, doi: 10.1021/ar980112j.

[97] J. M. Kroon *et al.*, "Nanocrystalline dye-sensitized solar cells having maximum performance," *Prog. Photovoltaics Res. Appl.*, vol. 15, no. 1, pp. 1–18, Jan. 2007, doi: 10.1002/pip.707.

[98] P. M. Sommeling *et al.*, "Influence of a TiCl4 post-treatment on nanocrystalline TiO 2 films in dye-sensitized solar cells," *J. Phys. Chem. B*, vol. 110, no. 39, pp. 19191–19197, 2006, doi: 10.1021/jp061346k.

[99] B. O'Regan and M. Gratzel, "A Low-Cost, High-Efficiency Solar-Cell Based on Dye-Sensitized Colloidal TiO2 Films," *Nature*, vol. 353, no. 6346, pp. 737–740, Oct. 1991, doi: 10.1038/353737a0.

[100] D. Liu *et al.*, "Reversible Electron Storage in an All-Vanadium Photoelectrochemical Storage Cell: Synergy between Vanadium Redox and Hybrid Photocatalyst," *ACS Catal.*, vol. 5, no. 4, pp. 2632–2639, 2015, doi: 10.1021/cs502024k.

[101] S. G. Chen, S. Chappel, Y. Diamant, and A. Zaban, "Preparation of Nb2O5 coated TiO2 nanoporous electrodes and their application in dye-sensitized solar cells," *Chem. Mater.*, vol. 13, no. 12, pp. 4629–4634, 2001, doi: 10.1021/cm010343b.

[102] D. Cahen, G. Hodes, M. Grätzel, J. F. Guillemoles, and I. Riess, "Nature of Photovoltaic Action in Dye-Sensitized Solar Cells," *J. Phys. Chem. B*, vol. 104, no. 9, pp. 2053–2059, 2000, doi: 10.1021/jp993187t.

[103] Y. Diamant, S. G. Chen, O. Melamed, and A. Zaban, "Core-shell nanoporous electrode for dye sensitized solar cells: The effect of the SrTiO3 shell on the electronic properties of the TiO2 core," *J. Phys. Chem. B*, vol. 107, no. 9, pp. 1977–1981, 2003, doi: 10.1021/jp027827v.

[104] J. van de Lagemaat, N.-G. Park, and A. J. Frank, "Influence of Electrical Potential Distribution, Charge Transport, and Recombination on the Photopotential and Photocurrent Conversion Efficiency of Dye-Sensitized Nanocrystalline TiO 2 Solar Cells: A Study by Electrical Impedance and Optical Modulation Te," *J. Phys. Chem. B*, vol. 104, no. 9, pp. 2044–2052, 2000, doi: 10.1021/jp993172v.

[105] L. M. Peter, "Dye-sensitized nanocrystalline solar cells," *Phys. Chem. Chem. Phys.*, vol. 9, no. 21, p. 2630, 2007, doi: 10.1039/b617073k.

[106] Z.-Q. Li, W.-C. Chen, F.-L. Guo, L.-E. Mo, L.-H. Hu, and S.-Y. Dai, "Mesoporous TiO2 Yolk-Shell Microspheres for Dye-sensitized Solar Cells with a High Efficiency

Exceeding 11%," *Sci. Rep.*, vol. 5, no. 1, p. 14178, 2015, doi: 10.1038/srep14178.

[107] E. Palomares, J. N. Clifford, S. A. Haque, T. Lutz, and J. R. Durrant, "Control of charge recombination dynamics in dye sensitized solar cells by the use of conformally deposited metal oxide blocking layers," *J. Am. Chem. Soc.*, vol. 125, no. 2, pp. 475–482, 2003, doi: 10.1021/ja027945w.

[108] Z. Liu, W. Hou, P. Pavaskar, M. Aykol, and S. B. Cronin, "Plasmon resonant enhancement of photocatalytic water splitting under visible illumination," *Nano Lett.*, vol. 11, no. 3, pp. 1111–1116, 2011, doi: 10.1021/nl104005n.

[109] X. Feng, K. Shankar, O. K. Varghese, M. Paulose, T. J. Latempa, and C. A. Grimes, "Vertically aligned single crystal TiO2nanowire arrays grown directly on transparent conducting oxide coated glass: Synthesis details and applications," *Nano Lett.*, vol. 8, no. 11, pp. 3781–3786, 2008, doi: 10.1021/nl802096a.

[110] W. Liu, B. Zou, J. Zhao, and H. Cui, "Optimizing sol-gel infiltration for the fabrication of high-quality titania inverse opal and its photocatalytic activity," *Thin Solid Films*, vol. 518, no. 17, pp. 4923–4927, 2010, doi: 10.1016/j.tsf.2010.02.043.

[111] G. K. Mor, K. Shankar, M. Paulose, O. K. Varghese, and C. A. Grimes, "Use of highly-ordered TiO 2 nanotube arrays in dye-sensitized solar cells," *Nano Lett.*, vol. 6, no. 2, pp. 215–218, 2006, doi: 10.1021/nl052099j.

[112] H. Kokubo, B. Ding, T. Naka, H. Tsuchihira, and S. Shiratori, "Multi-core cable-like TiO2 nanofibrous membranes for dye-sensitized solar cells," *Nanotechnology*, vol. 18, no. 16, pp. 165604–6, 2007, doi: 10.1088/0957-4484/18/16/165604.

[113] K. Fujihara, A. Kumar, R. Jose, S. Ramakrishna, and S. Uchida, "Spray deposition of electrospun TiO 2 nanorods for dye-sensitized solar cell," *Nanotechnology*, vol. 18, no. 36, p. 365709, 2007, doi: 10.1088/0957-4484/18/36/365709.

[114] M. Y. Song, D. K. Kim, K. J. Ihn, S. M. Jo, and D. Y. Kim, "Electrospun TiO2 electrodes for dye-sensitized solar cells," *Nanotechnology*, vol. 15, no. 12, pp. 1861–1865, 2004, doi: 10.1088/0957-4484/15/12/030.

[115] J. Wang, L. Zhao, V. S.-Y. Lin, and Z. Lin, "Formation of various TiO2 nanostructures from electrochemically anodized titanium," *J. Mater. Chem.*, vol. 19, no. 22, p. 3682, 2009, doi: 10.1039/b904247d.

[116] W. Guo *et al.*, "Rectangular Bunched Rutile TiO $_2$ Nanorod Arrays Grown on Carbon Fiber for Dye-Sensitized Solar Cells," *J. Am. Chem. Soc.*, vol. 134, no. 9, pp. 4437–4441, 2012, doi: 10.1021/ja2120585.

[117] Q. Huang, G. Zhou, L. Fang, L. Hu, and Z.-S. Wang, "TiO2 nanorod arrays grown from a mixed acid medium for efficient dye-sensitized solar cells," *Energy Environ.*

Sci., vol. 4, no. 6, p. 2145, 2011, doi: 10.1039/c1ee01166a.

[118] T. Morimoto *et al.*, "TiO 2 -Anatase Nanowire Dispersed Composite Electrode for Dye-Sensitized Solar Cells Parametric Optimization of Experimental Conditions for Dye-Sensitized Solar Cells based on Far-red Sensitive Squaraine Dye TiO 2 -Anatase Nanowire Dispersed Composite Ele," *J. Phys. Conf. Ser. J. Phys. Conf. Ser*, vol. 61, Accessed: Feb. 13, 2018. [Online]. Available: http://iopscience.iop.org/article/10.1088/1742-6596/61/1/220/pdf.

[119] C.-H. Ku and J.-J. Wu, "Chemical bath deposition of ZnO nanowire–nanoparticle composite electrodes for use in dye-sensitized solar cells," *Nanotechnology*, vol. 18, no. 50, p. 505706, 2007, doi: 10.1088/0957-4484/18/50/505706.

[120] Y. J. Kim *et al.*, "Formation of highly efficient dye-sensitized solar cells by hierarchical pore generation with nanoporous TiO2spheres," *Adv. Mater.*, vol. 21, no. 36, pp. 3668–3673, Sep. 2009, doi: 10.1002/adma.200900294.

[121] E. S. Kwak, W. Lee, N. C. Park, J. Kim, and H. Lee, "Compact inverse-opal electrode using non-aggregated TiO2 nanoparticles for dye-sensitized solar cells," *Adv. Funct. Mater.*, vol. 19, no. 7, pp. 1093–1099, 2009, doi: 10.1002/adfm.200801540.

[122] H. J. Koo, Y. J. Kim, Y. H. Lee, W. I. Lee, K. Kim, and N. G. Park, "Nano-embossed hollow spherical TiO2as bifunctional material for high-efficiency dye-sensitized solar cells," *Adv. Mater.*, vol. 20, no. 1, pp. 195–199, Jan. 2008, doi: 10.1002/adma.200700840.

[123] F. Sauvage *et al.*, "Hierarchical TiO2 photoanode for dye-sensitized solar cells," *Nano Lett.*, vol. 10, no. 7, pp. 2562–2567, 2010, doi: 10.1021/nl101198b.

[124] P. At, U. The, T. Ls, K. We, and F. Ls, "Preparation of Photonic Crystals Made of Air Spheres in Titania," vol. 281, no. August, pp. 802–805, 1998.

[125] Y. Cao *et al.*, "Fabrication of anatase titania inverse opal films using polystyrene templates," *Superlattices Microstruct.*, vol. 40, no. 3, pp. 155–160, 2006, doi: 10.1016/j.spmi.2006.07.005.

[126] G. I. N. Waterhouse and M. R. Waterland, "Opal and inverse opal photonic crystals: Fabrication and characterization," *Polyhedron*, vol. 26, no. 2, pp. 356–368, 2007, doi: 10.1016/j.poly.2006.06.024.

[127] Y. G. Seo, K. Woo, J. Kim, H. Lee, and W. Lee, "Rapid fabrication of an inverse opal TiO2 photoelectrode for DSSC using a binary mixture of TiO2 nanoparticles and polymer microspheres," *Adv. Funct. Mater.*, vol. 21, no. 16, pp. 3094–3103, 2011, doi: 10.1002/adfm.201002489.

[128] T. K. Rahul and N. Sandhyarani, "Nitrogen-fluorine co-doped titania inverse opals for

enhanced solar light driven photocatalysis," *Nanoscale*, vol. 7, no. 43, pp. 18259–18270, 2015, doi: 10.1039/C5NR04663G.

[129] T. K. Rahul and N. Sandhyarani, "In Situ Gold-Loaded Fluorinated Titania Inverse Opal Photocatalysts for Enhanced Solar-Light-Driven Hydrogen Production," *ChemNanoMat*, vol. 3, no. 7, pp. 503–510, 2017, doi: 10.1002/cnma.201700062.

[130] B. Liu and E. S. Aydil, "Growth of oriented single-crystalline rutile TiO 2 nanorods on transparent conducting substrates for dye-sensitized solar cells," *J. Am. Chem. Soc.*, vol. 131, no. 11, pp. 3985–3990, 2009, doi: 10.1021/ja8078972.

[131] J. Zhao, X. Wang, R. Chen, and L. Li, "Fabrication of titanium oxide nanotube arrays by anodic oxidation," *Solid State Commun.*, vol. 134, no. 10, pp. 705–710, 2005, doi: 10.1016/j.ssc.2005.02.028.

[132] W. Lee, M. Alhoshan, and W. H. Smyrl, "Titanium Dioxide Nanotube Arrays Fabricated by Anodizing Electrochemical Properties," *J. Electrochem. Soc.*, vol. 153, no. 11, pp. B499–B505, 2006, doi: 10.1149/1.2347098.

[133] E. Y. Kim, J. H. Park, and G. Y. Han, "Design of TiO2nanotube array-based water-splitting reactor for hydrogen generation," *J. Power Sources*, vol. 184, no. 1, pp. 284–287, 2008, doi: 10.1016/j.jpowsour.2008.05.059.

[134] J. H. Park, T.-W. Lee, and M. G. Kang, "Growth, detachment and transfer of highly-ordered TiO2 nanotube arrays: use in dye-sensitized solar cells," *Chem. Commun.*, no. 25, p. 2867, 2008, doi: 10.1039/b800660a.

[135] Y. S. Sohn, Y. R. Smith, M. Misra, and V. (Ravi) Subramanian, "Electrochemically assisted photocatalytic degradation of methyl orange using anodized titanium dioxide nanotubes," *Appl. Catal. B Environ.*, vol. 84, no. 3–4, pp. 372–378, 2008, doi: 10.1016/j.apcatb.2008.04.021.

[136] X. Wang *et al.*, "A metal-free polymeric photocatalyst for hydrogen production from water under visible light," *Nat. Mater.*, vol. 8, no. 1, pp. 76–80, Jan. 2009, doi: 10.1038/nmat2317.

[137] K. Shin, S. il Seok, S. H. Im, and J. H. Park, "CdS or CdSe decorated TiO2 nanotube arrays from spray pyrolysis deposition: use in photoelectrochemical cells," *Chem. Commun.*, vol. 46, no. 14, p. 2385, 2010, doi: 10.1039/b923022j.

[138] P. Zhong, X. Chen, H. Xi, Y. Lei, and X. Ma, "Freeze Drying as a Novel Approach to Improve Charge Transport in Titanium Dioxide Nanorod Arrays," *ChemElectroChem*, vol. 4, no. 11, pp. 2783–2787, 2017, doi: 10.1002/celc.201700572.

[139] Y. Yu and M. Lira-Cantu, "Solid state dye sensitized solar cells applying conducting organic polymers as hole conductors," *Phys. Procedia*, vol. 8, pp. 22–27, 2010, doi:

10.1016/j.phpro.2010.10.006.

[140] R. Grünwald and H. Tributsch, “Mechanisms of Instability in Ru-Based Dye Sensitization Solar Cells,” *J. Phys. Chem. B*, vol. 101, no. 96, pp. 2564–2575, 1997, doi: 10.1021/jp9624919.

[141] G. Oskam, B. V Bergeron, G. J. Meyer, and P. C. Searson, “Pseudohalogens for dye-sensitized TiO_{2} photoelectrochemical cells,” *J. Phys. Chem. B*, vol. 105, no. 29, pp. 6867–6873, 2001, doi: 10.1021/jp004411d.

[142] B. A. Gregg, F. Pichot, S. Ferrere, and C. L. Fields, “Interfacial Recombination Processes in Dye-Sensitized Solar Cells and Methods To Passivate the Interfaces,” *J. Phys. Chem. B*, vol. 105, no. 7, pp. 1422–1429, 2001, doi: 10.1021/jp003000u.

[143] Y. Hao *et al.*, “A small electron donor in cobalt complex electrolyte significantly improves efficiency in dye-sensitized solar cells,” *Nat. Commun.*, vol. 7, pp. 1–8, 2016, doi: 10.1038/ncomms13934.

[144] S. M. Feldt, E. A. Gibson, E. Gabrielsson, L. Sun, G. Boschloo, and A. Hagfeldt, “Design of organic dyes and cobalt polypyridine redox mediators for high-efficiency dye-sensitized solar cells,” *J. Am. Chem. Soc.*, vol. 132, no. 46, pp. 16714–16724, 2010, doi: 10.1021/ja1088869.

[145] J.-H. Yum *et al.*, “A cobalt complex redox shuttle for dye-sensitized solar cells with high open-circuit potentials,” *Nat. Commun.*, vol. 3, p. 631, 2012, doi: 10.1038/ncomms1655.

[146] A. M. C. Senevirathne, V. A. Seneviratne, O. A. Ileperuma, H. M. N. Bandara, and R. M. G. Rajapakse, “Novel Quasi-Solid-State Electrolyte Based on γ-Butyrolactone and Tetrapropylammonium Iodide for Dye-Sensitized Solar Cells Using Fumed Silica as the Gelling Agent,” *Procedia Eng.*, vol. 139, pp. 87–92, 2016, doi: 10.1016/j.proeng.2015.08.1117.

[147] S. V. N. and A. S. N. T. G. Deepak, G. S. Anjusree, K. R. Narendra Pai, Devika Subash, “Fabrication of a dye-sensitized solar cell module using spray pyrolysis deposition of a TiO2 colloid,” *RSC Adv.*, vol. 4, pp. 23299–23303, 2014.

[148] P. Wang, S. M. Zakeeruddin, J.-E. Moser, and M. Grätzel, “A New Ionic Liquid Electrolyte Enhances the Conversion Efficiency of Dye-Sensitized Solar Cells,” *J. Phys. Chem. B*, vol. 107, no. 48, pp. 13280–13285, 2003, doi: 10.1021/jp0355399.

[149] Y. Liu, H. Tsunoyama, T. Akita, and T. Tsukuda, “Preparation of ∼1 nm Gold Clusters Confined within Mesoporous Silica and Microwave-Assisted Catalytic Application for Alcohol Oxidation,” *J. Phys. Chem. C*, vol. 113, no. 31, pp. 13457–13461, 2009, doi: 10.1021/jp904700p.

[150] B. Guo, Z. Liu, L. Hong, and H. Jiang, “Sol gel derived photocatalytic porous TiO2 thin films,” *Surf. Coatings Technol.*, vol. 198, no. 1-3 SPEC. ISS., pp. 24–29, 2005, doi: 10.1016/j.surfcoat.2004.10.055.

[151] M. H. Mamat *et al.*, “Effect of annealing temperature on the surface morphology and electrical properties of aluminum doped zinc oxide thin films prepared by sol-gel spin-coating method,” *AIP Conf. Proc.*, vol. 1017, no. May, pp. 139–143, 2008, doi: 10.1063/1.2940614.

[152] G. Xi, Junting; Dahoudi, Naji AL; Zhang, Qifeng; Sun, Yueming; Cao, “Effect of Annealing Temperature on the Performances and Electrochemical Properties of TiO2 Dye-Sensitized Solar Cell,” *Sci. Adv. Mater.*, vol. 4, no. 7, pp. 727–733, 2012.

[153] B. M. John, S. W. Mugo, and J. M. Ngaruiya, “Effect of Annealing Rates on Surface Roughness of TiO 2 Thin films,” no. December, 2018, doi: 10.12691/jmpc-6-2-3.

[154] U. Bach *et al.*, “Solid-state dye-sensitized mesoporous TiO2 solar cells with high photon-to-electron conversion efficiencies,” *Nature*, vol. 395, no. 6702, pp. 583–585, 1998, doi: 10.1038/26936.

[155] M. Okuya, K. Nakade, and S. Kaneko, “Porous TiO 2 thin films synthesized by a spray pyrolysis deposition (SPD) technique and their application to dye-sensitized solar cells,” *Sol. Energy Mater. Sol. Cells*, vol. 70, pp. 425–435, 2002, doi: 10.1016/S0927-0248(01)00033-2.

[156] M. O. Abou-Helal and W. T. Seeber, “Preparation of TiO2 thin films by spray pyrolysis to be used as a photocatalyst,” *Appl. Surf. Sci.*, vol. 195, no. 1–4, pp. 53–62, 2002, doi: 10.1016/S0169-4332(02)00533-0.

[157] D. Li, H. Haneda, S. Hishita, N. Ohashi, and N. K. Labhsetwar, “Fluorine-doped TiO 2 powders prepared by spray pyrolysis and their improved photocatalytic activity for decomposition of gas-phase acetaldehyde,” *J. Fluor. Chem.*, vol. 126, no. 1, pp. 69–77, 2005, doi: 10.1016/j.jfluchem.2004.10.044.

[158] D. Li, H. Haneda, S. Hishita, and N. Ohashi, “Visible-light-driven N-F-codoped TiO2 photocatalysts. 1. Synthesis by spray pyrolysis and surface characterization,” *Chem. Mater.*, vol. 17, no. 10, pp. 2588–2595, 2005, doi: 10.1021/cm049100k.

[159] S.-Q. Fan, C.-J. Li, G.-J. Yang, L.-Z. Zhang, J.-C. Gao, and Y.-X. Xi, “Fabrication of Nano-TiO2 Coating for Dye-Sensitized Solar Cell by Vacuum Cold Spraying at Room Temperature,” *J. Therm. Spray Technol.*, vol. 16, no. 5–6, pp. 893–897, 2007, doi: 10.1007/s11666-007-9090-z.

[160] S. Q. Fan, G. J. Yang, C. J. Li, G. J. Liu, C. X. Li, and L. Z. Zhang, “Characterization of microstructure of nano-TiO2 coating deposited by vacuum cold spraying,” *Proc.*

Int. Therm. Spray Conf., vol. 15, no. December, pp. 513–517, 2006, doi: 10.1361/105996306X146901.

[161] C. D. Lokhande, B. O. Park, H. S. Park, K. D. Jung, and O. S. Joo, "Electrodeposition of TiO2and RuO2thin films for morphology-dependent applications," *Ultramicroscopy*, vol. 105, no. 1–4, pp. 267–274, 2005, doi: 10.1016/j.ultramic.2005.06.048.

[162] K. Wessels, M. Maekawa, J. Rathousky, and T. Oekermann, "One-step electrodeposition of TiO2/dye hybrid films," *Thin Solid Films*, vol. 515, no. 16 SPEC. ISS., pp. 6497–6500, 2007, doi: 10.1016/j.tsf.2006.11.081.

[163] B. Endrődi, E. Kecsenovity, K. Rajeshwar, and C. Janáky, "One-step Electrodeposition of Nanocrystalline TiO2 Films with Enhanced Photoelectrochemical Performance and Charge Storage," *ACS Appl. Energy Mater.*, p. acsaem.7b00289, 2018, doi: 10.1021/acsaem.7b00289.

[164] S. Z. Chu, S. Inoue, K. Wada, and S. Hishita, "Fabrication of TiO[sub 2]-Ru(O[sub 2])/Al[sub 2]O[sub 3] Composite Nanostructures on Glass by Al Anodization and Electrodeposition," *J. Electrochem. Soc.*, vol. 151, no. 1, p. C38, 2004, doi: 10.1149/1.1627346.

[165] T. V. Nguyen, H. C. Lee, M. Alam Khan, and O. B. Yang, "Electrodeposition of TiO2/SiO2nanocomposite for dye-sensitized solar cell," *Sol. Energy*, vol. 81, no. 4, pp. 529–534, 2007, doi: 10.1016/j.solener.2006.07.008.

[166] M. Wu *et al.*, "High photocatalytic activity enhancement of titania inverse opal films by slow photon effect induced strong light absorption," *J. Mater. Chem. A*, vol. 1, no. 48, p. 15491, 2013, doi: 10.1039/c3ta13574h.

[167] J. Xu, B. Yang, M. Wu, Z. Fu, Y. Lv, and Y. Zhao, "Novel N - F-Codoped TiO 2 Inverse Opal with a Hierarchical Meso/Macroporous Structure: Synthesis, Characterization, and Photocatalysis," pp. 15251–15259, 2010.

[168] E. S. Kwak, W. Lee, N. C. Park, J. Kim, and H. Lee, "Compact inverse-opal electrode using non-aggregated TiO 2 nanoparticles for dye-sensitized solar cells," *Adv. Funct. Mater.*, vol. 19, no. 7, pp. 1093–1099, 2009, doi: 10.1002/adfm.200801540.

[169] G. Lui, "Design of Novel Titanium Dioxide-Based Multifunctional Electrochemical Cells," University of Waterloo, 2018.

[170] G. Raza, "Titanium Dioxide Nanomaterials, Synthesis, Stability and Mobility in Natural and Synthetic Porous Media," The University of Birmingham, 2017.

[171] S. Bagheri, Z. A. Mohd Hir, A. Termeh Yousefi, and S. Bee Abdul Hamid, "Progress on mesoporous titanium dioxide: Synthesis, modification and applications,"

Microporous Mesoporous Mater., vol. 218, pp. 206–222, 2015, doi: 10.1016/j.micromeso.2015.05.028.

[172] S. Rouxel, D., Fleutot, S., Cherni, N., Darne, C., Gate, L., & Binet, "Synthesis of Nanoparticles of Titanium Dioxide TiO2 for Toxicological Studies: A Short Review," *Glob. J. Nanomedicine*, vol. 3, no. 1, p. 2, 2017.

[173] A. B. Djurišić, Y. H. Leung, and A. M. Ching Ng, "Strategies for improving the efficiency of semiconductor metal oxide photocatalysis," *Mater. Horizons*, vol. 1, no. 4, pp. 400–410, 2014, doi: 10.1039/c4mh00031e.

[174] S. Hoang, T. Q. Ngo, S. P. Berglund, R. R. Fullon, J. G. Ekerdt, and C. B. Mullins, "Improvement of solar energy conversion with Nb-incorporated TiO2 hierarchical microspheres," *ChemPhysChem*, vol. 14, no. 10, pp. 2270–2276, Jul. 2013, doi: 10.1002/cphc.201201092.

[175] E. Burstein, "Anomalous optical absorption limit in InSb [4]," *Phys. Rev.*, vol. 93, no. 3, pp. 632–633, 1954, doi: 10.1103/PhysRev.93.632.

[176] Y. Liu, Z. Wang, W. Wang, and W. Huang, "Engineering highly active TiO2 photocatalysts via the surface-phase junction strategy employing a titanate nanotube precursor," *J. Catal.*, vol. 310, pp. 16–23, 2014, doi: 10.1016/j.jcat.2013.03.024.

[177] S. Harrison and M. Hayne, "Photoelectrolysis Using Type-II Semiconductor Heterojunctions," *Sci. Rep.*, vol. 7, no. 1, pp. 1–11, 2017, doi: 10.1038/s41598-017-11971-x.

[178] *An Essential Guide to Electronic Material Surfaces and Interfaces*, vol. Semiconduc. .

[179] T. H. Lee and K. M. Ervin, "Reactions of copper group cluster anions with oxygen and carbon monoxide," *J. Phys. Chem.*, vol. 98, no. 40, pp. 10023–10031, 1994, doi: 10.1021/j100091a014.

[180] D. M. Cox, R. Brickman, K. Creegan, and A. Kaldor, "Gold clusters: reactions and deuterium uptake," *Zeitschrift für Phys. D Atoms, Mol. Clust.*, vol. 19, no. 4, pp. 353–355, 1991, doi: 10.1007/BF01448327.

[181] K. Awazu *et al.*, "A plasmonic photocatalyst consisting of silver nanoparticles embedded in titanium dioxide," *J. Am. Chem. Soc.*, vol. 130, no. 5, pp. 1676–1680, 2008, doi: 10.1021/ja076503n.

[182] J. Zhang *et al.*, "Engineering the Absorption and Field Enhancement Properties of Au-TiO2 Nanohybrids via Whispering Gallery Mode Resonances for Photocatalytic Water Splitting," *ACS Nano*, vol. 10, no. 4, pp. 4496–4503, 2016, doi: 10.1021/acsnano.6b00263.

[183] P. V. Kamat, "Manipulation of charge transfer across semiconductor interface. A

criterion that cannot be ignored in photocatalyst design," *J. Phys. Chem. Lett.*, vol. 3, no. 5, pp. 663–672, 2012, doi: 10.1021/jz201629p.

[184] P. V. Kamat, "Photophysical, photochemical and photocatalytic aspects of metal nanoparticles," *J. Phys. Chem. B*, vol. 106, no. 32, pp. 7729–7744, 2002, doi: 10.1021/jp0209289.

[185] A. Kudo and Y. Miseki, "Heterogeneous photocatalyst materials for water splitting," *Chem. Soc. Rev.*, vol. 38, no. 1, pp. 253–278, 2009, doi: 10.1039/b800489g.

[186] A. Takai and P. V. Kamat, "Capture, store, and discharge. Shuttling photogenerated electrons across TiO2-silver interface," *ACS Nano*, vol. 5, no. 9, pp. 7369–7376, 2011, doi: 10.1021/nn202294b.

[187] V. Subramanian, E. E. Wolf, and P. V. Kamat, "Green emission to probe photoinduced charging events in ZnO-Au nanoparticles. Charge distribution and Fermi-level equilibration," *J. Phys. Chem. B*, vol. 107, no. 30, pp. 7479–7485, 2003, doi: 10.1021/jp0275037.

[188] V. Subramanian, E. E. Wolf, and P. V. Kamat, "Catalysis with TiO2/Gold Nanocomposites. Effect of Metal Particle Size on the Fermi Level Equilibration," *J. Am. Chem. Soc.*, vol. 126, no. 15, pp. 4943–4950, 2004, doi: 10.1021/ja0315199.

[189] S. Chen *et al.*, "Gold nanoelectrodes of varied size: Transition to molecule-like charging," *Science (80-.).*, vol. 280, no. 5372, pp. 2098–2101, 1998, doi: 10.1126/science.280.5372.2098.

[190] J. J. Pietron, J. F. Hicks, and R. W. Murray, "Using electrons stored on quantized capacitors in electron transfer reactions," *J. Am. Chem. Soc.*, vol. 121, no. 23, pp. 5565–5570, 1999, doi: 10.1021/ja990320m.

[191] A. C. Templeton, W. P. Wuelfing, and R. W. Murray, "Monolayer-protected cluster molecules," *Acc. Chem. Res.*, vol. 33, no. 1, pp. 27–36, 2000, doi: 10.1021/ar9602664.

[192] P. K. Sudeep, K. Takechi, and P. V. Kamat, "Harvesting photons in the infrared. Electron injection from excited tricarbocyanine dye (IR-125) into TiO2 and Ag@TiO2 core-shell nanoparticles," *J. Phys. Chem. C*, vol. 111, no. 1, pp. 488–494, 2007, doi: 10.1021/jp0665022.

[193] S. Mubeen, G. Hernandez-Sosa, D. Moses, J. Lee, and M. Moskovits, "Plasmonic photosensitization of a wide band gap semiconductor: Converting plasmons to charge carriers," *Nano Lett.*, vol. 11, no. 12, pp. 5548–5552, 2011, doi: 10.1021/nl203457v.

[194] Y. Tian and T. Tatsuma, "Mechanisms and applications of plasmon-induced charge separation at TiO2 films loaded with gold nanoparticles," *J. Am. Chem. Soc.*, vol. 127, no. 20, pp. 7632–7637, 2005, doi: 10.1021/ja042192u.

[195] Z. Zhang, L. Zhang, M. N. Hedhili, H. Zhang, and P. Wang, “Plasmonic gold nanocrystals coupled with photonic crystal seamlessly on TiO 2 nanotube photoelectrodes for efficient visible light photoelectrochemical water splitting,” *Nano Lett.*, vol. 13, no. 1, pp. 14–20, 2013, doi: 10.1021/nl3029202.

[196] X. Shi, K. Ueno, N. Takabayashi, and H. Misawa, “Plasmon-enhanced photocurrent generation and water oxidation with a gold nanoisland-loaded titanium dioxide photoelectrode,” *J. Phys. Chem. C*, vol. 117, no. 6, pp. 2494–2499, 2013, doi: 10.1021/jp3064036.

[197] R. Siavash Moakhar *et al.*, “AuPd bimetallic nanoparticle decorated TiO2 rutile nanorod arrays for enhanced photoelectrochemical water splitting,” *J. Appl. Electrochem.*, vol. 48, no. 9, pp. 995–1007, 2018, doi: 10.1007/s10800-018-1231-1.

[198] A. Dawson and P. V. Kamat, “ Semiconductor−Metal Nanocomposites. Photoinduced Fusion and Photocatalysis of Gold-Capped TiO 2 (TiO 2 /Gold) Nanoparticles ,” *J. Phys. Chem. B*, vol. 105, no. 5, pp. 960–966, 2002, doi: 10.1021/jp0033263.

[199] M. Haro, R. Abargues, I. Herraiz-Cardona, J. Martínez-Pastor, and S. Giménez, “Plasmonic versus catalytic effect of gold nanoparticles on mesoporous TiO2electrodes for water splitting,” *Electrochim. Acta*, vol. 144, pp. 64–70, 2014, doi: 10.1016/j.electacta.2014.07.146.

[200] J. W. Yoon, T. Sasaki, and N. Koshizaki, “Dispersion of nanosized noble metals in TiO2 matrix and their photoelectrode properties,” *Thin Solid Films*, vol. 483, no. 1–2, pp. 276–282, 2005, doi: 10.1016/j.tsf.2005.01.006.

[201] A. Primo, A. Corma, and H. García, “Titania supported gold nanoparticles as photocatalyst,” *Phys. Chem. Chem. Phys.*, vol. 13, no. 3, pp. 886–910, 2011, doi: 10.1039/c0cp00917b.

[202] Y. C. Yen, J. A. Chen, S. Ou, Y. S. Chen, and K. J. Lin, “Plasmon-Enhanced Photocurrent using Gold Nanoparticles on a Three-Dimensional TiO2 Nanowire-Web Electrode,” *Sci. Rep.*, vol. 7, no. February, pp. 1–8, 2017, doi: 10.1038/srep42524.

[203] C. Seghetti, “Gold/TiO2 nanocomposites as photoactive materials for environmental remediation,” 2016.

[204] G. Kawamura, T. Arai, H. Muto, and A. Matsuda, “Charge behavior in a plasmonic photocatalyst composed of Au and TiO 2,” *Catal. Sci. Technol.*, vol. 8, no. 7, pp. 1813–1818, 2018, doi: 10.1039/c8cy00120k.

[205] A. Tanaka, K. Hashimoto, and H. Kominami, “A very simple method for the preparation of Au/TiO2 plasmonic photocatalysts working under irradiation of visible light in the range of 600-700 nm,” *Chem. Commun.*, vol. 53, no. 35, pp. 4759–4762,

2017, doi: 10.1039/c7cc01444a.

[206] G. Schmid and D. Fenske, “Metal clusters and nanoparticles,” *Philos. Trans. R. Soc. A Math. Phys. Eng. Sci.*, vol. 368, no. 1915, pp. 1207–1210, 2010, doi: 10.1098/rsta.2009.0281.

[207] R. Meyer, C. Lemire, S. K. Shaikhutdinov, and H. J. Freund, “Surface chemistry of catalysis by gold,” *Gold Bull.*, vol. 37, no. 1–2, pp. 72–124, 2004, doi: 10.1007/BF03215519.

[208] M. Valden, X. Lai, and D. W. Goodman, “Onset of catalytic activity of gold clusters on titania with the appearance of nonmetallic properties,” *Science (80-.).*, vol. 281, no. 5383, pp. 1647–1650, 1998, doi: 10.1126/science.281.5383.1647.

[209] K. Okazaki, S. Ichikawa, Y. Maeda, M. Haruta, and M. Kohyama, “Electronic structures of Au supported on TiO2,” *Appl. Catal. A Gen.*, vol. 291, no. 1–2, pp. 45–54, 2005, doi: 10.1016/j.apcata.2005.02.047.

[210] P. Maity, S. Xie, M. Yamauchi, and T. Tsukuda, “Stabilized gold clusters: From isolation toward controlled synthesis,” *Nanoscale*, vol. 4, no. 14, pp. 4027–4037, 2012, doi: 10.1039/c2nr30900a.

[211] D. P. Anderson *et al.*, “Chemically-synthesised, atomically-precise gold clusters deposited and activated on titania,” *Phys. Chem. Chem. Phys*, no. 15, pp. 3917–3929, 2013, doi: 10.1039/c3cp44005b.

[212] Jason Frankie Alvino, “The Characterisation, Photocatalytic Performance, and Theoretical Investigation of Small Gold Clusters Supported on Titanium Dioxide Nanoparticles,” The university of adelaid, 2015.

[213] D. P. Anderson *et al.*, “Chemically synthesised atomically precise gold clusters deposited and activated on titania. Part II,” 2013.

[214] A. Zaban, M. Greenshtein, and J. Bisquert, “Determination of the electron lifetime in nanocrystalline dye solar cells by open-circuit voltage decay measurements,” *ChemPhysChem*, vol. 4, no. 8, pp. 859–864, 2003, doi: 10.1002/cphc.200200615.

[215] G. Hodes, “Photoelectrochemical cell measurements: Getting the basics right,” *J. Phys. Chem. Lett.*, vol. 3, no. 9, pp. 1208–1213, 2012, doi: 10.1021/jz300220b.

[216] D. C. J. De Joseph I. Goldstein, Dale E. Newbury, Joseph R. Michael, Nicholas W.M. Ritchie, John Henry J. Scott, *Scanning Electron Microscopy and X-Ray Microanalysis*. Springers, 2017.

[217] O. H. Seeck and B. Murphy, Eds., *X-Ray Diffraction*. Jenny Stanford Publishing, 2015.

[218] J. Manassen, “Photoelectrochemical Energy Conversion and Storage,” *J. Electrochem. Soc.*, vol. 124, no. 4, p. 532, 1977, doi: 10.1149/1.2133344.

[219] G. Kim, M. Oh, and Y. Park, “Solar-rechargeable battery based on photoelectrochemical water oxidation: Solar water battery,” *Sci. Rep.*, vol. 6, no. September, pp. 1–9, 2016, doi: 10.1038/srep33400.

[220] M. Nagao, K. Kobayashi, Y. Yamamoto, T. Yamaguchi, A. Oogushi, and T. Hibino, “Rechargeable Metal-Air Proton-Exchange Membrane Batteries for Renewable Energy Storage,” *ChemElectroChem*, vol. 3, no. 2, pp. 247–255, 2016, doi: 10.1002/celc.201500473.

[221] Marcel Pourbaix, *Atlas of Electrochemical Equilibria in Aqueous Solutions*. Houston, Texas; Cebelcor, Brussels: NACE International, 1966.

[222] J. A. Bard and R. L. Faulkner, *Electrochemical Methods: Fundamentals and Applications*, Second edition., no. 4. 2000.

[223] K. Gelderman, L. Lee, and S. W. Donne, “Flat-band potential of a semiconductor: Using the Mott-Schottky equation,” *J. Chem. Educ.*, vol. 84, no. 4, pp. 685–688, 2007, doi: 10.1021/ed084p685.

[224] Y. X. Zu, X. Wu, and Y. Q. Lv, “Study on the DS/CDMA-CSMA multi-user communication systems,” *Commun. Comput. Inf. Sci.*, vol. 26 CCIS, pp. 98–104, 2009, doi: 10.1007/978-3-642-00205-2_12.

[225] Z. G. Ye, H. M. Meng, and D. B. Sun, “New degradation mechanism of Ti/IrO2 + MnO2 anode for oxygen evolution in 0.5 M H2SO4 solution,” *Electrochim. Acta*, vol. 53, no. 18, pp. 5639–5643, 2008, doi: 10.1016/j.electacta.2008.03.025.

[226] R. P. Brooker, C. J. Bell, L. J. Bonville, H. R. Kunz, and J. M. Fenton, “Determining Vanadium Concentrations Using the UV-Vis Response Method,” *J. Electrochem. Soc.*, vol. 162, no. 4, pp. A608–A613, 2015, doi: 10.1149/2.0371504jes.

[227] J. Barber, J. Mills, and A. Love, “Electrical diffuse layers and their influence on photosynthetic processes,” *FEBS Letters*, vol. 74, no. 2. pp. 174–181, 1977, doi: 10.1016/0014-5793(77)80841-7.

[228] N. Ghrairi and M. Bouaicha, “Structural, morphological, and optical properties of TiO2 thin films synthesized by the electro phoretic deposition technique,” *Nanoscale Res. Lett.*, vol. 7, no. 1, pp. 1–17, 2012, doi: 10.1186/1556-276X-7-1.

[229] D. C. Grahame, “The electrical double layer and the theory of electrocapillarity,” *Chem. Rev.*, vol. 41, no. 3, pp. 441–501, 1947, doi: 10.1021/cr60130a002.

[230] W. J. Albery, “Modulated Light Studies of the Electrochemistry of Semiconductors,” *J. Electrochem. Soc.*, vol. 134, no. 10, p. 2486, 1987, doi: 10.1149/1.2100227.

[231] N. J. Cherepy, G. P. Smestad, M. Grätzel, and J. Z. Zhang, “Ultrafast electron injection: Implications for a photoelectrochemical cell utilizing an anthocyanin dye-

sensitized TiO2 nanocrystalline electrode," *J. Phys. Chem. B*, vol. 101, no. 45, pp. 9342–9351, 1997, doi: 10.1021/jp972197w.

[232] K. P. Regan, C. Koenigsmann, S. W. Sheehan, S. J. Konezny, and C. A. Schmuttenmaer, "Size-dependent ultrafast charge carrier dynamics of WO3 for photoelectrochemical cells," *J. Phys. Chem. C*, vol. 120, no. 27, pp. 14926–14933, 2016, doi: 10.1021/acs.jpcc.6b04390.

[233] Q. Zhang *et al.*, "Highly efficient CdS/CdSe-sensitized solar cells controlled by the structural properties of compact porous TiO2 photoelectrodes," *Phys. Chem. Chem. Phys.*, vol. 13, no. 10, p. 4659, 2011, doi: 10.1039/c0cp02099k.

[234] J. Halme, J. Saarinen, and P. Lund, "Spray deposition and compression of TiO2 nanoparticle films for dye-sensitized solar cells on plastic substrates," *Sol. Energy Mater. Sol. Cells*, vol. 90, no. 7–8, pp. 887–899, 2006, doi: 10.1016/j.solmat.2005.05.013.

[235] H. Choi *et al.*, "The effect of TiCl 4 -treated TiO 2 compact layer on the performance of dye-sensitized solar cell," *Curr. Appl. Phys.*, vol. 12, no. 3, pp. 737–741, 2012, doi: 10.1016/j.cap.2011.10.011.

[236] S. J. Kim, S. D. Park, Y. H. Jeong, and S. Park, "Homogeneous precipitation of TiO2 ultrafine powders from aqueous TiOCl2 solution," *J. Am. Ceram. Soc.*, vol. 82, no. 4, pp. 927–932, 1999, doi: 10.1111/j.1151-2916.1999.tb01855.x.

[237] G. J. A. A. Soler-Illia, P. C. Angelomé, M. C. Fuertes, D. Grosso, and C. Boissiere, "Critical aspects in the production of periodically ordered mesoporous titania thin films," *Nanoscale*, vol. 4, no. 8, pp. 2549–2566, 2012, doi: 10.1039/c2nr11817c.

[238] C. J. Brinker, Y. Lu, A. Sellinger, and H. Fan, "ChemInform Abstract: Evaporation-Induced Self-Assembly: Nanostructures Made Easy," *ChemInform*, vol. 30, no. 28, p. no-no, 2010, doi: 10.1002/chin.199928288.

[239] S. Y. Choi, M. Mamak, N. Coombs, N. Chopra, and G. A. Ozin, "Thermally stable two-dimensional hexagonal mesoporous nanocrystalline anatase, meso-nc-TiO2: Bulk and crack-free thin film morphologies," *Adv. Funct. Mater.*, vol. 14, no. 4, pp. 335–344, 2004, doi: 10.1002/adfm.200305039.

[240] M. Yu *et al.*, "Solar-powered electrochemical energy storage: an alternative to solar fuels," *J. Mater. Chem. A*, vol. 4, no. 8, pp. 2766–2782, 2016, doi: 10.1039/C5TA06950E.

[241] M. Ge *et al.*, "A review of one-dimensional TiO_2 nanostructured materials for environmental and energy applications," *J. Mater. Chem. A*, vol. 4, no. 18, pp. 6772–6801, 2016, doi: 10.1039/C5TA09323F.

[242] C. Euvananont, C. Junin, K. Inpor, P. Limthongkul, and C. Thanachayanont, “TiO2 optical coating layers for self-cleaning applications,” *Ceram. Int.*, 2008, doi: 10.1016/j.ceramint.2007.09.043.

[243] A. Moretti *et al.*, “Investigation of different binding agents for nanocrystalline anatase TiO 2 anodes and its application in a novel, green lithium-ion battery,” *J. Power Sources*, vol. 221, pp. 419–426, 2013, doi: 10.1016/j.jpowsour.2012.07.142.

[244] J. Chong *et al.*, “A comparative study of polyacrylic acid and poly(vinylidene difluoride) binders for spherical natural graphite/LiFePO4 electrodes and cells,” *J. Power Sources*, vol. 196, no. 18, pp. 7707–7714, 2011, doi: 10.1016/j.jpowsour.2011.04.043.

[245] D. Vak *et al.*, “Fabrication of organic bulk heterojunction solar cells by a spray deposition method for low-cost power generation,” *Appl. Phys. Lett.*, vol. 91, no. 8, pp. 1–4, 2007, doi: 10.1063/1.2772766.

[246] I. M. Smallwood, *Handbook of Organic Solvent Properties*. 2012.

[247] Jacob N. Israelachvili, *Intermolecular and Surface Forces*, Thied edit. San Diego, 2011.

[248] D. Zheng, J. Huang, Y. Zheng, and J. Yu, “High performance airbrush spray coated organic solar cells via tuning the surface tension and saturated vapor pressure of different ternary solvent systems,” *Org. Electron.*, vol. 25, pp. 275–282, 2015, doi: 10.1016/j.orgel.2015.07.001.

[249] W. P. Lee and A. F. Routh, “Why do drying films crack?,” *Langmuir*, vol. 20, no. 23, pp. 9885–9888, 2004, doi: 10.1021/la049020v.

[250] J. A. Byrne, B. R. Eggins, N. M. D. Brown, B. McKinney, and M. Rouse, “Immobilisation of TiO2 powder for the treatment of polluted water,” *Appl. Catal. B Environ.*, vol. 17, no. 1–2, pp. 25–36, 1998, doi: 10.1016/S0926-3373(97)00101-X.

[251] N. I. of S. and Technology and technology, “WebBook de Chimie NIST, SRD 69.” .

[252] G. Syrrokostas, M. Giannouli, and P. Yianoulis, “Effects of paste storage on the properties of nanostructured thin films for the development of dye-sensitized solar cells,” *Renew. Energy*, vol. 34, no. 7, pp. 1759–1764, 2009, doi: 10.1016/j.renene.2008.12.029.

[253] A. Abdellah *et al.*, “Successive spray deposition of P3HT/PCBM organic photoactive layers: Material composition and device characteristics,” *Adv. Funct. Mater.*, vol. 22, no. 19, pp. 4078–4086, 2012, doi: 10.1002/adfm.201200548.

[254] H. Y. Park, K. Kim, D. Y. Kim, S. K. Choi, S. M. Jo, and S. Y. Jang, “Facile external treatment for efficient nanoscale morphology control of polymer solar cells using a

gas-assisted spray method," *J. Mater. Chem.*, vol. 21, no. 12, pp. 4457–4464, 2011, doi: 10.1039/c0jm03899g.

[255] A. P. Xagas, E. Androulaki, A. Hiskia, and P. Falaras, "Preparation, fractal surface morphology and photocatalytic properties of TiO2 films," *Thin Solid Films*, vol. 357, no. 2, pp. 173–178, 1999, doi: 10.1016/S0040-6090(99)00561-1.

[256] G. Strotos, M. Gavaises, A. Theodorakakos, and G. Bergeles, "Numerical investigation on the evaporation of droplets depositing on heated surfaces at low Weber numbers," *Int. J. Heat Mass Transf.*, vol. 51, no. 7–8, pp. 1516–1529, 2008, doi: 10.1016/j.ijheatmasstransfer.2007.07.045.

[257] M. E. R. Moffat, J.R., Sefiane, K., Shanahan, "Nanofluid Droplet Evaporation Kinetics and Wetting Dynamics on Flat Substrates," *J. Nano Res. 7*, pp. 75–80, 2009.

[258] P. Kebarle, "A brief overview of the present status of the mechanisms involved in electrospray mass spectrometry," *J. Mass Spectrom.*, vol. 35, no. 7, pp. 804–817, 2000, doi: 10.1002/1096-9888(200007)35:7<804::AID-JMS22>3.0.CO;2-Q.

[259] S. Ben Ameur *et al.*, "Physical investigations on undoped and Fluorine doped SnO2 nanofilms on flexible substrate along with wettability and photocatalytic activity tests," *Mater. Sci. Semicond. Process.*, vol. 61, no. December 2016, pp. 17–26, 2017, doi: 10.1016/j.mssp.2016.12.019.

[260] N. L. Tarwal and P. S. Patil, "Superhydrophobic and transparent ZnO thin films synthesized by spray pyrolysis technique," *Appl. Surf. Sci.*, vol. 256, no. 24, pp. 7451–7456, 2010, doi: 10.1016/j.apsusc.2010.05.089.

[261] B. Bhushan and Y. C. Jung, "Micro- and nanoscale characterization of hydrophobic and hydrophilic leaf surfaces," *Nanotechnology*, vol. 17, no. 11, pp. 2758–2772, 2006, doi: 10.1088/0957-4484/17/11/008.

[262] C. Xu, L. Fang, Q. Huang, B. Yin, H. Ruan, and D. Li, "Preparation and surface wettability of TiO2 nanorod films modified with triethoxyoctylsilane," *Thin Solid Films*, vol. 531, pp. 255–260, 2013, doi: 10.1016/j.tsf.2012.12.039.

[263] Y. C. Kim, "Evaporation of nanofluid droplet on heated surface," *Adv. Mech. Eng.*, vol. 7, no. 4, pp. 1–8, 2015, doi: 10.1177/1687814015578358.

[264] L. Lopez, W. A. Daoud, D. Dutta, B. C. Panther, and T. W. Turney, "Effect of substrate on surface morphology and photocatalysis of large-scale TiO 2 films," *Appl. Surf. Sci.*, vol. 265, pp. 162–168, 2013, doi: 10.1016/j.apsusc.2012.10.156.

[265] C. Barry Carter and M. Grant Norton, *Ceramic materials: Science and engineering*. 2007.

[266] C. M. Firdaus, M. S. B. Shah Rizam, M. Rusop, and S. Rahmatul Hidayah,

"Characterization of ZnO and ZnO: TiO2 thin films prepared by sol-gel spray-spin coating technique," *Procedia Eng.*, vol. 41, no. Iris, pp. 1367–1373, 2012, doi: 10.1016/j.proeng.2012.07.323.

[267] S. Mahshid, M. Askari, and M. S. Ghamsari, "Synthesis of TiO2 nanoparticles by hydrolysis and peptization of titanium isopropoxide solution," *J. Mater. Process. Technol.*, vol. 189, no. 1–3, pp. 296–300, 2007, doi: 10.1016/j.jmatprotec.2007.01.040.

[268] M. A. Khan, M. Shaheer Akhtar, and O. B. Yang, "Synthesis, characterization and application of sol-gel derived mesoporous TiO2 nanoparticles for dye-sensitized solar cells," *Sol. Energy*, vol. 84, no. 12, pp. 2195–2201, 2010, doi: 10.1016/j.solener.2010.08.008.

[269] P. Pookmanee and S. Phanichphant, "Titanium dioxide powder prepared by a sol-gel method," *J. Ceram. Process. Res.*, vol. 10, no. 2, pp. 167–170, 2009.

[270] V. Gourinchas Courtecuisse, J. F. Bocquet, K. Chhor, and C. Pommier, "Modeling of a continuous reactor for TiO2 powder synthesis in a supercritical fluid - Experimental validation," *J. Supercrit. Fluids*, vol. 9, no. 4, pp. 222–226, 1996, doi: 10.1016/s0896-8446(96)90052-2.

[271] P. Malliga, J. Pandiarajan, N. Prithivikumaran, and K. Neyvasagam, "Influence of Film Thickness on Structural and Optical Properties of Sol – Gel Spin Coated TiO2 Thin Film," *IOSR J. Appl. Phys.*, vol. 6, no. 1, pp. 22–28, 2014, doi: 10.9790/4861-06112228.

[272] D. R. Hummer, P. J. Heaney, and J. E. Post, "Thermal expansion of anatase and rutile between 300 and 575 K using synchrotron powder X-ray diffraction," *Powder Diffr.*, vol. 22, no. 4, pp. 352–357, 2007, doi: 10.1154/1.2790965.

[273] B. Henkel, A. Vahl, O. C. Aktas, T. Strunskus, and F. Faupel, "Self-organized nanocrack networks: A pathway to enlarge catalytic surface area in sputtered ceramic thin films, showcased for photocatalytic TiO2," *Nanotechnology*, vol. 29, no. 3, 2018, doi: 10.1088/1361-6528/aa9d35.

[274] L. Vesce, R. Riccitelli, G. Soscia, T. M. Brown, A. Di Carlo, and A. Reale, "Optimization of nanostructured titania photoanodes for dye-sensitized solar cells: Study and experimentation of TiCl4treatment," *J. Non. Cryst. Solids*, vol. 356, no. 37–40, pp. 1958–1961, 2010, doi: 10.1016/j.jnoncrysol.2010.05.070.

[275] S. Y. Choi *et al.*, "3D hexagonal (R-3m) mesostructured nanocrystalline titania thin films: Synthesis and characterization," *Adv. Funct. Mater.*, vol. 16, no. 13, pp. 1731–1738, 2006, doi: 10.1002/adfm.200500507.

[276] B. W. Eggiman, M. P. Tate, and H. W. Hillhouse, "Rhombohedral structure of highly

ordered and oriented self-assembled nanoporous silica thin films," *Chem. Mater.*, vol. 18, no. 3, pp. 723–730, 2006, doi: 10.1021/cm0520766.

[277] P. Y. Steinberg, M. M. Zalduendo, G. Giménez, G. J. A. A. Soler-Illia, and P. C. Angelomé, "TiO2 mesoporous thin film architecture as a tool to control Au nanoparticles growth and sensing capabilities," *Phys. Chem. Chem. Phys.*, vol. 21, no. 20, pp. 10347–10356, 2019, doi: 10.1039/c9cp01896d.

[278] M. C. Fuertes, M. Marchena, M. C. Marchi, A. Wolosiuk, and G. J. A. A. Soler-Illia, "Controlled deposition of silver nanoparticles in mesoporous single- Or multilayer thin films: From tuned pore filling to selective spatial location of nanometric objects," *Small*, vol. 5, no. 2, pp. 272–280, 2009, doi: 10.1002/smll.200800894.

[279] A. Gibaud, S. Dourdain, and G. Vignaud, "Analysis of mesoporous thin films by X-ray reflectivity, optical reflectivity and grazing incidence small angle X-ray scattering," *Appl. Surf. Sci.*, vol. 253, no. 1 SPEC. ISS., pp. 3–11, 2006, doi: 10.1016/j.apsusc.2006.05.121.

[280] A. Van der Lee, "Grazing incidence specular reflectivity: Theory, experiment, and applications," *Solid State Sci.*, vol. 2, no. 2, pp. 257–278, 2000, doi: 10.1016/S1293-2558(00)00119-9.

[281] B. Liu and E. S. Aydil, "Growth of oriented single-crystalline rutile TiO 2 nanorods on transparent conducting substrates for dye-sensitized solar cells," *J. Am. Chem. Soc.*, vol. 131, no. 11, pp. 3985–3990, 2009, doi: 10.1021/ja8078972.

[282] A. A. Shinkle, A. E. S. Sleightholme, L. T. Thompson, and C. W. Monroe, "Electrode kinetics in non-aqueous vanadium acetylacetonate redox flow batteries," *J. Appl. Electrochem.*, vol. 41, no. 10, pp. 1191–1199, 2011, doi: 10.1007/s10800-011-0314-z.

[283] G. Chen and H. Liu, "Understanding the Reduction Kinetics of Aqueous Vanadium(V) and Transformation Products Using Rotating Ring-Disk Electrodes," *Environ. Sci. Technol.*, vol. 51, no. 20, pp. 11643–11651, 2017, doi: 10.1021/acs.est.7b02021.

[284] E. C. Tyo and S. Vajda, "Catalysis by clusters with precise numbers of atoms," *Nat. Nanotechnol.*, vol. 10, no. 7, pp. 577–588, 2015, doi: 10.1038/NNANO.2015.140.

[285] R. Jin, C. Zeng, M. Zhou, and Y. Chen, "Atomically Precise Colloidal Metal Nanoclusters and Nanoparticles: Fundamentals and Opportunities," *Chem. Rev.*, vol. 116, no. 18, pp. 10346–10413, 2016, doi: 10.1021/acs.chemrev.5b00703.

[286] J. Turkevich, P. C. Stevenson, and J. Hillier, "A study of the nucleation and growth processes in the synthesis of colloidal gold," *Discuss. Faraday Soc.*, vol. 11, no. c, pp. 55–75, 1951, doi: 10.1039/DF9511100055.

[287] V. Poonthiyil, V. B. Golovko, and A. J. Fairbanks, "Control of gold nanostructure

morphology by variation of temperature and reagent ratios in the Turkevich reaction," *Aust. J. Chem.*, vol. 68, no. 6, pp. 858–862, 2015, doi: 10.1071/CH14446.

[288] J. Y. Ruzicka *et al.*, "Toward Control of Gold Cluster Aggregation on TiO2 via Surface Treatments," *J. Phys. Chem. C*, vol. 119, no. 43, pp. 24465–24474, 2015, doi: 10.1021/acs.jpcc.5b07732.

[289] D. Buso, J. Pacifico, A. Martucci, and P. Mulvaney, "Gold-nanoparticle-doped TiO2 semiconductor thin films: Optical characterization," *Adv. Funct. Mater.*, vol. 17, no. 3, pp. 347–354, 2007, doi: 10.1002/adfm.200600349.

[290] A. Ayati, A. Ahmadpour, F. F. Bamoharram, B. Tanhaei, M. Mänttäri, and M. Sillanpää, "A review on catalytic applications of Au/TiO2 nanoparticles in the removal of water pollutant," *Chemosphere*, vol. 107, pp. 163–174, 2014, doi: 10.1016/j.chemosphere.2014.01.040.

[291] E. Pedrueza *et al.*, "Novel method of preparation of gold-nanoparticle-doped TiO2 and SiO2 plasmonic thin films: Optical characterization and comparison with Maxwell-Garnett modeling," *Adv. Funct. Mater.*, vol. 21, no. 18, pp. 3502–3507, 2011, doi: 10.1002/adfm.201101020.

[292] F. Frederix *et al.*, "Biosensing Based on Light Absorption of Nanoscaled Gold and Silver Particles," *Anal. Chem.*, vol. 75, no. 24, pp. 6894–6900, 2003, doi: 10.1021/ac0346609.

[293] N. Chandrasekharan and P. Y. Kainat, "Improving the photoelectrochemical performance of nanostructured TiO2 films by adsorption of gold nanoparticles," *J. Phys. Chem. B*, vol. 104, no. 46, pp. 10851–10857, 2000, doi: 10.1021/jp0010029.

[294] P. Wongwisate, S. Chavadej, E. Gulari, T. Sreethawong, and P. Rangsunvigit, "Effects of monometallic and bimetallic Au-Ag supported on sol-gel TiO2 on photocatalytic degradation of 4-chlorophenol and its intermediates," *Desalination*, vol. 272, no. 1–3, pp. 154–163, 2011, doi: 10.1016/j.desal.2011.01.016.

[295] B. Tian, C. Li, F. Gu, and H. Jiang, "Synergetic effects of nitrogen doping and Au loading on enhancing the visible-light photocatalytic activity of nano-TiO2," *Catal. Commun.*, vol. 10, no. 6, pp. 925–929, 2009, doi: 10.1016/j.catcom.2008.12.029.

[296] D. Matthey *et al.*, "Enhanced bonding of gold nanoparticles on oxidized TiO2(110)," *Science (80-.).*, vol. 315, no. 5819, pp. 1692–1696, 2007, doi: 10.1126/science.1135752.

[297] C. M. Pharr and P. R. Griffiths, "Infrared Spectroelectrochemical Analysis of Adsorbed Hexacyanoferrate Species Formed during Potential Cycling in the Ferrocyanide/Ferricyanide Redox Couple," *Anal. Chem.*, vol. 69, no. 22, pp. 4673–

4679, 1997, doi: 10.1021/ac961120l.

[298] P. H. Daum and C. G. Enke, “Electrochemical Kinetics of the Ferri—Ferrocyanide Couple on Platinum,” *Anal. Chem.*, vol. 41, no. 4, pp. 653–656, 1969, doi: 10.1021/ac60273a007.

[299] P. A. Rock, “The standard oxidation potential of the ferrocyanide-ferricyanide electrode at 25° and the entropy of ferrocyanide ion,” *J. Phys. Chem.*, vol. 70, no. 2, pp. 576–580, 1966, doi: 10.1021/j100874a042.

[300] A. A. Shinkle, A. E. S. Sleightholme, L. T. Thompson, and C. W. Monroe, “Electrode kinetics in non-aqueous vanadium acetylacetonate redox flow batteries,” *J. Appl. Electrochem.*, vol. 41, no. 10, pp. 1191–1199, 2011, doi: 10.1007/s10800-011-0314-z.

[301] R. P. Mitra, D. V. S. Jain, A. K. Bannerjee, and K. V. Raghavachari, “Role of free radicals in the photo-oxidation of Fe+2 in acidic solutions of ferrocyanide [11],” *Nature*, vol. 200, no. 4902. pp. 163–164, 1963, doi: 10.1038/200163a0.

[302] S. Izawa and D. R. Ort, “Photooxidation of ferrocyanide and iodide ions and associated phosphorylation in NH2OH-treated chloroplasts,” *BBA - Bioenerg.*, vol. 357, no. 1, pp. 127–143, Jul. 1974, doi: 10.1016/0005-2728(74)90118-2.

[303] R. K. Clayton and S. C. Straley, “Photochemical Electron Transport in Photosynthetic Reaction Centers: IV. Observations Related to the Reduced Photoproducts,” *Biophys. J.*, vol. 12, no. 10, pp. 1221–1234, 1972, doi: 10.1016/S0006-3495(72)86158-7.

[304] S. J. Konopka and B. McDuffie, “Diffusion Coefficients of Ferri- and Ferrocyanide Ions in Aqueous Media, Using Twin-Electrode Thin-Layer Electrochemistry,” *Anal. Chem.*, vol. 42, no. 14, pp. 1741–1746, 1970, doi: 10.1021/ac50160a042.

[305] A. A. Shinkle, A. E. S. Sleightholme, L. D. Griffith, L. T. Thompson, and C. W. Monroe, “Degradation mechanisms in the non-aqueous vanadium acetylacetonate redox flow battery,” in *Journal of Power Sources*, May 2012, vol. 206, pp. 490–496, doi: 10.1016/j.jpowsour.2010.12.096.

[306] Q. Liu, A. E. S. Sleightholme, A. A. Shinkle, Y. Li, and L. T. Thompson, “Non-aqueous vanadium acetylacetonate electrolyte for redox flow batteries,” *Electrochem. commun.*, vol. 11, no. 12, pp. 2312–2315, Dec. 2009, doi: 10.1016/j.elecom.2009.10.006.

[307] D. P. Anderson *et al.*, “Chemically-synthesised, atomically-precise gold clusters deposited and activated on titania,” *Phys. Chem. Chem. Phys.*, vol. 15, no. 11, pp. 3917–3929, 2013, doi: 10.1039/c3cp44005b.

[308] Y. Shichibu and K. Konishi, “HCL-induced nuclearity convergence in diphosphine-protected ultrasmall gold clusters: A novel synthetic route to ‘Magic-Number’ Au13

clusters," *Small*, vol. 6, no. 11, pp. 1216–1220, 2010, doi: 10.1002/smll.200902398.

[309] X. K. Wan, S. F. Yuan, Z. W. Lin, and Q. M. Wang, "A chiral gold nanocluster Au20 protected by tetradentate phosphine ligands," *Angew. Chemie - Int. Ed.*, vol. 53, no. 11, pp. 2923–2926, 2014, doi: 10.1002/anie.201308599.

[310] W. W. Weare, S. M. Reed, M. G. Warner, and J. E. Hutchison, "Improved synthesis of small (dCORE ≈ 1.5 nm) phosphine-stabilized gold nanoparticies [14]," *J. Am. Chem. Soc.*, vol. 122, no. 51, pp. 12890–12891, 2000, doi: 10.1021/ja002673n.

Appendix A

Solvent characteristics

The solvent characteristics are shown in the table F.1:

Solvent	Boiling temperature	refractive index	dipole moment (D)	viscosity (mPa s)
Water	100 ºC	1.332	1.84	0.8937 (at 25 ºC)
Ethanol	79 ºC	1.611	1.69	1.074 (at 25 ºC)
Isopropanol	82.6 ºC	1.378	1.66	1.96 (at 25 ºC)
Terpineol	217 ºC	1.482		
Ethylene glycol	197.3 ºC	1.431		
Butanol	117 ºC	1.399	1.66	2.52 (at 25 ºC)

TABLE F.1: different solvent characteristics

Appendix B: list of materials

G.1 Electrolyte material

$VOSO_4$: Vanadium (IV) sulfate oxide hydrate 99.9%, Alfa Aesar.

VCl_3: Vanadium (III) chloride 97%, Sigma Aldrich.

$FeSO_4$: Iron (II) sulfate 7-hydrate, Analytical reagent, BDH.

$K_4Fe(CN)_6$: Potassium Ferrocynide, AMALAR.

Potassium Nitrate: Potassium Nitrate, Analytical reagent, UNIVAR.

H_2SO_4: Sulfuric Acid, UNIVAR.

G.2 Semiconductor layers material

TiO_2 P-25: Titanium dioxide P-25, Degussa.

Titanium isopropoxide: Titanium (IV) isopropoxide 97%, Sigma Aldrich.

Titanium butoxide: Titanium (IV) butoxide 97%, Sigma Aldrich.

SBR: Styrene Butadiene Rubber binder for Li-ion battery anode, MTI.

CMC: Carboxyl Methyl Cellulose sodium salt, medium viscosity, Sigma Aldrich.

SiC: Silicon Carbide nanopowder (SiC, >99%, 45 - 65 nm, cubic), US research Nanomaterials, Inc.

G.3 Solvents

Terpineol: Terpineol 90%, Sigma Aldrich.

Ethanol: Ethanol Absolute, analytical grade, Lab Serv.

Isopropanol: Propan-2-ol, analytical reagent grade, Fisher.

Butanol: Butan-2-ol BDH.

Polyethylene glycol: Terpineol 90%, Sigma Aldrich.

Acetone: Acetone, analytical reagent grade, Fisher.

Methanol: Methanol HPLC grade, Fisher.

Ethylene glycol: Ethylene glycol, Malinkrodt.

Appendix C: deposition process Supplementary Information

a. Deposition process

The two different deposition processes used were the airbrush spray deposition and the ultrasonic spray deposition.

Airbrush spray deposition: The airbrush deposition is a primary deposition method used in painting or for creating some carbon electrodes. The liquid solution was sprayed by airflow which blowed droplets on a heat FTO substrate with a mask for depositing a specific area (Figures S.1). The airflow was controlled by the air pressure choose in entrance of the spray gun and by the position of the trigger. For all the experiment, the trigger was at its maximum and so leted the air entirely pass by the nozzle. The solution was filled into the tank, and the deposition pattern was created by a controller which piloted the left/right and the up/down tray. The controller created a deposition pattern corresponding to twice the mask openings to surely cover all the area. The mask wass composed of three oblong holes of 1 cm^2 to avoid a shadowing effect. The mask was screwed to a support which contained the three FTO slides and to the hot plate. The temperature can be changed by using a controller link to a temperature probe inside the hotplate. The issue of this method was a lack of reproducibility due to the airflow forming the droplets and a control of the amount deposit not precise enough.

a)

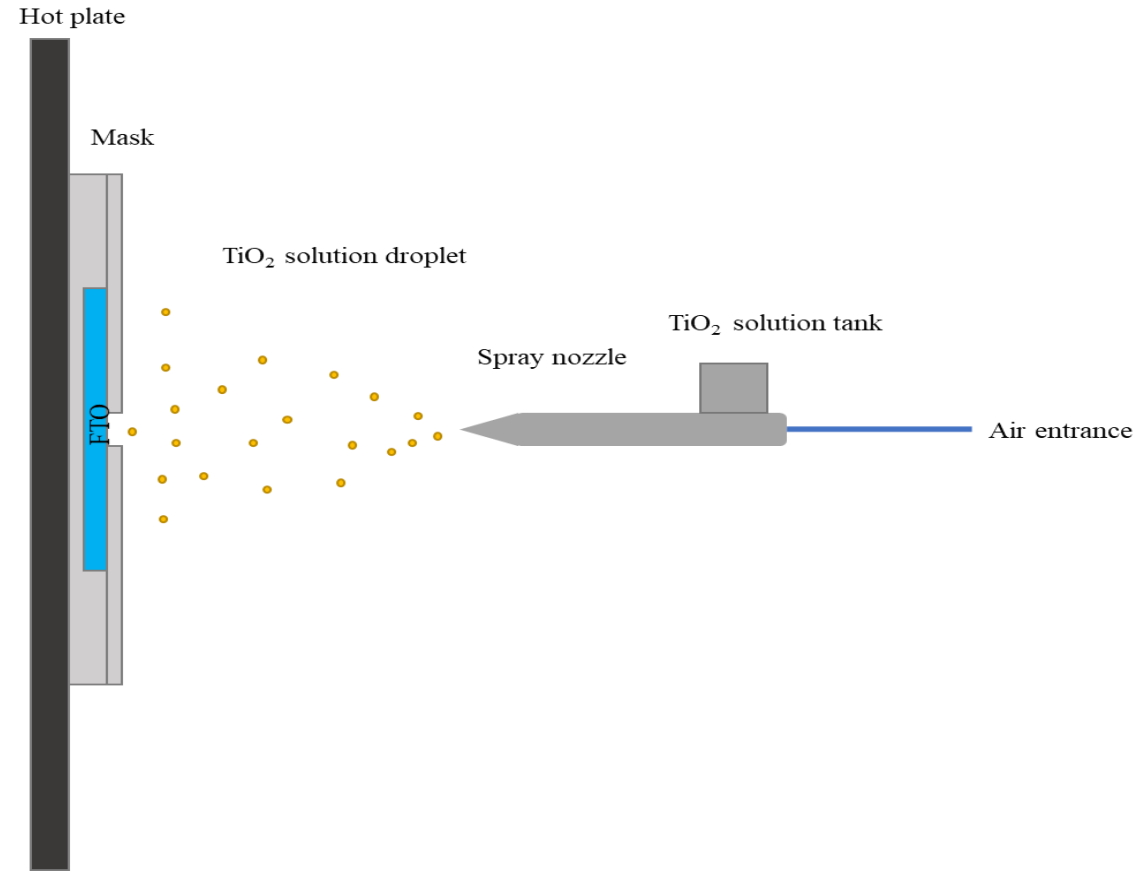

b)

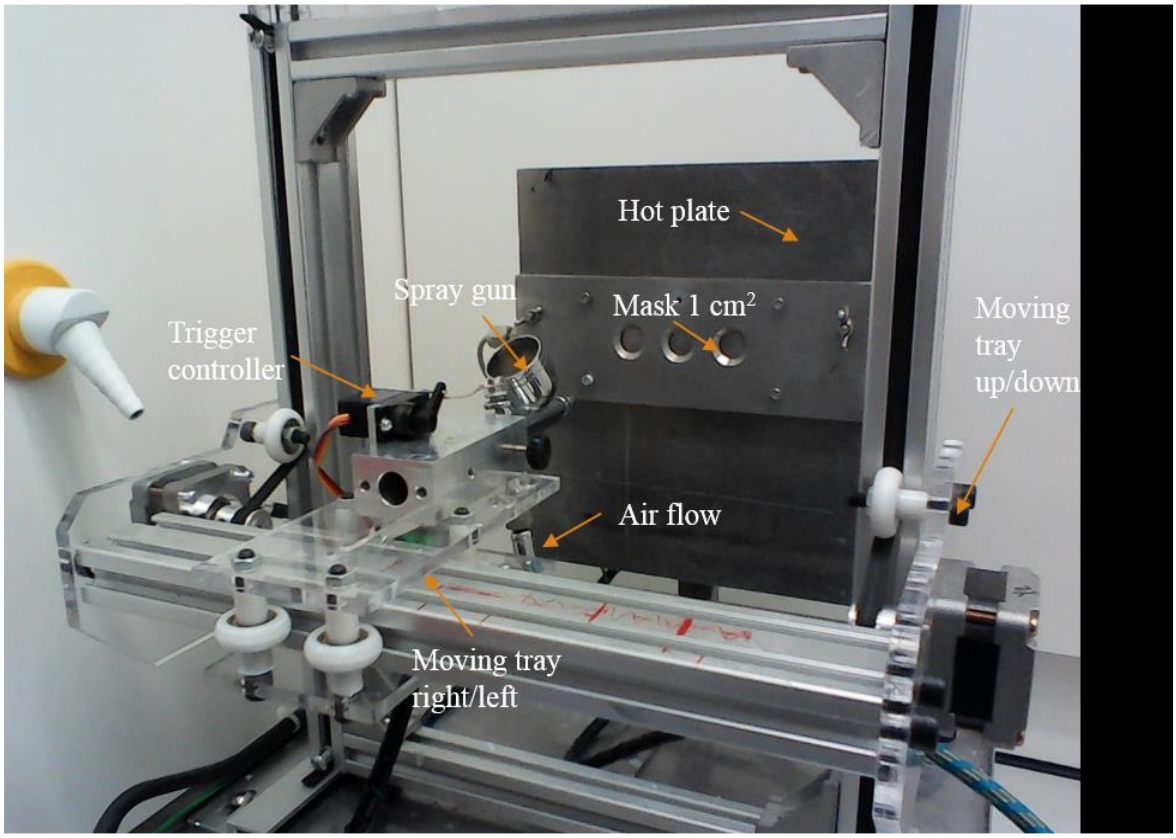

Figures S.1: a) scheme and b) picture of the automatic airbrush spray deposition process.

Ultrasonic spray deposition: The ultrasonic spray deposition is a variation of the previous deposition process, the airbrush spray coating. The liquid solution was sprayed ,this time not by airflow but by an ultrasonic signal, which formed a mist and pushed the droplets on the substrate (Figures S.2). Airflow was still used but only to guide the mist straight avoiding asignificant effect of the external airflow changes. The airflow was 30 mm min^{-1}. The ultrasonic nozzle (Sonozap) received a signal of 60 kHz. The solution was feed by a syringe pump (New Era Pump System Inc.) at 1 mL min^{-1}. The hot plate was placed under the spray nozzle to help by gravity the droplet to reach the substrate. The reproducibility of this method increased compare to the airbrush spray and allowed the use of titanium isopropoxide very sensitive to moisture which could be presented in the compressed air of the airbrush spray.

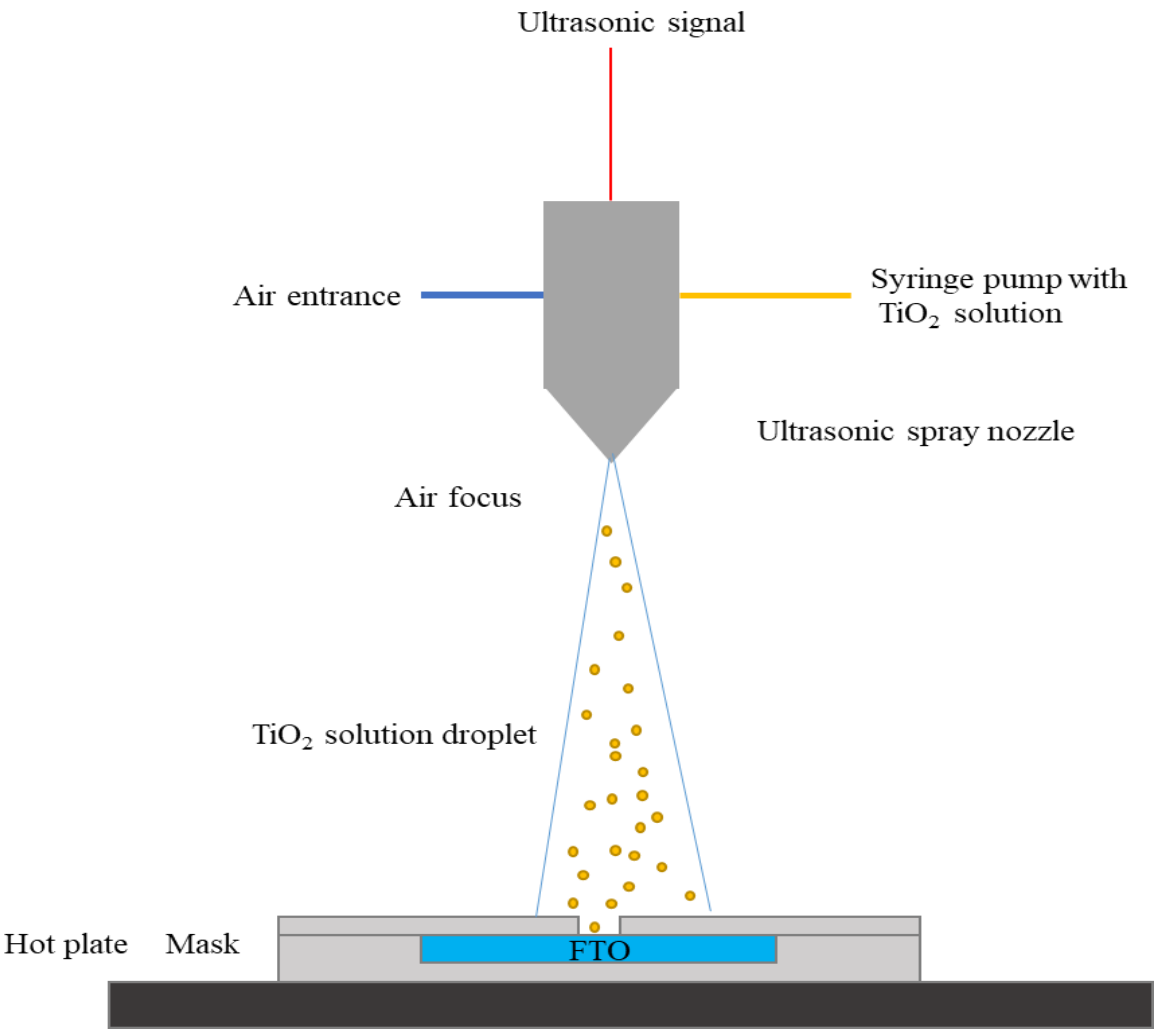

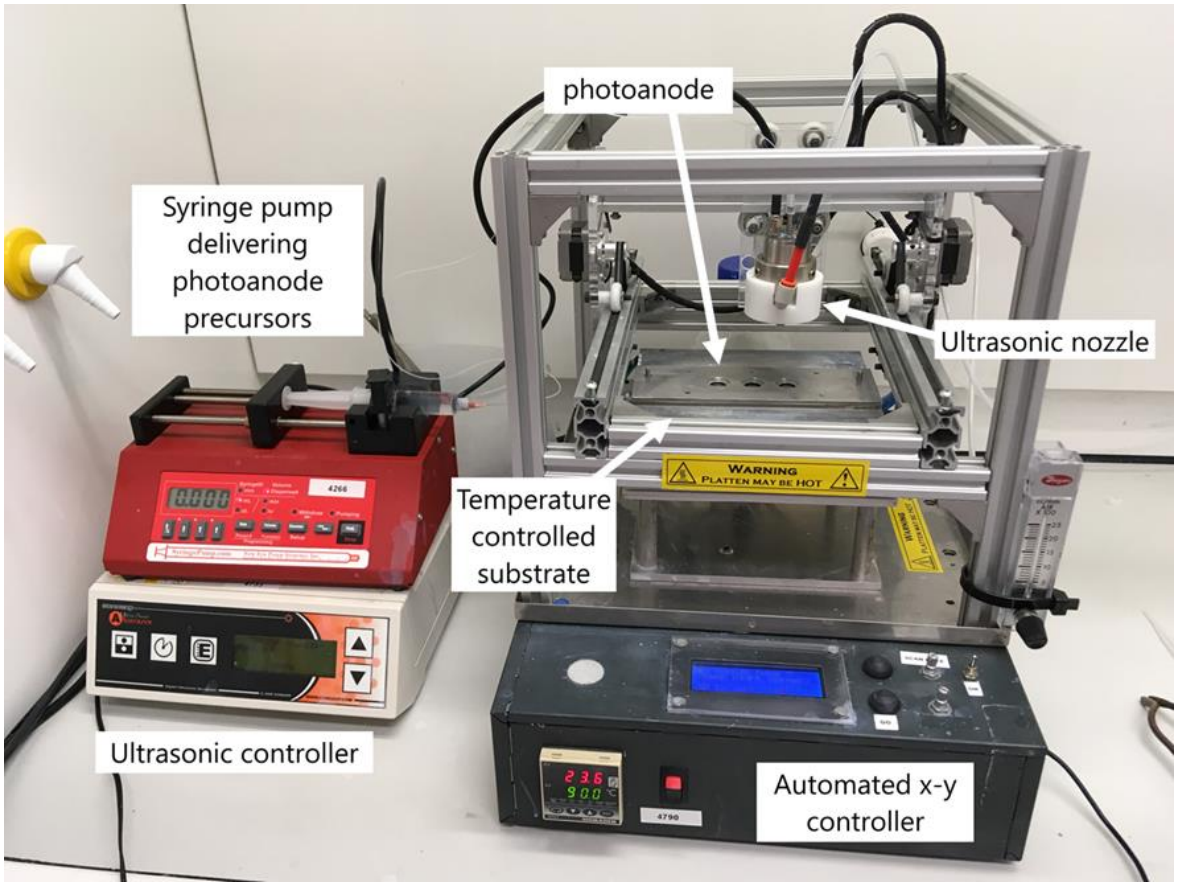

Figures S.2: a) schem and b) picture of the automatic ultrasonic spray deposition process.

b. Photoelectrochemical test

The photoelectrochemical test was composed of two glasses cell connected with a 117 Nafion membrane (Figure S.3). The photoanode was pressed against in the neck of the positive half cell. This half cell was filled with a 0.1 M $VOSO_4$ solution dissolved in 0.5 M H_2SO_4. The negative half cell was composed of an 0.5 M H_2SO_4 solution. Three electrode setup: the working electrode was the photoelectrode clip with small crocodile clip to the potentiostat (Gamry instrument 3000) then the reference electrode (Ag|AgCl) was deep in the positive half cell electrolyte. Finally, the counter electrode was composed of a Pt wire place in the negative half cell electrolyte.

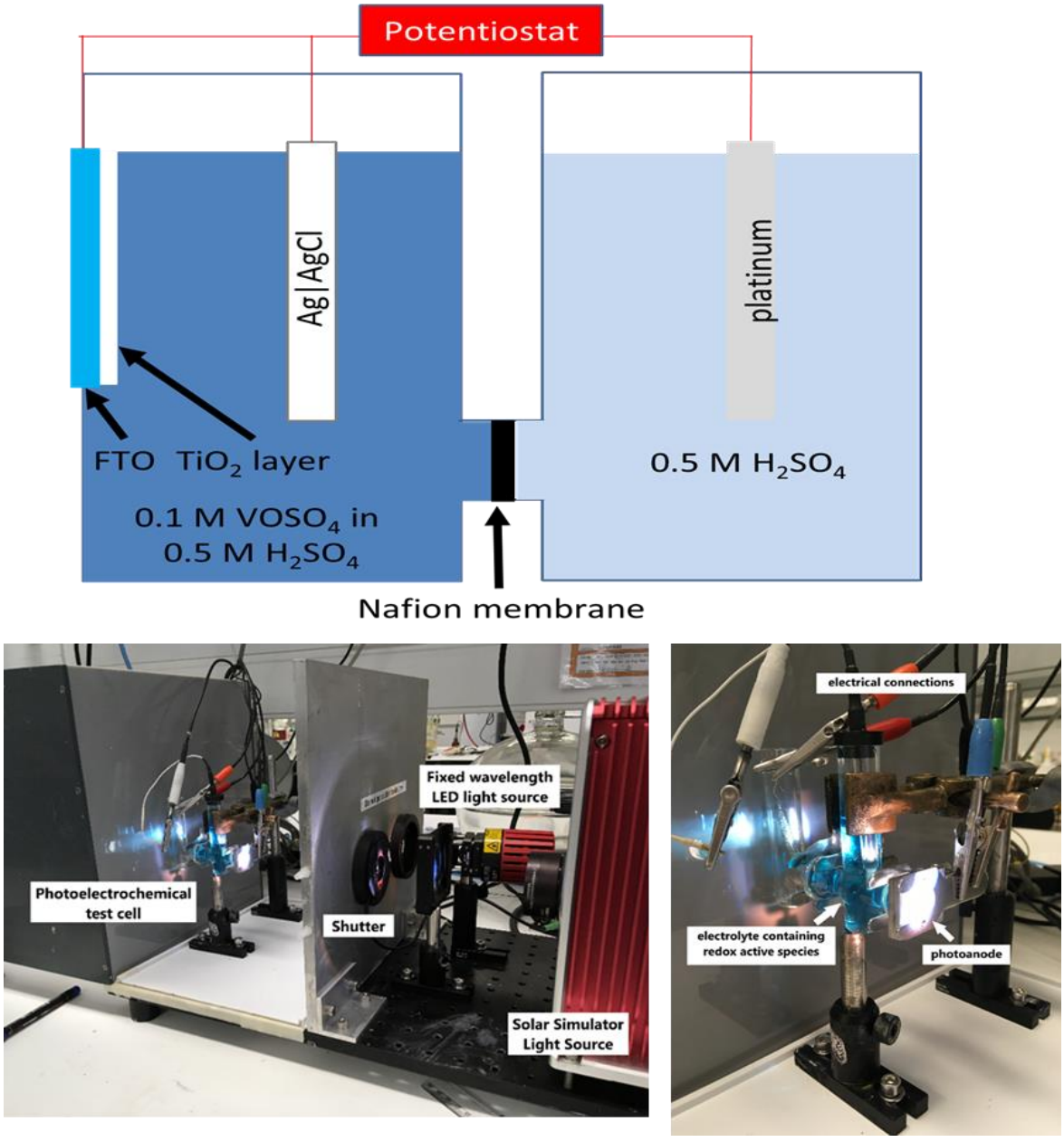

Figures S.3: a) schem and b) picture of the photoelectrochemical test bench

c. Characterisation

The use analytical instruments for the characterisation are mentioned below:

Scanning Electron Microscopy: The microstructure and surface morphology of the gold clusters on carbon paper samples were recorded by SEM instrument (JEOL JSM-7000 F) operating at accelerating voltage of 15 kV.

d. Materials

All the necessary chemicals were purchased from well-established suppliers (Merck, Fisher chemical and Sigma Aldrich) and used without any further purification. The solvents were methanol, absolute ethanol (Fisher), propan-2-ol (UNIVAR, analytical grade), butan-2-ol (UNIVAR), butan-1-ol (UNIVAR) and Milli Q water. The titanium isopropoxide was supplied

by Sigma Aldrich, and its purity is > 97%. TiO_2 powder used was P-25 Degussa with a purity of 99.9%, and average particles size of 20 nm. This powder is composed of 85% of anatase TiO_2 and 15% of rutile. The FTO TEC 10 glasses were purchased from Odissa unpattern with a size of 20 mm x 15 mm and a thickness of 1.1 mm. The resistance of the FTO layer was 9.39 $\pm$ 0.16 $\Omega.s^{-1}$.

Appendix D: Materials and methods for produced Au nanoclusters

All the necessary chemicals were purchased from well-established suppliers (Merck, Fisher chemical and Sigma Aldrich) and used without any further purification. FTO slides were purchased from Ossila

$[Au_6(dppp)_4](NO_3)_2$: $[Au_6(dppp)_4](NO_3)_2$ was synthesised following the method reported in the literature. Briefly, 100 mg of $[Au_9(PPh_3)_8](NO_3)_3$ was dissolved in 10 mL dichloromethane (DCM). 200 mg of 1,3-bis(diphenylphosphino)propane (20-fold molar excess) dissolved in 5 mL DCM was added to the stirring solution. The colour of the solution change from reddish to orangish briefly and immediately changed to blue, indicating the ligand exchange. The reaction mixture was further stirred for 30 minutes prior to subsequent pouring into a 100 mL petroleum ether. The obtained product was precipitated at 0 ˚C overnight. The blue colour solids were then collected by centrifugation. The product was washed with petroleum ether (2 × 20 mL), a 9:1 petroleum ether / CH_2Cl_2 mixture (2 × 10 mL) and finally by diethyl ether (3 × 20 mL). The product was dissolved in 5 mL of methanol and crystallised by vapour diffusion of 40 mL of diethyl ether (Et_2O) over a week in 60 mL jar. The yield of product was ca. 50 mg (*ca.* 46.33% yield by gold atom). The identity of the cluster was confirmed by ^{31}P-NMR (in CD_3OD) with two singlets of equal intensity at δ_1 = 54 ppm and δ_2 = 62 ppm (w.r.t. 85% H_3PO_4) (Figure A1). The UV-Vis absorption spectrum of the cluster has peaks at 325, 430, 507 and 589 nm.

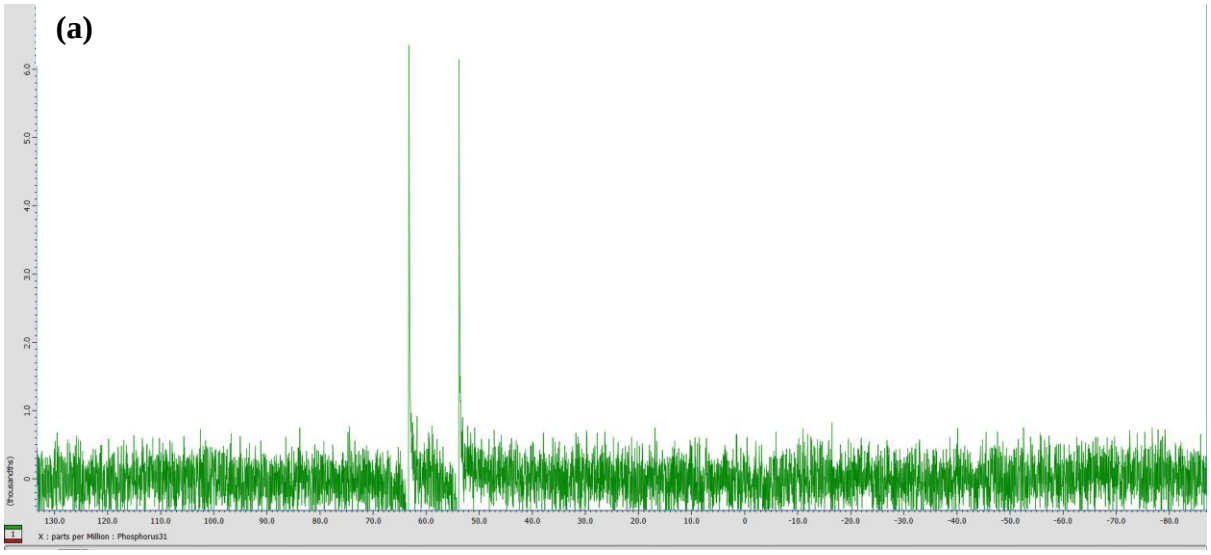

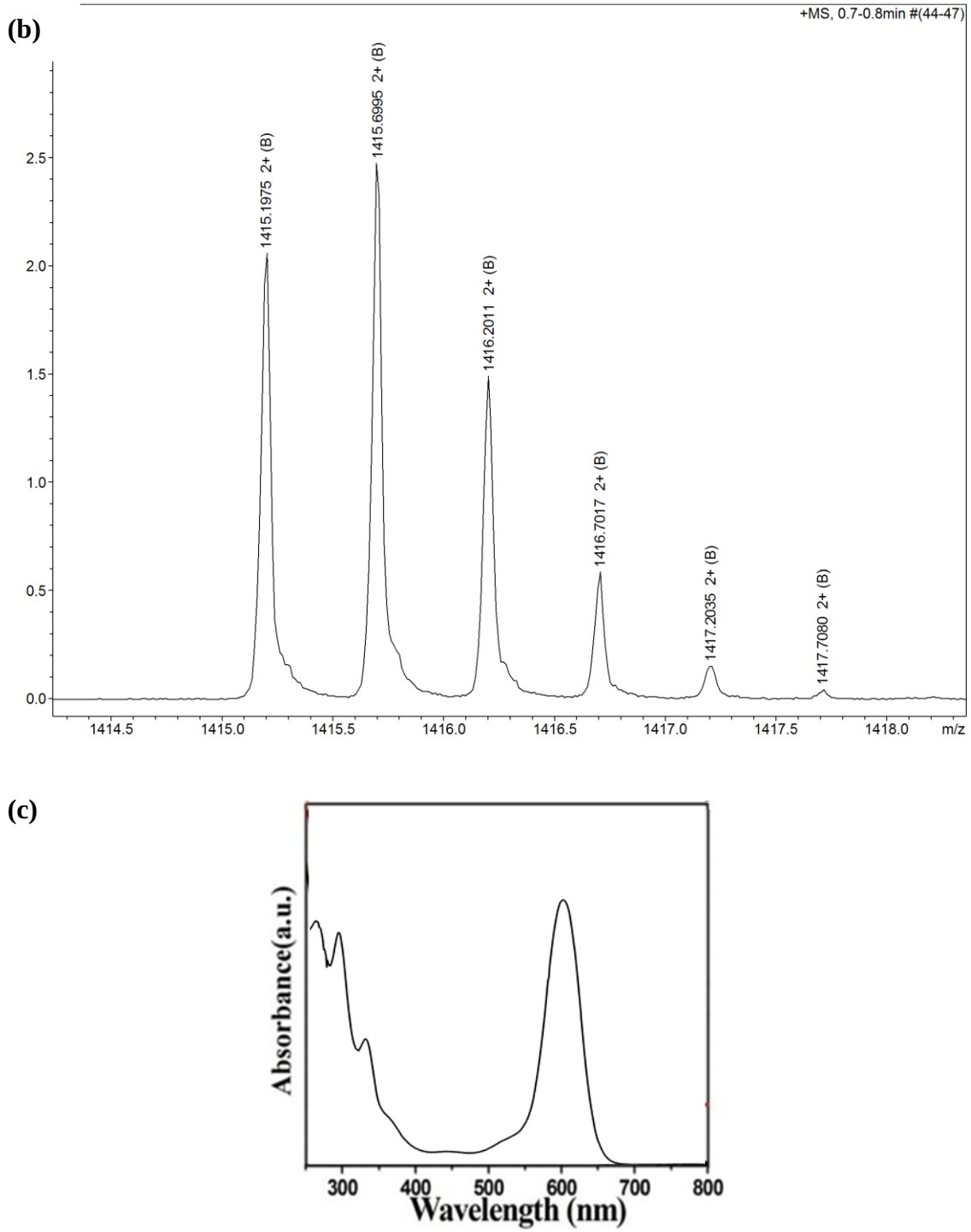

Figure A1: (a) ^{31}P-NMR of $[Au_6(dppp)_4](NO_3)_2$ (b) ESI-MS of $[Au_6(dppp)_4](NO_3)_2$ (c) UV-Vis spectrum of $[Au_6(dppp)_4](NO_3)_2$.

$[Au_9(PPh_3)_8](NO_3)_3$: $[Au_9(PPh_3)_8](NO_3)_3$ was prepared following a report from Anderson *et al.* [313]. 1 g of gold phosphine nitrate ($AuPPh_3NO_3$) was dissolved in 75 mL ethanol. 18 mg $NaBH_4$ dissolved in 5 mL ethanol was added to the reaction mixture. The colour of the solution immediately change to red prior to quickly turning to deep red. The reaction mixture was stirred for 3 hours. The red colour mixture was centrifuged, any solid was discarded. The supernatant

was dried using a rotary evaporator. The crude product was dissolved in 25 mL dichloromethane, centrifuged; any solids discarded. The solvent was removed under reduced pressure using a rotary evaporator without heating. The red colour residue was washed with 2 × 25 mL tetrahydrofuran (THF) yielding a green colour product. This green colour product was further washed with 3 × 25mL petroleum ether. The crude product was dried prior to dissolving in 10 mL methanol and crystallising *via* vapour diffusion crystallisation using 60 mL diethyl ether in an 80 mL jar over a week. The obtained crystal was washed with diethyl ether (Et_2O) and dried in vacuum. The yield of $[Au_9(PPh_3)_8](NO_3)_3$ was 190 mg (*ca.*23 % by Au atom). The identity of the cluster was confirmed by ^{31}P-NMR in $CDCl_3$ with a single peak at $\delta = 57$ ppm (w.r.t. 85% H_3PO_4), and presence of $[Au_9(PPh_3)_8]^{3+}$ (m/z ≈ 1240) in ESI-MS. The UV-Vis absorption was observed at 442, 424, 354 and 316 nm (Figure A2).

(a)

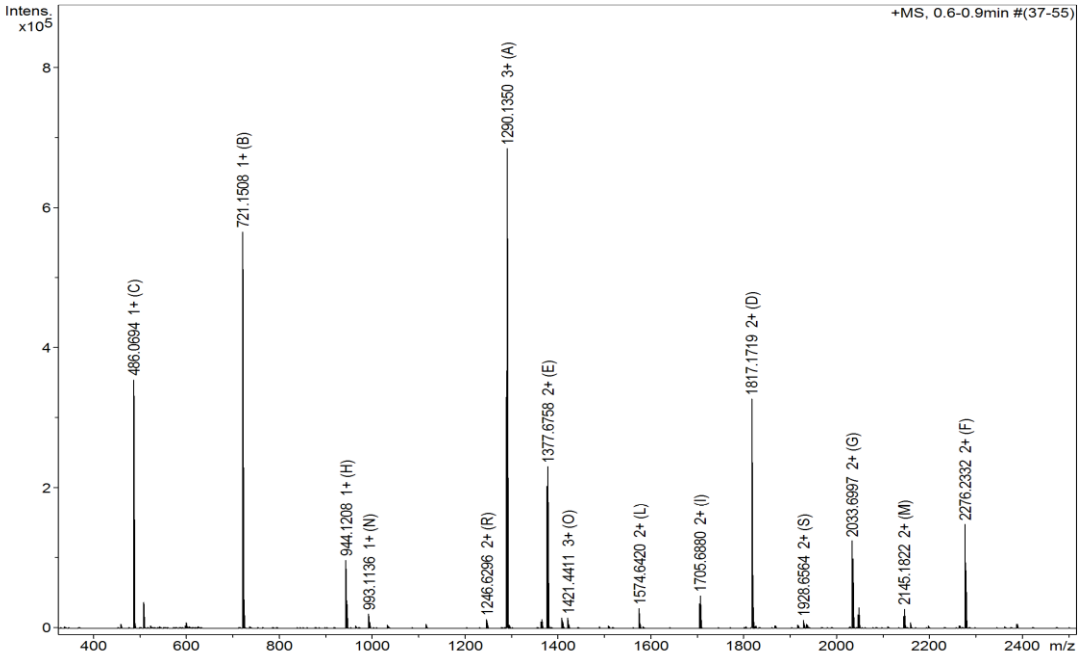

(b)

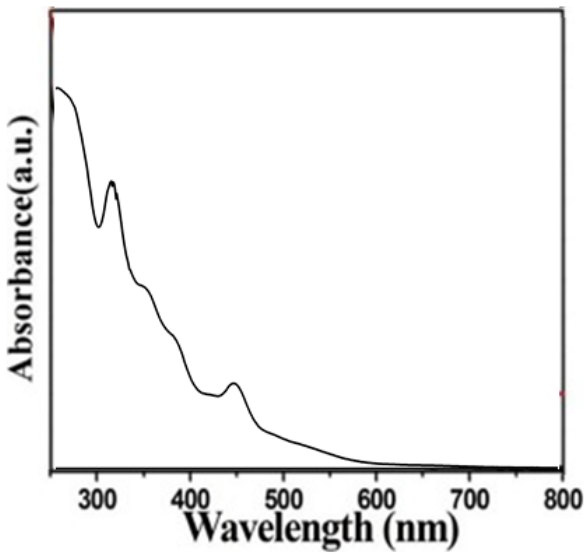

Figure A2: (a) ESI-MS of $Au_9(PPh_3)_8](NO_3)_3$ (b) UV-Vis spectrum of $[Au_9(PPh_3)_8](NO_3)_3$.

$[Au_{11}(PPh_3)_8]\ NO_3Cl_2$

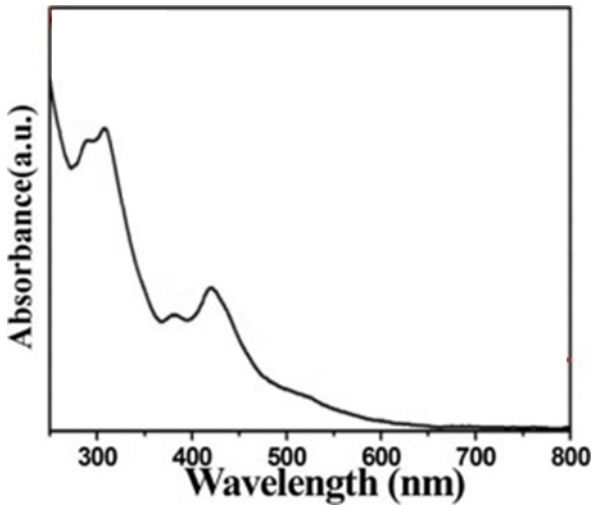

Figure A3: UV-Vis spectrum of $[Au_{13}(dppe)_5Cl_2]Cl_3$.

$[Au_{13}(dppe)_5Cl_2]Cl_3$: Synthesis of $[Au_{13}(dppe)_5Cl_2]Cl_3$ was performed following the method reported by Shichibu and Konishi [314]. 300 mg of $Au_2(dppe)Cl_2$ was dissolved in 240 mL, and then $NaBH_4$ (66 mg) suspension in ethanol (10 mL) was added to this solution. The colour of the solution changed from colourless to dark red, the stirring continued for 3 hours. The

reaction mixture was centrifuged (any solids discarded) and the supernatant was dried by rotary evaporation. The product was extracted using ethanol (50 mL), centrifuged and 1 mL of neat HCl was added and stirred overnight. The solvent was removed using a rotary evaporator; the product was then precipitated from diethyl ether (100 mL) overnight at 0 ˚C. ^{31}P-NMR of the crude product in CD_3OD showed a peak at $\delta = 37$ ppm, indicating the presence of $Au_2dppeCl_2$. The product was precipitated in Et_2O and washed with 9:1 petroleum ether/DCM mixture (4 × 50 mL). Finally, the product was dissolved in methanol (8 mL) and crystallised *via* vapour diffusion of diethyl ether (50 mL) in a 100 mL jar for seven days. The yield of product was *ca.* 70 mg (*ca.* 28% by Au atom). The identity of the cluster was confirmed using ^{31}P-NMR (Figure A3) and ESI-MS (m/z = 1541 corresponding $[Au_{13}(dppe)_5Cl_2]^{3+}$). The UV-Vis spectrum showed the peaks at 306, 366 and 486 nm.

(a)

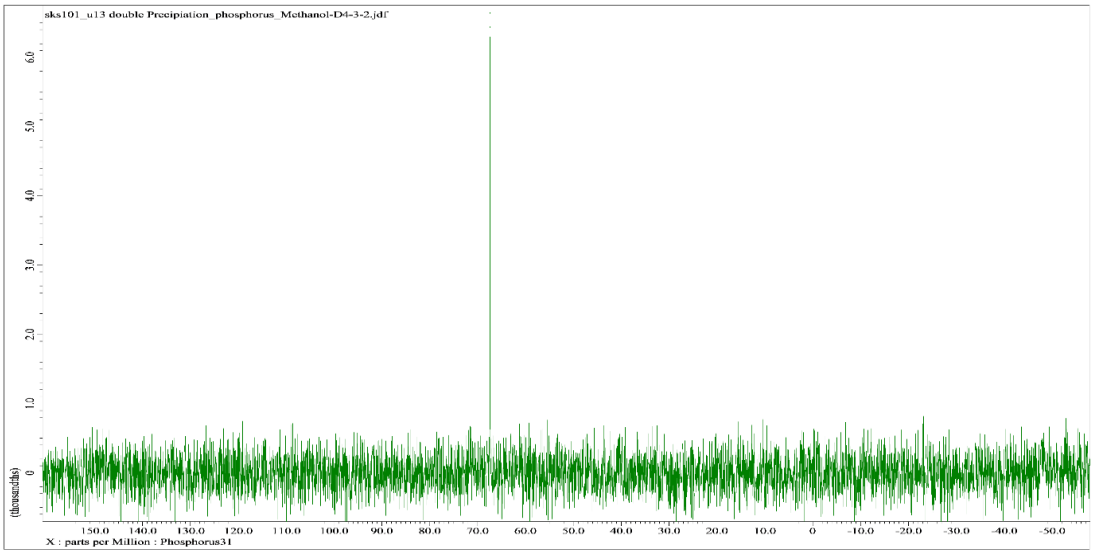

(b)

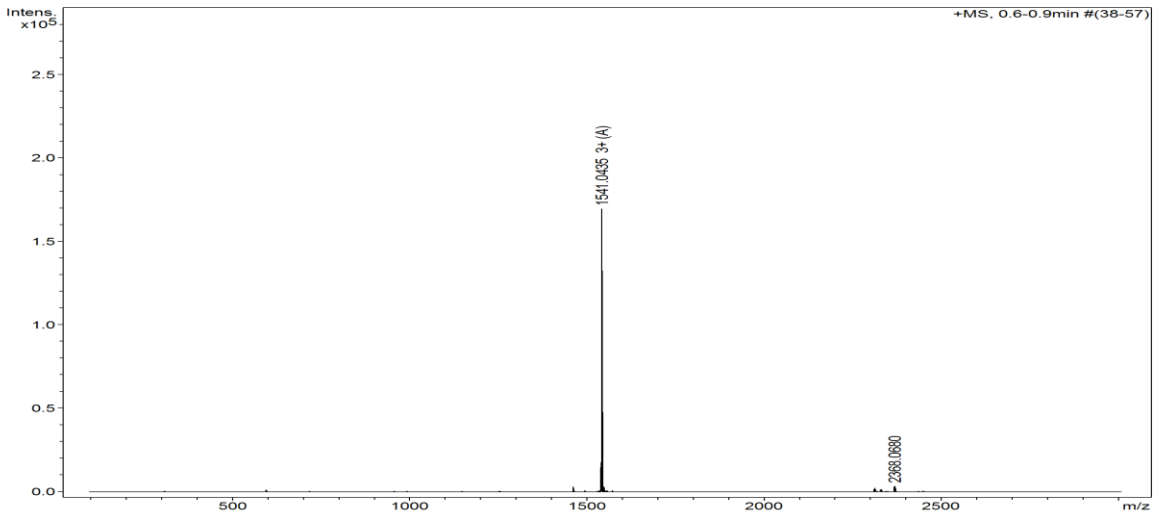

(c)

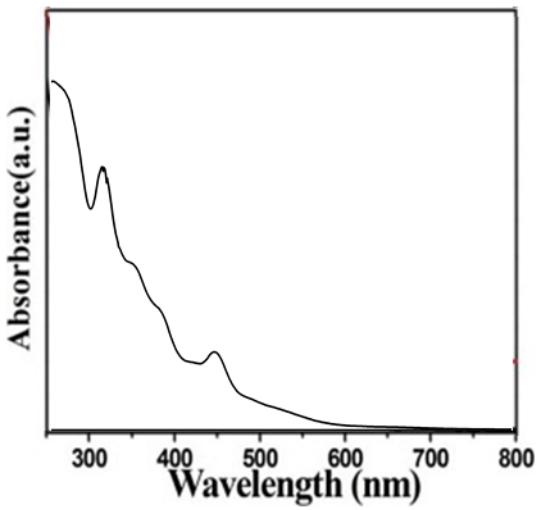

Figure A4: (a) ^{31}P-MR of Au_{13}, (b) ESI-MS spectrum of $[Au_{13}(dppe)_5Cl_2]Cl_3$ (c) UV-Vis spectrum of $[Au_{13}(dppe)_5Cl_2]Cl_3$.

$[Au_{20}(PP_3)_4]$ Cl_4 was synthesised according to the previous procedure detailed by Wan *et al.*[315] Reaction was performed in the absence of light. A solution of $NaBH_4$ (22.1 mg in 3.0 ml EtOH) was added dropwise to a solution of $[Au_4(PP_3)](Cl)_4$ (93.4 mg) in DCM (80 ml) under stirring (900 rpm). The mixture was then stirred for 10 hrs. The solution was then evaporated to dryness using reduced pressure evaporation to give a black solid. The solid was dissolved in DCM (3.0 ml) and MeOH (0.1 ml), and the solution was centrifuged at 10000 rpm for 4 min. The brown supernatant was poured off and filtered, and a dark solid precipitated with the addition of excess n-pentane. The mixture was then centrifuged at 10000 rpm for 10 min and the supernatant poured off leaving a dark solid. This dissolution-precipitation procedure was repeated until the supernatant became colourless which yielded $[Au_{20}(PP_3)_4](Cl)_4$. $[Au_{20}(PP_3)_4](Cl)_4$ spectrum was recorded in $CDCl_3$. The ^{31}P-NMR gave a singlet at δ 64.01 ppm, singlet at δ 54.62 ppm, a quadruplet at δ 47.63 ppm, a singlet at δ 40.50 ppm, a singlet at δ 37.94 ppm, a singlet at δ 32.00 ppm, and a singlet at δ 18.40 ppm.

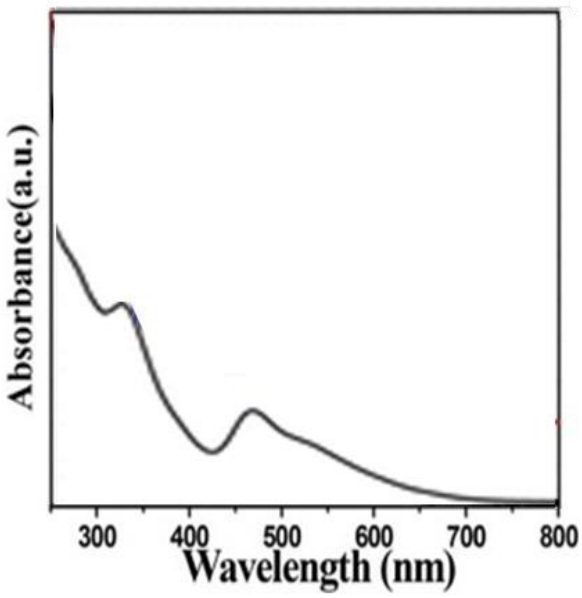

Figure A5: UV-Vis spectrum of $[Au_{20}(PP_3)_4]$ Cl_4.

1.5 nm gold cluster $Au_{101}(PPh_3)_{25}Cl_5$: $Au_{101}(PPh_3)_{25}Cl_5$ was synthesised following the method reported by Anderson *et al.*[313], [316]. Chloroauric acid (1 g) was dissolved in 60 mL of water, and 60 mL toluene added. 1.4 g tetraoctylammonium bromide was added to stirring solution as the phase transfer agent. After 10 minutes of stirring, 2.3 g triphenyl phosphine added changed the colour of the solution to dark red. The reaction mixture was stirred for 3 hours. The organic phase was separated using a funnel and washed with aqueous NaCl saturated solution (2 × 50mL) and water (3 × 50mL). The organic phase was dried using a rotary evaporator without heating. The product was dissolved in 35 mL chloroform, centrifuged (any solid discarded), and precipitated in 500 mL pentane at 0 ˚C. The precipitate was collected with centrifugation and washed with various solvent/solvent-mixtures to remove $AuPPh_3Cl$ impurities as follows.

100 mL hexanes followed by 100 mL 2: 3 MeOH: H_2O (two times)

100 mL hexanes followed by 100 mL 1: 1 MeOH: H2O (two times)

150 mL 3: 1 pentane: chloroform (two times)

150 mL 2: 1 pentane: chloroform (two times)

150 mL 1: 1 pentane: chloroform (two times)

Finally, the crude product was dissolved in 30 mL chloroform, centrifuged (any solid discarded) and dried under reduced pressure. The purity of the product was studied with ^{1}H-NMR spectra of the product Total of 240 mg (*ca.* 47% yield by Au atom) clusters was obtained.